Multistage Polymer Networks for Designing Optical and Optically Processed Materials

by

ALEXANDER J. OSTERBAAN

B.S., Hope College, 2020

M.S., University of Colorado Boulder, 2022

A thesis submitted to the

Faculty of the Graduate School of the

University of Colorado in partial fulfillment

of the requirement for the degree of

Doctor of Philosophy

Department of Chemical and Biological Engineering

2025

Committee Members:

Dr. Christopher N. Bowman

Dr. Ryan C. Hayward

Dr. Timothy J. White

Dr. Robert R. McLeod

Dr. Jeffrey W. Stansbury

ABSTRACT

Osterbaan, Alexander (Ph.D., Department of Chemical and Biological Engineering)

Multistage Polymer Networks for Designing Optical and Optically Processed Materials

Thesis directed by Professor Christopher N. Bowman

This thesis explores the design of multistage polymer networks to separate desirable end-use properties from those optimal for processing purposes. Sequential control of light, heat, or other external stimuli enables this feat. Additional control is provided by spatial patterning of light as employed in the fields of holography, mechanophotopatterning, and volumetric additive manufacturing. Therefore, by comparing mechanical, geometrical, and optical properties throughout the stages of production, this work demonstrates the benefit of a multistep approach.

The first part of this thesis pertains to the implementation of a 3-stage network to prepare glassy holographic photopolymers. In Chapter 3, the combination of a urethane matrix, acrylate writing monomer, and a latent rigid core epoxide, enabled holographic writing in the desired rubbery state. Subsequent epoxide activation resulted in a final T_g of 101 °C with a storage modulus on the order of GPa at ambient temperature. A corresponding diffraction efficiency of 89% with 0.3% haze was achieved in 50 μm thin films.

The second part of this thesis focuses on the use of a dual-cure approach to spatially fix the topography of mechanophotopatterned films. In Chapter 4, this work prevented further

topographical evolution via allyl sulfide dynamics by increasing the crosslinking density and T_g following patterning. The inclusion of 65 wt% bisphenol A diglycidyl ether mitigated the residual dynamics upon homopolymerization with a thermally latent acid. Surface features fixed by this cure remain within 1% of their original height after extended light exposure. Furthermore, in Chapter 5, the dual-cure system was employed to provide spatially fixed and consistent results to validate a computational model.

The final part of this thesis employs a multistage approach to prepare a negative photoresist for VAM. In Chapter 6, a polyurethane scaffold with degradable thioester linkages was combined with a variety of low-viscosity methacrylate writing monomers. Therefore, this scaffold provides accessibility to these monomers, and the mechanical properties they provide, without object settling due to gravity during the printing process. The scaffolding was later removed by aminolysis with little damage to the printed parts or their mechanical properties. Further, added inhibitor and real-time chemical and mechanical monitoring enabled high resolution printing with consistent timing.

DEDICATION

For Elizabeth

Acknowledgements

This was not a solo quest. I am eternally thankful for the support, collaboration, advice, and wisdom provided by all those who have surrounded me in the endeavor. First, I thank my advisor, Dr. Christopher Bowman, for guiding me through this process. In retrospect I am thankful for the entire range of feedback, from encouraging me when I desperately needed to know there was a path forward, to taking me down a peg when I needed that most. Additionally, I would like to thank the rest of my committee members, Dr. Timothy White, Dr. Robert McLeod, Dr. Jeffrey Stansbury, and particularly Dr. Ryan Hayward who co-advised me for the early years of this journey.

My gratitude runs deeply for the members of the Bowman lab. Dr. Marianela Trujillo-Lemon, I greatly appreciate your kindness and joy for all things synthesis. You took the time needed; and have thus passed on a calm spirit to safely and successfully make materials that were originally out of my comfort zone. Dr. Benjamin Fairbanks, your input was paramount in learning how to think critically about the little things. You were always ready and willing to provide advice ranging from tweaking a large design to providing a small sanity check. Dr. Meagan Arguien, your scientific input was fantastic; however, I would like to take this moment to highlight the laughs and moments of mutual understanding. This must have stemmed from developing ourselves in the same crucible, and it helped maintain the necessary sanity to continue forward. Zack Mora, I was excited to have you as a mentee, but am now happy to call you both peer and friend— You got this!

The bond formed with the McLeod lab can also not be understated. Andrew Sias and Gabe Seymour, it has been an absolute pleasure to work with you both. I greatly appreciate how we can approach problems from wildly different backgrounds to enhance both of our fields. When I call Elizabeth walking back from SEEC, she instantly knows if I just talked with one or both of you based solely on the joy and energy in my voice.

To my Woodford family: Thank you for your unending support for both Elizabeth and me as we navigated this season together. You all have been a blessing in vastly more ways than I can articulate.

To my parents: From when I was a boy and you taught math games to now, you have always pushed me to succeed. You not only embraced, but fostered, my inner nerd with open arms. I am eternally grateful for everything that you have put in to nurture me to be me.

Elizabeth— I could not have done this without you. Not because you dramatically improve my writing (which is also true), but because of the daily support. You celebrated with me in the highest highs and helped me in the lowest lows. Your counsel is of immeasurable value. You engaged in the hard job supporting me doing a Ph.D. and that means the world.

Table of Contents

LIST OF TABLES

LIST OF SCHEMES

LIST OF FIGURES

Chapter 1: Introduction

1.1 Overview

The global value of photopolymers is currently in the billions and continues to grow at a rapid pace.[1] A wide array of light-induced reactions provide key benefits as reactions are rapidly triggered under ambient conditions with spatiotemporal control. These benefits beget the wide implementation in industries including adhesives, microelectronics, dentistry, coatings, and additive manufacturing.[2–5] Processing these materials is as facile as pour and cure, to as precise as integrated circuit preparation, two photon printing, and beyond. The importance of capable materials design to leverage the available processing methodologies to their highest potential cannot be understated.

1.2 Background

Photons in the visible or UV range provide two orders of magnitude more energy at ambient conditions than thermal energy.[6] The ability to harness this photo-energy to perform multiple reactions is the key to the majority of photopolymerizations. These processes are divided into the steps of initiation, propagation, and termination,[7] as shown in Figure 1.1. In the initiation step, light is absorbed by a chromophore in order to create an active center. This process are done directly by cleaving a bond, or indirectly by interacting with another species to produce the active center.[8,9] Commonly, this active center is a radical or cation, though anionic processes should not be neglected.

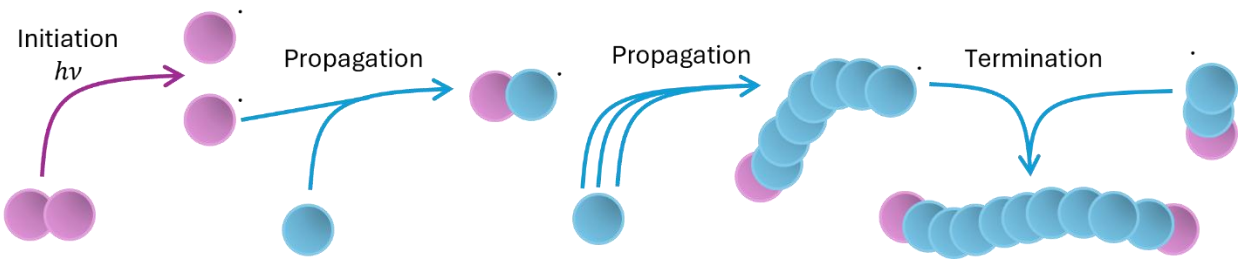

Figure 1.1. Simple representation of a radical chain growth polymerization. Initiator is cleaved directly, followed by multiple monomer additions. Bimolecular termination ends the process and consumes the radical active center.

Upon initiation, it is desirable for the active center to undergo multiple sequential events, i.e., to propagate. In the context of a typical acrylate or methacrylate radical homopolymerization, this results in a growing polymer chain. Other processes, such as the step-growth thiol-ene reaction, use chain transfer to repeatedly couple pairs of moieties without growing a chain.[10–12] Regardless of mechanism, propagation of a single active center occurs hundreds of times before terminating, allowing for the formation of polymers with only small amounts of initiator.

Finally, termination considerations are relevant. In the radical context, termination occurs when radicals recombine. This process is energetically favorable relative to propagation, and therefore initiation rate (and therefore current radical concentration), is crucial to understanding the relative rate of termination. Alternatively to termination events, polymerization rate severely decreases due to vitrification, which occurs when there is insufficient free volume for radicals to continue propagating.[7]

In addition to facile bond formation, light provides spatiotemporal control in that exposure occurs precisely where and when desired.[13–15] For a photoinduced process to

occur, a photon must be absorbed. Therefore, if a region is not exposed due to masking of the area (physical or otherwise), the reaction will not progress in that region which enables the photopatterning process. Historically, this benefit was used for patterning letterpress printing plates;[16] but now, it is being leveraged in the ever-growing semiconductor[17,18] and additive manufacturing industries[19,20] amongst others.

1.3 Thermosets and Thermoplastics

Lifecycle considerations of plastic materials are of ever increasing importance. For these life cycle considerations, one critical distinction within polymer products is that between thermally reprocessable thermoplastics and crosslinked thermosets with fixed structures.[21] Although the necessary temperature may not always be feasible for use, thermoplastics flow upon thermal stimulus allowing reshaping, and therefore recycling by these means. Common household recyclables, such as polyethylene, polystyrene, and polypropylene fall under this category.[22] The simplest case of polymers within this class are linear in architecture, though more complicated topographies, such as branched or star, are also thermally reprocessable. Thermoplastics are frequently advantageous due to their processing and reprocessing capabilities, particularly in that polymerization may occur independently of the application geometry.[23,24] Additionally, thermoplastics have superior toughness relative to thermosets.[25,26]

In contrast, thermosets contain covalent crosslinks which prevent flow under thermal stimulus and prevent dissolution when exposed to even good solvents. This behavior is advantageous due to increased mechanical strength, thermal stability, and chemical resistance.[21] These networks are formed via the inclusion of multifunctional monomers to

serve as these crosslinking sites. Network formation, or gelation, occurs when the weight average molecular weight of the polymer approaches infinity and thus the network percolates the available space (Figure 1.2). In practice, the polymer fully spans, or percolates, the space available. For step growth polymers, the conversion corresponding to the gel point is readily estimated by the Flory-Stockmayer method.[27–30]

Equation 1.1

$$p_c = \frac{1}{\sqrt{r(f_A - 1)(f_B - 1)}}$$

where p_c is the critical gel point conversion, r is the stoichiometric ratio of functional groups A and B ($r \leq 1$), and f_A is the functionality of compound containing group A. In systems with multiple monomers of varied functionality, f is replaced with the functionality weighted average (f_w).

Equation 1.2

$$f_w = \frac{\sum f_i^2 N_i}{\sum f_i N_i}$$

where f_i is the functionality of species i and N_i is the moles of that species.

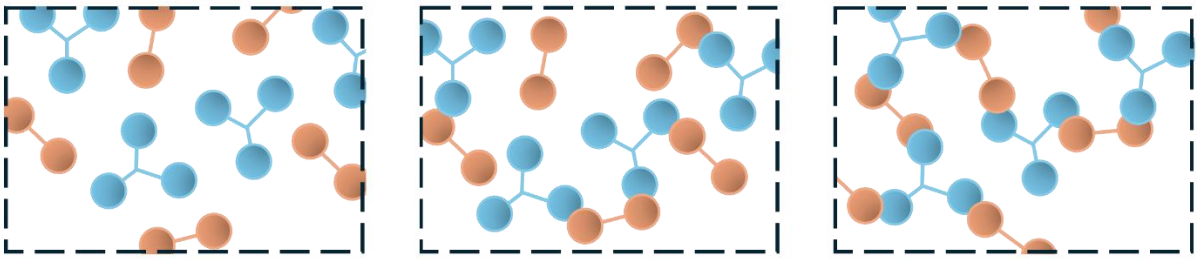

Figure 1.2. Step growth polymerization between two-functional and three-functional monomers to form a thermoset. Gelation occurs once the polymer percolates the space. In this case, Equation 1.2 estimates the critical conversion as 71% in the stoichiometric case.

Theoretically, if conversion above p_c is achieved, a network is expected. However, defects, including side reactions and loops, make the true gel point conversion higher than this prediction.

Although thermosets do not flow even at high temperature, this behavior does not prevent reprocessing by other means. Notably, physical reprocessing, such as the grinding of rubber tires is common for reuse. Additionally, chemical degradation is a significant consideration for the reduction or reuse of plastic waste. It should be noted that reverse engineering Eq 1 enables prediction of the bond cleavage necessary for degelation in degradable networks.

1.4 Covalent Adaptable Networks

Since Tobolosky in 1948 first analyzed stress relaxing rubbers and determined that thermally initiated disulfide exchange was responsible for the stress relaxation, covalent adaptable networks (CANs) (or what he referred to as “chemorheology”) have grown in popularity as a means to bridge thermosets and thermoplastics.[31] These networks are covalently crosslinked, thus thermosets— however, the topography of the materials is capable of rearrangement via the reversible addition or exchange of dynamic covalent bonds. Bond rearrangement is triggered by stimuli including heat,[32–40] light,[41–49] and pH,[50–56] in order to reprocess materials as if they were thermoplastics (Figure 1.3). As such, CANs have the capacity to have the thermomechanical benefits of thermosets with the processing capacity of thermoplastics.

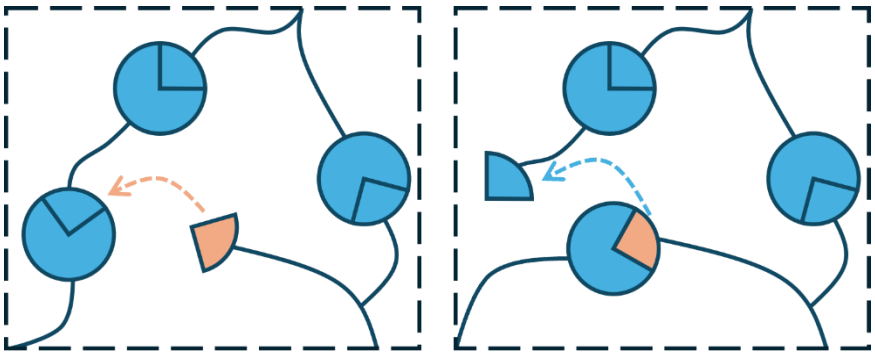

Figure 1.3. Dynamic covalent bonds lead to topographic rearrangement of the network.

Furthermore, the triggering stimuli and bond exchange rate are controlled by the specific choice of the dynamic covalent chemistry. For example, boronic esters are readily dynamic under ambient conditions[57,58] while Diels-Alder CANs typically necessitate temperatures in the range of 80-120 °C for reasonable processing rates.[39,59] Alternatively, thioester systems are tunable by the choice of nucleophilic or basic catalyst.[53,60] The inclusion of a thermally active moiety results in creep and thus reshaping over long timelines. As such, low creep thermal CANs are of significant interest within the field.

In contrast, photoactivated radically-mediated CANs, such as allyl sulfides and trithiocarbonates, have limited creep downside[41] and have the additional benefits provided by the spatiotemporal control of light.[46,61,62] Therefore, this sub-class of CANs holds promise for applications where a light stimulus is feasible. Within these processes, it is crucial that light reaches the desired reprocessing area and that there is an initiation event (added initiator or self-initiator) which allows for the dynamic cascade. Due to these considerations, there are severe limitations for applications beyond processing of thin films and at interfaces.

1.5 Multistage Networks

The concept of dual-cure networks is most frequently associated with interpenetrating networks (IPNs). However, dual-cure processes are not inherently limited to IPNs. Rather, these networks are a subset of multistage polymer networks. This expansion of definition allows for numerous processing steps within the lifetime of the material; each of which modifies the properties to suit its particular stage. For example, dual-cure dental adhesives allow for the material to be manipulated into place prior to a final set. The first stage mechanics are key to ensuring that the parts are properly seated, while the second stage ensures a long-lasting bond.[2,63–65]

Scheme 1.1. Multistage networks enable different properties throughout the life cycle of a polymer network. Steps are controlled by sequential stimuli, and the design of the system informs the number of steps, change in properties, and the possibility of reversible steps.

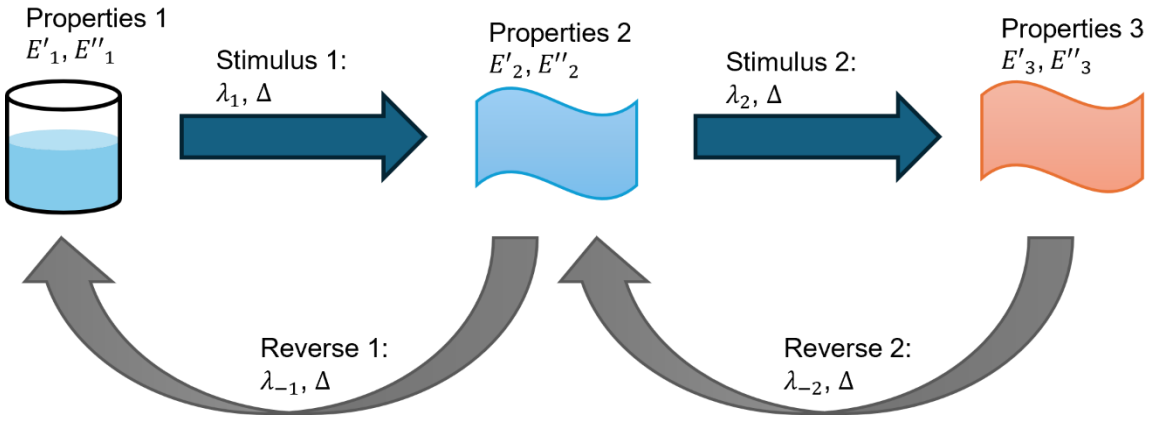

Overall, the key to a multistage network is sequence-controlled orthogonality. The first stage must be prepared without triggering the second. Therefore, stimuli and mechanisms must be independent; or at least, ordered in such a manner that they do not interfere with each other. In a basic case, thermal postprocessing may follow a photoactivated

process— a method that is common for stereolithography (SLA), digital light processing (DLP), and other 3D printing methods to increase conversion and mechanical properties.[59,66–68] This approach is preferable over attempting to maximize conversion within the photopatterning process as the material often vitrifies under ambient conditions. Alternate methods may be leveraged, though with additional design considerations, such as using multiple wavelengths to activate chromophores in sequence.[69–72]

1.6 Applications of Photoinduced Processes

The rapid curing, and spaciotemporal control, of light has been widely implemented in industrial polymer processing from examples stemming back to cinnamate-based printing plates[16] to the modern photolithography implementation in the preparation of integrated circuit boards,[3,73,74] dental fillings,[4,44,75–78] and vat 3D printing.[5,79–82] 3D printing has been of particular interest due to increasingly rapid prototyping capacity and custom fabrication of small batch or otherwise geometrically difficult to manufacture thermoset parts.

1.6.1 Mechanophotopatterning

Solids processing, such as cutting, molding, and extruding, are of standard utility to transform raw materials into useful final products. Mechanophotopatterning seeks to add to this list of facile methodologies by combining controlled light exposure with a strained elastomer to result in patterned surface topography. Mechanophotopatterning processes fall into two categories to date: (1) dynamic[52,62,83] and (2) dual-cure.[84–86] Within dynamic systems, such as the seminal work by Kloxin et al.,[62] a dynamic moiety is activated due to light exposure (i.e. allyl sulfide), resulting in local stress relaxation, and

therefore flow of the material as the dynamic moieties relax within the exposed region.[62] In contrast, dual-cure methodologies result in a polymer structural evolution that ultimately results in a mechanical change, e.g., increasing the modulus of the patterned area. Upon release, the combination of residual stress and patterned modulus result in a patterned film.

Both methods presented produce topographic films under strain and are easily modified to allow for a molding variant. However, each has a respective downside. Although allyl sulfides are not directly thermally stimulated, the dynamic capacity persists toward further light exposure or other radical producing events. As such, patterns prepared by this method are subject to undesired evolution. In contrast, the dual-cure methodologies limits lie with its inability to be further processed as all network modifications are permanent changes and inherently limit the magnitude to which the material is patterned in the first place.

1.6.2 Holography

Volume holograms leverage diffraction to direct light as a function of wavelength and angle and are of substantial interest due to their applications in data storage,[87–89] optical security,[90,91] and displays.[89,92–95] Of most recent interest is the potential for these parts to be included in augmented reality displays.[95]

The simplest form for testing these materials is the volume holographic grating (VHG), which is prepared via a sinusoidal distribution of refractive index as shown in Figure 1.4. The result is a single-order light diffraction with high efficiency and an angle dependence that has been well described by Kogelnik's coupled wave theory.[96] In

practice, the simplest photopolymer VHGs are prepared via the exposure of a sinusoidal interference pattern on a film with two phases. A matrix or binder allows for the desired transport phenomena and mechanics for, as well as refractive index contrast with, a mobile writing monomer.[97–99] The transport of the monomer is critical, as the preparation of the grating is not only dependent on the polymerization of monomer in the bright fringes, but also the diffusion of unreacted monomer from the dark regions to the bright fringes.

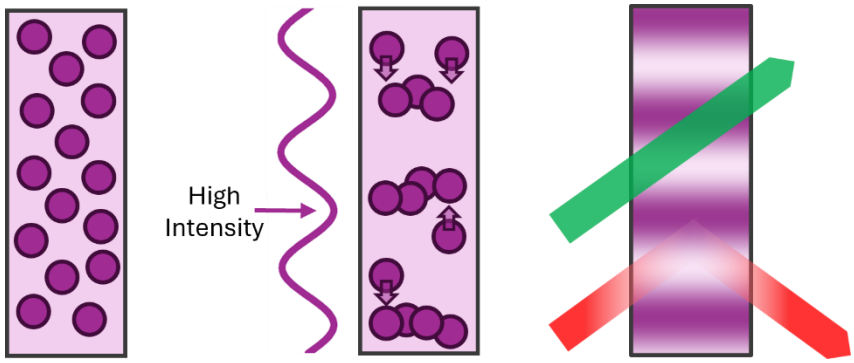

Figure 1.4. Preparation of photopolymer VHG. Monomer within a matrix is patterned by a sinusoidal light pattern and migrates by diffusion during the exposure. The result product is a wavelength and angle sensitive diffraction grating.

1.6.3 Tomographic Volumetric Additive Manufacturing

The benefits provided by rapid prototyping and custom manufacturing continue to lead to rises with the utilization of 3D printing, particularly within the photopolymer's market. Within the realm of digital light processing (DLP), the development and implementation of oxygen-permeable membranes is critical to achieving rapid print rates.[20,100,101] Vat polymerization methods are not without limitations, however. Notably, layer lines within prints result in heterogeneity in mechanics.[102,103]

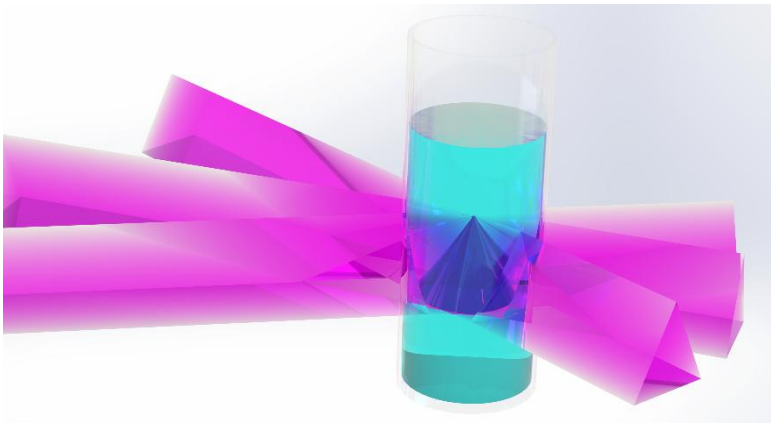

Figure 1.5. Volumetric additive manufacturing enables simultaneous 3D printing of a cone via tomographic triangular projections.

In contrast, tomographic volumetric additive manufacturing (VAM) is a methodology to prepare a part simultaneously (Figure 1.5). By projecting an image set from a variety of different angles, oxygen inhibition is overcome, and sufficient conversion occurs only within the volume of interest. Since this occurs simultaneously, the resulting product does not have layer lines and boasts potentially rapid timescales without being tethered to a build plate.[104–108] Unlike DLP, VAM is in its infancy and would benefit from specific resin design, rather than defaulting to materials intended for other vat polymerization techniques.[109]

1.7 Research Outline

This thesis includes the design and study of photopolymer systems that leverage the spatiotemporal control of light for patterning in conjunction with varied properties throughout life stages. In chapter 3, a multistage network approach in the form of a three-stage urethane/acrylate/epoxy to allowed for postprocessing of volume holographic

photopolymer gratings to a glassy state. A control study of thermal post-processing chemistry and conditions was conducted using diffraction efficiency as a stand-in for hologram fidelity. The study demonstrates the use of matrix attachment as key to retaining fidelity at elevated temperatures. Subsequently, photopolymer films containing low refractive index polyurethane matrix and latent epoxy in combination with high refractive index acrylate writing monomer were prepared. Thermomechanical properties were evaluated on the neat films by dynamic mechanical analysis. Written holograms were evaluated after patterning, optical flood cure, and final thermal epoxy homopolymerization cure demonstrating retention of the written grating. Atomic force microscopy was leveraged to probe the surface topography and modulus of the rubbery and glassy holograms at the nanoscale. Device application was demonstrated in the form of lamination, curing, and the resulting strong outcoupling from a cylindrical lens.

Chapter 4, a dual-cure urethane/epoxy network methodology is combined with photoactivated dynamic covalent chemistry to allow for the fixation of mechanophotopatterned topography in thin films. This chapter discusses the benefit of this sequentially photopatternable and thermally fixable system as a means to overcome limitations of previous mechanophotopatterning materials and methods. Specifically, long duration stress relaxation under 405 nm light is presented to demonstrate current limitations. Topography is assessed by optical profilometry to demonstrate loss of surface features in control samples in contrast with cured dual-cure equivalents. Thermomechanical properties of the polymers in their respective cure states are evaluated by dynamic mechanical analysis as a function of temperature. The findings demonstrate that dual-cure mechanophotopatternable films have excellent topography

fidelity and are a critical step towards employment of this facile technique. Traditional resolution testing was performed and the remaining limitations of the technique, which would benefit from modeling efforts, were noted. Chapter 5 extends this work by validating a finite element simulation that predicts final topography from exposure pattern. This validation is a valuable step toward precise manufacturing by the mechanophotopatterning method.

Finally, in Chapter 6 thioesters were employed as the degradable moiety in for a widely compatible scaffold structure methodology to enhance volumetric additive manufacturing methods. Final parts with moduli ranging 3 orders of magnitude (low MPa to high 100 MPa) were produced. Unprinted scaffold was degraded with minor damage to the parts, including less than 2% mass loss for glassy parts. The addition of an inhibitor coupled with real-time chemical and mechanical evolution provided reliable contrast between in-part and out-of-part regions. Further, these kinetics informed the timing of the printing process and thus allowed for consistent timing printing of small features, as demonstrated by 250 μm rods.

1.8 References

(1) *Photopolymers Market Size, Share & Growth Report, 2030*. https://www.grandviewresearch.com/industry-analysis/photopolymers-market-report (accessed 2025-03-15).

(2) Park, C.-H.; Lee, S.-W.; Park, J.-W.; Kim, H.-J. Preparation and Characterization of Dual Curable Adhesives Containing Epoxy and Acrylate Functionalities. *React. Funct. Polym.* **2013**, *73* (4), 641–646. https://doi.org/10.1016/j.reactfunctpolym.2013.01.012.

(3) Yang, D.; Shi, Y.; Yu, X. Photomask and Photoresist. In *Handbook of Integrated Circuit Industry*; Wang, Y., Chi, M.-H., Lou, J. J.-C., Chen, C.-Z., Eds.; Springer Nature: Singapore, 2024; pp 1717–1742. https://doi.org/10.1007/978-981-99-2836-1_78.

(4) Boulden, J. E.; Cramer, N. B.; Schreck, K. M.; Couch, C. L.; Bracho-Troconis, C.; Stansbury, J. W.; Bowman, C. N. Thiol–Ene–Methacrylate Composites as Dental Restorative Materials. *Dent. Mater.* **2011**, *27* (3), 267–272. https://doi.org/10.1016/j.dental.2010.11.001.

(5) Bagheri, A.; Jin, J. Photopolymerization in 3D Printing. *ACS Appl. Polym. Mater.* **2019**, *1* (4), 593–611. https://doi.org/10.1021/acsapm.8b00165.

(6) Saleh, B. E. A.; Teich, M. C. *Fundamentals of Photonics*; John Wiley & Sons, 2019.

(7) Odian, G. Radical Chain Polymerization. In *Principles of Polymerization*; John Wiley & Sons, Ltd, 2004; pp 199–349. https://doi.org/10.1002/047147875X.ch2.

(8) Albini, A. Norrish' Type I and II Reactions and Their Role in the Building of Photochemical Science. *Photochem. Photobiol. Sci.* **2021**, *20* (1), 161–181. https://doi.org/10.1007/s43630-020-00003-9.

(9) Bond, S. G.; Ebdon, J. R. Photolysis of Vinyl Ketone Copolymers: 3. Norrish Type 1 versus Modified Norrish Type 2 Chain Scission in Some Methyl Methacrylate-Aryl Vinyl Ketone Copolymers. *Polymer* **1994**, *35* (19), 4079–4082. https://doi.org/10.1016/0032-3861(94)90578-9.

(10) P. Sutherland, B.; Kabra, M.; J. Kloxin, C. Expanding the Thiol–X Toolbox: Photoinitiation and Materials Application of the Acid-Catalyzed Thiol–Ene (ACT) Reaction. *Polym. Chem.* **2021**, *12* (10), 1562–1570. https://doi.org/10.1039/D0PY01593H.

(11) Hoyle, C. E.; Bowman, C. N. Thiol–Ene Click Chemistry. *Angew. Chem. Int. Ed.* **2010**, *49* (9), 1540–1573. https://doi.org/10.1002/anie.200903924.

(12) Hoyle, C. E.; Lee, T. Y.; Roper, T. Thiol–Enes: Chemistry of the Past with Promise for the Future. *J. Polym. Sci. Part Polym. Chem.* **2004**, *42* (21), 5301–5338. https://doi.org/10.1002/pola.20366.

(13) Adzima, B. J.; Tao, Y.; Kloxin, C. J.; DeForest, C. A.; Anseth, K. S.; Bowman, C. N. Spatial and Temporal Control of the Alkyne–Azide Cycloaddition by Photoinitiated

Cu(II) Reduction. *Nat. Chem.* **2011**, *3* (3), 256–259. https://doi.org/10.1038/nchem.980.
(14) Aubert, S.; Bezagu, M.; Spivey, A. C.; Arseniyadis, S. Spatial and Temporal Control of Chemical Processes. *Nat. Rev. Chem.* **2019**, *3* (12), 706–722. https://doi.org/10.1038/s41570-019-0139-6.
(15) Xi, W.; Peng, H.; Aguirre-Soto, A.; Kloxin, C. J.; Stansbury, J. W.; Bowman, C. N. Spatial and Temporal Control of Thiol-Michael Addition via Photocaged Superbase in Photopatterning and Two-Stage Polymer Networks Formation. *Macromolecules* **2014**, *47* (18), 6159–6165. https://doi.org/10.1021/ma501366f.
(16) Unruh, C. C.; Leubner, G. W.; Smith, J. A. C. Light-Sensitive Polymers for Making Printing Plates. US2861058A, November 18, 1958. https://patents.google.com/patent/US2861058A/en (accessed 2025-02-02).
(17) Hein, P. R.; Miller, H. C.; Brewster, W. D. Photopolymer for Use as a Solder Mask. US4666821A, May 19, 1987. https://patents.google.com/patent/US4666821A/en (accessed 2025-02-02).
(18) Liang, S.; Yan, P.-Y.; Zhang, G. High Performance EUV Mask. US20040126670A1, July 1, 2004. https://patents.google.com/patent/US20040126670A1/en (accessed 2025-02-02).
(19) Rossegger, E.; Höller, R.; Reisinger, D.; Strasser, J.; Fleisch, M.; Griesser, T.; Schlögl, S. Digital Light Processing 3D Printing with Thiol–Acrylate Vitrimers. *Polym. Chem.* **2021**, *12* (5), 639–644. https://doi.org/10.1039/D0PY01520B.
(20) Tumbleston, J. R.; Shirvanyants, D.; Ermoshkin, N.; Janusziewicz, R.; Johnson, A. R.; Kelly, D.; Chen, K.; Pinschmidt, R.; Rolland, J. P.; Ermoshkin, A.; Samulski, E. T.; DeSimone, J. M. Continuous Liquid Interface Production of 3D Objects. *Science* **2015**, *347* (6228), 1349–1352. https://doi.org/10.1126/science.aaa2397.
(21) Odian, G. Step Polymerization. In *Principles of Polymerization*; John Wiley & Sons, Ltd, 2004; pp 39–197. https://doi.org/10.1002/047147875X.ch2.
(22) Grigore, M. E. Methods of Recycling, Properties and Applications of Recycled Thermoplastic Polymers. *Recycling* **2017**, *2* (4), 24. https://doi.org/10.3390/recycling2040024.
(23) Pricci, A.; de Tullio, M. D.; Percoco, G. Analytical and Numerical Models of Thermoplastics: A Review Aimed to Pellet Extrusion-Based Additive Manufacturing. *Polymers* **2021**, *13* (18), 3160. https://doi.org/10.3390/polym13183160.
(24) Schäfer, C.; Meyer, S. P.; Osswald, T. A. A Novel Extrusion Process for the Production of Polymer Micropellets. *Polym. Eng. Sci.* **2018**, *58* (12), 2264–2275. https://doi.org/10.1002/pen.24847.
(25) Chen, D.; Li, J.; Yuan, Y.; Gao, C.; Cui, Y.; Li, S.; Wang, H.; Peng, C.; Liu, X.; Wu, Z.; Ye, J. A New Strategy to Improve the Toughness of Epoxy Thermosets by Introducing the Thermoplastic Epoxy. *Polymer* **2022**, *240*, 124518. https://doi.org/10.1016/j.polymer.2022.124518.

(26) Hogg, P. J. Toughening of Thermosetting Composites with Thermoplastic Fibres. *Mater. Sci. Eng. A* **2005**, *412* (1), 97–103. https://doi.org/10.1016/j.msea.2005.08.028.
(27) Flory, P. J. Molecular Size Distribution in Three Dimensional Polymers. I. Gelation1. *J. Am. Chem. Soc.* **1941**, *63* (11), 3083–3090. https://doi.org/10.1021/ja01856a061.
(28) Stockmayer, W. H. Theory of Molecular Size Distribution and Gel Formation in Branched Polymers II. General Cross Linking. *J. Chem. Phys.* **1944**, *12* (4), 125–131. https://doi.org/10.1063/1.1723922.
(29) Stockmayer, W. H. Molecular Distribution in Condensation Polymers. *J. Polym. Sci.* **1952**, *9* (1), 69–71. https://doi.org/10.1002/pol.1952.120090106.
(30) Pinner, S. H. Functionality of Non-Equivalent Mixtures. *J. Polym. Sci.* **1956**, *21* (97), 153–157. https://doi.org/10.1002/pol.1956.120219718.
(31) Mochulsky, M.; Tobolsky, A. V. Chemorheology of Polysulfide Rubbers. *Ind. Eng. Chem.* **1948**, *40* (11), 2155–2163. https://doi.org/10.1021/ie50467a030.
(32) Capelot, M.; Unterlass, M. M.; Tournilhac, F.; Leibler, L. Catalytic Control of the Vitrimer Glass Transition. *ACS Macro Lett.* **2012**, *1* (7), 789–792. https://doi.org/10.1021/mz300239f.
(33) Lei, Z. Q.; Xiang, H. P.; Yuan, Y. J.; Rong, M. Z.; Zhang, M. Q. Room-Temperature Self-Healable and Remoldable Cross-Linked Polymer Based on the Dynamic Exchange of Disulfide Bonds. *Chem. Mater.* **2014**, *26* (6), 2038–2046. https://doi.org/10.1021/cm4040616.
(34) Lyon, G. B.; Cox, L. M.; Goodrich, J. T.; Baranek, A. D.; Ding, Y.; Bowman, C. N. Remoldable Thiol–Ene Vitrimers for Photopatterning and Nanoimprint Lithography. *Macromolecules* **2016**, *49* (23), 8905–8913. https://doi.org/10.1021/acs.macromol.6b01281.
(35) Chen, L.; Zhang, L.; Griffin, P. J.; Rowan, S. J. Impact of Dynamic Bond Concentration on the Viscoelastic and Mechanical Properties of Dynamic Poly(Alkylurea-Co-Urethane) Networks. *Macromol. Chem. Phys.* **2020**, *221* (1), 1900440. https://doi.org/10.1002/macp.201900440.
(36) Chen, T.; Fang, L.; Li, X.; Gao, D.; Lu, C.; Xu, Z. Self-Healing Polymer Coatings of Polyurea-Urethane/Epoxy Blends with Reversible and Dynamic Bonds. *Prog. Org. Coat.* **2020**, *147*, 105876. https://doi.org/10.1016/j.porgcoat.2020.105876.
(37) Chen, F.; Gao, F.; Zhong, J.; Shen, L.; Lin, Y. Fusion of Biobased Vinylogous Urethane Vitrimers with Distinct Mechanical Properties. *Mater. Chem. Front.* **2020**, *4* (9), 2723–2730. https://doi.org/10.1039/D0QM00302F.
(38) Engelen, S.; Dolinski, N. D.; Chen, C.; Ghimire, E.; Lindberg, C. A.; Crolais, A. E.; Nitta, N.; Winne, J. M.; Rowan, S. J.; Du Prez, F. E. Vinylogous Urea - Urethane Vitrimers: Accelerating and Inhibiting Network Dynamics through Hydrogen Bonding. *Angew. Chem. n/a* (n/a), e202318412. https://doi.org/10.1002/ange.202318412.

(39) Adzima, B. J.; Kloxin, C. J.; DeForest, C. A.; Anseth, K. S.; Bowman, C. N. 3D Photofixation Lithography in Diels–Alder Networks. *Macromol. Rapid Commun.* **2012**, *33* (24), 2092–2096. https://doi.org/10.1002/marc.201200599.
(40) Fan, C.-J.; Wen, Z.-B.; Xu, Z.-Y.; Xiao, Y.; Wu, D.; Yang, K.-K.; Wang, Y.-Z. Adaptable Strategy to Fabricate Self-Healable and Reprocessable Poly(Thiourethane-Urethane) Elastomers via Reversible Thiol–Isocyanate Click Chemistry. *Macromolecules* **2020**, *53* (11), 4284–4293. https://doi.org/10.1021/acs.macromol.0c00239.
(41) Cook, W. D.; Chausson, S.; Chen, F.; Le Pluart, L.; Bowman, C. N.; Scott, T. F. Photopolymerization Kinetics, Photorheology and Photoplasticity of Thiol–Ene–Allylic Sulfide Networks. *Polym. Int.* **2008**, *57* (3), 469–478. https://doi.org/10.1002/pi.2357.
(42) Fenoli, C. R.; Bowman, C. N. Synthesis of Novel Trithiocarbonate and Allyl Sulfide Containing Monomers. *Polym. Chem.* **2013**, *5* (1), 62–68. https://doi.org/10.1039/C3PY00709J.
(43) Galli, P.; Evans, R. A.; Bertarelli, C.; Bianco, A. Cyclic Allylic Sulfide Based Photopolymer for Holographic Recording Showing High Refractive Index Modulation. *J. Polym. Sci.* **2021**, *59* (13), 1399–1413. https://doi.org/10.1002/pol.20210192.
(44) Park, H. Y.; Kloxin, C. J.; Scott, T. F.; Bowman, C. N. Covalent Adaptable Networks as Dental Restorative Resins: Stress Relaxation by Addition–Fragmentation Chain Transfer in Allyl Sulfide-Containing Resins. *Dent. Mater.* **2010**, *26* (10), 1010–1016. https://doi.org/10.1016/j.dental.2010.06.007.
(45) Yavitt, F. M.; Brown, T. E.; Hushka, E. A.; Brown, M. E.; Gjorevski, N.; Dempsey, P. J.; Lutolf, M. P.; Anseth, K. S. The Effect of Thiol Structure on Allyl Sulfide Photodegradable Hydrogels and Their Application as a Degradable Scaffold for Organoid Passaging. *Adv. Mater.* **2020**, *32* (30), 1905366. https://doi.org/10.1002/adma.201905366.
(46) Sowan, N.; Song, H. B.; Cox, L. M.; Patton, J. R.; Fairbanks, B. D.; Ding, Y.; Bowman, C. N. Light-Activated Stress Relaxation, Toughness Improvement, and Photoinduced Reversal of Physical Aging in Glassy Polymer Networks. *Adv. Mater.* **2021**, *33* (5), 2007221. https://doi.org/10.1002/adma.202007221.
(47) Kloxin, C. J.; Scott, T. F.; Bowman, C. N. Stress Relaxation via Addition−Fragmentation Chain Transfer in a Thiol-Ene Photopolymerization. *Macromolecules* **2009**, *42* (7), 2551–2556. https://doi.org/10.1021/ma802771b.
(48) Park, H. Y.; Kloxin, C. J.; Abuelyaman, A. S.; Oxman, J. D.; Bowman, C. N. Stress Relaxation via Addition–Fragmentation Chain Transfer in High Tg, High Conversion Methacrylate-Based Systems. *Macromolecules* **2012**, *45* (14), 5640–5646. https://doi.org/10.1021/ma300228z.

(49) Accardo, J. V.; McClure, E. R.; Mosquera, M. A.; Kalow, J. A. Using Visible Light to Tune Boronic Acid–Ester Equilibria. *J. Am. Chem. Soc.* **2020**, *142* (47), 19969–19979. https://doi.org/10.1021/jacs.0c08551.
(50) Brown, T. E.; Carberry, B. J.; Worrell, B. T.; Dudaryeva, O. Y.; McBride, M. K.; Bowman, C. N.; Anseth, K. S. Photopolymerized Dynamic Hydrogels with Tunable Viscoelastic Properties through Thioester Exchange. *Biomaterials* **2018**, *178*, 496–503. https://doi.org/10.1016/j.biomaterials.2018.03.060.
(51) Accardo, J. V.; Kalow, J. A. Reversibly Tuning Hydrogel Stiffness through Photocontrolled Dynamic Covalent Crosslinks. *Chem. Sci.* **2018**, *9* (27), 5987–5993. https://doi.org/10.1039/C8SC02093K.
(52) Worrell, B. T.; McBride, M. K.; Lyon, G. B.; Cox, L. M.; Wang, C.; Mavila, S.; Lim, C.-H.; Coley, H. M.; Musgrave, C. B.; Ding, Y.; Bowman, C. N. Bistable and Photoswitchable States of Matter. *Nat. Commun.* **2018**, *9* (1), 2804. https://doi.org/10.1038/s41467-018-05300-7.
(53) Kuenstler, A. S.; Bowman, C. N. Catalytic Control of Crystallization in Dynamic Networks. *ACS Macro Lett.* **2023**, 133–139. https://doi.org/10.1021/acsmacrolett.2c00703.
(54) Zeng, X.; Liu, G.; Tao, W.; Ma, Y.; Zhang, X.; He, F.; Pan, J.; Mei, L.; Pan, G. A Drug-Self-Gated Mesoporous Antitumor Nanoplatform Based on pH-Sensitive Dynamic Covalent Bond. *Adv. Funct. Mater.* **2017**, *27* (11), 1605985. https://doi.org/10.1002/adfm.201605985.
(55) Ren, G.; Wang, L.; Chen, Q.; Xu, Z.; Xu, J.; Sun, D. pH Switchable Emulsions Based on Dynamic Covalent Surfactants. *Langmuir* **2017**, *33* (12), 3040–3046. https://doi.org/10.1021/acs.langmuir.6b04546.
(56) Tauk, L.; Schröder, A. P.; Decher, G.; Giuseppone, N. Hierarchical Functional Gradients of pH-Responsive Self-Assembled Monolayers Using Dynamic Covalent Chemistry on Surfaces. *Nat. Chem.* **2009**, *1* (8), 649–656. https://doi.org/10.1038/nchem.400.
(57) Soman, B.; Evans, C. M. Effect of Precise Linker Length, Bond Density, and Broad Temperature Window on the Rheological Properties of Ethylene Vitrimers. *Soft Matter* **2020**. https://doi.org/10.1039/D0SM01544J.
(58) Mei, B.; Evans, C. M.; Schweizer, K. S. Self-Consistent Theory for Structural Relaxation, Dynamic Bond Exchange Times, and the Glass Transition in Polymeric Vitrimers. *Macromolecules* **2024**. https://doi.org/10.1021/acs.macromol.4c00038.
(59) Berg, G. J.; Gong, T.; Fenoli, C. R.; Bowman, C. N. A Dual-Cure, Solid-State Photoresist Combining a Thermoreversible Diels–Alder Network and a Chain Growth Acrylate Network. *Macromolecules* **2014**, *47* (10), 3473–3482. https://doi.org/10.1021/ma500244r.
(60) T. Worrell, B.; Mavila, S.; Wang, C.; M. Kontour, T.; Lim, C.-H.; K. McBride, M.; B. Musgrave, C.; Shoemaker, R.; N. Bowman, C. A User's Guide to the Thiol-

Thioester Exchange in Organic Media: Scope, Limitations, and Applications in Material Science. *Polym. Chem.* **2018**, *9* (36), 4523–4534. https://doi.org/10.1039/C8PY01031E.
(61) Hu, Y.; Podgórski, M.; Mavila, S.; Sinha, J.; Fairbanks, B. D.; McLeod, R. R.; Bowman, C. N. Dynamic Polymer Binder with Light-Regulated Molecular Weight via Addition–Fragmentation Chain Transfer for Holographic Recording. *Macromolecules* **2023**, *56* (6), 2536–2541. https://doi.org/10.1021/acs.macromol.2c02334.
(62) Kloxin, C. J.; Scott, T. F.; Park, H. Y.; Bowman, C. N. Mechanophotopatterning on a Photoresponsive Elastomer. *Adv. Mater.* **2011**, *23* (17), 1977–1981. https://doi.org/10.1002/adma.201100323.
(63) Shim, J. S.; Lee, S. Y.; Song, S.-Y.; Jha, N.; Ryu, J. J. Polymerization Efficiency of Dental Dual-Cured Resin Cement Light-Cured at Various Times after the Initiation of Chemical Activation. *Int. J. Polym. Mater. Polym. Biomater.* **2020**, *69* (10), 622–628. https://doi.org/10.1080/00914037.2019.1596912.
(64) Faria-e-Silva, A. L.; Casselli, D. S. M.; Lima, G. S.; Ogliari, F. A.; Piva, E.; Martins, L. R. M. Kinetics of Conversion of Two Dual-Cured Adhesive Systems. *J. Endod.* **2008**, *34* (9), 1115–1118. https://doi.org/10.1016/j.joen.2008.06.016.
(65) Foxton, R. M.; Nakajima, M.; Tagami, J.; Miura, H. Bonding of Photo and Dual-Cure Adhesives to Root Canal Dentin. *Oper. Dent.-Univ. Wash.-* **2003**, *28* (5), 543–551.
(66) Griffini, G.; Invernizzi, M.; Levi, M.; Natale, G.; Postiglione, G.; Turri, S. 3D-Printable CFR Polymer Composites with Dual-Cure Sequential IPNs. *Polymer* **2016**, *91*, 174–179. https://doi.org/10.1016/j.polymer.2016.03.048.
(67) Chen, K.; Campbell, J. A.; Lewis, D. A. Influence of Postprinting Conditions on Morphologies in a Three-Dimensional Printable Dual-Cure Interpenetrating Dimethacrylate/Epoxy Polymer Network. *ACS Appl. Polym. Mater.* **2022**, *4* (12), 9076–9084. https://doi.org/10.1021/acsapm.2c01435.
(68) Dizon, J. R. C.; Gache, C. C. L.; Cascolan, H. M. S.; Cancino, L. T.; Advincula, R. C. Post-Processing of 3D-Printed Polymers. *Technologies* **2021**, *9* (3), 61. https://doi.org/10.3390/technologies9030061.
(69) Decker, C. Kinetic Study and New Applications of UV Radiation Curing. *Macromol. Rapid Commun.* **2002**, *23* (18), 1067–1093. https://doi.org/10.1002/marc.200290014.
(70) Lin, J.-T.; Cheng, D.-C.; Chen, K.-T.; Liu, H.-W. Dual-Wavelength (UV and Blue) Controlled Photopolymerization Confinement for 3D-Printing: Modeling and Analysis of Measurements. *Polymers* **2019**, *11* (11), 1819. https://doi.org/10.3390/polym11111819.
(71) van der Laan, H. L.; Burns, M. A.; Scott, T. F. Volumetric Photopolymerization Confinement through Dual-Wavelength Photoinitiation and Photoinhibition. *ACS Macro Lett.* **2019**, *8* (8), 899–904. https://doi.org/10.1021/acsmacrolett.9b00412.

(72) Zhang, X.; Xi, W.; Huang, S.; Long, K.; Bowman, C. N. Wavelength-Selective Sequential Polymer Network Formation Controlled with a Two-Color Responsive Initiation System. *Macromolecules* **2017**, *50* (15), 5652–5660. https://doi.org/10.1021/acs.macromol.7b01117.
(73) Oh, M. S.; Lee, J. H.; Hong, C.; Lee, H.-N.; Kim, C. K. Development of Photolithography Process for Printed Circuit Board Using Liquid Crystal Mask in Place of Photomask. *Jpn. J. Appl. Phys.* **2012**, *51* (9S2), 09MF16. https://doi.org/10.1143/JJAP.51.09MF16.
(74) Wang, Q.; Yuan, G. H.; Kiang, K. S.; Sun, K.; Gholipour, B.; Rogers, E. T. F.; Huang, K.; Ang, S. S.; Zheludev, N. I.; Teng, J. H. Reconfigurable Phase-Change Photomask for Grayscale Photolithography. *Appl. Phys. Lett.* **2017**, *110* (20), 201110. https://doi.org/10.1063/1.4983198.
(75) Cramer, N. B.; Couch, C. L.; Schreck, K. M.; Boulden, J. E.; Wydra, R.; Stansbury, J. W.; Bowman, C. N. Properties of Methacrylate–Thiol–Ene Formulations as Dental Restorative Materials. *Dent. Mater.* **2010**, *26* (8), 799–806. https://doi.org/10.1016/j.dental.2010.04.005.
(76) Cramer, N. B.; Couch, C. L.; Schreck, K. M.; Carioscia, J. A.; Boulden, J. E.; Stansbury, J. W.; Bowman, C. N. Investigation of Thiol-Ene and Thiol-Ene–Methacrylate Based Resins as Dental Restorative Materials. *Dent. Mater.* **2010**, *26* (1), 21–28. https://doi.org/10.1016/j.dental.2009.08.004.
(77) Ge, J.; Trujillo, M.; Stansbury, J. Synthesis and Photopolymerization of Low Shrinkage Methacrylate Monomers Containing Bulky Substituent Groups. *Dent. Mater.* **2005**, *21* (12), 1163–1169. https://doi.org/10.1016/j.dental.2005.02.002.
(78) Lu, H.; Carioscia, J. A.; Stansbury, J. W.; Bowman, C. N. Investigations of Step-Growth Thiol-Ene Polymerizations for Novel Dental Restoratives. *Dent. Mater.* **2005**, *21* (12), 1129–1136. https://doi.org/10.1016/j.dental.2005.04.001.
(79) Ahn, D.; Stevens, L. M.; Zhou, K.; Page, Z. A. Rapid High-Resolution Visible Light 3D Printing. *ACS Cent. Sci.* **2020**, *6* (9), 1555–1563. https://doi.org/10.1021/acscentsci.0c00929.
(80) Shin, S.; Kwon, Y.; Hwang, C.; Jeon, W.; Yu, Y.; Paik, H.-J.; Lee, W.; Kwon, M. S.; Ahn, D. Visible-Light-Driven Rapid 3D Printing of Photoresponsive Resins for Optically Clear Multifunctional 3D Objects. *Adv. Mater.* **2024**, *36* (19), 2311917. https://doi.org/10.1002/adma.202311917.
(81) del Barrio, J.; Sánchez-Somolinos, C. Light to Shape the Future: From Photolithography to 4D Printing. *Adv. Opt. Mater.* **2019**, *7* (16), 1900598. https://doi.org/10.1002/adom.201900598.
(82) Schwartz, J. J.; Boydston, A. J. Multimaterial Actinic Spatial Control 3D and 4D Printing. *Nat. Commun.* **2019**, *10* (1), 791. https://doi.org/10.1038/s41467-019-08639-7.

(83) Fan, F.; Liu, C.; Wang, S.; Lv, J.; Li, W.; Fu, Y.; Xu, H. Swelling-Induced 3D Photopatterning on a Diselenide-Containing Elastomer. *J. Mater. Chem. C* **2019**, *7* (35), 10777–10782. https://doi.org/10.1039/C9TC03536B.
(84) Romeo, A.; Lacour, S. P. Concurrent Photopatterning of Elastic Modulus and Structures in Photosensitive Silicone Elastomers. *Extreme Mech. Lett.* **2015**, *3*, 1–7. https://doi.org/10.1016/j.eml.2015.04.002.
(85) Podgórski, M.; Nair, D. P.; Chatani, S.; Berg, G.; Bowman, C. N. Programmable Mechanically Assisted Geometric Deformations of Glassy Two-Stage Reactive Polymeric Materials. *ACS Appl. Mater. Interfaces* **2014**, *6* (9), 6111–6119. https://doi.org/10.1021/am405371r.
(86) Ma, S. J.; Mannino, S. J.; Wagner, N. J.; Kloxin, C. J. Photodirected Formation and Control of Wrinkles on a Thiol–Ene Elastomer. *ACS Macro Lett.* **2013**, *2* (6), 474–477. https://doi.org/10.1021/mz400166e.
(87) Trentler, T. J.; Boyd, J. E.; Colvin, V. L. Epoxy Resin−Photopolymer Composites for Volume Holography. *Chem. Mater.* **2000**, *12* (5), 1431–1438. https://doi.org/10.1021/cm9908062.
(88) Peng, H.; Nair, D. P.; Kowalski, B. A.; Xi, W.; Gong, T.; Wang, C.; Cole, M.; Cramer, N. B.; Xie, X.; McLeod, R. R.; Bowman, C. N. High Performance Graded Rainbow Holograms via Two-Stage Sequential Orthogonal Thiol–Click Chemistry. *Macromolecules* **2014**, *47* (7), 2306–2315. https://doi.org/10.1021/ma500167x.
(89) Castagna, R.; Di Donato, A.; Francescangeli, O.; Lucchetta, D. E. Polymer-Based High Diffraction Efficiency and High Resolution Volume Holographic Transmission Gratings. *Chemosensors* **2022**, *10* (9), 356. https://doi.org/10.3390/chemosensors10090356.
(90) Lim, K. T. P.; Liu, H.; Liu, Y.; Yang, J. K. W. Holographic Colour Prints for Enhanced Optical Security by Combined Phase and Amplitude Control. *Nat. Commun.* **2019**, *10* (1), 25. https://doi.org/10.1038/s41467-018-07808-4.
(91) Fang, X.; Ren, H.; Gu, M. Orbital Angular Momentum Holography for High-Security Encryption. *Nat. Photonics* **2020**, *14* (2), 102–108. https://doi.org/10.1038/s41566-019-0560-x.
(92) Li, B.; Wang, J.; Chen, C.; Li, Y.; Yang, R.; Chen, N. Spherical Self-Diffraction for Speckle Suppression of a Spherical Phase-Only Hologram. *Opt. Express* **2020**, *28* (21), 31373–31385. https://doi.org/10.1364/OE.401679.
(93) Sang, X.; Fan, F. C.; Choi, S.; Jiang, C.; Yu, C.; Yan, B.; Dou, W. Three-Dimensional Display Based on the Holographic Functional Screen. *Opt. Eng.* **2011**, *50* (9), 091303. https://doi.org/10.1117/1.3596176.
(94) Sabel, T.; Lensen, M. C.; Sabel, T.; Lensen, M. C. Volume Holography: Novel Materials, Methods and Applications. In *Holographic Materials and Optical Systems*; IntechOpen, 2017. https://doi.org/10.5772/67001.

(95) Schowengerdt, B. Materials and Process Considerations for AR Glasses. In *Advances in Patterning Materials and Processes XLI*; SPIE, 2024; Vol. 12957, p 129570E. https://doi.org/10.1117/12.3012902.
(96) Kogelnik, H. Coupled Wave Theory for Thick Hologram Gratings. *Bell Syst. Tech. J.* **1969**, *48* (9), 2909–2947. https://doi.org/10.1002/j.1538-7305.1969.tb01198.x.
(97) Colburn, W. S.; Haines, K. A. Volume Hologram Formation in Photopolymer Materials. *Appl. Opt.* **1971**, *10* (7), 1636–1641. https://doi.org/10.1364/AO.10.001636.
(98) Colvin, V. L.; Larson, R. G.; Harris, A. L.; Schilling, M. L. Quantitative Model of Volume Hologram Formation in Photopolymers. *J. Appl. Phys.* **1997**, *81* (9), 5913–5923. https://doi.org/10.1063/1.364378.
(99) Karpov, G. M.; Obukhovsky, V. V.; Smirnova, T. N.; Lemeshko, V. V. Spatial Transfer of Matter as a Method of Holographic Recording in Photoformers. *Opt. Commun.* **2000**, *174* (5), 391–404. https://doi.org/10.1016/S0030-4018(99)00712-9.
(100) Lian, Q.; Yang, F.; Xin, H.; Li, D. Oxygen-Controlled Bottom-up Mask-Projection Stereolithography for Ceramic 3D Printing. *Ceram. Int.* **2017**, *43* (17), 14956–14961. https://doi.org/10.1016/j.ceramint.2017.08.014.
(101) DeSimone, J. M.; Ermoshkin, A.; Ermoshkin, N.; Samulski, E. T. Continuous Liquid Interphase Printing. US9205601B2, December 8, 2015. https://patents.google.com/patent/US9205601B2/en (accessed 2025-02-02).
(102) Paral, S. K.; Lin, D.-Z.; Cheng, Y.-L.; Lin, S.-C.; Jeng, J.-Y. A Review of Critical Issues in High-Speed Vat Photopolymerization. *Polymers* **2023**, *15* (12), 2716. https://doi.org/10.3390/polym15122716.
(103) Andreu, A.; Su, P.-C.; Kim, J.-H.; Ng, C. S.; Kim, S.; Kim, I.; Lee, J.; Noh, J.; Subramanian, A. S.; Yoon, Y.-J. 4D Printing Materials for Vat Photopolymerization. *Addit. Manuf.* **2021**, *44*, 102024. https://doi.org/10.1016/j.addma.2021.102024.
(104) Kelly, B. E.; Bhattacharya, I.; Heidari, H.; Shusteff, M.; Spadaccini, C. M.; Taylor, H. K. Volumetric Additive Manufacturing via Tomographic Reconstruction. *Science* **2019**, *363* (6431), 1075–1079. https://doi.org/10.1126/science.aau7114.
(105) Loterie, D.; Delrot, P.; Moser, C. High-Resolution Tomographic Volumetric Additive Manufacturing. *Nat. Commun.* **2020**, *11* (1), 852. https://doi.org/10.1038/s41467-020-14630-4.
(106) Bhattacharya, I.; Toombs, J.; Taylor, H. High Fidelity Volumetric Additive Manufacturing. *Addit. Manuf.* **2021**, *47*, 102299. https://doi.org/10.1016/j.addma.2021.102299.
(107) de Beer, M. P.; van der Laan, H. L.; Cole, M. A.; Whelan, R. J.; Burns, M. A.; Scott, T. F. Rapid, Continuous Additive Manufacturing by Volumetric Polymerization Inhibition Patterning. *Sci. Adv.* **2019**, *5* (1), eaau8723. https://doi.org/10.1126/sciadv.aau8723.

(108) Shusteff, M.; Browar, A. E. M.; Kelly, B. E.; Henriksson, J.; Weisgraber, T. H.; Panas, R. M.; Fang, N. X.; Spadaccini, C. M. One-Step Volumetric Additive Manufacturing of Complex Polymer Structures. *Sci. Adv.* **2017**, *3* (12), eaao5496. https://doi.org/10.1126/sciadv.aao5496.

(109) Madrid-Wolff, J.; Toombs, J.; Rizzo, R.; Bernal, P. N.; Porcincula, D.; Walton, R.; Wang, B.; Kotz-Helmer, F.; Yang, Y.; Kaplan, D.; Zhang, Y. S.; Zenobi-Wong, M.; McLeod, R. R.; Rapp, B.; Schwartz, J.; Shusteff, M.; Talyor, H.; Levato, R.; Moser, C. A Review of Materials Used in Tomographic Volumetric Additive Manufacturing. *MRS Commun.* **2023**, *13* (5), 764–785. https://doi.org/10.1557/s43579-023-00447-x.

Chapter 2: Objectives

This thesis focuses on multistage polymer processing to prepare photosensitive materials in a physical state that does not match the final property requirements. This methodology both simplifies and enables the steps required for optically processed materials. Transformation between stages takes the form of a sequentially-controlled light, heat, mechanical, and chemical driven steps. The design of this sequence is critical to the design and implementation of the final products, showcasing the correct geometric, optical, and thermomechanical properties.

Three multistage sequence-controlled platforms were designed in the development of this thesis. Each benefited from a distinct sequence of events, including: catalytic bulk polymerization at ambient; photopatterned polymerization; elevated temperature bulk polymerization; photopatterned dynamic covalent stress relaxation; bulk chemical degradation; mechanical strain; and mechanical molding. The optimal reaction sequence, and therefore property control, is achieved by the choices of initiators and their corresponding monomers. Each step was designed so that the previous stimuli would not preemptively trigger the sequential reactions. As such, the correct combinations of light absorbed by a not-yet-used chromophore, the introduction of heat, or the introduction of an outside chemical source, were paramount to these designs. The achievement of the following specific aims demonstrates the benefits of this multistage network across an array of applications.

Specific Aim 1 - Design a multistage network to enable the preparation of glassy holographic photopolymers.

A three-stage network system comprised of a polyurethane matrix, acrylate writing monomer, and epoxide post-cure, was designed and implemented. Composition and processing conditions were analyzed to enhance the mechanical and optical properties, including high diffraction efficiency, low haze, high modulus, and high glass transition temperature. Holographic polymer films were prepared via patterned light exposure at 405 nm followed by a semiorthogonal 365 nm flood exposure, and subsequent thermal postprocessing to facilitate the cationic epoxide homopolymerization. Nanoscale mechanics confirmed high moduli in the entirety of the patterned region. Furthermore, geometric manipulation of this platform for device applications, notably curved displays, was demonstrated. Aim 1 is explored in Chapter 3 of this thesis.

Specific Aim 2 - Develop a materials platform to permanently fix the topography of photodynamically driven regioselective stress relaxation in polymer networks.

Covalent adaptable networks containing allyl sulfides capable of radical-mediated exchange, were integrated with a dual cure epoxide methodology, similar to that used in Aim 1. This system enabled topographical patterning via spatiotemporal control over stress relaxation within a strained sample, with subsequent shape fixing via orthogonal thermal cationic epoxide cure. Susceptibility of the single stage system to additional photoinduced spatial evolution, following initial patterning, was demonstrated and contrasted with the

dual cure system. Additionally, a model for this system was developed and experimentally validated. Aim 2 is explored in both Chapters 4 and 5 of this thesis.

Specific Aim 3 - Enable high-contrast volumetric additive manufacturing (VAM), through the implementation of writing monomer attachment to degradable scaffolds.

A degradable matrix with methacrylate writing monomer attachment points, and delayed writing monomer gelation kinetics, was developed to provide improved dose-response performance and enhance in-situ curing capabilities for the light-induced VAM process. The chemical environment of the scaffolding was readily tunable to compatibilize a wide array of monomers and consequently tune the final part mechanics. Undesired polymerization was prevented by the non-linearity associated with using radical scavengers such as oxygen and stable nitroxide radicals. Furthermore, the scaffolding was designed with degradable thioester linkages, such that the printed part was revealed by degradation of the unprinted scaffold following exposure. Specifically, degradation conditions, in the form of aminolysis, were evaluated to ensure degradation of the scaffold, with minimal damage to the desired part, via mass loss and tensile mechanics studies. Additionally, 2D and 3D final print resolution, and critical dimension, fidelity was analyzed. Aim 3 is explored in Chapter 6 of this thesis.

Completion of these specific aims contributes to the field of polymer science by overcoming the mismatch between desirable processing conditions and end-use properties. Specifically, the preparation of a glassy holographic photopolymer system developed in Aim 1 enables tunable thermomechanical properties and self-supporting

films. Additionally, this method reduces abrasion risk of exposed films and thermal stability is enhanced. The dual-cure mechanophotopatterning technique presented in Aim 2, allows for the versatile application of a facile technique that was previously limited by undesired evolution after patterning. It furthermore enables consistent characterization to validate a model toward improving part-pattern design. Lastly, Aim 3 provides a versatile scaffolding method for VAM that enables not only a library of otherwise inaccessible monomers, but also provides consistent printing with high resolution. Furthermore, this photoresist overcomes standard VAM limitations associated with sinkage due to gravity.

Chapter 3: Multistage Networks for Glassy Holographic Photopolymers

This chapter has been submitted as a manuscript to ACS Applied Material and Interfaces with the following coauthors: Alexander J. Osterbaan, Andrew N. Sias, Marianela Trujillo-Lemon, Kieran Fung, Jason P. Killgore, Robert R. McLeod, and Christopher N. Bowman

Holographic writing performed by Andrew N. Sias
Nanomechanical analysis performed by Kieran Fung and Jason P. Killgore

3.1 Abstract

In the writing of holographic photopolymers, the addition of a third stage cure to the typical polyurethane matrix and acrylate writing monomer steps is used here to modify the ultimate thermomechanical properties of the final holographic photopolymer. Inclusion of a thermally latent, low refractive index epoxide homopolymerization increases the T_g from a value of -22 °C during the writing step to a final T_g of 101 °C after the epoxide cure. Critically, the diffraction grating structure is retained with high fidelity, an index contrast of 0.0057, and a diffraction efficiency of 89% achieved in these materials. Ultimately, the glassy nature of these materials promotes thermal and dimensional stability of the final holographic material.

3.2 Introduction

In the field of optics, volume holograms leverage the recording of an interference pattern through the depth of a transparent material to diffract light. These holograms are of interest for their applications in displays,[1,2] sensors,[3,4] and optical security[5,6] where practical implementation into devices depends on both the recording material and the patterning methodology used. The preparation of holographic photopolymers has specific benefits over other methodologies, as these systems allow for the transport of writing monomer during the actual writing process. Typically facilitated by having a rubbery matrix or binder, high mobility enables the monomer to diffuse to the high light intensity fringes; thereby maximizing the contrast.[7–10] This factor, combined with the photo-driven writing methodology, enables high-fidelity holographic gratings to be developed throughout the volume of the material as presented in Scheme 3.1.

Scheme 3.1. Holographic photopolymer overview. (a) Writing monomer dispersed in a rubbery matrix of thickness L. (b) Sinusoidal light patterning with spatial period Λ enables diffusion driven polymerization where writing monomer diffuses to areas of high intensity light. (c) Final distribution of high index written polymer matches the intensity of the sinusoidal pattern. (d) Wavelength selectivity of diffraction grating.

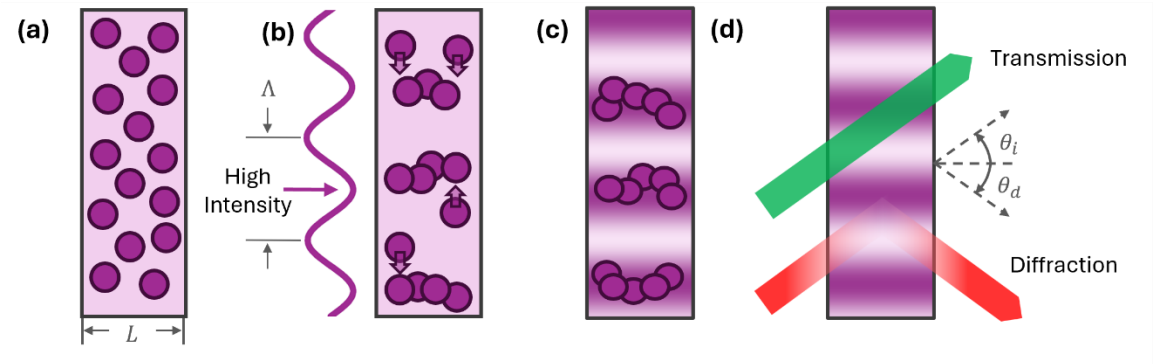

Maximizing the refractive index contrast between regions of high and low intensity exposure, or fringes, is key to successful implementation and high diffraction efficiency; and as such, has been a primary focus of the field.[7,11–13] Despite efforts to enhance the refractive index contrast, increases in the theoretical optical performance are only relevant if the materials are also able to withstand the applications' subsequent mechanical and geometric requirements.[14,15] Therefore, exploration of these characteristics is key to advancing both the practical usage of transmission holograms, as well as their effectiveness in the widespread realm of optical devices. Furthermore, it is crucial to optimize both optical and mechanical performance in transmission holograms. However, a drawback of holographic photopolymeric materials is the required scaffold mechanics since transport is necessary to create high contrast holograms.[16] Ergo, glassy polymer systems are not appropriate during the writing stage since they do not allow for sufficient writing monomer mobility even though in many cases the ultimate implementation of these materials would benefit significantly from having the hologram in a glassy matrix.

In particular, for some applications involving more demanding operating environments, it is desirable for the final holographic film to be mechanically fixed after optical processing in order to prevent performance degradation triggered by thermal and mechanical deformations. For example, the use of volume holographic optical elements (V-HOEs) in head-mounted displays and solar concentrators shows great promise for commercial viability if the durability of the final product is improved for outdoor or even space-faring applications.[17,18] Scaled deployment of such devices requires high recording functionality at nominal industrial conditions. Therefore, a malleable, low modulus

material, is not ideal for the final form even though such a matrix is necessary for the initial holographic pattern development. To enable facile holographic pattern formation in combination with desirable thermomechanical properties, it is critical to account for processing prior to cementation of a system.

This temporal tunability is readily accomplished using a dual-cure matrix system (Scheme 3.2). Additionally, a novel dual-cure approach allows for basic processibility following the holographic writing process— permitting the molding of holographic materials into structures in which recording is not feasible.[19,20] The strategy behind dual-cure networks is to prepare a first-stage material in a processable (typically rubbery), state that does not match the desired end-state mechanics. In this initial state, the native material is able to be processed, laminated, patterned, molded, or otherwise manipulated, prior to its final cure. As such, the end-state benefits from the coveted mechanical properties coupled with specific applications— including, but not limited to, shape memory, lithography, optical systems, adhesives, and additive manufacturing.[21–26] Therefore, the resulting product will maintain the modifications made in the processing stage. This attribute is critical as these modifications could not be attained, or at least not to the same effectiveness, via a single step process.[27,28] Thus, dual-cure methods have been leveraged in a variety of chemistry systems; including urethane/acrylate,[29,30] acrylate/epoxide,[22–24] and thiol-ene/epoxide[31,32] systems, among others.

Scheme 3.2. Schematic representation of the preparation of multistage holographic photopolymer films. (a) Monomer mixture comprised of writing monomer (blue), matrix precursors (black), and latent epoxy (gold). (b) Stage 1 urethane network formed at

ambient with free writing monomer and epoxide. (c) Structured illumination to create patterned acrylate cure. (d) High temperature thermal epoxide cure, increasing T_g and modulus, but retaining the holographic pattern.

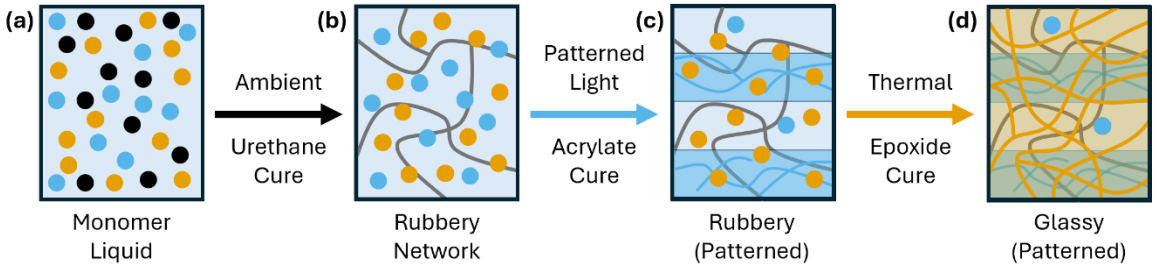

Leveraging this strategy, this work demonstrates a three-stage urethane/acrylate/epoxide system which achieves the preparation of a glassy holographic photopolymer films, while allowing for holographic writing in the loosely crosslinked, rubbery, state.

3.3 Experimental

3.3.1. Materials

Desmodur N 3900 was donated by Covestro AG. Pentaerythritol ethoxylate (3/4 EO/OH), was purchased from Molecular Dimensions. All other materials were purchased from common suppliers (Tokyo Chemical Industries, MilliporeSigma, Fisher Scientific, and AA Blocks), and used as received without further purification. Outside 1,3-bis(phenylthio)-2-propyl urethane acrylate (BPTPUA) synthesis, the reactants and monomers used include polytetrahydrofuran ($M_n \approx 1000$), 3,4-epoxycyclohexylmethyl-3',4'-epoxycyclohexane carboxylate (ECC), 2-hydroxyethyl acrylate (HEA), trimethylolpropane triacrylate (TMPTA), diphenyl(2,4,6-trimethylbenzoyl)phosphine oxide (TPO), and mixed triarylsulfonium hexafluoroantimonate salts (TAS-SbF_6, 50 wt% in propylene carbonate).

3.3.2 1,3-Bis(phenylthio)-2-propyl Urethane Acrylate (BPTPUA), Synthesis

The synthesis of BPTPUA was adapted from a previously reported procedure[33] and details are found in the Supporting Information. ^{1}H and ^{13}C NMR of BPTPUA available in Figures S3.1 and S3.2, respectively.

3.3.3 Preparation of Holographic Polymer Thin Films

The 3-stage system samples were composed of scaffold formulation, writing monomer, and latent epoxide. On a 10-gram scale, polytetrahydrofuran 1000 (1.08 g, 1.08 mmol), was combined with BPTPUA (2.50 g, 4.35 mmol), ECC (4.80 g, 19.0 mmol), pentaerythritol ethoxylate 3/4 EO/OH (0.20 g, 0.75 mmol), HEA (0.03 g, 0.27 mmol), TMPTA (0.08 g, 0.27 mmol), TPO (0.03 g, 0.09 mmol), and TAS-SbF_6 (0.3 g, 0.44 mmol). It should be noted that the BPTPUA contains trace stannous catalyst from synthesis which catalyzes the matrix-forming urethane reaction.

The mixture was stirred and degassed prior to the addition of stoichiometric multifunctional isocyanate in the form of Desmodur N 3900 (0.98 g, 1.93 mmol). The resin is then promptly vortexed, degassed, and cast on glass slides (Fischer Brand, 75 x 25 x 1 mm), with 50 μm vinyl shims (Precision Brand), as spacers and clamped with binder clips. If it was desirable for the film to be released, or retained on the substrate, slides were fluorinated- or methacrylate-functionalized, respectively. Alternatively, samples for mechanical analysis were prepared with 250 μm spacers and the slides were treated with Rain-X as the resulting haze was not of concern. Completion of the polyurethane formation (stage 1), was verified by mid-IR by following the disappearance of the isocyanate peak at ~2250 cm-1 (Figure S3.5).

3.3.4 Holographic Recording

The volume holographic grating (VHG) was the chosen V-HOE for material characterization and permits highly efficient, single-order light diffraction only when the Bragg phase-matching condition is met; otherwise allowing the light to transmit unperturbed.[34] Bragg diffraction produces a strong output wave at the angle θ_d and is readily predicted for a given grating period Λ, material thickness L, readout wavelength λ, and incident angle θ_i of the readout light (Scheme 3.1). Unslanted phase-transmission VHGs were recorded in 50 μm thick stage 1 photopolymer samples cast between glass microscope slides. A narrowband λ = 405 nm laser diode (Coherent OBIS 405 nm LX 40 mW SF) was used in a two-beam plane-wave interference recording setup (Figure S3.4). The beams were intersected at the recording plane with an internal half-angle of 8° off the normal to the surface of the planar recording package to produce a grating period of $\Lambda = 974$ nm. The recording beams were s-polarized and power-matched to maximize fringe visibility. A black polydimethylsiloxane (PDMS) film was adhered to the terminal side of the recording package to extinguish unwanted back reflections.[35] Holographic exposures were performed with a total incident irradiance of 8.0 mW/cm^2 for 3.1 s.

3.3.5 VHG Characterization

Bragg curve analysis is used to extract the magnitude of the refractive index modulation contrast n_1, providing an assessment metric for the conversion of writing monomer to written polymer during and after recording.[36] The Bragg curve is the angular-dependent diffraction efficiency $\eta(\theta)$ if a VHG and peaks at the Bragg-matching angle

θ_0.[34] Post-exposure readout was performed by aligning a non-destructive $\lambda_{read} = 635$ nm, 1 mm diameter probe beam (Thorlabs PL202) to the center of the 7x7 mm square exposure area and rotating the VHG 12° about the Bragg condition while capturing the power of the transmitted and diffracted light from the grating on power meters (Newport 2936-R and 918D-UV x2). The VHG Bragg curves are then fit to Kogelnik's well-established coupled wave theory (CWT), as implemented by Uchida, to extract the magnitude of the refractive index modulation contrast, n_1.[37,38] Each hologram was measured three times: first in the uncured state 90 s after the exposure was finished, then after the optical flood cure, and finally after the thermal cure; as outlined below.

3.3.6 Material Post-Write Processing

After holographic exposures were completed, the samples were uniformly flood cured to stabilize the VHGs and consume any unreacted monomer by illuminating the sample with homogenous 405 ± 7 nm light (Thorlabs SOLIS-405C) at an irradiance of 1.5 mW/cm^2 for 15 min.

Following optical flood curing, samples were exposed with filtered 320-390 nm light (EFOS Acticure A4000) at an irradiance of 20 mW/cm^2 for 7.5 min per side to release the photoacid trigger for the epoxide cure. Samples were then heated for 4 h at 150 ºC to cure the epoxide resin and achieve the final stage 3 state.

3.3.7 Refractive Index Measurements

The refractive index of the photopolymer system was measured using a Metricon Model 2010/M prism coupler at $\lambda_n = 636.6$ nm in TE mode at 30 °C. Samples were

measured in bulk with no hologram present. Each sample was measured in the uncured, optically cured, and thermally cured state.

3.3.8 Haze Measurements

Haze generation was measured in holograms processed to the stage 3 glassy state using a haze meter (BYK Instruments haze-gard i) according to the ASTM D1003-21 standard test method. Unexposed regions of the sample were measured as a background haze reference value, then subtracted from measurements taken from the center of holographic exposure regions.

3.3.9 Mechanical Analysis

A TA Instruments RSA-G2 was used for dynamic mechanical analysis (DMA). Rubbery thin film samples (n = 3, 250 μm x 10 mm x 30 mm), were heated from -80 °C to 150 °C, while glassy stage 3 samples were heated to 200 °C, at a ramp rate of 3 °C and with a frequency of 1 Hz and oscillatory strain of 0.03%. Samples were run in tension under a force tracking condition starting at 0.1 N with 25% axial to dynamic feedback to adjust for variability in modulus. The T_g was determined as the peak of the tan delta curve. Acrylate monomers were cured via filtered 3 mW/cm^2, 400-500 nm light (EFOS Acticure A4000) for 15 min. Epoxide monomers were subsequently reacted via the combination of photoacid activation (20 mW/cm^2, 320-390 nm light, EFOS Acticure A4000, 7.5 min each side), followed by a 4 h thermal cure at 150 °C.

3.3.10 Nanomechanical Analysis

Reduced modulus values of the hologram surfaces were measured by instrumented indentation (Hysitron TI 950, Bruker, USA) with a conospherical tip radius of 18.74 μm. Indentation force of 2500 μN was used on glassy samples whereas 10 μN was used on the rubbery samples. These loads ensured sufficient indentation depth for analysis on the respective samples. The load function consisted of a 12 s loading segment, a 30 s dwell period where maximum load was held constant, followed by 2 s unloading segment. The long dwell and rapid unloading minimized the effects of creep on unloading stiffness.[39] A 4 mm x 4 mm array of 100 indents was performed such that both flood cured out-of-hologram (unpatterned), and in-hologram (patterned), regions were characterized. Unloading curves were fit to the Oliver-Pharr model to obtain reduced modulus values.

To characterize nanoscale mechanical heterogeneity within the holographic patterns, atomic force microscopy (AFM) measurements (Dimension Icon, Bruker, USA) were performed. Due to the differences in modulus between rubbery and glassy samples, two different cantilevers of nominal spring constant 0.25 N/m (SAA-HPI-30, Bruker, USA) or 200 N/m (RTESPA-525-30, Bruker, USA) were chosen, respectively. Both cantilevers exhibit factory-measured 30 nm radius tips and the individual spring constants were factory calibrated by laser doppler vibrometry. For the 0.25 N/m cantilever, optical lever sensitivity (OLS) was calibrated by a force versus distance measurement on a silicon wafer. Modulus values resulting from a Johnson-Kendall-Roberts fit for the rubber are reported without any adjustable parameters. For the 200 N/m cantilever, the large spring constant complicates accurate OLS calibration by either thermal methods or force versus

distance spectroscopy. In response, OLS was treated as an adjustable parameter in the DMT model that was used to match AFM and instrumented indentation results for the glassy hologram. Samples were imaged in the force volume mode, with forces optimized to ensure that indentation depth did not exceed the well-defined 30 nm portion of the tip. Atomic force microscopy in peak force tapping mode was also used to measure the height periodicity of the grating patterns.

3.3.11 Outcoupling Demonstration

A device demonstration was constructed to show the robustness of the material and hologram fidelity when molded to a curved substrate after fabrication and post-processing steps. A 635 nm, 3 mm diameter probe laser (Thorlabs PL202) was aligned through a high-index coupling prism (Thorlabs ADG-6, $n = 1.965$ at $\lambda = 633$ nm) into the planar side of a 300 mm focal-length plano-convex cylindrical lens (Melles Griot 01LCP137, $n = 1.457$ at $\lambda = 633$ nm) such that the beam was in a total internal reflection (TIR) condition within the confines of the lens. A VHG with a Bragg-match condition corresponding to the internal reflection angle of the entrapped beam was fabricated as an output coupler and laminated to the convex-side of the cylinder lens. The lens-hologram system was then subjected to the stage 3 material post-processing conditions outlined above to create a monolithic curved waveguide with a glassy VHG output coupler.

3.4 Results and Discussion

3.4.1 Multistage Holographic and Optical Performance

Scheme 3.3 outlines the specific compounds used for preparation of a multistage glassy photopolymer hologram via post-writing epoxide homopolymerization. This system contains the synthesized high refractive index writing monomer, BPTPUA, mixed with a low refractive index combination of an epoxide, ECC, and loose polyurethane matrix as presented. The inclusion of TMPTA and HEA help retain the holographic structure,[40] particularly during the thermal post-processing steps. Crucially, the hydroxyl group on HEA connects to the stage 1 polyurethane network providing a handle to covalently connect the written acrylic polymer to the matrix as it is being patterned. In combination with the crosslinking provided by TMPTA, the tethered and crosslinked written polymer is thus incapable of transport under thermal stimulus. In contrast, the holographic structure achieved by forming a linear unattached polymer is lost upon heating due to chain diffusion (Table S3.1 and Figure S3.3). Additional considerations for the design were explored for their impact on the diffraction efficiency at different reaction stages, and the results are found in the Supporting Information.

Scheme 3.3. Specific chemical components of the multistage network for the preparation of glassy holographic photopolymers. Although presented as if in stage 2, the hydroxy on HEA reacts in the stage 1 urethane matrix formation while the acrylate reacts in the stage 2 holographic pattern formation.

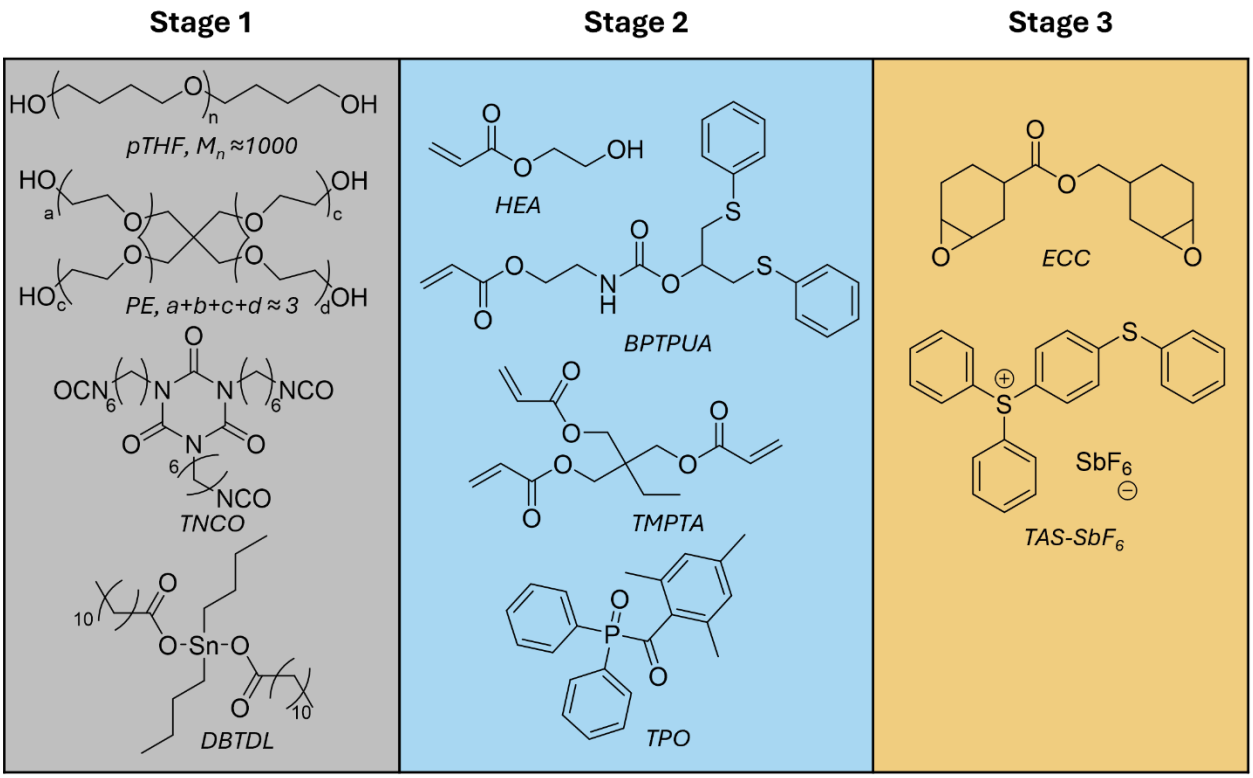

To demonstrate optical performance, representative Bragg readout and post-processing results of these holograms are presented in Figure 3.1. Holograms are recorded while the material is in the rubbery state, yielding a high diffraction efficiency of 89 ± 5% and an index contrast value (n_1) of 0.0062 ± 0.0001. Following writing, the holograms and unexposed regions undergo a 15 min flood cure initiated by a uniform 405 nm LED light to extinguish any photoactive writing species and finalize grating fidelity. Notably, low intensity light is leveraged in this step (1.5 mW/cm^2) to promote long chains, and thus stability. In contrast, progressing directly to the subsequent, 320-390 nm cure, intended for photoacid activation would result in substantial inhomogeneity in residual acrylate reaction due to light attenuation. Minor losses in n_1 were noted (n_1 = 0.0059 ± 0.0001), following this critical step to stabilizing the final pattern.

To facilitate glassy polymer formation in the final reaction stage, the cationic photoinitiator is initially activated by 320-390 nm filtered light from a mercury arc lamp. Although a thermally-triggered acid could be leveraged instead, a photoacid provides shelf stability and the specific selection of TAS-SbF_6 is low yellowing (Figure S3.8). Following activation, the epoxide was thermally cured for 4 hours at 150 °C resulting in a significant increase in the glass transition temperature and crosslink density of the polymer network. The structure of the holographic grating structure was clearly retained after the mechanical transformation occurred, maintaining the desired post-write optical properties and a high diffraction efficiency. However, this epoxide cure results in two key modifications to the final hologram. First, shrinkage from the thermal cure reduces the final thickness of the sample. This phenomenon is apparent in the decreased frequency of null spacings in the thermally cured Bragg curve and is easily compensated for by adjusting the writing angles to achieve the final desired grating period. Second, curing the epoxide results in an increase in the material's average refractive index (Table S3.3). This increase is of further consequence as, from the optical perspective, the role of the low refractive epoxide monomer is to replace part of the low refractive index polyurethane matrix. Index increase of the matrix relative to a polyurethane only binder[33] (n = 1.47), or a previous stage, reduces the maximum performance in the hologram. Thus, the modulation contrast is expected to decrease upon epoxide polymerization, and the corresponding slight decrease in diffraction efficiency and the final decreased index modulation, as shown in Table 1, arise. The final stage material has a bulk index of 1.5152 and a haze value of 0.4 $\pm$ 0.1%. Further haze analysis is available in Table S3.6. Critically,

holographic performance is maintained at elevated temperatures in both stage 2 and stage 3 media as demonstrated in Figure S3.9 and Tables S3.4 and S3.5.

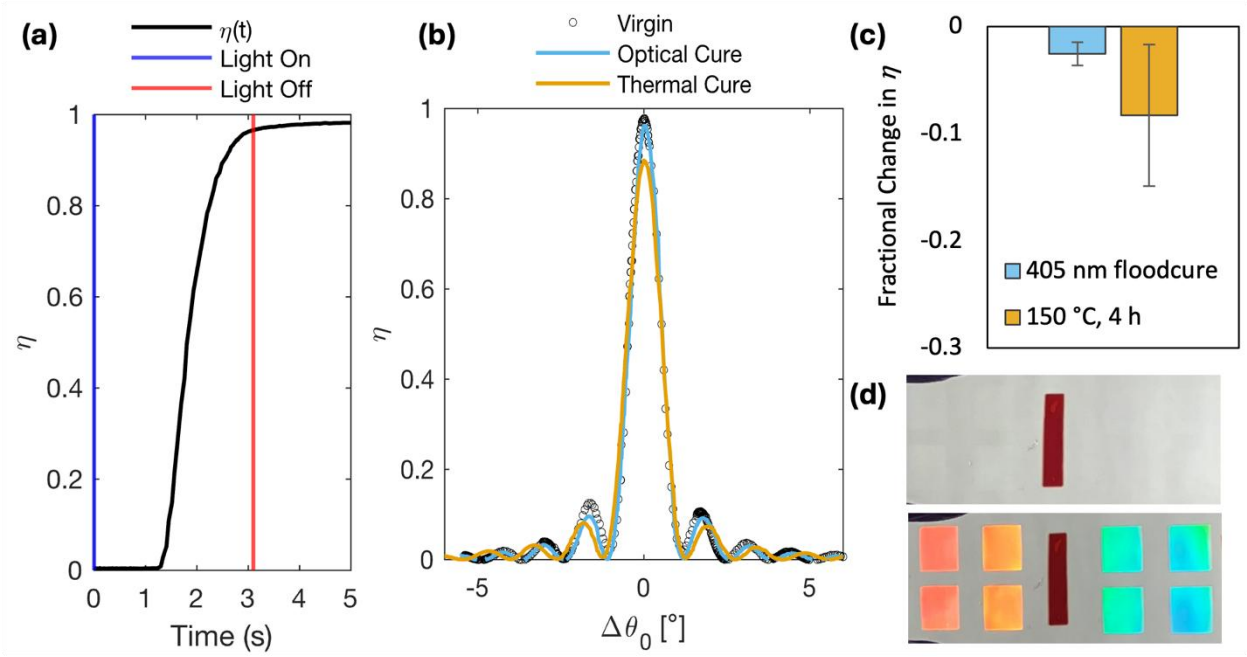

Figure 3.1. Phase-transmission VHG through the transformation from uncured exposure to the final glassy film. Samples are comprised of a polyurethane matrix and contain 30 wt% BPTPUA and 48 wt% ECC. (a) Representative diffraction efficiency evolution during holographic writing (405 nm laser, 8 mW/cm^2). (b) Representative change in Bragg curve following post-processing steps. The optical cure consists of exposure to 405 nm, 1.5 mW/cm^2 LED light for 15 min. Similarly, the photoacid for the epoxide cure is triggered with a 15 min exposure to light from 320-390 nm filtered Hg arc lamp at 20 mW/cm^2 prior to a 4 h, 150 °C thermal cure. Side-lobe fidelity is further demonstrated on a logarithmic scale in Figure S3.10. (c) Loss of diffraction efficiency upon floodcure and thermal post-processing. (d) Picture of a typical hologram following thermal post-processing demonstrating angle-wavelength dependent diffraction between off-Bragg (top) and on-Bragg (bottom) angles.

Cure State	η %	$n_1 \pm 0.0001$	$L \pm 0.3$ (μm)
Uncured	97 ± 1	0.0062	44.8
Flood Cure	96 ± 2	0.0059	44.7
Thermal Cure	89 ± 5	0.0057	40.9

Table 3.1. VHG characterization properties as fit to CWT for the uncured, optically cured, and thermally cured states for samples containing 30 wt% BPTPUA and 48 wt% ECC. The optical cure consists of exposure to 405 nm, 1.5 mW/cm^2 LED light for 15 min. Similarly, the photoacid for the epoxide cure is triggered with a 15 min exposure to 320-390 nm light at 20 mW/cm^2 prior to a 4 h, 150 °C thermal cure. Triplicate samples were processed and measured to obtain statistics.

The final modulation of 0.0057 ± 0.0001 is notably lower than that of rubbery polymer holographic formulations that are optimized for maximum index modulation as the focus here is on achievement of a high glass transition temperature hologram. Here, the epoxide serves as a diluent partially replacing the typical matrix and also inherently limiting the quantity of writing monomer. Further, the epoxide has a higher refractive index than the matrix both before and after polymerization, reducing contrast relative to the standard formulation. Therefore, the work herein serves as a proof of concept for the post-modification of holographic photopolymers and a distinct optimization of the writing monomer would be needed to further enhance the optical properties for applications, such as high modulation.

3.4.2 Multistage Thermomechanical Performance

The glass transition temperatures (T_g), storage modulus and loss modulus of each of the three stages were assessed via dynamic mechanical analysis (DMA) as shown in Figure 2. The first stage polyurethane had the desired rubbery state for the writing process

with a T_g of -34 ± 1 °C. The acrylate writing monomer was then polymerized by a 400-500 nm filtered mercury arc lamp flood cure, which was used since it ideally does not trigger the photoacid. Under 3 mW/cm^2 irradiance, 97% acrylate conversion is observed after 15 min (Figure S3.6). The T_g following this flood cure increases to -22 ± 1 °C and is accompanied by an order of magnitude increase in the crosslinking density as estimated by the rubbery plateau of the storage modulus. Therefore, although the network retains its rubbery state during the writing process, the increase in crosslink density may impact diffusion rates relevant to patterning the hologram. The final system cure is performed via illumination by 320-390 nm filtered light to activate the photoacid, followed by a 150 °C thermal post-cure to reach a final epoxide conversion of 72% (Figure S3.7). The resulting material had a desirably high T_g of 101 ± 8 °C along with a storage modulus at 25 °C of 1.4 ± 0.2 GPa. Further analysis, including tanδ full-width at half-max and the crosslink density for stages is presented in Tables S3.2.

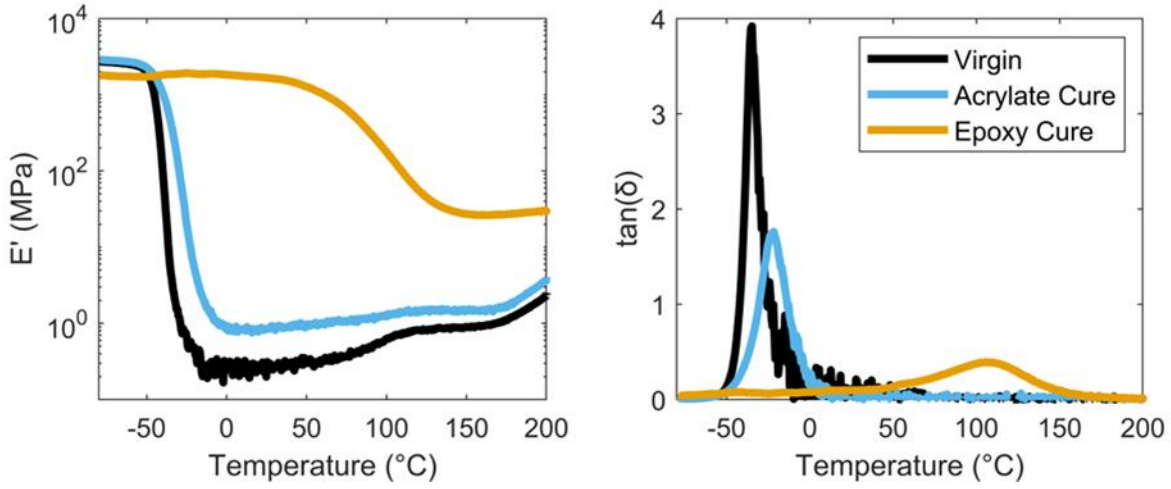

Figure 3.2. Representative thermomechanical analysis of multistage holography system. Acrylate cure consists of exposure to 400-500 nm, 3 mW/cm^2 light for 15 minutes. Similarly, the photoacid for the epoxide cure is triggered with 320-390 nm, 20 mW/cm^2 for

7.5 min each side prior to a 4 h 150 °C thermal cure. A final T_g of 101 °C was obtained. Increases in the rubbery plateau are attributed to curing of later stage monomers.

3.4.3 Nanomechanical Analysis

Nanoindentation was performed on the multistage VHGs to assess spatial modulus dependence and as a calibrant reference for AFM. Interestingly, although the entire sample was optically flood cured at low intensity, the reduced modulus within the written region is statistically greater than that outside (Figure 3.3a). In contrast, the same trend is not clearly present in the glassy stage following thermal epoxide cure. Rather, there is general spatial heterogeneity as stiffer and more compliant regions are noted both within and outside the written hologram region (Figure 3.3b). Full nanoindentation maps are available in Figure S3.11-3.12.

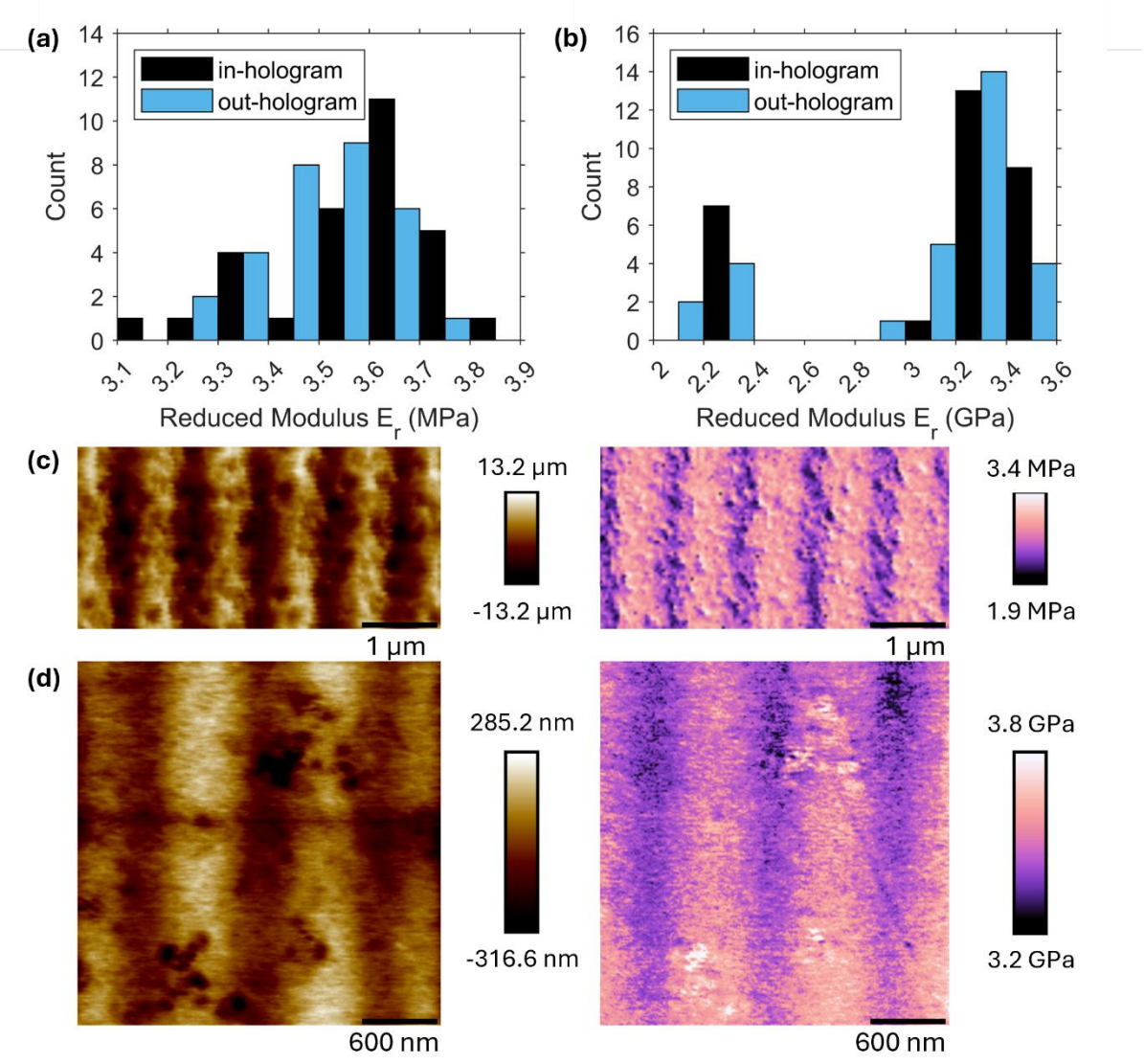

Figure 3.3. (a-b) Nanoindentation comparison inside and outside the exposed hologram region in optically cured (405 nm, 1.5 mW/cm^2, 15 min), and thermally cured (320-390 nm, 20 mW/cm^2, 15 min activation followed by 150 °C, 4h), multistage VHG, respectively. (c-d) AFM of topography and modulus of the optically cured and thermally cured multistage VHG, respectively.

To investigate an even smaller size scale, holograms were assessed by AFM for both topography and mechanical heterogeneity of the stages of the multistage VHG

(Figure 3.3c-d). Via careful selection of cantilever, the moduli of both the rubbery and glassy stages can be assessed with high resolution. For the rubbery state, a peak-to-trough amplitude of 22 ± 3 nm is observed. The troughs of this topography relate to the higher modulus which is expected to be from the bright fringes of the writing process. Therefore, for this system, the shrinkage due to acrylate polymerization and the potential for latent epoxide to be expelled from the bright fringes outweighs the diffusion of writing monomer from the dark fringes into the bright fringes. Overall, the modulus contrast is consistent, though slightly reduced, relative to the comparison of the virgin and optically cured neat films as assessed by DMA. This behavior is anticipated as writing monomer will polymerize at a relatively reduced rate in the dark fringes during the writing, and residual monomer is intended to be consumed in the flood cure.

Following the epoxide activation and thermal cure, the topography contrast is dramatically reduced to an amplitude of 5 ± 1 nm. This result may stem from a variety of factors during the thermal cure and subsequent cooling, including thermal expansion, dynamic polyurethane relaxation, and shrinkage forces. Contrary to the rubbery state, the high modulus fringes are now coupled with the peaks of the topology, though contrast is also low. Therefore, the epoxide content of the dark fringes is marginally higher. Critically, the entire cure film retains GPa modulus as desired.

3.4.4 Geometry Manipulation and Application

Finally, the use of a dual cure system enables manipulation of planar-written films into alternative geometries. The scheme outlined in Figure 3.4 demonstrates the simple case of laminating a VHG sample around a cylindrical substrate to form a monolithic optical system. After writing a VHG in the preferred flat geometry, the rubbery grating was

laminated onto a cylindrical lens in the desired location, photo-activated, and thermally cured. The resulting glassy film is then able to outcouple light that is otherwise trapped within the cylindrical lens by a total internal reflection condition. The dual cure system therefore enables both geometric and mechanical modifications without sacrificing grating efficiency.

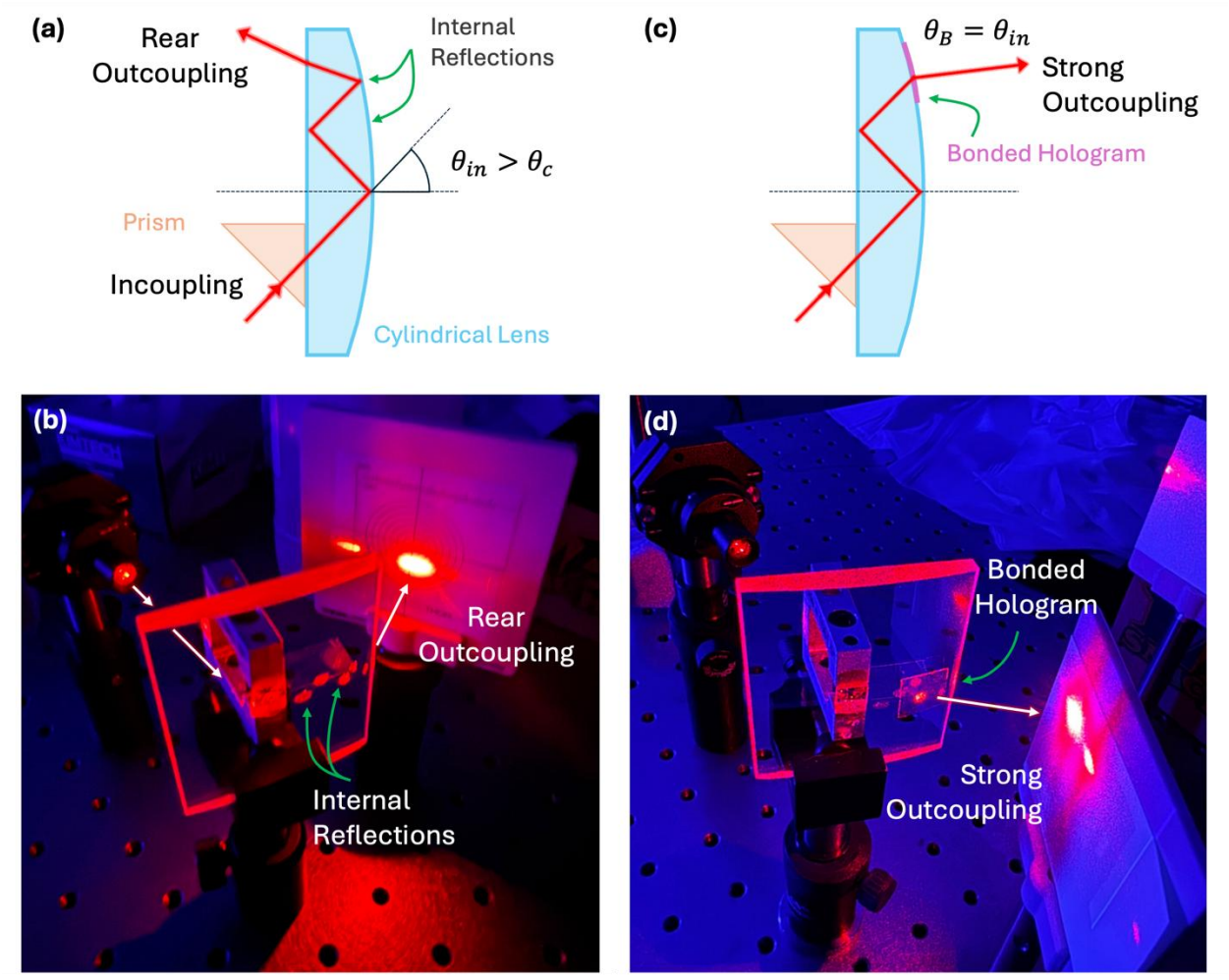

Figure 3.4. Application of a high-efficiency glassy VHG to curved substrate. (a) Schematic diagram (shown from above) of a red laser is incoupled at an angle θ_{in} greater than the critical angle θ_c to produce a total internal reflection condition and confine the beam within the bounds of a cylindrical lens. (b) Photograph of the setup shown in (a)

where the multiple reflections scattering from the outer surfaces of the lens are visible. (c) Schematic of a VHG with a Bragg condition θ_B corresponding to the internal angle of the red beam laminated upon and thermally bound to the surface of the lens. (d) Photograph of the setup shown in (c), strong outcoupling from the lens to the viewing screen indicates that the totally internally reflected red beam is Bragg-matched to the glassy VHG laminated to the surface of the lens. Laminated film is a 50 μm thick VHG based on a polyurethane matrix containing 30 wt% BPTPUA and 48 wt% ECC.

3.5 Conclusions

The sequence-controlled urethane/acrylate/epoxide multistage preparation of glassy photopolymer holograms is presented. The final epoxide cure modifies the thermomechanical properties of the thin films from those necessary for writing, while maintaining the fidelity of the optical pattern. This process enables hologram writing with the benefits of photopolymer systems while also allowing additional postprocessing steps to enhance the material mechanics or fix a modified V-HOE geometry, such as the lamination of a VHG about a cylinder as presented. The final cured product of this process has a refractive index modulation contrast of 0.0057 in combination with a T_g of 101 °C.

3.6 Notes

Publications of the National Institute of Standards and Technology (NIST), an agency of the US government, are not subject to copyright. Commercial equipment, instruments, or materials are identified only in order to adequately specify certain procedures. In no case does such identification imply recommendation or endorsement

by NIST, nor does it imply that the products identified are necessarily the best available for the purpose. The authors declare no competing financial interest.

3.7 References

(1) Chen, X.; Tagami, N.; Konno, H.; Nakamura, T.; Takeyama, S.; Pan, X.; Yamaguchi, M. Computational See-through Screen Camera Based on a Holographic Waveguide Device. *Opt. Express* **2022**, *30* (14), 25006–25019. https://doi.org/10.1364/OE.462111.

(2) Sang, X.; Fan, F. C.; Choi, S.; Jiang, C.; Yu, C.; Yan, B.; Dou, W. Three-Dimensional Display Based on the Holographic Functional Screen. *Opt. Eng.* **2011**, *50* (9), 091303. https://doi.org/10.1117/1.3596176.

(3) Yetisen, A. K. The Prospects for Holographic Sensors. In *Holographic Sensors*; Yetisen, A. K., Ed.; Springer International Publishing: Cham, 2015; pp 149–162. https://doi.org/10.1007/978-3-319-13584-7_7.

(4) Davies, S.; Hu, Y.; Jiang, N.; Blyth, J.; Kaminska, M.; Liu, Y.; Yetisen, A. K. Holographic Sensors in Biotechnology. *Adv. Funct. Mater.* **2021**, *31* (47), 2105645. https://doi.org/10.1002/adfm.202105645.

(5) Lim, K. T. P.; Liu, H.; Liu, Y.; Yang, J. K. W. Holographic Colour Prints for Enhanced Optical Security by Combined Phase and Amplitude Control. *Nat. Commun.* **2019**, *10* (1), 25. https://doi.org/10.1038/s41467-018-07808-4.

(6) Fang, X.; Ren, H.; Gu, M. Orbital Angular Momentum Holography for High-Security Encryption. *Nat. Photonics* **2020**, *14* (2), 102–108. https://doi.org/10.1038/s41566-019-0560-x.

(7) Hu, Y.; Kowalski, B. A.; Mavila, S.; Podgórski, M.; Sinha, J.; Sullivan, A. C.; McLeod, R. R.; Bowman, C. N. Holographic Photopolymer Material with High Dynamic Range (Δn) via Thiol–Ene Click Chemistry. *ACS Appl. Mater. Interfaces* **2020**, *12* (39), 44103–44109. https://doi.org/10.1021/acsami.0c08872.

(8) Pi, H.; Li, W.; Shi, Z.; Chen, H.; Jiang, X. Effect of Monomers on the Holographic Properties of Poly(Vinyl Alcohol)-Based Photopolymers. *ACS Appl. Polym. Mater.* **2020**, *2* (11), 5208–5218. https://doi.org/10.1021/acsapm.0c00960.

(9) Zhao, G.; Mouroulis, P. Diffusion Model of Hologram Formation in Dry Photopolymer Materials. *J. Mod. Opt.* **1994**, *41* (10), 1929–1939. https://doi.org/10.1080/09500349414551831.

(10) Sheridan, J. T.; Lawrence, J. R. Nonlocal-Response Diffusion Model of Holographic Recording in Photopolymer. *JOSA A* **2000**, *17* (6), 1108–1114. https://doi.org/10.1364/JOSAA.17.001108.

(11) Guo, B.; Wang, M.; Zhang, D.; Sun, M.; Bi, Y.; Zhao, Y. High Refractive Index Monomers for Improving the Holographic Recording Performance of Two-Stage Photopolymers. *ACS Appl. Mater. Interfaces* **2023**, *15* (20), 24827–24835. https://doi.org/10.1021/acsami.3c01446.

(12) Guo, B.; Wang, M.; Zhang, D.; Sun, M.; Gao, H.; Bi, Y.; Zhao, Y. High-Performance Holographic Photopolymers Based on Low Refractive Index Host Matrices

Containing Fluoroelastomers. *ACS Appl. Polym. Mater.* **2024**, *6* (5), 2964–2971. https://doi.org/10.1021/acsapm.3c03180.
(13) Galli, P.; Evans, R. A.; Bertarelli, C.; Bianco, A. Cyclic Allylic Sulfide Based Photopolymer for Holographic Recording Showing High Refractive Index Modulation. *J. Polym. Sci.* **2021**, *59* (13), 1399–1413. https://doi.org/10.1002/pol.20210192.
(14) Xiong, J.; Yin, K.; Li, K.; Wu, S.-T. Holographic Optical Elements for Augmented Reality: Principles, Present Status, and Future Perspectives. *Adv. Photonics Res.* **2021**, *2* (1), 2000049. https://doi.org/10.1002/adpr.202000049.
(15) Schowengerdt, B. Materials and Process Considerations for AR Glasses. In *Advances in Patterning Materials and Processes XLI*; SPIE, 2024; Vol. 12957, p 129570E. https://doi.org/10.1117/12.3012902.
(16) Lawrence, J. R.; O'Neill, F. T.; Sheridan, J. T. Photopolymer Holographic Recording Material. *Optik* **2001**, *112* (10), 449–463. https://doi.org/10.1078/0030-4026-00091.
(17) Mikulchyk, T.; Oubaha, M.; Kaworek, A.; Duffy, B.; Lunzer, M.; Ovsianikov, A.; E-Gul, S.-; Naydenova, I.; Cody, D. Synthesis of Fast Curing, Water-Resistant and Photopolymerizable Glass for Recording of Holographic Structures by One- and Two-Photon Lithography. *Adv. Opt. Mater.* **2022**, *10* (6), 2102089. https://doi.org/10.1002/adom.202102089.
(18) Ferrara, M. A.; Borbone, F.; Coppola, G. Holographic Optical Lenses Recorded on a Glassy Matrix-Based Photopolymer for Solar Concentrators. *Photonics* **2021**, *8* (12), 585. https://doi.org/10.3390/photonics8120585.
(19) Li, B.; Wang, J.; Chen, C.; Li, Y.; Yang, R.; Chen, N. Spherical Self-Diffraction for Speckle Suppression of a Spherical Phase-Only Hologram. *Opt. Express* **2020**, *28* (21), 31373–31385. https://doi.org/10.1364/OE.401679.
(20) Han, H.; Wang, J.; Wu, Y.; Zhang, J. Optical Realization of 360° Cylindrical Holography. *Opt. Express* **2022**, *30* (11), 19597–19610. https://doi.org/10.1364/OE.458406.
(21) Berg, G. J.; Gong, T.; Fenoli, C. R.; Bowman, C. N. A Dual-Cure, Solid-State Photoresist Combining a Thermoreversible Diels–Alder Network and a Chain Growth Acrylate Network. *Macromolecules* **2014**, *47* (10), 3473–3482. https://doi.org/10.1021/ma500244r.
(22) Park, C.-H.; Lee, S.-W.; Park, J.-W.; Kim, H.-J. Preparation and Characterization of Dual Curable Adhesives Containing Epoxy and Acrylate Functionalities. *React. Funct. Polym.* **2013**, *73* (4), 641–646. https://doi.org/10.1016/j.reactfunctpolym.2013.01.012.
(23) Griffini, G.; Invernizzi, M.; Levi, M.; Natale, G.; Postiglione, G.; Turri, S. 3D-Printable CFR Polymer Composites with Dual-Cure Sequential IPNs. *Polymer* **2016**, *91*, 174–179. https://doi.org/10.1016/j.polymer.2016.03.048.

(24) Chen, K.; Campbell, J. A.; Lewis, D. A. Influence of Postprinting Conditions on Morphologies in a Three-Dimensional Printable Dual-Cure Interpenetrating Dimethacrylate/Epoxy Polymer Network. *ACS Appl. Polym. Mater.* **2022**, *4* (12), 9076–9084. https://doi.org/10.1021/acsapm.2c01435.
(25) Nair, D. P.; Cramer, N. B.; Gaipa, J. C.; McBride, M. K.; Matherly, E. M.; McLeod, R. R.; Shandas, R.; Bowman, C. N. Two-Stage Reactive Polymer Network Forming Systems. *Adv. Funct. Mater.* **2012**, *22* (7), 1502–1510. https://doi.org/10.1002/adfm.201102742.
(26) Narayanan, J.; Jungman, M. J.; Patton, D. L. Hybrid Dual-Cure Polymer Networks via Sequential Thiol–Ene Photopolymerization and Thermal Ring-Opening Polymerization of Benzoxazines. *React. Funct. Polym.* **2012**, *72* (11), 799–806. https://doi.org/10.1016/j.reactfunctpolym.2012.07.012.
(27) King, N.; Tay, F.; Pashley, D.; Hashimoto, M.; Ito, S.; Brackett, W.; Garcia-Godoy, F.; Sunico, M. Conversion of One-Step to Two-Step Self-Etch Adhesives for Improved Efficacy and Extended Application. *Am. J. Dent.* **2005**, *18*, 126–134.
(28) Chappelow, C. C.; Pinzino, C. S.; Power, M. D.; Holder, A. J.; Morrill, J. A.; Jeang, L.; Eick, J. D. Photoreactivity of Vinyl Ether/Oxirane-Based Resin Systems. *J. Appl. Polym. Sci.* **2002**, *86* (2), 314–326. https://doi.org/10.1002/app.10961.
(29) Decker, C.; Masson, F.; Schwalm, R. Dual-Curing of Waterborne Urethane-Acrylate Coatings by UV and Thermal Processing. *Macromol. Mater. Eng.* **2003**, *288* (1), 17–28. https://doi.org/10.1002/mame.200290029.
(30) Studer, K.; Decker, C.; Beck, E.; Schwalm, R. Thermal and Photochemical Curing of Isocyanate and Acrylate Functionalized Oligomers. *Eur. Polym. J.* **2005**, *41* (1), 157–167. https://doi.org/10.1016/j.eurpolymj.2004.09.004.
(31) Guzmán, D.; Ramis, X.; Fernández-Francos, X.; Serra, A. Preparation of Click Thiol-Ene/Thiol-Epoxy Thermosets by Controlled Photo/Thermal Dual Curing Sequence. *RSC Adv.* **2015**, *5* (123), 101623–101633. https://doi.org/10.1039/C5RA22055F.
(32) Guzmán, D.; Ramis, X.; Fernández-Francos, X.; De la Flor, S.; Serra, A. New Bio-Based Materials Obtained by Thiol-Ene/Thiol-Epoxy Dual Curing Click Procedures from Eugenol Derivates. *Eur. Polym. J.* **2017**, *93*, 530–544. https://doi.org/10.1016/j.eurpolymj.2017.06.026.
(33) Alim, M. D.; Glugla, D. J.; Mavila, S.; Wang, C.; Nystrom, P. D.; Sullivan, A. C.; McLeod, R. R.; Bowman, C. N. High Dynamic Range (Δn) Two-Stage Photopolymers via Enhanced Solubility of a High Refractive Index Acrylate Writing Monomer. *ACS Appl. Mater. Interfaces* **2018**, *10* (1), 1217–1224. https://doi.org/10.1021/acsami.7b15063.
(34) Moharam, M. G.; Young, L. Criterion for Bragg and Raman-Nath Diffraction Regimes. *Appl. Opt.* **1978**, *17* (11), 1757. https://doi.org/10.1364/AO.17.001757.

(35) Miller, D. B.; Alim, M. D.; McLeod, R. R. Reflection Suppression via Elastomeric Films. *Opt. Lett.* **2019**, *44* (24), 6021. https://doi.org/10.1364/OL.44.006021.
(36) Kowalski, B. A.; McLeod, R. R. Design Concepts for Diffusive Holographic Photopolymers. *J. Polym. Sci. Part B Polym. Phys.* **2016**, *54* (11), 1021–1035. https://doi.org/10.1002/polb.24011.
(37) Kogelnik, H. Coupled Wave Theory for Thick Hologram Gratings. *BELL Syst. Tech. J.* **1969**.
(38) Uchida, N. Calculation of Diffraction Efficiency in Hologram Gratings Attenuated along the Direction Perpendicular to the Grating Vector. *J. Opt. Soc. Am.* **1973**, *63* (3), 280. https://doi.org/10.1364/JOSA.63.000280.
(39) Yang, S.; Zhang, Y.-W.; Zeng, K. Analysis of Nanoindentation Creep for Polymeric Materials. *J. Appl. Phys.* **2004**, *95* (7), 3655–3666. https://doi.org/10.1063/1.1651341.
(40) Hu, Y.; Trujillo-Lemon, M.; Sias, A. N.; Dobson, A. L.; Podgórski, M.; Singh, J.; Mavila, S.; McLeod, R. R.; Bowman, C. N. Reducing Haze of Holographic Gratings Recorded in a Two-Stage Photopolymer. *Macromolecules* **2025**. https://doi.org/10.1021/acs.macromol.4c02398.

3.8 Supporting Information

3.8.1. Procedure for Materials Synthesis

Writing monomer synthesis

Commercially available reagents were used without further purification. Thiophenol and epichlorohydrin were purchased from Alfa Aesar. 1,8-diazabicyclo[5.4.0]undec-7-ene (DBU) was purchased from Chem Impex International. Reagent-grade triethylamine (Et_3N) was purchased from Fisher Scientific. 4-bromobenzenethiol and 2-isocyanatoethyl acrylate (IEA) from TCI Chemicals. Dibutyl tin dilaurate (DBTDL) was purchased from Sigma-Aldrich.

NMR spectra were recorded on a Bruker AVANCE-III 400 NMR spectrometer in chloroform-d. All chemical shifts are reported in ppm relative to the chloroform solvent peak (δ= 7.26 ppm).

1,3-Bis-(phenylthio)-2-propanol (BPTP):

The synthesis of BPTP was adapted from previously reported literature.[1] To a 250 mL round-bottomed flask equipped with a magnetic stir bar, 16 mL of thiophenol (157 mmol, 2.2 equiv.) was stirred with 23 mL of DBU (154 mmol, 2.2 equiv.) in 230 mL of toluene (0.3 M, wrt epichlorohydrin) for 10 min. Following this, 5.5 mL of epichlorohydrin (70.3 mmol, 1.0 equiv.) was added dropwise. The reaction vessel was allowed to stir at room temperature for 16 h. After this period, the volatiles were removed under reduced pressure, and the residue was then diluted with dichloromethane (DCM) and washed with 1 M HCl (2 x 100 mL), distilled water (2 x 100 mL), and brine (1 x 50 mL). The combined organic extracts were dried over anhydrous $MgSO_4$, filtered, and concentrated under

reduced pressure. The crude product was purified by silica-gel column chromatography using 80/20 ratio of hexane to EtOAc as an eluent to yield 17.1 g of a colorless, low viscosity liquid (88% yield).

Mid-IR (cm^{-1}): 3414 (O-H); 3056 (C-$H_{aromatic}$); 2918 (C-$H_{aliphatic}$); 816; 734, 688 (C-$H_{aromatic}$).

^{1}H NMR (400 MHz, $CDCl_3$): d 7.39-7.36 (m, 4H), 7.31-7.29 (m, 4H), 7.27-7.20 (m, 2H), 3.90-3.84 (m,1H), 3.23 (dd, J = 13.2, 5.1 Hz, 2H), 3.09 (dd, J = 13.8, 7.2 Hz, 2H), 2.87 (bs, 1H).

^{13}C NMR (101 MHz, CDCl3, 25 °C): d 135.1, 130.2, 129.4, 126.7, 68.3, 40.2.

1,3-Bis(phenylthio)-2-propyl urethane acrylate (BPTPUA):

To a 250 mL round-bottomed flask equipped with a magnetic stir bar, 21.70 g of BPTP (78 mmol, 1.0 equiv.) was added and diluted with 120 mL of DCM (0.3 M wrt BPTP) and stirred for 10 min under argon atmosphere and 11.07g (78 mmol, 1.0 equiv.) of 2-isocyanatoethyl acrylate was added dropwise to the flask under argon atmosphere followed by 1 drop (~15 mg), of DBTDL. The reaction mixture was allowed to stir at 50 °C for 24 h. Mid-IR was used to verify reaction completion following disappearance of isocyanate peak at ~2250 cm^{-1}. After this period, the volatiles were removed under reduced pressure. The crude product was used without further purification and stored as a DCM solution in a -20 °C freezer to avoid polymerization. The title compound BPTPUA is a light yellow, low viscosity liquid (100% yield).

Mid-IR (cm^{-1}): 3358 (N-H); 3057(C-$H_{aromatic}$); 2943 (C-$H_{aliphatic}$); 1716 (C=O); 1634,1618 (C=C); 809, 733, 689 (C-$H_{aromatic}$); 924 (=C-H).

^{1}H NMR (400 MHz, $CDCl_3$): d 7.42-7.40 (m, 4H), 7.33-7.29 (m, 4H), 7.24-7.22 (m, 2H), 6.45 (dd, J = 17.3, 1.6 Hz, 1H), 6.17 (dd, J = 17.3, 10.4 Hz, 1H), 5.89 (dd, J = 10.4, 1.6 Hz, 1H), 5.02 (p, J = 6.0 Hz, 1H), 4.87 (m, 1H), 4.19 (m, 2H), 3.41 (m, 2H), 3.30 (m, 4H). ^{13}C NMR (101 MHz, $CDCl_3$) δ 171.20, 166.00, 155.40, 135.49, 131.53, 129.73, 129.00, 127.96, 126.44, 77.45, 77.41, 77.13, 77.10, 76.81, 76.78, 72.60, 63.48, 60.43, 40.03, 36.47, 21.10, 14.23.

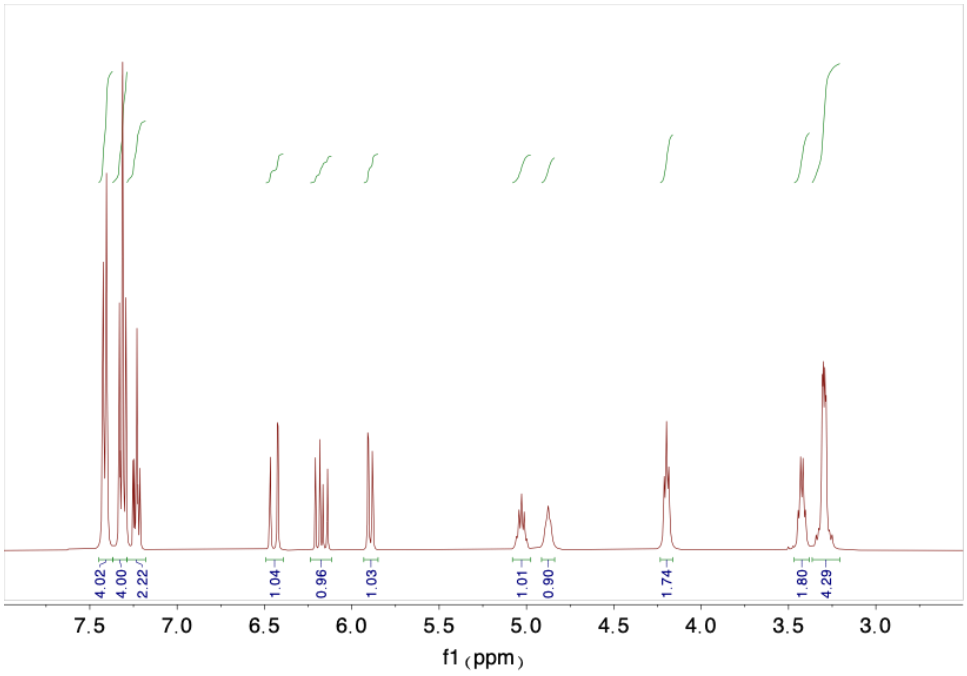

Figure S3.1. ^{1}H NMR of BPTPUA in $CDCl_3$.

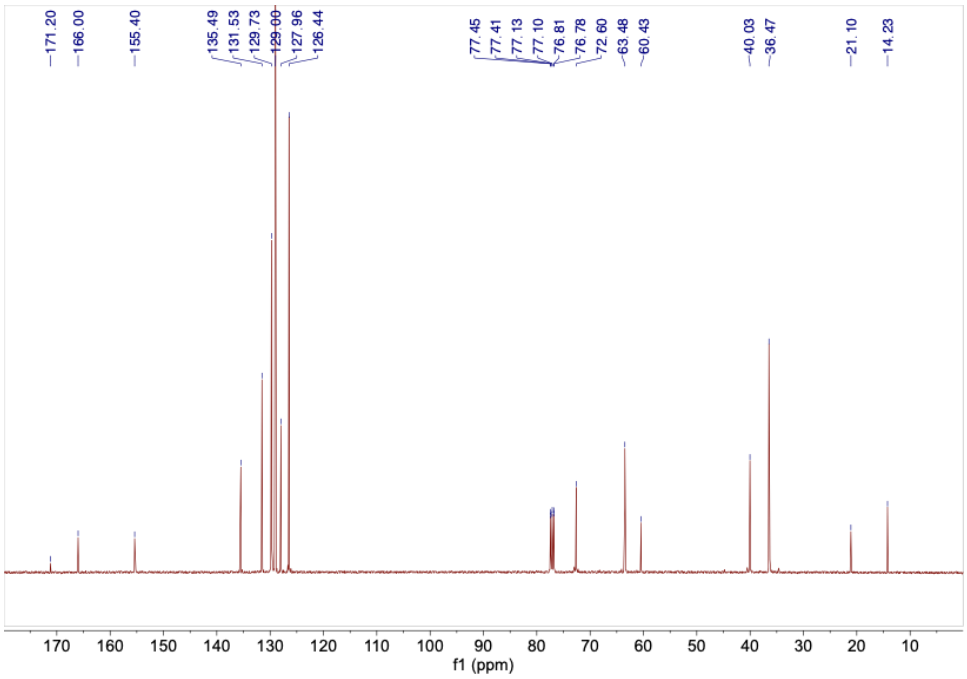

Figure S3.2. ^{13}C NMR of BPTPUA in $CDCl_3$.

Slide functionalization

Silanization methodology was adapted from a previous procedure.[2] Slides were cleaned consistent with in piranha solution 30:70 (hydrogen peroxide : sulfuric acid), for 1h, washed with DI water, and dried with air. For fluorination treatment, slides were then sealed in a pressure vessel with 300 µL of tridecafluoro-1,1,2,2-(tetrahydrooctyl)triethoxysilane (Gelest), and placed in an oven at 125 °C overnight. Residual fluorinating agent was removed by 15 min of sonication in ethanol and the slides were dried with air. For methacrylate treatment, slides were soaked in 1.5% v/v 3-(trimethoxysilyl)propyl methacrylate and 0.5% v/v n-propylamine in toluene for 2 h, washed with methanol, and dried with air and then stored in a desiccator under vacuum.

3.8.2 Supplementary Figures and Analysis

System development fundamental postprocessing studies

As post-modification of photopolymer holograms has not been extensively investigated, it was critical that the effects of contributing factors to the proposed system under thermal treatment be monitored. Prior to the development of the title system, a preliminary study was performed to investigate the fundamental phenomena. Benzyl acrylate (BA) was selected as a readily available commercial writing monomer for this purpose, albeit with a significantly lower refractive index than the BPTPUA. For control experiments, unslanted VHGs were recorded to a peak diffraction efficiency of 50%. Measuring the peak diffraction efficiency and its change due to the various post-processing steps serves as a first-order approximation of deleterious effects to the written grating, including loss of refractive index contrast.

Film preparation for the three-stage glassy system is described in the body. Control films were prepared in a similar fashion; however, as the writing monomers do not inherently contain the DBTDL urethane catalyst, all components were mixed and degassed prior to the final addition of trace DBTDL (~1 μL per gram of resin, diluted in DCM). Additionally, the larger pentaerythritol ethoxylate (15/4 EO/OH) was used to due easier accessibility, though potentially less favorable for matrix environment. Compositions for all formulations are listed in the table below.

wt% of formulation	Base	+HEMA	+Acid
Pentaerythritol ethoxylate (15/4)	--	7.6	7.7
pTHF 1k	54.8	35.7	34.5
TNCO	19.7	26.7	26.8
TPO	0.5	0.5	0.5
Benzyl acrylate	25	25	25
HEA	--	4.5	3.8
BF_3-ethylamine	--	--	2

Table S3.1. Formulation details as described by wt% of total formulation.

To achieve the desired glass transition temperature and respective mechanics in the dual-cure system, a thermal postcure is necessary. As such, all stage 3 samples were subjected to a 16 h thermal post-cure at 120 ºC, read out, and then followed by an additional 16 h, 150 ºC post-cure. Results of the study are summarized in Figure S3.3. In the base case, a substantial loss in diffraction efficiency was noted after the optical floodcure alone with further losses occurring in the thermal step. This effect is posited to be due to the transport of the written polymer out of the fringes. As such, the desired transport phenomena for writing ultimately have a negative impact on hologram fidelity if the polymer formed in stage 2 has sufficient mobility to diffuse itself. It should also be noted that the hologram is not lost, and therefore a portion of written polymer is either

sufficiently large enough to resist diffusion out of the written regions, is crosslinked by side reactions, or has undergone a chain transfer process resulting in attachment to the matrix.

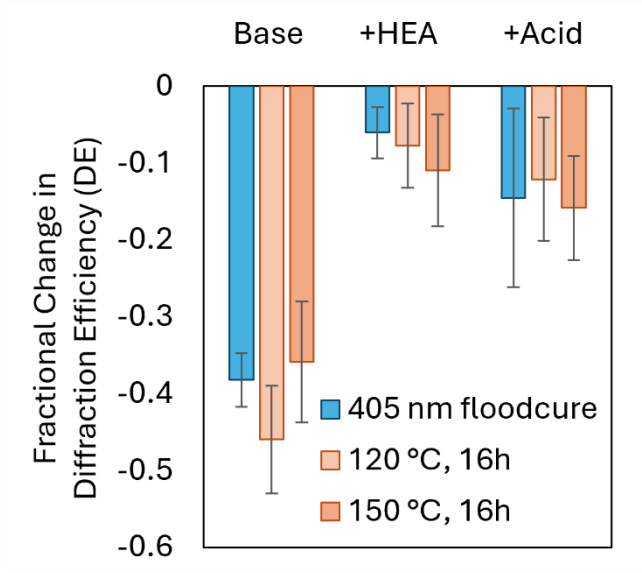

Figure S3.3. Change in diffraction efficiency from an initial 50% upon 405 nm floodcure (1.5 mW/cm^2, 15 min) and thermal treatment. Error bars represent the standard deviation. Base formulation is 30 wt% BA in polyurethane matrix. The addition of HEA prevents losses. The subsequent addition of acid (borontrifluoride-ethylamine) does not result in statistically significant deviation, though an increase in variability is noted.

To overcome this limitation, a matrix attachment point is added by incorporation of 2-hydroxylethyl acrylate (HEA) into the polyurethane matrix.[3] This approach provides direct connection of the written polymer to the matrix and therefore the losses in the base formulation are not observed in the samples with the HEA handle.

Since this system has numerous esters, acid-driven transesterification is a potential concern. A thermally latent acid, borontrifluoride-ethylamine (2 wt%), was added to the

previous formulation and resulted in minor losses in diffraction efficiency; however, the shot-to-shot inconsistency should be noted. Overall, transesterification was not deemed a concern as no statistically significant difference was observed in the post-processing of this holographic photopolymer system under these conditions.

Leveraging the information from the fundamental study to enable glassy holographic photopolymers, the multistage system was designed. First, high refractive index contrast is necessary for writing high-efficiency holograms. Therefore, BPTPUA (n=1.58, 30 wt%), was employed with a 1 wt% equivalent of TPO as the photoinitiator. The larger size of BPTPUA with respect to BA provides added benefit in the form of reducing polymer diffusion and volumetric shrinkage. Second, HEA was employed in this system to enable covalent attachment of the writing polymer to the matrix, preventing loses shown in Figure S3.3. Third, and finally, a final glass transition temperature of approximately 100 ºC was deemed sufficient to withstand the majority of device implementation requirements. Therefore, the low index, high crosslink-density epoxy, ECC (n=1.50), was employed and tuned to 48 wt% of the formulation to achieve the desired mechanics.

Additional considerations for multistage holographic photopolymer system

The following details the purpose of the individual components within the final system.

Polytetrahydrofuran 1000 (pTHF): Base component of polyurethane matrix. Long chain with preferable environment for writing monomer mobility.

Desmodur N3900 (TNCO): Base component of polyurethane matrix. Multifunctional isocyanate for crosslinking.

Pentaerythritol ethoxylate (3/4 EO/OH): Additional hydroxy crosslinker for polyurethane matrix. Accounts for the addition monofunctional hydroxy in the form of HEA. The 3/4 variant was used to reduce impact on the matrix environment, though this impact was not extensively studied. Amount was tuned such that the theoretical gel point via the Flory-Stockmayer method[4] was 52%. Theoretical critical gel point (p_c) in the stoichiometric case is:

$$p_c = \frac{1}{\sqrt{1 - f_{w,NCO}}\sqrt{1 - f_{w,OH}}}$$

where f_w is the weighted functionality

$$f_w = \frac{\sum f_i^2 N_i}{\sum f_i N_i}$$

Dibutyltin dilaurate (DBTDL): Catalyst for urethane formation. It is used trace in synthesis of BPTPUA and is retained for the matrix formation.

2-Hydroxyethyl acrylate (HEA): Connection point for holographic written polymer to matrix. Maintains structure of hologram over time and under heat as demonstrated in Figure 3.2. Reduces crosslink density of polyurethane and must be accounted for respectively.

Trimethylolpropane triacrylate (TMPTA): Additional crosslinker to prevent written polymer mobility. Does not need to be accounted for in urethane crosslink density and therefore limits the amount of pentaerythritol ethoxylate that needs to be added.

1,3-Bis(phenylthio)-2-propyl urethane acrylate (BPTPUA): Holographic writing monomer. High refractive index (1.5782), relative to other components.

Diphenyl (2,4,6-trimethylbenzoyl)-phosphine oxide (TPO): High efficiency, low yellowing photoinitiator for holographic writing at 405 nm.

3,4-Epoxycyclohexylmethyl-3',4'-epoxycyclohexane carboxylate (ECC): Low refractive index, low viscosity, rigid core, multifunctional epoxy. Enable high T_g final stage via cationic homopolymerization.

Triarylsulfonium hexafluoroantimonate salts (TAS-SbF_6): Low yellowing, cationic photoinitiator at for 365 nm epoxy homopolymerization. Sequence controlled orthoganality with holographic writing as is not trigger by 405 nm light or energy transfer with other components.

Light sources

Light exposures were performed with an EFOS Acticure A4000 using a Lumen Dynamics mercury arc bulb (PN 012-60850), filtered at 400-500 nm or 320-390 nm. Light intensities were measured with a Thorlabs PM100D radiometer, equipped with a Thorlabs S120VC photodiode sensor, relative to the 405 nm and 365 nm setting respectively. Floodcures immediately following holographic writing were performed using a 405 $\pm$ 7 nm LED (Thorlabs SOLIS-405C), and intensity was measured similarly.

Holographic recording and hologram characterization

The volume holographic grating

The simplest form of the V-HOE for material testing is the volume holographic grating (VHG), which permits highly efficient single-order light diffraction only when the Bragg phase-matching condition is met; otherwise allowing the light to transmit unperturbed.[5] Bragg diffraction can be predicted for a given grating period Λ, material thickness L, readout wavelength λ, and incident angle θ_i of the readout light (manuscript Figure 3.1). The Bragg condition for a phase-transmission VHG read out with a given wavelength is a single, phase-matched output wave at a specific diffraction angle θ_d.

Bragg curve metrology for VHGs

A plane-wave input to an appropriately thick phase-transmission VHG has an angular-dependent diffraction efficiency $\eta(\theta)$ called the Bragg curve and peaks at the Bragg-matching angle θ_0.[5] Under these conditions, Kogelnik's well-established coupled wave theory (CWT) for VHGs, as implemented by Uchida, dictates that the magnitude of

the diffraction efficiency is entirely dependent on the refractive index modulation contrast n_1 induced within the grating during recording.[6,7] Extracting this value by fitting the measured Bragg curve to CWT provides an assessment metric for the conversion of writing monomer to written polymer during and after recording.[8]

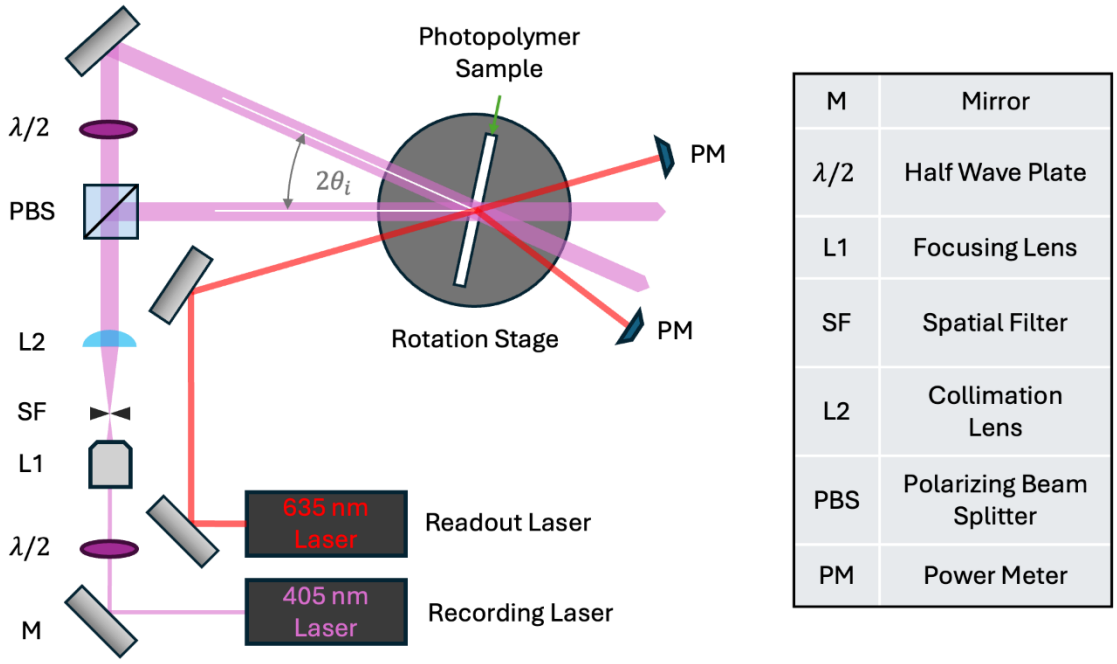

M	Mirror
$\lambda/2$	Half Wave Plate
L1	Focusing Lens
SF	Spatial Filter
L2	Collimation Lens
PBS	Polarizing Beam Splitter
PM	Power Meter

Figure S3.4. Schematic of optical layout for holographic recording and readout characterization.

Isocyanate reaction monitoring

FT-IR (Nicolet 8700), was used to verify isocyanate depletion for the formation of urethanes in the preparation of the stage 1 material. The sample was prepared between KBr plates and monitored in mid-IR for the disappearance of the isocyanate peak at 2270 cm^{-1}.

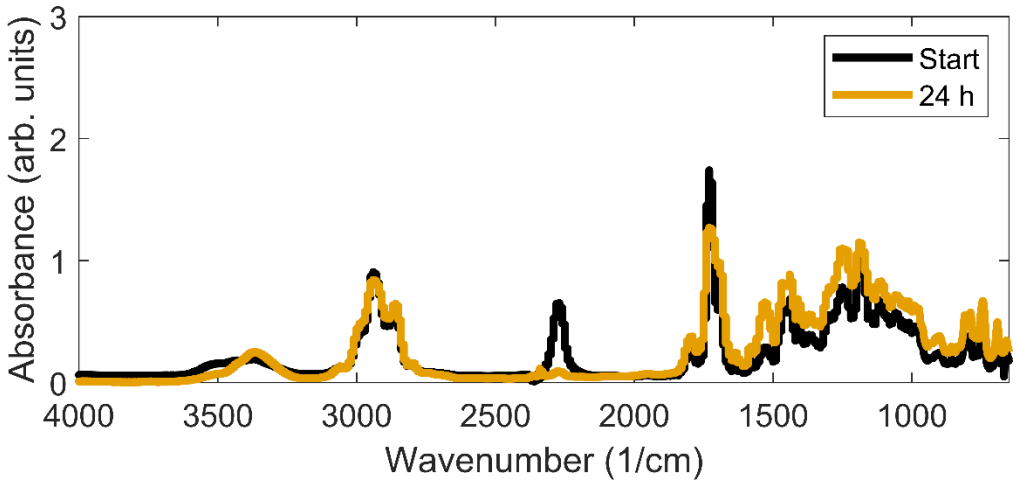

Figure S3.5. Disappearance of the isocyanate peak signaling completion of polyurethane reaction used to prepare stage 1 network.

Additional analysis of thermomechanical properties

DMA was performed on a TI Instruments RAS-G2 as described in the body. Full width at half maximum (FWHM) of the tan(delta) curve, was assessed as a metric for homogeneity. Crosslink density (ρ_c) was estimated at a temperature of T_g + 50 °C according to

$$\rho_c = \frac{E'}{3RT}$$

where *R* is the ideal gas constant and E' is the modulus at temperature *T*, evaluated in this case where $T = T_g$ + 50 °C.[9]

	T_g (°C)	**FWHM (°C)**	**ρ_c (mM)**
Stage 1 network	-34 ± 1	11.5 ± 0.7	44 ± 14
Stage 2 network	-22 ± 1	20.7 ± 0.8	110 ± 20
Stage 3 network	101 ± 8	67.0 ± 2.0	1900 ± 800

Table S3.2. Tabulated DMA results for three-stage glassy system. Increases in T_g correlated with increases in heterogeneity and crosslink density as would be expected. Large FWHM is expected in Stage 3 due to chain growth of epoxides via homopolymerization.

Kinetic evolution of multistage cures

BPTPUA synthetic steps and functional group conversion in network stages were analyzed using a Nicolet 8700 FTIR spectrometer in transmission mode. Acrylate kinetics were assessed by near-IR in 250 μm films between glass, while epoxy kinetics were assessed by mid-IR between salt plates.

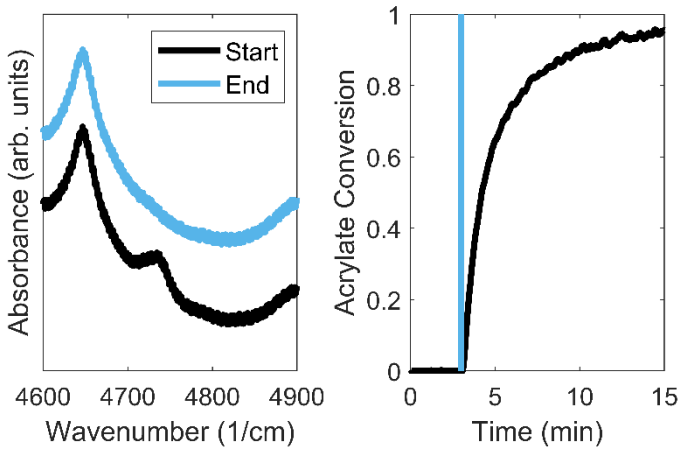

Figure S3.6. Kinetic evolution of acrylate assessed by FT-IR. Conversion is assessed by tracking the peak at 4735 cm^{-1}. The sample is exposed to 3 mW/cm^2 of 400-500 nm light starting at 3 min (blue).

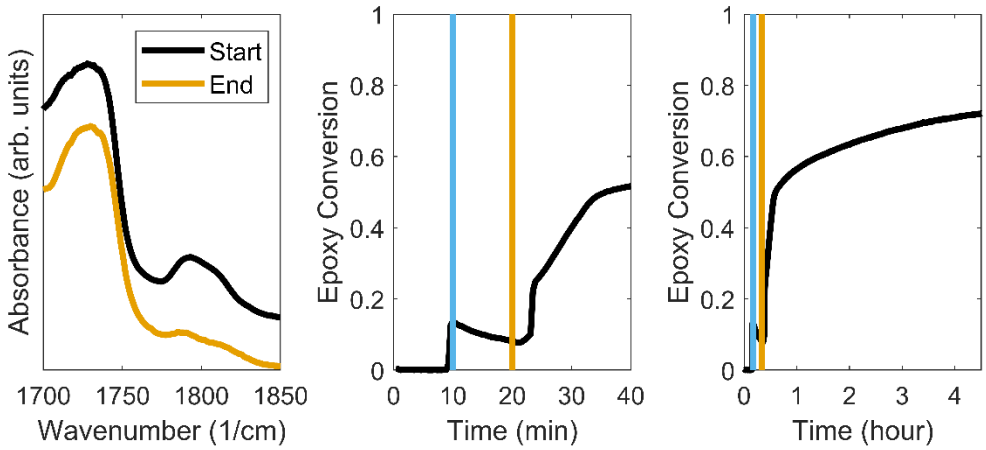

Figure S3.7. Kinetic evolution of epoxy assessed by FT-IR. Conversion is assessed by tracking the peak at 1800 cm^{-1}. 320-390 nm light (100 mW/cm^2, 10 min) activates the TAS-SbF_6 at 10 min (blue). Some conversion is noted, which is attributed to the photothermal effect. At 20 min (orange), the temperature is ramped to 150 °C (~10 min) and held for the remainder of the cure.

UV-Vis of multistage films

UV-Vis of 250 μm thin films were assessed by Thermo Scientific Evolution 300.

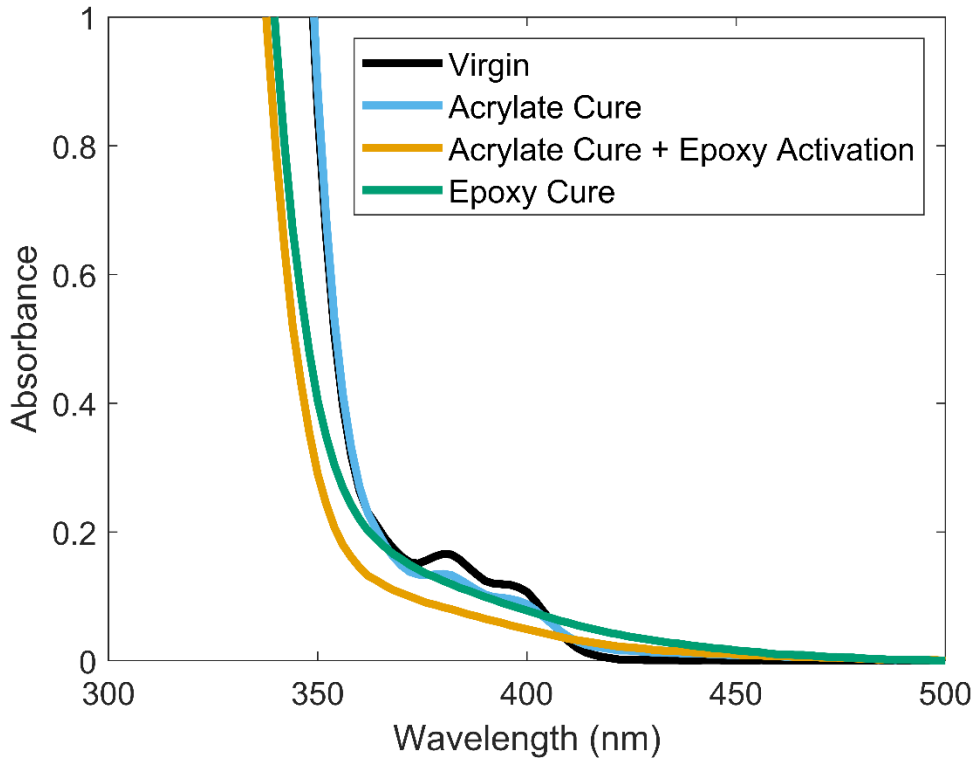

Figure S3.8. UV-Vis of 250 μm thin films throughout the multistage processing. TPO peaks bleach under 400-500 nm exposure (3 mW/cm^2, 15 min), and are lost following epoxy activation at 320-390 nm (20 mW/cm^2, 7.5 min each side). Slight yellowing was noted upon thermal cure (150 °C, 4h).

Refractive index measurements

The refractive indices of liquid samples were measured using an Abbe refractometer at the sodium-d line (589.3 nm) at room temperature. The refractive index of polymeric films was measured using a Metricon 2010/M prism coupler at a wavelength of 636.6 nm under ambient conditions.

Material	**Refractive Index**
BPTPUA[a]	1.5782
ECC[a]	1.4989
ECC – polymerized[a]	1.5218
Stage 1 network[b]	1.5136
Stage 2 network[b]	1.5135
Stage 3 network[b]	1.5152

Table S3.3. Refractive indices of (a) monomers at 589.3 nm in Abbe refractometer or (b) network stages using 636.6 nm in prism coupler.

Temperature effect on holographic performance

The final photopolymer system is designed to maintain its optical characteristics over the temperature range 22 – 70 °C. The baseline refractive index of the material was measured using a Metricon 2010/M prism coupler at a wavelength of 636.6 nm. The media was brought to measurement temperatures by heating both the measurement prism and the coupling piston of the prism coupler. Holograms were brought to measurement temperatures by attaching a ring-shaped heating element to the front and back surface of the holographic exposure and measuring a Bragg curve through the heating element aperture at the required temperatures (Thorlabs HT10KR1). A k-type thermocouple was attached to the polymer and measured on a temperature log to verify the polymer temperature (Tecpel DTM-322 Temperature and Humidity meter). Diffraction efficiency analysis was performed on the measured Bragg curves in accordance with the methods outlined in supplemental information section 6.

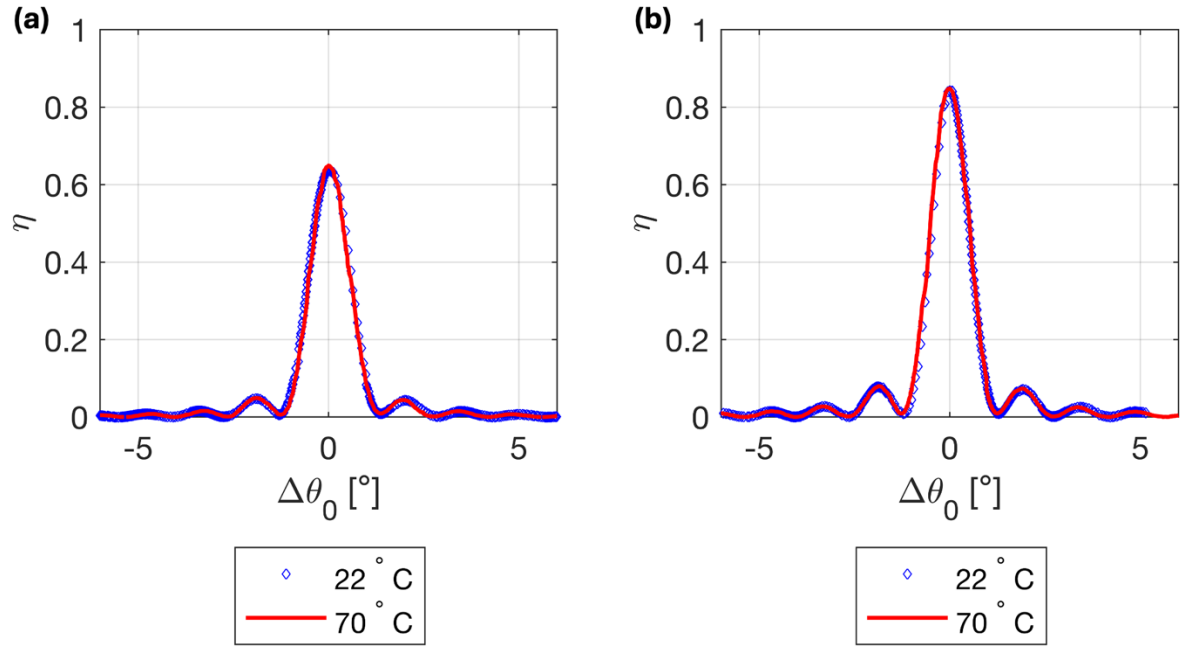

Figure S3.9. Bragg curve readouts showing optical stability of VHGs at 22 and 70 °C (a) in the rubbery stage-2 state and (b) in the glassy stage-3 state.

Media State	$\mathbf{T}$ $\pm \mathbf{0.05}$ (℃)	$\boldsymbol{\eta}$ $\pm \mathbf{0.05}$ (%)	$\mathbf{n_1}$ $\pm \mathbf{0.0001}$	$\mathbf{L}$ $\pm \mathbf{0.3}$ $(\boldsymbol{\mu m})$	$\mathbf{n_0}$ $\pm \mathbf{0.0001}$
Stage 2 (Rubbery)	22.1	63.7	0.0045	39.5	1.5135
	70.0	64.9	0.0044	40.5	1.5136
Stage 3 (Glassy)	22.1	84.2	0.0054	40.9	1.5152
	70.0	84.9	0.0056	40.4	1.5153

Table S3.4. Temperature dependent holographic properties as measured. The properties listed include media temperature T, diffraction efficiency η, refractive index modulation contrast n_1, media thickness L, and baseline refractive index n_0.

Media State	$\boldsymbol{\Delta\eta}$ $\pm \mathbf{0.05}$ (%)	$\mathbf{\Delta n_1}$ $\pm \mathbf{0.0001}$	$\mathbf{\Delta L}$ $\pm \mathbf{0.3}$ $(\boldsymbol{\mu m})$	$\mathbf{\Delta n_0}$ $\pm \mathbf{0.0001}$
Stage 2 (Rubbery)	1.2	-0.0001	$+1.1$	0.0001
Stage 3 (Glassy)	0.7	$+0.0002$	-0.6	0.0001

Table S3.5. Change in holographic properties over the temperature difference $\Delta T = (70.0 - 22.1)$ ℃.

Haze generation analysis

Haze generation was measured in the three network stages using a haze-gard i haze meter from BYK Instruments according to the ASTM D1003-21 standard test method. Triplicate sample regions were selected for measurements a) within the exposure area of the holograms and b) in “background” regions distinctly distant from holographic exposures. The nominal thickness of each sample was $50 \pm 1\ \mu\mathrm{m}$. All measurements were made using CIE illuminant C. The haze of the background is subtracted from the haze of the exposure region, yielding the exposure-induced haze.

Total Luminous Transmittance: Background (%)	**Percent Haze:** Background (%)	**Total Luminous Transmittance:** Exposure Region (%)	**Percent Haze:** Exposure Region (%)	**Exposure-Induced Haze (%)**
91.4 ± 0.1	0.29 ± 0.06	91.5 ± 0.04	0.41 ± 0.06	0.1 ± 0.1

Table S3.6. Transmittance and haze measurements of Stage 3 holographic media. Exposure region measurements were taken in the center of the holographic exposure, background measurements were taken in unexposed regions of the sample.

Bragg curve analysis through processing conditions

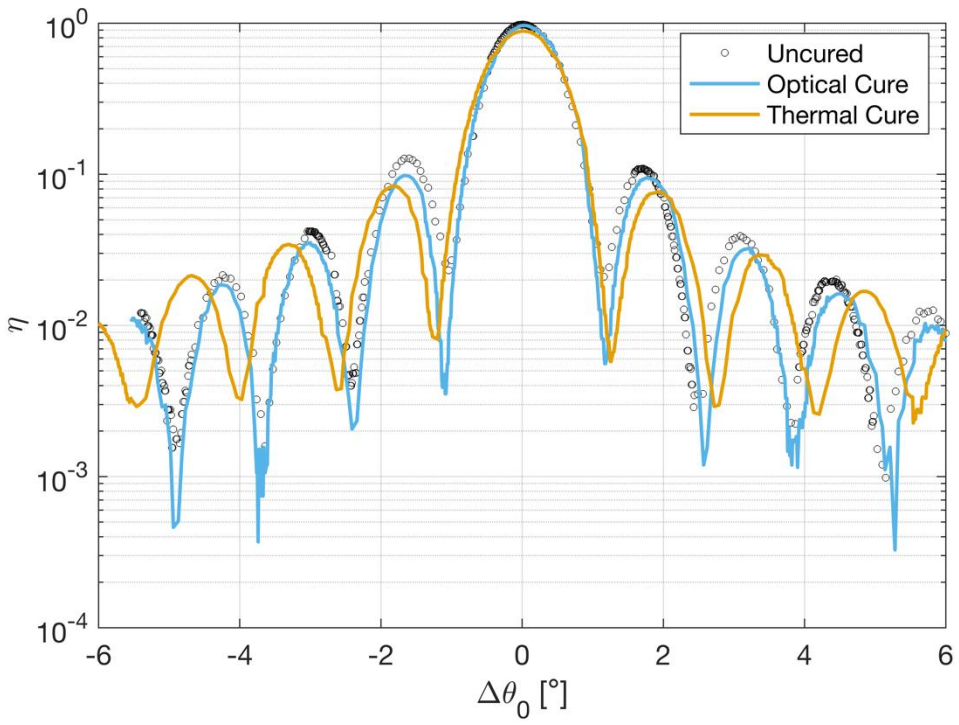

Figure S3.10. Representative Bragg curve of phase-transmission VHG through the transformation from uncured exposure to the final glassy film shown on a logarithmic y-axis. The optical cure consists of exposure to 405 nm, 1.5 mW/cm^2 LED light for 15 min. Similarly, the photoacid for the epoxy cure is triggered with a 15 min exposure of 320-390 nm light at 20 mW/cm^2 prior to a 4 h, 150 °C thermal cure. Bragg curve analysis performed as outlined in supplementary information section 6.

Nanoindentation mapping

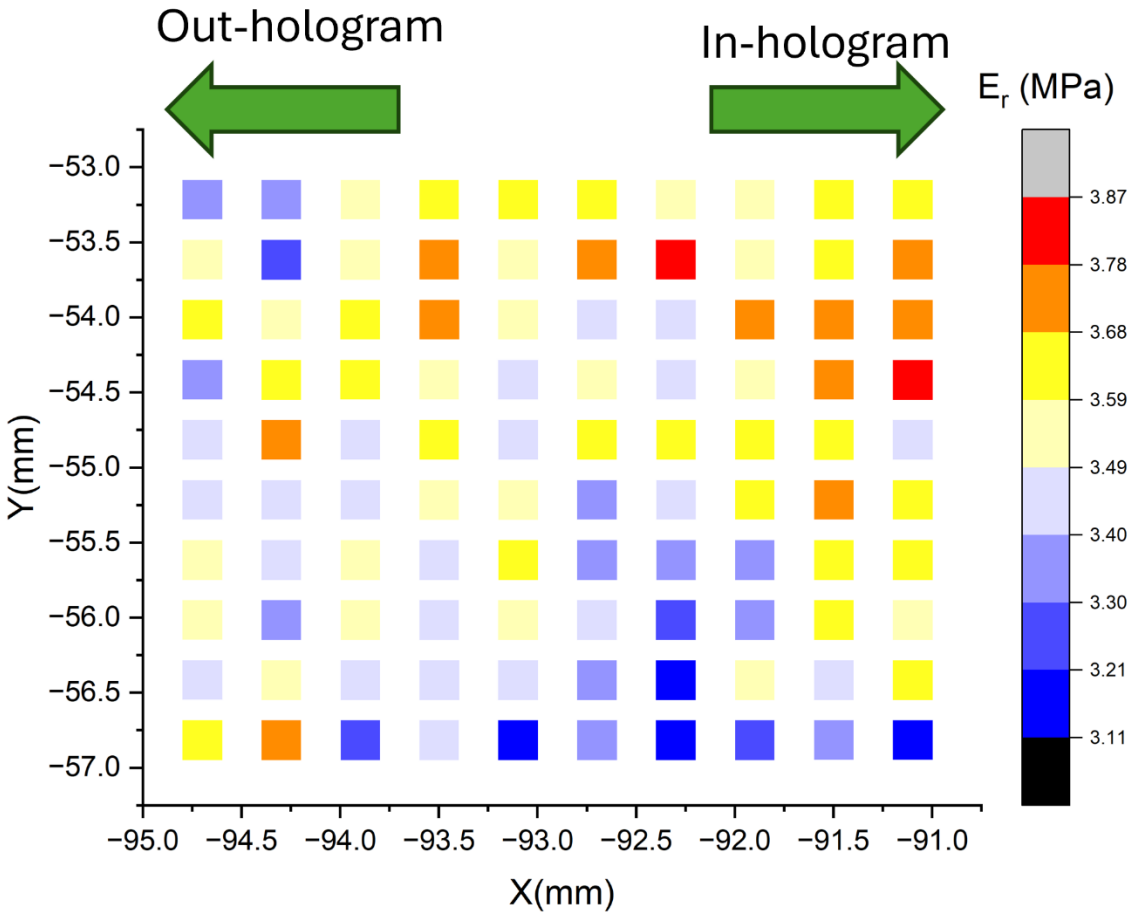

Figure S3.11. Reduced modulus map of optically cured (405 nm, 1.5 mW/cm^2, 15 min), multistage VHG. In-hologram is statistically stiffer than out-of-hologram.

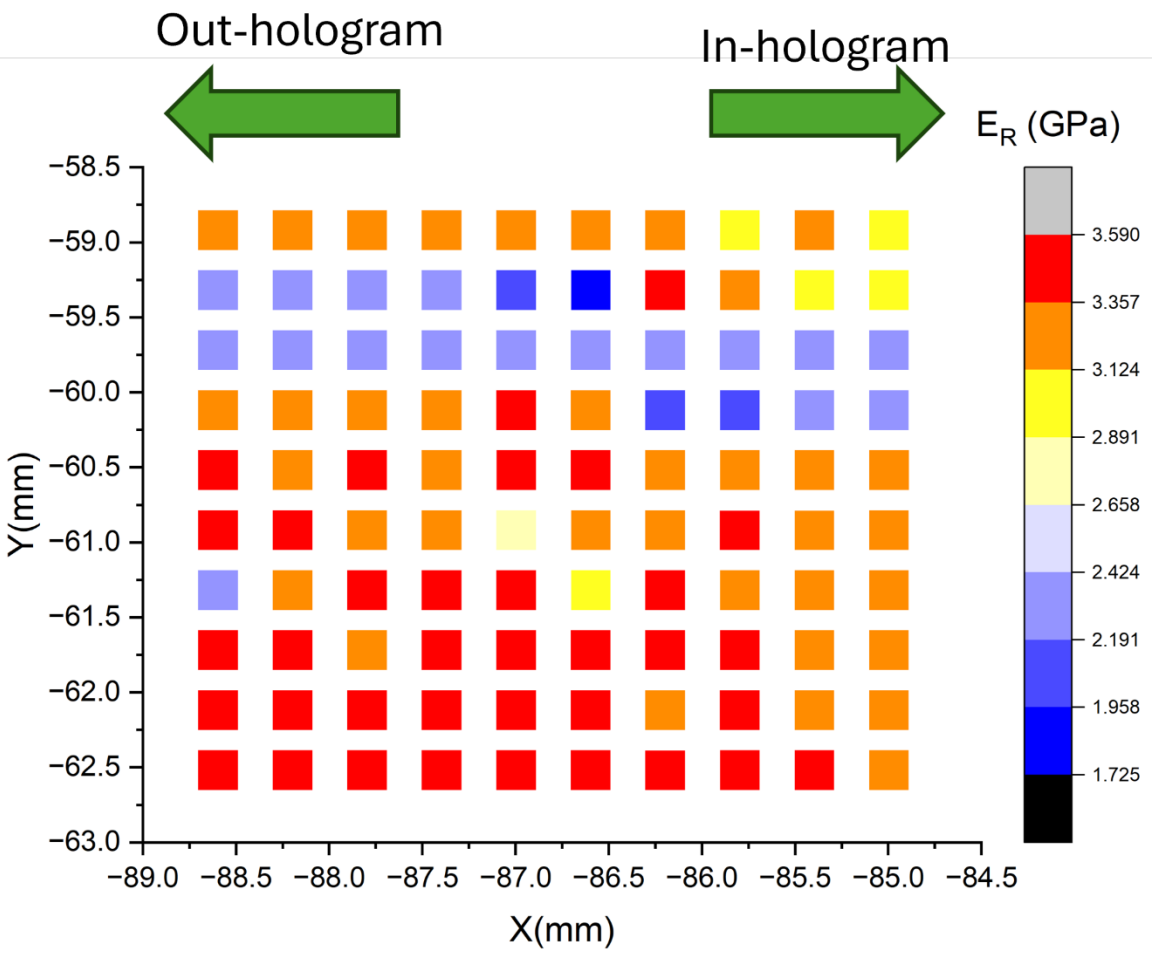

Figure S3.12. Reduced modulus map of thermally cured (320-390 nm, 20 mW/cm^2, 15 min activation followed by 150 °C, 4h), multistage VHG. Heterogeneity is not consistent with a shift from in-hologram to out-of-hologram.

3.8.3 Additional References

(1) Alim, M. D.; Glugla, D. J.; Mavila, S.; Wang, C.; Nystrom, P. D.; Sullivan, A. C.; McLeod, R. R.; Bowman, C. N. High Dynamic Range (Δn) Two-Stage Photopolymers via Enhanced Solubility of a High Refractive Index Acrylate Writing Monomer. *ACS Appl. Mater. Interfaces* **2018**, *10* (1), 1217–1224. https://doi.org/10.1021/acsami.7b15063.

(2) Harant, A. W.; Khire, V. S.; Thibodaux, M. S.; Bowman, C. N. Thiol−Ene Photopolymer Grafts on Functionalized Glass and Silicon Surfaces. *Macromolecules* **2006**, *39* (4), 1461–1466. https://doi.org/10.1021/ma0522007.

(3) Hu, Y.; Trujillo-Lemon, M.; Sias, A. N.; Dobson, A. L.; Podgórski, M.; Singh, J.; Mavila, S.; McLeod, R. R.; Bowman, C. N. Reducing Haze of Holographic Gratings Recorded in a Two-Stage Photopolymer. *Macromolecules* **2025**. https://doi.org/10.1021/acs.macromol.4c02398.

(4) Stockmayer, W. H. Theory of Molecular Size Distribution and Gel Formation in Branched Polymers II. General Cross Linking. *J. Chem. Phys.* **1944**, *12* (4), 125–131. https://doi.org/10.1063/1.1723922.

(5) Moharam, M. G.; Young, L. Criterion for Bragg and Raman-Nath Diffraction Regimes. *Appl. Opt.* **1978**, *17* (11), 1757. https://doi.org/10.1364/AO.17.001757.

(6) Kogelnik, H. Coupled Wave Theory for Thick Hologram Gratings. *BELL Syst. Tech. J.* **1969**.

(7) Uchida, N. Calculation of Diffraction Efficiency in Hologram Gratings Attenuated along the Direction Perpendicular to the Grating Vector. *J. Opt. Soc. Am.* **1973**, *63* (3), 280. https://doi.org/10.1364/JOSA.63.000280.

(8) Kowalski, B. A.; McLeod, R. R. Design Concepts for Diffusive Holographic Photopolymers. *J. Polym. Sci. Part B Polym. Phys.* **2016**, *54* (11), 1021–1035. https://doi.org/10.1002/polb.24011.

(9) Hiemenz, P. C.; Lodge, T. P. *Polymer Chemistry*, 2nd ed.; CRC Press: Boca Raton, 2007. https://doi.org/10.1201/9781420018271.

Chapter 4: Dual-Cure Dynamic Networks for Mechanophotopatterning of Surface Topography*

*Manuscript published under the same name in *Macromolecules* **2025**, 58, 4, 1975–1981

4.1 Abstract

Control of thin film surface features is critical in the fields of optics, biologics, electronics, and microfluidics, among others. Although facile in method, implementation of mechanophotopatterning has been chemically constrained, resulting in an undesired evolution or a limited processing window. This work overcomes these limitations by combining dynamic covalent chemistry to alter the surface relief with a dual-cure approach that increases the crosslink density and glass transition temperature following patterning to permanently fix the structure. The inclusion of a photosensitive dynamic covalent moiety, in the form of an allyl sulfide, allows for spatiotemporal stress relaxation control, and the associated formation of topographic patterns when the elastomer is exposed to light under strain. Typically, the resulting topography remains susceptible to undesirable evolution as the network's dynamic capacity persists. To mitigate the residual dynamics, 65 wt% bisphenol A diglycidyl ether is included, in combination with a thermally latent acid, to facilitate a post-topography altering cationic polymerization which permanently fixes the topography through large changes in crosslink density and glass transition. Feature height of films fixed by this cure remain within 100 nm (<1% change), of their original dimensions.

4.2 Introduction

Materials processing techniques that provide for spatiotemporal control (i.e. user-defined specification of where and when a process occurs), have proven instrumental in many applications. The capacity for spatiotemporal control varies drastically based on the stimuli used (such as heat, pH, mechanical strain, or light), and the particular chemistry of the material undergoing the process. Light-mediated spatiotemporal control of photopolymerization and photocrosslinking enables capabilities that would be otherwise inaccessible.[1–3] Industrially, this spatiotemporal control is vital for processes such as lithography[4,5] and photoinduced additive manufacturing.[6,7] More broadly, photo-responsive materials are triggered to undergo material property changes precisely when and where desired. In the context of polymeric materials, available reactions include, but are not limited to not just polymerization,[8,9] but also degradation,[10,11] and facilitating dynamic covalent bond exchange.[12] Herein, two sequential processes are induced – dynamic bond exchange to induce surface relief and subsequent polymerization to increase the glass transition temperature.

Covalent adaptable networks (CANs), leverage dynamic covalent bonds to allow for reprocessing and reworking of otherwise intractable crosslinked polymer networks. Upon the application of a stimulus, dynamic bond rearrangement enables stress relaxation while still maintaining the same longterm network properties following removal of the stimulus. Much of the field focuses on stimuli that impact the bulk material, such as heat[13–15] and pH,[16–18] in systems including Diels-Alder,[19] transesterification,[20] hindered urea,[21,22] and disulfide exchange reactions.[23,24] However, spatial control over dynamic

covalent chemistry is achieved via photoinduced processes, such as the radically mediated allyl sulfide,[25–28] trithiocarbonate,[29] and disulfide[10,30] exchange reactions.

One specific process that benefits from this additional control of allyl sulfide dynamics, provided by light, is the mechanophotopatterning (MPP) process introduced by Kloxin et al.[27] In this process, a photoplastic elastomer is strained and then selectively exposed to light via photopatterned irradiation. The resulting material displays topographical patterning with valleys where photomediated relaxation of the applied stress resulted in defined, localized thinning (Scheme 4.1) due to irreversible, viscoelastic flow. This process demonstrates promise for applications that leverage surface properties impacted by topography such in the fields of optics,[31,32] biology,[33,34] microfluidics,[35,36] and electronics.[35,37] However, since the dynamic nature remains active, these materials remain susceptible to creep and other undesired topographical evolution processes.

Scheme 4.1. (a) Dynamic covalent allyl sulfide exchange. (b) Stretching an elastomer containing the radically mediated allyl sulfide allows for surface patterning evolution due to localized stress relaxation.

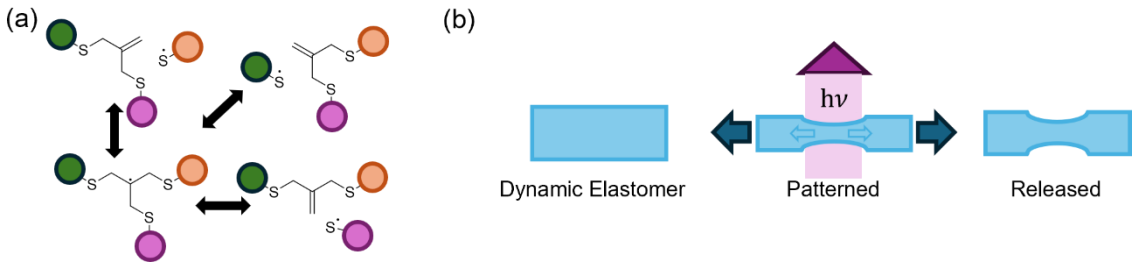

Due in part to this consideration, other works have investigated alternative MPP methodologies that do not leverage dynamic covalent chemistry. These works leverage dual-cure systems to selectively increase crosslink density of a film in a strained state[38–

[41] or by other mechanical manipulation.[42–46] Upon strain release, the contraction of these films differs locally as a function of crosslink density and therefore a topographical pattern emerges. Consequently, this methodology is not without its own limitations as the potential for further patterning is dramatically reduced due to monomer consumption. In contrast, a dynamic system can be strained and further patterned until a satisfactory pattern is reached.[27] Additionally, upon strain release, residual forces act upon the films resulting in topographical consequences; notably, buckling. Similarly, other structural deficits cannot be solely resolved in dual-cure methodology. A dynamic system, alternatively, overcomes defect limitations by allowing for further stress relaxation to reprocess.

Motivated by these limitations, this work combines benefits of dynamic covalent chemistry and dual-cure methodologies to enable a dynamically patternable, yet fixable, material. By synthesizing elastomers that contain both allyl sulfide moieties and polymerizable epoxy groups, full spatiotemporal dynamic capacity is maintained up until an orthogonal, thermally initiated epoxy homopolymerization is used to lock the material in its final conformation. Furthermore, this platform allows for more topography control, via mechanophotopatterning, both during and after the patterning process than those to date. Thus, this novel methodology, that is both dynamic and dual-cure, provides a gateway for implementation in optical, electronic, and microfluidic devices.

4.3 Experimental

4.3.1 Materials

A previously reported procedure was performed to prepare the dynamic allyl sulfide diol moiety (ASdiol, Scheme 4.2).[29] All other materials were purchased from commercial sources and used without further purification. Sodium metal, 3-chloro-2-chloromethyl-1-propene, bisphenol A diglycidyl ethoxylate (BADGE), 2-mercaptoethanol, polytetrahydrofuran (M_n = 1000 g/mol), hexamethylene diisocyante (HDI), 2-methyl-4′-(methylthio)-2-morpholinopropiophenone (Irgacure 907, I907), borontrifluoride ethylamine complex, and dibutyltin dilaurate were purchased from Sigma Aldrich. Desmodur N3900 polyisocyanate was donated by Covestro AG.

4.3.2 Thin Film Preparation

To prepare MPP films, a resin was prepared containing 65 wt% BADGE, 8.2 wt% Desmodur N3900, 7.9 wt% ASdiol, 7.6 wt% polytetrahydrofuran (M_n = 1000 g/mol), 4.3 wt% HDI, 5 wt% Irgacure 907, and 2 wt% borontrifluoride ethylamine. Overall, there is a stoichiometric amount of isocyanate and alcohol groups under the assumption that the 3% BADGE has dimerized which is consistent with the high end of the supplier's provided range. Furthermore, the polyurethane networks theoretical gel point conversion is 90% according to the Flory-Stockmayer equation (see SI for further details).[47,48] Films were mixed until homogenous, degassed, and a catalytic amount of DBTDL (500 ppm) was added from a 5% (v/v) stock solution in DCM. The resin was promptly vortexed and degassed prior to being cast between Rain-X treated glass slides

with 250 μm vinyl spacers. Afterwards, films were allowed to set overnight at ambient temperature.

4.3.3 Mechanical Testing

Photoinduced stress relaxation experiments were carried out on a TA instruments RSA G2. Films were cut (10 mm x 20 mm) and strained by 20%. After allowing 3 minutes to achieve steady state deformation, dynamic exchange was initiated via a Thorlabs M405L2-C5 LED emitting 405 nm light with set intensity within the range of 5-20 mW/cm^2, as determined by a Thorlabs PM1000D radiometer equipped with a Thorlabs S120VC photodiode sensor.

Dynamic temperature sweeps were performed in a similar manner. Rubbery thin film samples (n = 3) were heated from -80 to 100 °C while glassy films were heated from 25 to 200 °C. Samples were heated at a ramp rate of 3 °C and with a frequency of 1 Hz and oscillatory strain of 0.03%. The T_g was determined as the peak of the tan delta curve.

4.3.4 Mechanophotopatterning

Films were cut (20 mm x 40 mm) and mounted on the two wide sites of a biaxial capable stretcher (Science Edge BFSFM-X50-Y45) and strained by 20% linearly (15 mm to 18 mm). The unused mounting sites were separated sufficiently to not interfere. The strained sample was aligned in the exposure system with 638 nm patterned light such that the exposure was in the middle of the sample to minimize edge effects. The sample was then exposed to 20 mW/cm^2 of patterned 405 nm light for 40 min. The

pattern was achieved via a digital micromirror device (Vialux V-9001) with each resulting 4.58 μm pixel (2.47 μm for resolution testing), either set off or always on for the duration of the exposure, in conjunction with a laser (Civil Laser, 405 nm, 3.5 W, multimode fiber-coupled). A schematic of the relevant optics is shown in Scheme S4.1. Following patterning, the films were laminated on glass or taped over a 0.5-inch inner-diameter 18-8 stainless steel washer (1.125-inch outer-diameter), prior to thermal treatment and topography assessment.

4.3.5 Thermal Treatment

Prior to topography assessment by optical profilometry, all samples underwent a 16 h thermal cure at 150 °C to trigger the epoxy homopolymerization. Samples were held in glass petri dishes for the duration of the thermal cure to prevent forced flow within the oven from affecting the material, notably in the case when films were suspended over washers.

4.3.6 Optical Profilometry

Topography was assessed by a Keyence VK-X1000 optical profilometer using a 50x magnification lens and measured by a 404 nm laser. Individual images were automatically stitched to map the area of interest. Furthermore, all samples were thermally treated prior to measurement to prevent evolution due to the measurement laser.

4.3.7 Transfer Printing

To achieve the desired transfer printing process, a thin layer of ink was applied to cured and patterned films by lightly drawing a Sharpie marker across the surface of the films, limiting one stroke per area. The films were then lightly pressed on to a sheet of paper and pealed to reveal the transferred print that appears as the negative of the original mask. A red Sharpie was selected due to its advantageous wetting properties with respect to those of the thermally cured films. Ink is transferred from the Sharpie only to the elevated portions of the pattern which subsequently transfer the ink to the paper.

4.4 Results and Discussion

This work demonstrates patterning and subsequent fixing of surface topography through sequence controlled dynamic exchange and dual (two stage) cure polymerizations. In stage 1, the material is rubbery and undergoes patterned stress relaxation via the radical-mediated allyl sulfide addition-fragmentation reaction. This stress relaxation allows for the desired patterning. Stage 2 is prompted by a sequence controlled orthogonal thermal cure of otherwise latent acid and epoxy.[49] The resulting cationic homopolymerization raises the glass transition temperature and crosslink density of the network, thereby both modifying its mechanics and mitigating rearrangement.

Scheme 4.2. (a) Compounds used to prepare multistage MPP films. (b) Multistage control MPP films. The desired topography is susceptible to further evolution during stage 1. Additional crosslinking of the system prevents bulk rearrangement, thereby fixing the desired topography.

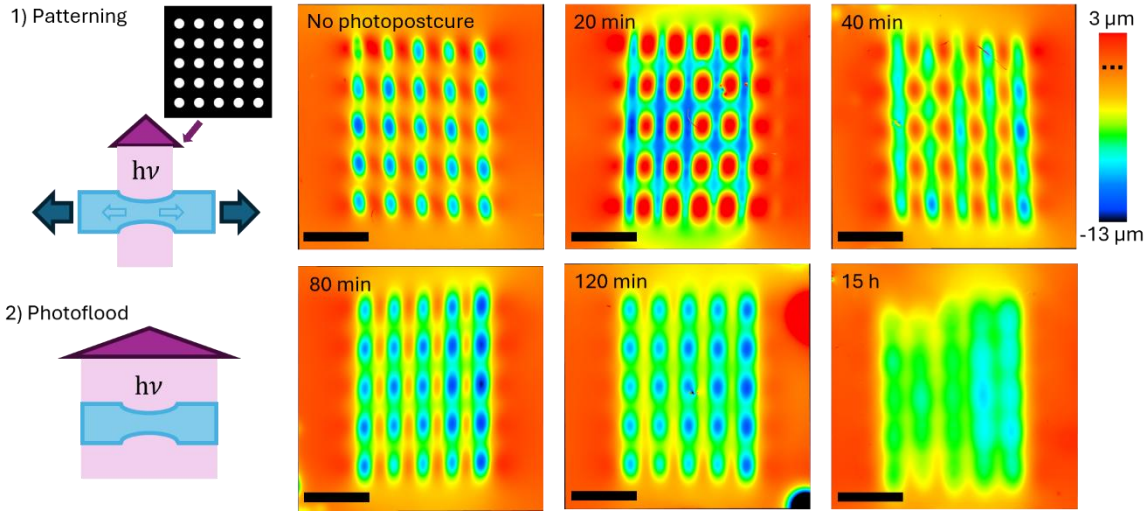

4.4.1 Dynamics

To create uniform surface features without warping, MPP films should be optically thin so that the stress relaxation is homogenous throughout the depth of the material. Additionally, as the allyl sulfide is not self-initiating, there must be sufficient photoinitiating species to allow for all the desired patterning steps. A large amount of Irgacure 907 (5 wt%), is included to provide an ample processing window for the material. Due to its low absorbance at 405 nm, the 250 µm thick films used in this study are optically thin (16% attenuation at 405 nm, Figure S4.7). The initiator, exhibiting a half-life of nearly 5 hours at an intensity of 20 mW/cm^2 (Figure S4.5), persists well beyond the MPP process. The stress relaxation of this formulation at various intensities, as well as its long duration

dynamics are demonstrated in Figure 4.1. It should be noted that the relaxation timescale of the film is dependent not only on the initiator concentration and light intensity, but also upon the stress imparted on the film. For example, higher light intensities or shorter wavelength light could readily be used to accelerate the relaxation process. Critically, the complete stress relaxation of these films demonstrates patterning capabilities, and that negligible epoxy reaction has occurred that would limit the exchange phenomena within the stage 1 films.

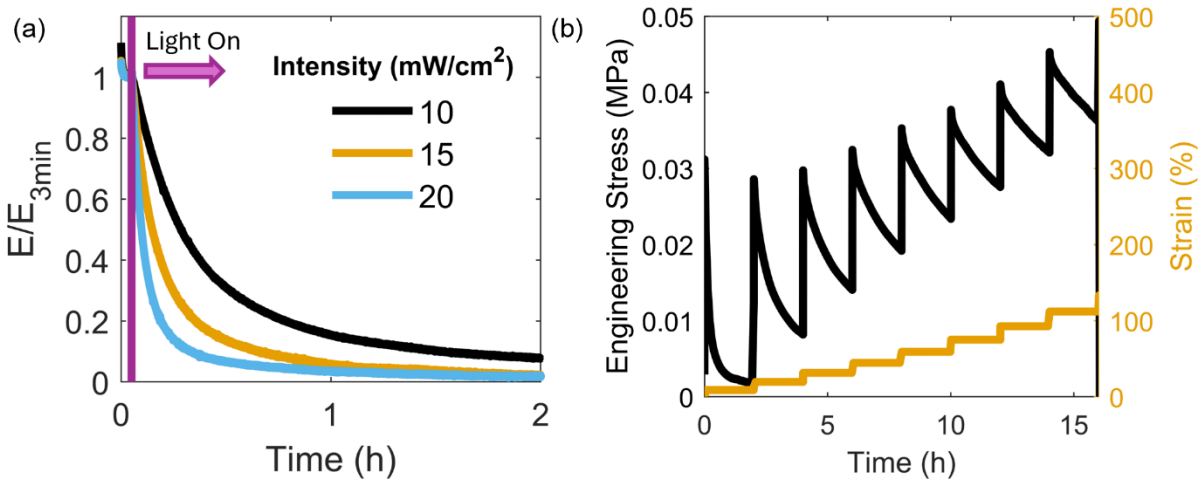

Figure 4.1. (a) Representative light intensity dependent stress relaxation of stage 1 allyl sulfide based films under 20% strain at various intensities of 405 nm light (LED), turned on at 3 min. (b) Sequential stress relaxation demonstrating active dynamics over a broad processing window. Sample strained an additional 10% relative to current extension every 2 hours and under continuous 405 nm, 20 mW/cm^2 exposure.

A significant limitation of MPP is the potential for the pattern to evolve after the desired processing is completed due to light exposure, other radical producing events, or spontaneous bond exchange. To demonstrate this phenomenon, patterned samples were

subjected to varied light conditions following the initial patterning. The loss of fidelity of the patterned topography is shown in Figure 4.2, noting an 88% decrease in feature amplitude in addition to the loss of shape fidelity after 15 hours of exposure. Due to stresses related to strain release and surface tension, the patterned sample does not have uniform spatial relaxation.

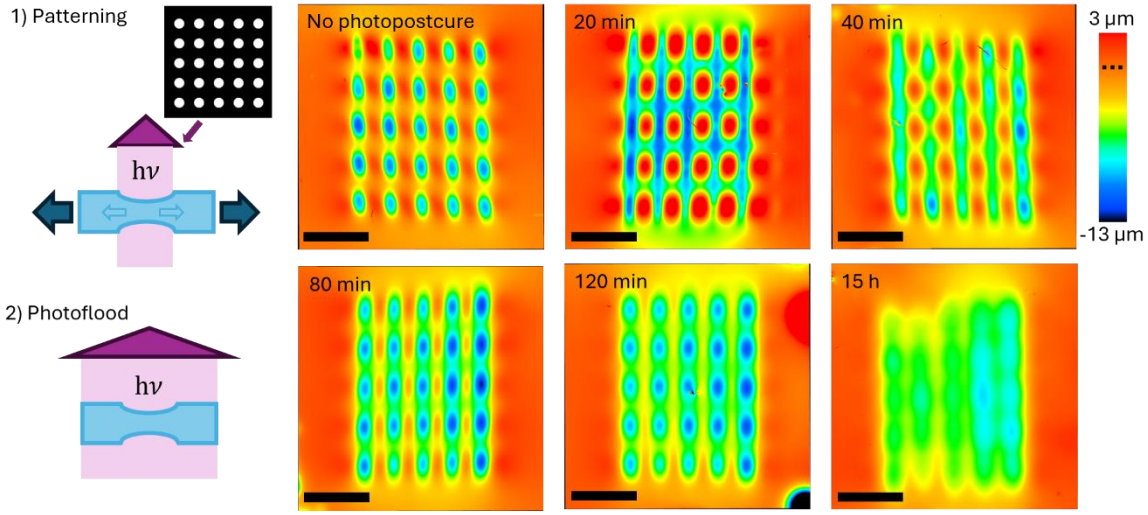

Figure 4.2. Patterned array of circles followed by photoflood postcure. Samples were strained by 20% horizontally and patterned (252 µm diameter circles with 252 µm spacing between circles), with 20 mW/cm^2, 405 nm laser for 40 min. Films were released, laminated on glass, and exposed in the absence of any additional strain to 405 nm LED (20 mW/cm^2) for varied durations. Patterns are lost due to surface tension combined with the dynamic bond exchange. Surface topography assessed by optical profilometry. Films are thermally cured following all light exposure steps. Scale bars are 1 mm, with a 16 µm color profile height range.

4.4.2 Dual-Cure

While the dynamic nature of these materials facilitates complex patterning and repatterning, the material evolution shown in Figure 4.2 is preventable upon reaching the desired surface characteristics through the inclusion of unreacted epoxy with a latent initiator that facilitates a second stage, vitrifying cure. Not only does this inclusion allow for fixing of the topography, but the resulting polymerization also dramatically affects the film mechanics. Due to the dual-cure approach, the dynamic properties leveraged to perform MPP are eliminated in the final product. Accordingly, the inclusion of a sufficient quantity of the rigid core epoxy, bisphenol A diglycidyl ether (BADGE), results in a glassy polymer network of higher crosslink density. As shown in Figure 4.3, a thermal cure of 65 wt% BADGE at 150 °C for 16 h results in a change in T_g, from -12 ± 3 °C to 96 ± 6 °C and a final storage modulus of 1.6 ± 0.2 GPa at 25 °C. In-situ chemical and mechanical kinetics are available in Figure S4.11 and S4.13 respectively.

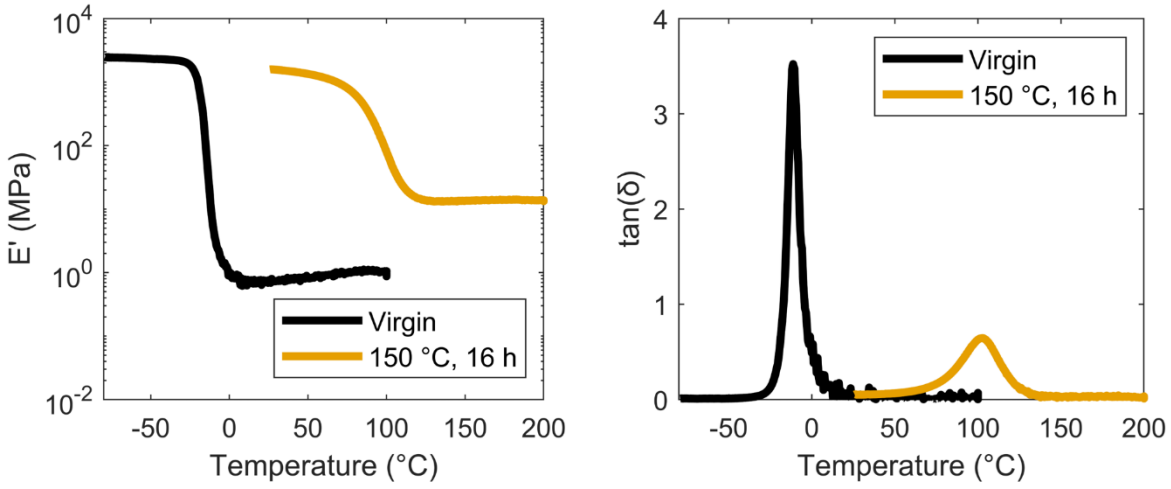

Figure 4.3. Representative temperature sweeps to compare initial and thermally cured materials. T_g increased from -12 to 96 °C along with a large increase in rubbery modulus and crosslink density.

4.4.3 Topography Fixing

In addition to modifying the properties of the final stage, a dual-cured urethane-epoxy network provides the critical feature of preventing further topographical development through dynamic bond exchange (Scheme 4.3). Preventing further evolution stems from two-fold effect of the intertwining epoxy network. First, the epoxy contribution is a non-dynamic percolated network and therefore is itself incapable of rearrangement. Secondly, the transition to a glassy material dramatically reduces free volume, increases the modulus by orders of magnitude, and simultaneously reduces chain mobility, all of which inhibit the material from being capable to rearrange.[50] Therefore, although the allyl sulfide is still susceptible to radical mediated exchange, the bulk polymer network itself has very limited capacity to rearrange.

Scheme 4.3. Dual-cure MPP for dynamic covalent photopatterning and irreversible thermal topography fixing. Stage 1 allows for patterning via photoinduced, radically mediated, allyl sulfide addition-fragmentation. Stage 2 fixes the material through a thermally triggered cationic epoxy homopolymerization. The stage 2 material is no longer susceptible to stress relaxation through dynamic bond exchange.

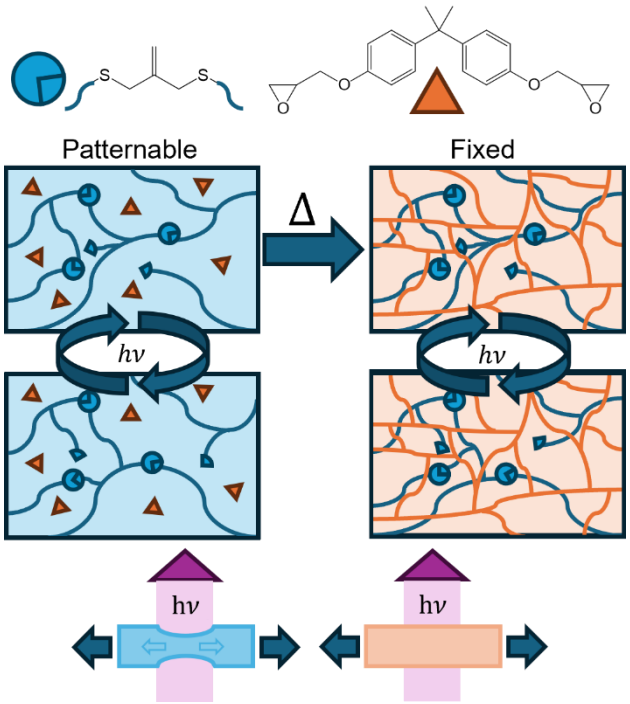

The connectivity of the epoxy stage with the polyurethane matrix is similar to that of an interpenetrating network, though side reactions and impurities, notably alcohol groups on epoxy oligomers, that link the urethane and epoxy networks likely prevent this from being rigorously true. This network structure, including the formation of a crosslinked epoxy network without any dynamic bonds, is advantageous as it provides covalent connections for the second stage epoxy network. The glassy state of the final film also has a role in the phenomenon due to the reduction of free volume and mobility, though it should be noted that stress relaxation has been previously observed in glassy films.[51] Figure 4.4 demonstrates a maintained topography, as assessed by optical profilometry,

after 16 h of exposure to 20 mW/cm^2, 405 nm light in a thermally cured sample containing 65 wt% BADGE. The initial and final topographic images differ with a standard deviation of 80 nm, which is less than 1% of the feature size. All assessments were taken after the epoxy cure, and therefore any evolution due to the thermal cure, though not expected, cannot be verified. Further analysis also demonstrates a less than 1% change in feature height (Figures S4.14 and S4.15). In contrast, an epoxy-free control is still capable of stress relaxation following thermal treatment (Figure S4.5). Stress relaxation, mechanical changes, and pattern retention were also performed on samples containing only 30 wt% BADGE (Figures S4.17-S4.19) which also demonstrated excellent fidelity. However, the modulus and T_g of the final stage are both reduced by the decreased epoxy content.

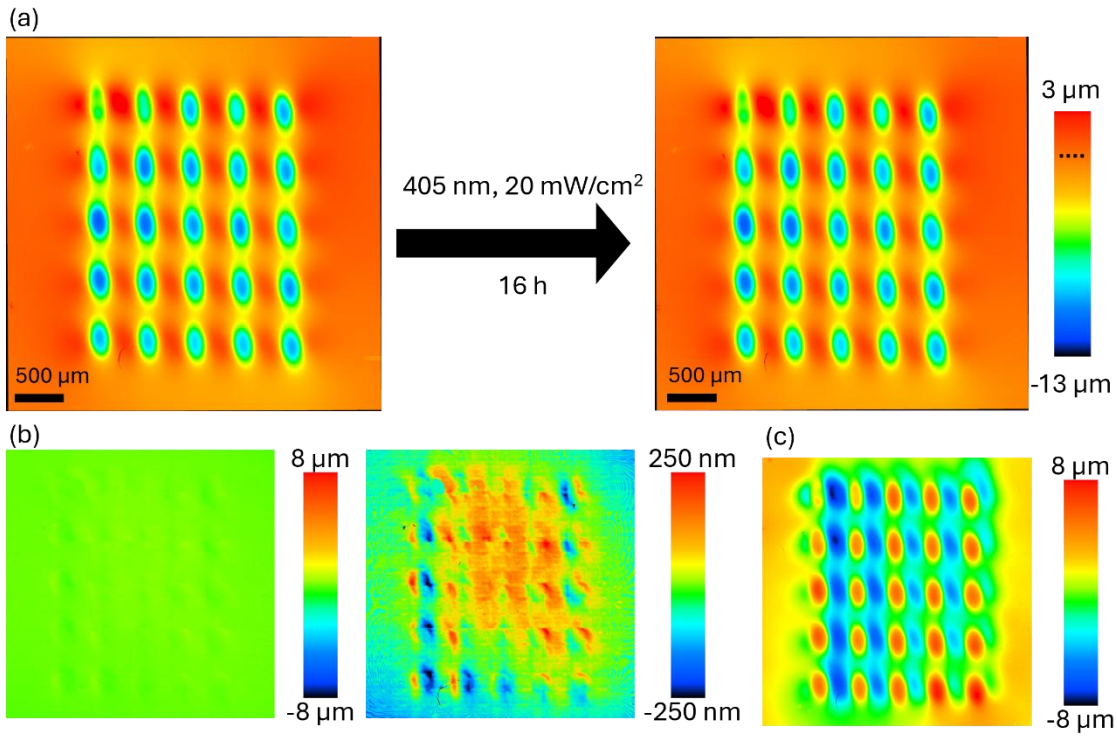

Figure 4.4. Topography is fixed following thermal epoxy cure (150 °C, 20h). (a) Surface profile, as mapped by optical profilometry, does not evolve when exposed to light that

would otherwise trigger dynamic rearrangement. (b) Difference of topography, shown on two scales, relative to the mean of cured films demonstrates minimal changes (c) Difference in topography relative to 15 h cure in Figure 4.2 demonstrates loss of fidelity without the thermal cure stage.

Due to the mechanism of the mechanophotopatterning process, assessing standard considerations, such as resolution and designing patterns for applications, lead to additional aspects that necessitate further investigation. Notably, the development of patterns is dependent not only on the strain field that is applied, but also by how all the features interact with each other and with that field as a function of time. This behavior is readily demonstrated via a standard resolution and critical dimension assessment such as the one shown in Figure 4.5a-c (replicates of this image are presented in Figure S4.20). As depicted, the feature dimensions and depth substantially change dependent on the direction that the uniaxial strain is applied, as one would expect. Furthermore, there is a trade-off between the feature depth and size. The film thickness relative to the desired feature depth is also of consideration— though not explored in this study. Further investigation, to include modeling of the complex rheological behavior of the CANs material, into the development of patterns is necessary to make robust small and/or sharp features by this methodology. Therefore, microfluidic and optical devices, although proposed, necessitate further advances in the technique, particularly with respect to understanding how the overall pattern is influenced by numerous factors. This work seeks to help enable such studies by providing a robust platform for detailed analysis. Under the current constraints, however, a facile application of this platform in its current form is

presented for transfer printing with results from that printing process presented in Figure 4.5d-f.

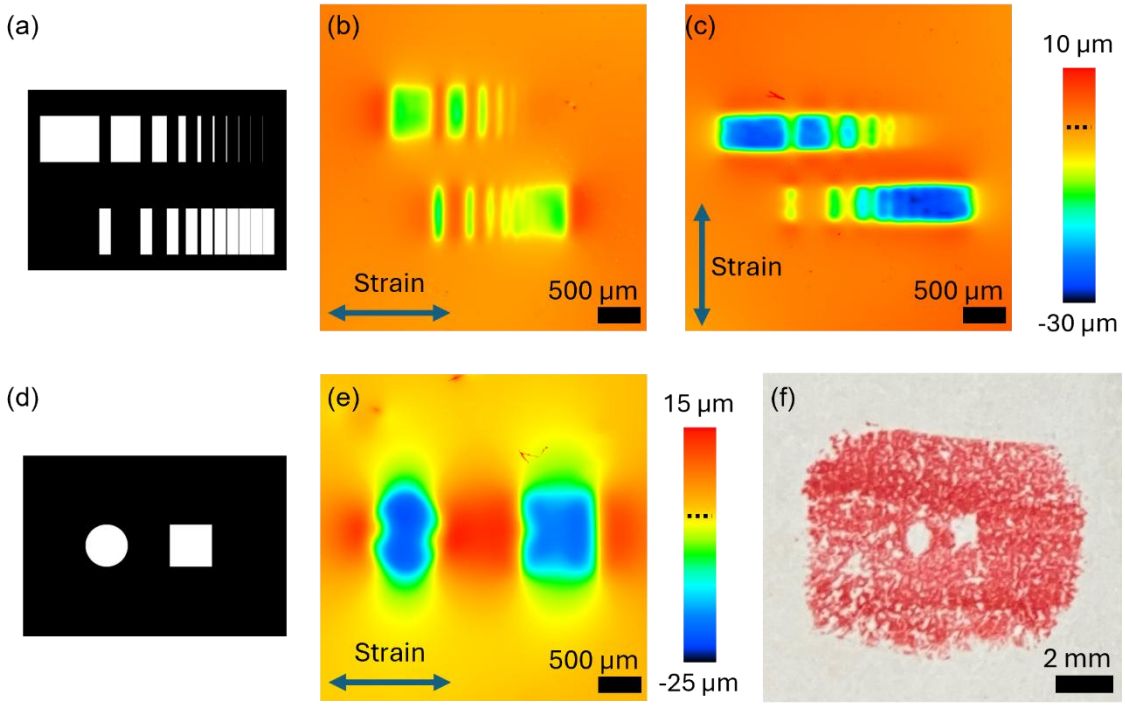

Figure 4.5. (a) Test pattern for critical dimension and resolution. Smallest rectangles are single pixel width (2.47 μm), doubling in size to each progressive line. (b-c) Topography of resolution pattern as assessed by optical profilometry with horizontal and vertical strain directions respectively. Resolution is coupled with depth of feature and strain field; but a limit of approximately 80 μm is noted in this context. (d) Photomask of a circle and square (both 802 μm), for stamping example. (e) Topography of the resulting pattern. (f) Transfer printing of red Sharpie marker with negative circle and square patterns. All patterns were applied to 250 μm thin films under 20% strain and exposed for 40 min at 20 mW/cm^2 with a 405 nm laser.

4.5 Conclusions

Here, we introduce a material with orthogonal chemistries which enables dynamic covalent mechanophotopatterning and subsequent fixation of the topography. Both photoinduced stress relaxation and the related surface topography evolution were demonstrated in the first stage of the material while a final stage, which prevented these features from evolving further, was triggered thermally. This system couples the advantages of the dynamic and dual-cure variants of spatiotemporal pattering of strained films. As such, this methodology enables sequential patterning capacity and the prevention of undesired evolution of the final product.

4.6 Acknowledgments

The authors thank the Materials Instrumentation & Multi-Modal Imaging Core for the use of their optical profilometer.

4.7 References

(1) Adzima, B. J.; Tao, Y.; Kloxin, C. J.; DeForest, C. A.; Anseth, K. S.; Bowman, C. N. Spatial and Temporal Control of the Alkyne–Azide Cycloaddition by Photoinitiated Cu(II) Reduction. *Nat. Chem.* **2011**, *3* (3), 256–259. https://doi.org/10.1038/nchem.980.

(2) Xi, W.; Peng, H.; Aguirre-Soto, A.; Kloxin, C. J.; Stansbury, J. W.; Bowman, C. N. Spatial and Temporal Control of Thiol-Michael Addition via Photocaged Superbase in Photopatterning and Two-Stage Polymer Networks Formation. *Macromolecules* **2014**, *47* (18), 6159–6165. https://doi.org/10.1021/ma501366f.

(3) Aubert, S.; Bezagu, M.; Spivey, A. C.; Arseniyadis, S. Spatial and Temporal Control of Chemical Processes. *Nat. Rev. Chem.* **2019**, *3* (12), 706–722. https://doi.org/10.1038/s41570-019-0139-6.

(4) Ito, T.; Okazaki, S. Pushing the Limits of Lithography. *Nature* **2000**, *406* (6799), 1027–1031. https://doi.org/10.1038/35023233.

(5) del Barrio, J.; Sánchez-Somolinos, C. Light to Shape the Future: From Photolithography to 4D Printing. *Adv. Opt. Mater.* **2019**, *7* (16), 1900598. https://doi.org/10.1002/adom.201900598.

(6) Somers, P.; Münchinger, A.; Maruo, S.; Moser, C.; Xu, X.; Wegener, M. The Physics of 3D Printing with Light. *Nat. Rev. Phys.* **2024**, *6* (2), 99–113. https://doi.org/10.1038/s42254-023-00671-3.

(7) Bagheri, A.; Jin, J. Photopolymerization in 3D Printing. *ACS Appl. Polym. Mater.* **2019**, *1* (4), 593–611. https://doi.org/10.1021/acsapm.8b00165.

(8) Corrigan, N.; Yeow, J.; Judzewitsch, P.; Xu, J.; Boyer, C. Seeing the Light: Advancing Materials Chemistry through Photopolymerization. *Angew. Chem. Int. Ed.* **2019**, *58* (16), 5170–5189. https://doi.org/10.1002/anie.201805473.

(9) Schwartz, J. J.; Boydston, A. J. Multimaterial Actinic Spatial Control 3D and 4D Printing. *Nat. Commun.* **2019**, *10* (1), 791. https://doi.org/10.1038/s41467-019-08639-7.

(10) Fairbanks, B. D.; Singh, S. P.; Bowman, C. N.; Anseth, K. S. Photodegradable, Photoadaptable Hydrogels via Radical-Mediated Disulfide Fragmentation Reaction. *Macromolecules* **2011**, *44* (8), 2444–2450. https://doi.org/10.1021/ma200202w.

(11) Rånby, B. Photodegradation and Photo-Oxidation of Synthetic Polymers. *J. Anal. Appl. Pyrolysis* **1989**, *15*, 237–247. https://doi.org/10.1016/0165-2370(89)85037-5.

(12) Podgórski, M.; Fairbanks, B. D.; Kirkpatrick, B. E.; McBride, M.; Martinez, A.; Dobson, A.; Bongiardina, N. J.; Bowman, C. N. Toward Stimuli-Responsive Dynamic Thermosets through Continuous Development and Improvements in Covalent Adaptable Networks (CANs). *Adv. Mater.* **2020**, *32* (20), 1906876. https://doi.org/10.1002/adma.201906876.

(13) Bracher, P. J.; Snyder, P. W.; Bohall, B. R.; Whitesides, G. M. The Relative Rates of Thiol–Thioester Exchange and Hydrolysis for Alkyl and Aryl Thioalkanoates in

Water. *Orig. Life Evol. Biospheres* **2011**, *41* (5), 399–412. https://doi.org/10.1007/s11084-011-9243-4.
(14) Sowan, N.; Lu, Y.; Kolb, K. J.; Cox, L. M.; Long, R.; Bowman, C. N. Enhancing the Toughness of Composites via Dynamic Thiol–Thioester Exchange (TTE) at the Resin–Filler Interface. *Polym. Chem.* **2020**, *11* (29), 4760–4767. https://doi.org/10.1039/D0PY00563K.
(15) Wang, C.; Mavila, S.; Worrell, B. T.; Xi, W.; Goldman, T. M.; Bowman, C. N. Productive Exchange of Thiols and Thioesters to Form Dynamic Polythioester-Based Polymers. *ACS Macro Lett.* **2018**, *7* (11), 1312–1316. https://doi.org/10.1021/acsmacrolett.8b00611.
(16) Ren, G.; Wang, L.; Chen, Q.; Xu, Z.; Xu, J.; Sun, D. pH Switchable Emulsions Based on Dynamic Covalent Surfactants. *Langmuir* **2017**, *33* (12), 3040–3046. https://doi.org/10.1021/acs.langmuir.6b04546.
(17) Zeng, X.; Liu, G.; Tao, W.; Ma, Y.; Zhang, X.; He, F.; Pan, J.; Mei, L.; Pan, G. A Drug-Self-Gated Mesoporous Antitumor Nanoplatform Based on pH-Sensitive Dynamic Covalent Bond. *Adv. Funct. Mater.* **2017**, *27* (11), 1605985. https://doi.org/10.1002/adfm.201605985.
(18) Tauk, L.; Schröder, A. P.; Decher, G.; Giuseppone, N. Hierarchical Functional Gradients of pH-Responsive Self-Assembled Monolayers Using Dynamic Covalent Chemistry on Surfaces. *Nat. Chem.* **2009**, *1* (8), 649–656. https://doi.org/10.1038/nchem.400.
(19) Chen, X.; Dam, M. A.; Ono, K.; Mal, A.; Shen, H.; Nutt, S. R.; Sheran, K.; Wudl, F. A Thermally Re-Mendable Cross-Linked Polymeric Material. *Science* **2002**, *295* (5560), 1698–1702. https://doi.org/10.1126/science.1065879.
(20) Montarnal, D.; Capelot, M.; Tournilhac, F.; Leibler, L. Silica-Like Malleable Materials from Permanent Organic Networks. *Science* **2011**, *334* (6058), 965–968. https://doi.org/10.1126/science.1212648.
(21) Bin Rusayyis, M. A.; Torkelson, J. M. Reprocessable and Recyclable Chain-Growth Polymer Networks Based on Dynamic Hindered Urea Bonds. *ACS Macro Lett.* **2022**, *11* (4), 568–574. https://doi.org/10.1021/acsmacrolett.2c00045.
(22) Patel, T.; Oh, J. K. Dynamic Covalent Adaptive Polymer Network Materials Based on Hindered Urea Bonds. *J. Macromol. Sci. Part A* **2023**, *0* (0), 1–14. https://doi.org/10.1080/10601325.2023.2206860.
(23) Mochulsky, M.; Tobolsky, A. V. Chemorheology of Polysulfide Rubbers. *Ind. Eng. Chem.* **1948**, *40* (11), 2155–2163. https://doi.org/10.1021/ie50467a030.
(24) Fava, A.; Iliceto, A.; Camera, E. Kinetics of the Thiol-Disulfide Exchange. *J. Am. Chem. Soc.* **1957**, *79* (4), 833–838. https://doi.org/10.1021/ja01561a014.
(25) Cook, W. D.; Chausson, S.; Chen, F.; Le Pluart, L.; Bowman, C. N.; Scott, T. F. Photopolymerization Kinetics, Photorheology and Photoplasticity of Thiol–Ene–

Allylic Sulfide Networks. *Polym. Int.* **2008**, *57* (3), 469–478. https://doi.org/10.1002/pi.2357.
(26) Park, H. Y.; Kloxin, C. J.; Scott, T. F.; Bowman, C. N. Covalent Adaptable Networks as Dental Restorative Resins: Stress Relaxation by Addition–Fragmentation Chain Transfer in Allyl Sulfide-Containing Resins. *Dent. Mater.* **2010**, *26* (10), 1010–1016. https://doi.org/10.1016/j.dental.2010.06.007.
(27) Kloxin, C. J.; Scott, T. F.; Park, H. Y.; Bowman, C. N. Mechanophotopatterning on a Photoresponsive Elastomer. *Adv. Mater.* **2011**, *23* (17), 1977–1981. https://doi.org/10.1002/adma.201100323.
(28) Kloxin, C. J.; Scott, T. F.; Bowman, C. N. Stress Relaxation via Addition−Fragmentation Chain Transfer in a Thiol-Ene Photopolymerization. *Macromolecules* **2009**, *42* (7), 2551–2556. https://doi.org/10.1021/ma802771b.
(29) Fenoli, C. R.; Bowman, C. N. Synthesis of Novel Trithiocarbonate and Allyl Sulfide Containing Monomers. *Polym. Chem.* **2013**, *5* (1), 62–68. https://doi.org/10.1039/C3PY00709J.
(30) J. Bongiardina, N.; M. Soars, S.; Podgorski, M.; N. Bowman, C. Radical-Disulfide Exchange in Thiol–Ene–Disulfidation Polymerizations. *Polym. Chem.* **2022**, *13* (27), 3991–4003. https://doi.org/10.1039/D2PY00172A.
(31) Shore, B. W.; Perry, M. D.; Britten, J. A.; Boyd, R. D.; Feit, M. D.; Nguyen, H. T.; Chow, R.; Loomis, G. E.; Li, L. Design of High-Efficiency Dielectric Reflection Gratings. *JOSA A* **1997**, *14* (5), 1124–1136. https://doi.org/10.1364/JOSAA.14.001124.
(32) Cox, L. M.; Li, Z.; Sowan, N.; Nair, D.; Xiao, J.; Bowman, C. N.; Ding, Y. Reconfigurable Surface Patterns on Covalent Adaptive Network Polymers Using Nanoimprint Lithography. *Polymer* **2014**, *55* (23), 5933–5937. https://doi.org/10.1016/j.polymer.2014.09.024.
(33) Mitra, J.; Tripathi, G.; Sharma, A.; Basu, B. Scaffolds for Bone Tissue Engineering: Role of Surface Patterning on Osteoblast Response. *RSC Adv.* **2013**, *3* (28), 11073–11094. https://doi.org/10.1039/C3RA23315D.
(34) Zhang, S.; Yan, L.; Altman, M.; Lässle, M.; Nugent, H.; Frankel, F.; Lauffenburger, D. A.; Whitesides, G. M.; Rich, A. Biological Surface Engineering: A Simple System for Cell Pattern Formation. *Biomaterials* **1999**, *20* (13), 1213–1220. https://doi.org/10.1016/S0142-9612(99)00014-9.
(35) Romeo, A.; Lacour, S. P. Concurrent Photopatterning of Elastic Modulus and Structures in Photosensitive Silicone Elastomers. *Extreme Mech. Lett.* **2015**, *3*, 1–7. https://doi.org/10.1016/j.eml.2015.04.002.
(36) Priest, C. Surface Patterning of Bonded Microfluidic Channels. *Biomicrofluidics* **2010**, *4* (3), 032206. https://doi.org/10.1063/1.3493643.

(37) Nguyen, P. Q. M.; Yeo, L.-P.; Lok, B.-K.; Lam, Y.-C. Patterned Surface with Controllable Wettability for Inkjet Printing of Flexible Printed Electronics. *ACS Appl. Mater. Interfaces* **2014**, *6* (6), 4011–4016. https://doi.org/10.1021/am4054546.
(38) Fan, F.; Liu, C.; Wang, S.; Lv, J.; Li, W.; Fu, Y.; Xu, H. Swelling-Induced 3D Photopatterning on a Diselenide-Containing Elastomer. *J. Mater. Chem. C* **2019**, *7* (35), 10777–10782. https://doi.org/10.1039/C9TC03536B.
(39) Podgórski, M.; Nair, D. P.; Chatani, S.; Berg, G.; Bowman, C. N. Programmable Mechanically Assisted Geometric Deformations of Glassy Two-Stage Reactive Polymeric Materials. *ACS Appl. Mater. Interfaces* **2014**, *6* (9), 6111–6119. https://doi.org/10.1021/am405371r.
(40) Ma, S. J.; Mannino, S. J.; Wagner, N. J.; Kloxin, C. J. Photodirected Formation and Control of Wrinkles on a Thiol–Ene Elastomer. *ACS Macro Lett.* **2013**, *2* (6), 474–477. https://doi.org/10.1021/mz400166e.
(41) Worrell, B. T.; McBride, M. K.; Lyon, G. B.; Cox, L. M.; Wang, C.; Mavila, S.; Lim, C.-H.; Coley, H. M.; Musgrave, C. B.; Ding, Y.; Bowman, C. N. Bistable and Photoswitchable States of Matter. *Nat. Commun.* **2018**, *9* (1), 2804. https://doi.org/10.1038/s41467-018-05300-7.
(42) Chen, D.; Ni, C.; Xie, L.; Li, Y.; Deng, S.; Zhao, Q.; Xie, T. Homeostatic Growth of Dynamic Covalent Polymer Network toward Ultrafast Direct Soft Lithography. *Sci. Adv.* **2021**, *7* (43), eabi7360. https://doi.org/10.1126/sciadv.abi7360.
(43) Pei, Z.; Yang, Y.; Chen, Q.; Wei, Y.; Ji, Y. Regional Shape Control of Strategically Assembled Multishape Memory Vitrimers. *Adv. Mater.* **2016**, *28* (1), 156–160. https://doi.org/10.1002/adma.201503789.
(44) Li, J.; Li, T.; Ma, X.; Su, Z.; Yin, J.; Jiang, X. Light-Induced Programmable 2D Ordered Patterns Based on a Hyperbranched Poly(Ether Amine) (hPEA)-Functionalized Graphene Film. *ACS Appl. Mater. Interfaces* **2021**, *13* (1), 1704–1713. https://doi.org/10.1021/acsami.0c15099.
(45) Hou, H.; Yin, J.; Jiang, X. Reversible Diels–Alder Reaction To Control Wrinkle Patterns: From Dynamic Chemistry to Dynamic Patterns. *Adv. Mater.* **2016**, *28* (41), 9126–9132. https://doi.org/10.1002/adma.201602105.
(46) Wang, S.; Li, B.; Zheng, J.; Surat'man, N. E. B.; Wu, J.; Wang, N.; Xu, X.; Zhu, J.; Loh, X. J.; Li, Z. Nanotechnology in Covalent Adaptable Networks: From Nanocomposites to Surface Patterning. *ACS Mater. Lett.* **2023**, *5* (2), 608–628. https://doi.org/10.1021/acsmaterialslett.2c01083.
(47) Flory, P. J. Molecular Size Distribution in Three Dimensional Polymers. I. Gelation1. *J. Am. Chem. Soc.* **1941**, *63* (11), 3083–3090. https://doi.org/10.1021/ja01856a061.
(48) Stockmayer, W. H. Theory of Molecular Size Distribution and Gel Formation in Branched Polymers II. General Cross Linking. *J. Chem. Phys.* **1944**, *12* (4), 125–131. https://doi.org/10.1063/1.1723922.

(49) Ghaemy, M. The Polymerization Mechanism and Kinetics of DGEBA with BF3-EDA. *Eur. Polym. J.* **1998**, *34* (8), 1151–1156. https://doi.org/10.1016/S0014-3057(97)00247-4.
(50) Ruiz de Luzuriaga, A.; Solera, G.; Azcarate-Ascasua, I.; Boucher, V.; Grande, H.-J.; Rekondo, A. Chemical Control of the Aromatic Disulfide Exchange Kinetics for Tailor-Made Epoxy Vitrimers. *Polymer* **2022**, *239*, 124457. https://doi.org/10.1016/j.polymer.2021.124457.
(51) Sowan, N.; Song, H. B.; Cox, L. M.; Patton, J. R.; Fairbanks, B. D.; Ding, Y.; Bowman, C. N. Light-Activated Stress Relaxation, Toughness Improvement, and Photoinduced Reversal of Physical Aging in Glassy Polymer Networks. *Adv. Mater.* **2021**, *33* (5), 2007221. https://doi.org/10.1002/adma.202007221.

4.8 Supporting Information

4.8.1. Procedure for Materials Synthesis

Synthesis of 2-[2-(2-Hydroxy-ethylsulfanylmethyl)-allylsulfanyl]-ethanol (ASdiol)

The synthesis of allyl sulfide diol was performed following previous literature.[1] To a 500 mL 3-neck round bottom flask equipped with a condenser and addition funnel, 300 mL of methanol was added. 10.1 g of sodium was (0.44 mol, 1 equiv) added at 0 °C. After all the sodium had solubilized, 27.6 mL mecrcaptoethanol (0.97 mol, 2.2 equiv), was added and the solution was brought to reflux. While at reflux, 22.4 g of 3-chloro-2-chloromethyl-1-propene (0.44 mol, 1 equiv), was added dropwise. The solution was allowed to reflux overnight. The solution was allowed to cool to room temperature, filtered, and reduced in vacuo. The crude material was taken up in 250 mL DI water and extracted with ether (4x80 mL). The extract was washed with 150 mL brine and dried over sodium sulfate prior to reduction in vacuo. The final product was obtained via vacuum distillation (150 °C, 0.16 Torr), to yield 17.8 g of ASdiol. Yield 48%. ^{1}H NMR (400 MHz, $CDCl_3$, δ): 5.03 (s, 2H), 3.72 (t, 4H), 3.32 (s, 4H), 2.65 (t, 4H), 2.07 (s, OH, 2H).

Formulation Details

Due to slight amounts of homopolymerization in production, BADGE oligomers have pendant alcohol end-groups. In the context of using large amounts of this epoxy alongside isocyanate-alcohol based polyurethane formation, additional isocyanate was included to maintain stoichiometric quantities of alcohol and isocyanate. Additionally, epoxy defects should be considered when predicting the critical gel point by Flory-Stockmayer method.[2,3] The following resin was prepared with a theoretical gel point of 90%.

Chemical	Mass (g)	Equivalents	Functionality (-OH or -NCO)	wt% of Total
PolyTHF 1k	0.92	1.0	2	7.6
BADGE	7.9	25	0.03	65
Desmodur N3900	1.0	2.2	2.8	8.2
HDI	0.52	3.4	2	4.3
ASdiol	0.96	5.0	2	7.9
I907	0.61	2.4	--	5.0
BF_3 ethylamine	0.24	2.3	--	2.0

Table S4.1. Formulation details on a 1-gram scale of Desmodur N3900.

Theoretical critical gel point (p_c) in the stoichiometric case is:

$$p_c = \frac{1}{\sqrt{1 - f_{w,NCO}}\sqrt{1 - f_{w,OH}}}$$

where f_w is the weighted functionality

$$f_w = \frac{\sum f_i^2 N_i}{\sum f_i N_i}$$

where f_i is the functionality of a molecule, and N_i is the number of molecules.[3] In this case, $f_{w,NCO}$ was 2.31 under the assumption that Desmodur N3900 contributes a functionality of 2.8 as an estimate according to the supplier's described isocyanate content. Under the assumption of 3% hydroxy equivalent per BADGE, which is on the high end of the supplier's range, and the approximation that these defects were primarily dimers, $f_{w,OH}$ was approximated as 1.94. In combination, this results in the desired gel point of 90%.

Furthermore, this methodology can be used to predict if sufficient ASdiol is included for dynamics. As a first approximation, if all the ASdiol is cleaved into two f = 1 fragments, $f_{w,OH}$ drops to 1.16. As a result, the theoretical gel point conversion increases to an unachievable 220% and therefore complete dynamic rearrangement due to the included dynamic moieties is anticipated.

The inclusion of HDI in the formulation not only ensures the above dynamics, but also decreases the crosslink density relative to the use of only Desmodur N3900. As the Desmodur N3900 is the only crosslinker, the crosslink density of the film can be readily estimated as 100 mM. This is consistent with an estimate derived from the rubbery modulus of the dynamic mechanical analysis (Figure 4.2) of 80 ± 30 mM at T_g + 50 °C according to the following:

$$\rho_{crosslinks} = \frac{E'}{3RT}$$

where E' is the storage modulus at temperature T in the rubbery regime.[4]

Polyurethane formation is monitored by FT-IR for the disappearance of the isocyanate peak (Figure S4.2).

4.8.2 Supplementary Figures and Analysis

Light Sources and Optics

For all experiments except patterning, a Thorlabs 405 nm LED (M405L2-C5 equipped with COP5-A collimation adapter) was used. Intensity was assessed by Thorlabs PM100D radiometer equipped with a Thorlabs S120VC photodiode sensor. For the patterning system a 638 nm laser (100 mW, pigtail fiber-coupled, Civil Laser), was used for alignment while a 405 nm laser (3.5 W, 405 nm, multimode fiber-coupled, Civil Laser), was used for exposure. Intensities were also assessed by a Thorlabs PM16-121 photodiode sensor integrated into the system.

Scheme S4.1. 2D exposure system. A digital micromirror device (DMD), Vialux V-9001, is illuminated by collimated 405 and 638 nm light. Images are projected from the DMD and are imaged through a doubly-telecentric imaging system (lenses L1 and L2) to a stretched sample with a magnification of -0.33. An aperture is situated at the Fourier plane of the imaging system to block spurious diffraction orders from the DMD. The 638 nm light is used to align the sample at the image plane of the imaging system while the 405 nm light is used to expose the sample.

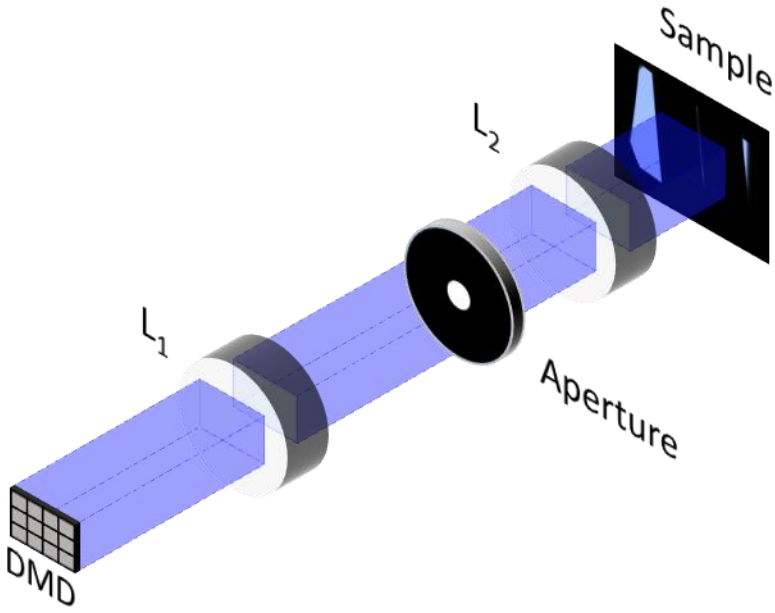

Mechanophotopatterning Process Images

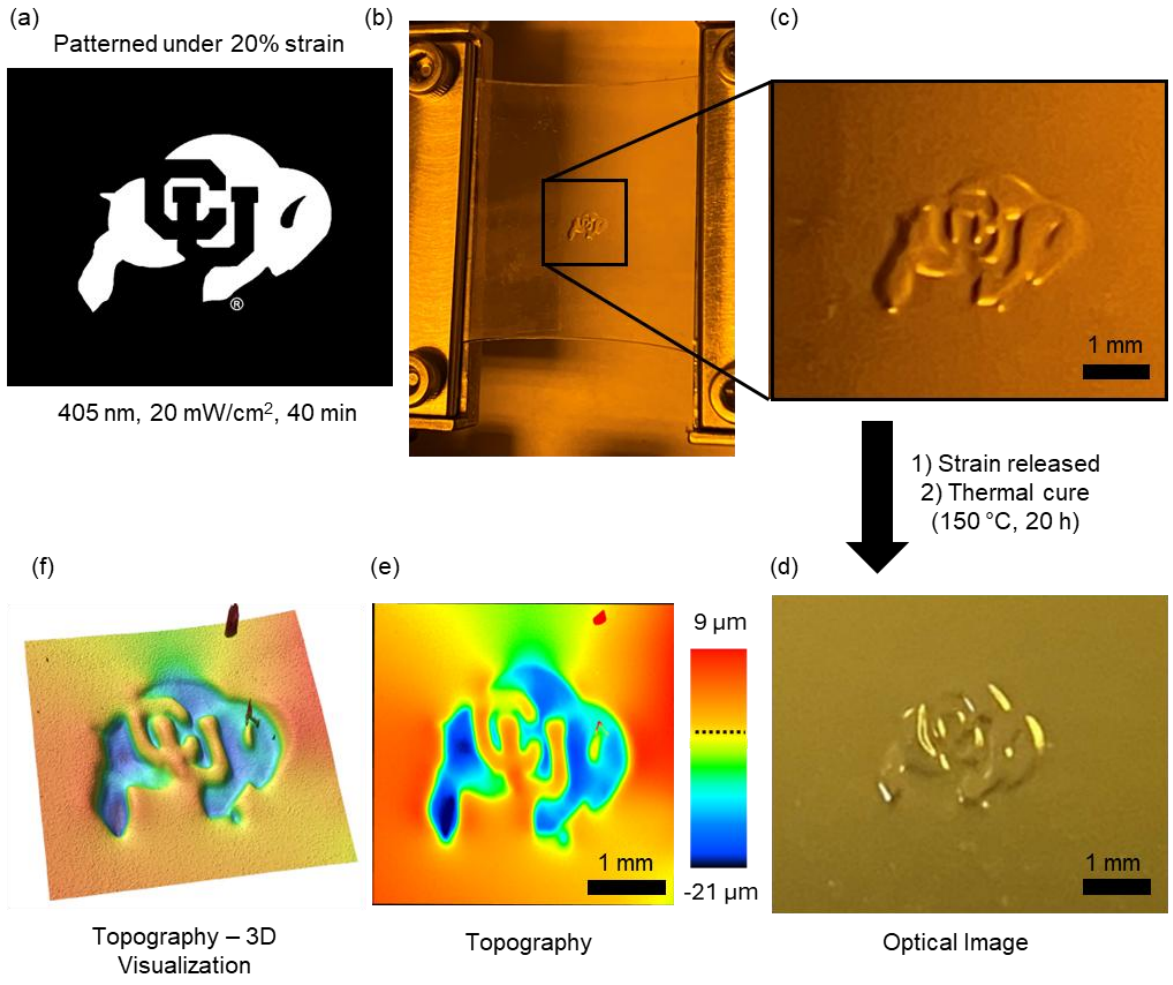

Figure S4.1. (a) Example photomask for patterning of (b) film in stretcher. (c) Optical image of resulting surface pattern. (d) Optical image of pattern following strain release and stage 2 cure. (e) Topography as assessed by optical profilometry and (f) associated 3D rendering with 15x height magnification.

Isocyanate Reaction Monitoring

FT-IR (Nicolet 8700), was used to verify isocyanate depletion for the formation of urethanes in the preparation of the stage 1 material. The sample was prepared between KBr plates and monitored in mid-IR for the disappearance of the isocyanate peak at 2270 cm^{-1}.

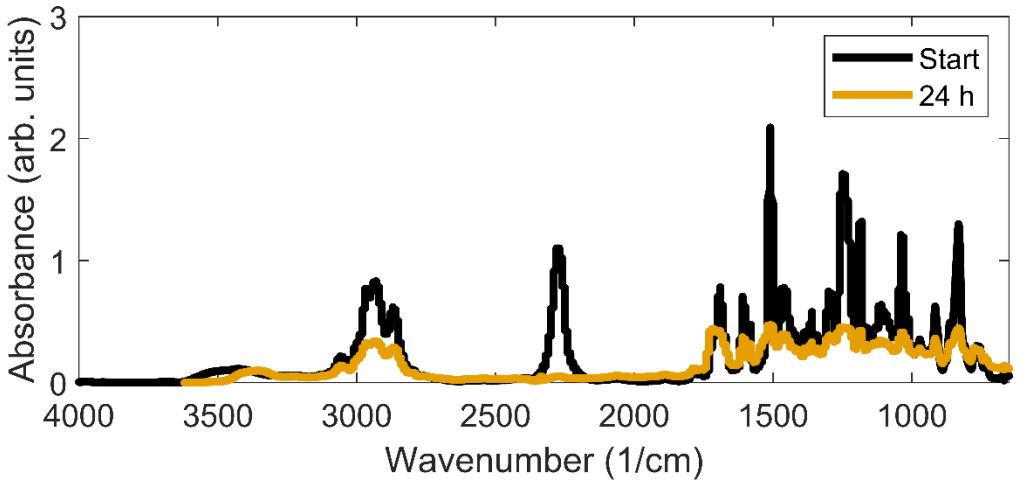

Figure S4.2. Disappearance of the isocyanate peak signaling completion of polyurethane reaction used to prepare stage 1 network.

Stress Relaxation Fit

Stress relaxation data were fit using the summation of exponentials to account for the viscoelastic response to the photoinduced dynamic process. Fitting was accomplished via MATLAB's lsqcurvefit function in accordance with the generalized Maxwell-Wiechert model for viscoelastic response:

$$\frac{E}{E_0} = \sum_n A_n e^{-\frac{t}{\tau_n}}$$

where τ is the characteristic timescale, A is the relative size, and n is the number of elements.[5] The progressive increase in quantity of exponentials fits the data progressively better, as assessed by the residuals. This is due to effects including initiator depletion as well as chain confirmation impacts on allyl sulfide moiety rearrangement.

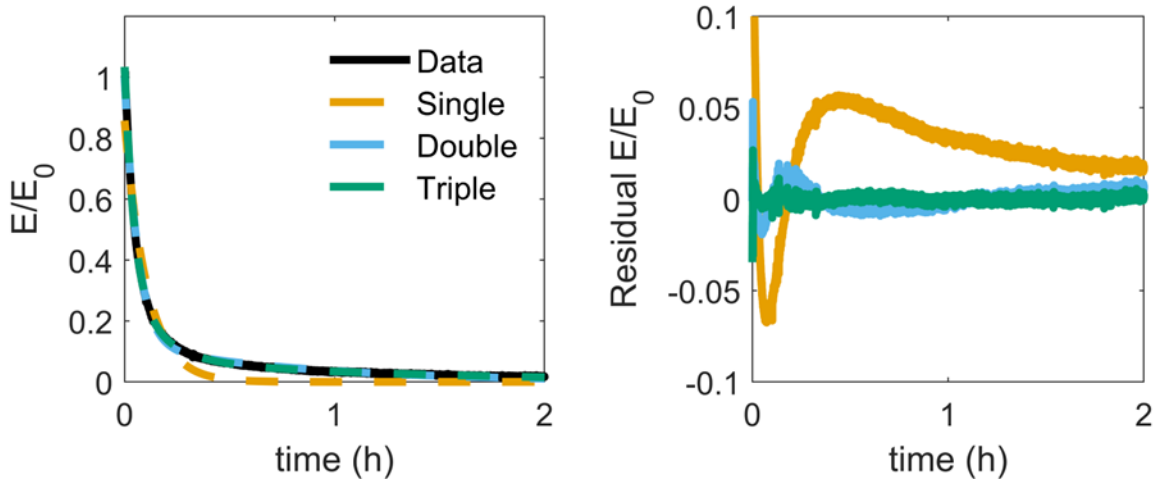

Figure S4.3. Fits (left) and residuals (right) for fitting various quantities of summed exponentials for stress relaxation data (20 mW/cm^2, 405 nm).

Sequential Stress Relaxation Analysis

The sequential stress relaxation presented in Figure 4.1 yields additional information pertaining to the long-term performance of stress relaxation and the decrease of initiator content. Stress relaxation is dependent on the strain provided and the associated viscoelastic response; however, neglecting this variable can be modeled as a single exponential dependent on initiator concentration on the basis of the following differential equation for a single Maxwell element.

$$\frac{dE}{dt} = -\frac{E}{\tau}$$

where τ is the time constant for relaxation. Under the assumption that initiator dependence dominates, τ is inversely proportional to initiator concentration. Therefore, it can be used as a stand-in to determine half-life under constant irradiation conditions. The half-life of I907, under the 405 nm LED at an intensity of 20 mW/cm^2, as determined by this method is 4.7 h. Based on its absorbance at 405 nm, this corresponds to a quantum yield of 0.12, which, for reference, is consistent with previously reported values at 365 nm, varying from 0.13 to 0.3,[6–8] by the following analysis:

$$[PI] \sim \frac{1}{\tau}$$

$$\frac{d[PI]}{dt} = -\phi\varepsilon I^*[PI]$$

where $[PI]$ is the photoinitiator concentration, ϕ is the quantum yield, ε is the molar absorptivity, and I^* is the molar flux of incident photons.

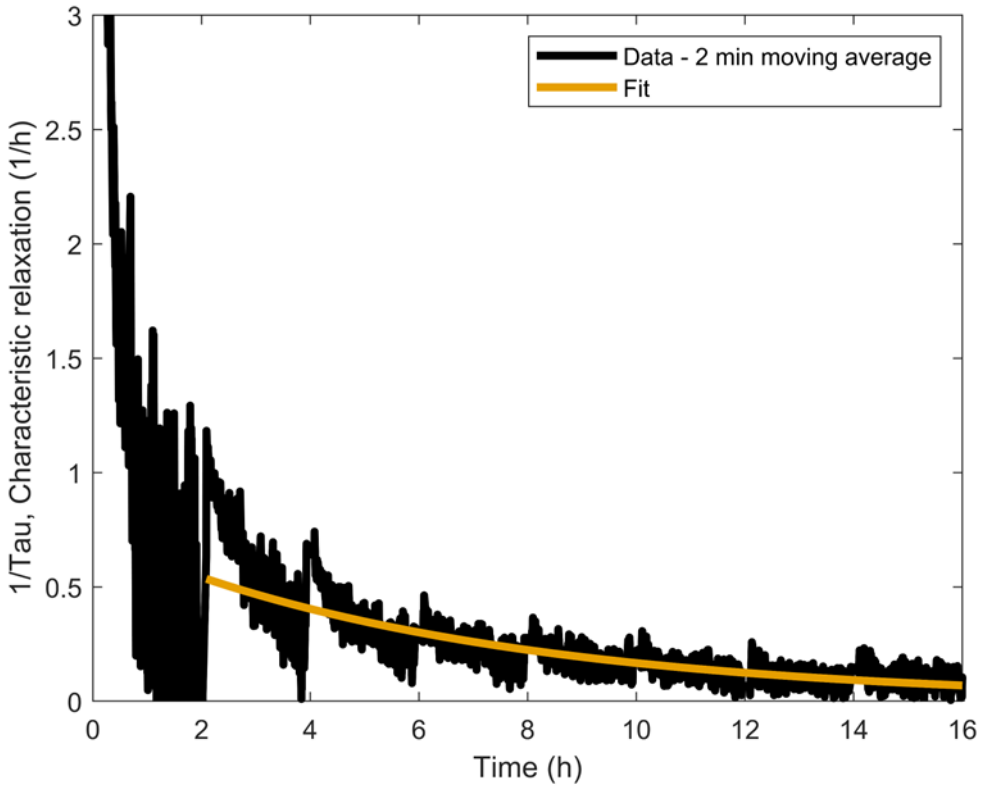

Figure S4.4. Determination of initiator half-life from long time behavior of sequential stress relaxation. 1/Tau is proportional to initiator concentration when the impact of stress on-the-relaxation is minimal. Data was filtered for outliers and averaged over 2 min width bins, then fit to a single exponential for times exceeding 2 hours. The fit corresponds to a half-life of 4.7 hours under 20 mW/cm^2, 405 nm LED exposure.

Stress Relaxation of Epoxy-free Control

An epoxy-free control was prepared with the substitution of benzyl acetate (Sigma Aldrich), for BADGE. Virgin and thermally treated (150°C, 20h), samples both demonstrate stress relaxation behavior. Both samples relax slower than the title formulation, but it should be noted that the thermal treated sample relaxes slower than its native counterpart. Contribution factors include the minor denaturing of I907 (Figure S4.6) and the associated photodarkening at 405 nm (Figure S4.5).

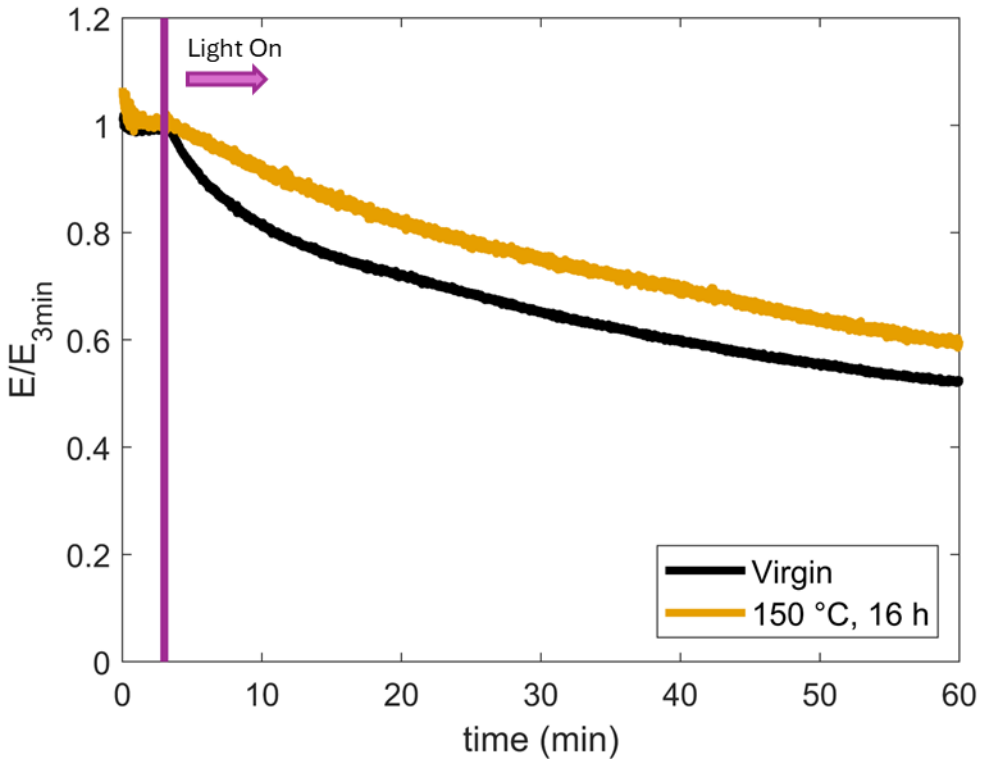

Figure S4.5. Stress relaxation of control samples not containing dual-cure epoxy. Samples were strained by 20%, allowed to settle for 3 min, and then the light was turned on. Light source was a 405 nm LED, 20 mW/cm^2. Raw data was filtered to remove outlier timepoints.

UV-Vis of I907 and Films

UV-Vis spectra of Irgacure 907 in acetonitrile were assessed by Thermo Scientific Evolution 300 in 1 cm path cuvettes. Although I907 is typically used as a 365 nm photoinitiator, it has a sufficient tail out to 405, enabling applications that benefit from 1) large depth of cure, 2) large loadings, or 3) slow kinetics. Based on of 1 wt% I907 case presented in Figure 4.1, the Napierian molar absorptivity at 405 nm can be calculated to be 4.9 L/mol-cm.

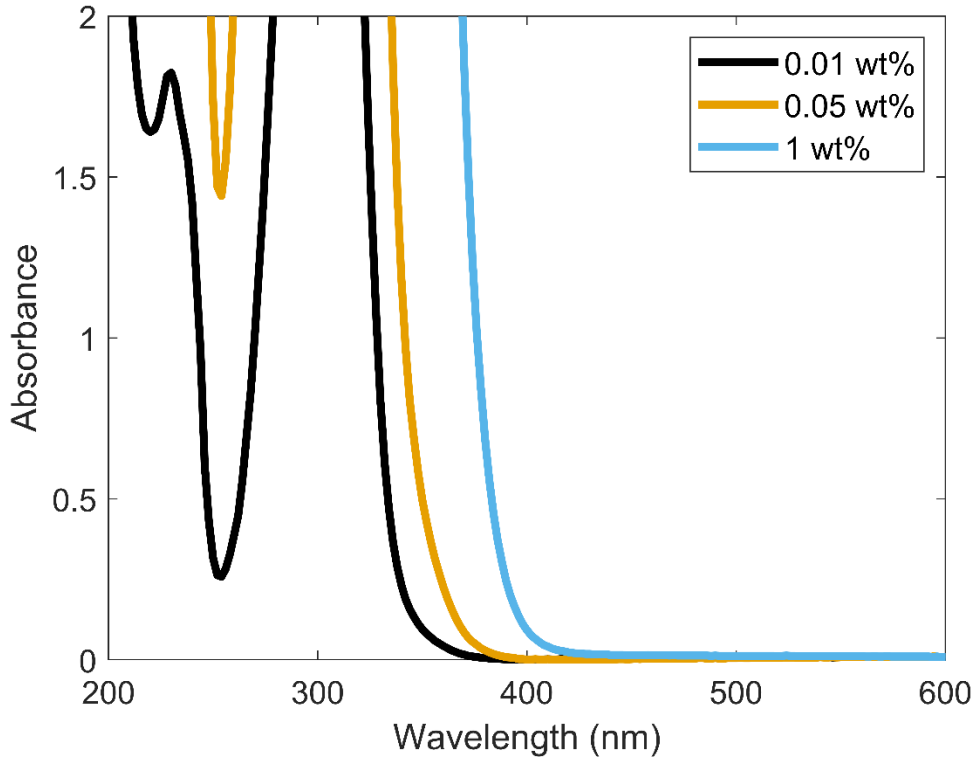

Figure S4.6. UV-Vis of various loadings of I907 in acetonitrile. The tail relevant for 405 nm exposure is shown at high (1 wt%) loading.

Adjusting for the increased density of the films (assuming that of BADGE = 1.17), relative to acetonitrile, and the 5 wt% loading of I907, an absorbance of 0.01, or

approximately 2.5% attenuation, over the 250 μm form factor. For comparison, absorbance spectra were obtained of the 250 μm thick films between glass slides before and after thermal cure. In practice, 16% attenuation is observed in the films, due to other absorbing species and interfacial considerations.

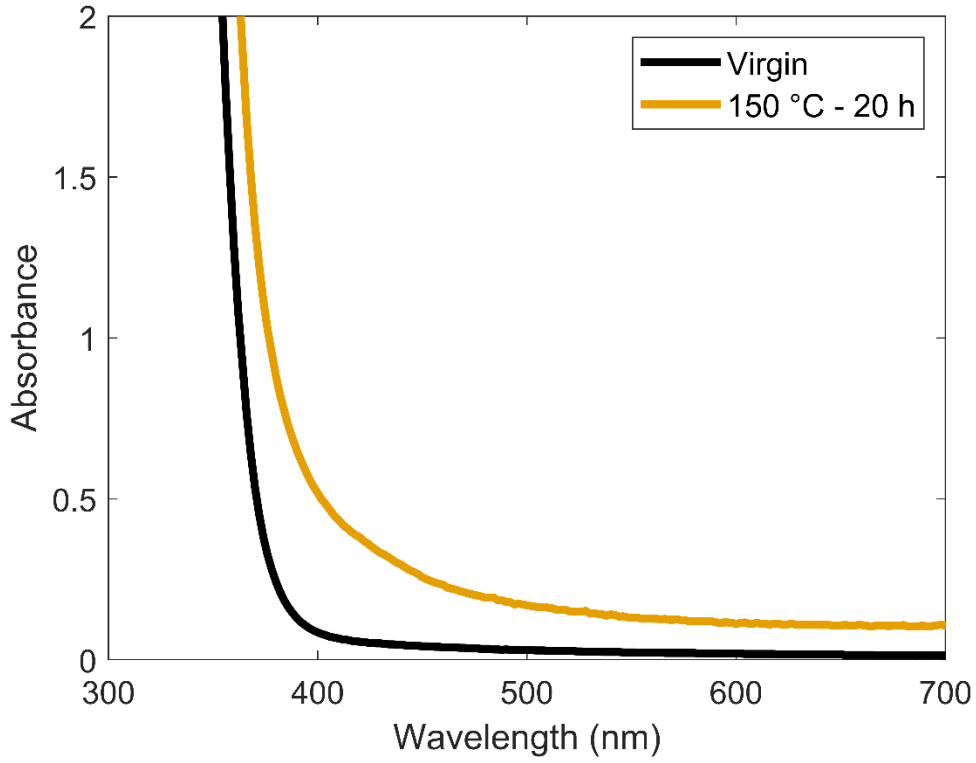

Figure S4.7. UV-Vis of MPP films prior to and after thermal cure.

After cure, the absorbance spectrum is consistent with the visually noted yellow color. It should also be noted for future exposures that attenuation at 405 nm increased to 66%. This is sufficient to result in inhomogeneity through the thickness of the sample, but not sufficient attenuation to prevent dynamic rearrangement of the bulk. Furthermore, for the objectives of this work, light access to the depth relevant to patterned surface features is still prevalent.

Thermal Treatment of Irgacure 907

To assess the effect of the thermal treatment on the photoinitiator, I907 was heated for 20 h at 150 °C. A fresh sample was compared to the thermally treated sample, which notably browned. A Bruker Avance-III 400 was used to determine chemical difference by ^{1}H NMR in $CDCl_3$. Although some additional peaks appear, the I907 appears to be sufficiently intact for use as a photoinitiator. Therefore, the thermal treatment of the initiator alone does not suffice to prevent dynamic stimulation by denaturing the monomer.

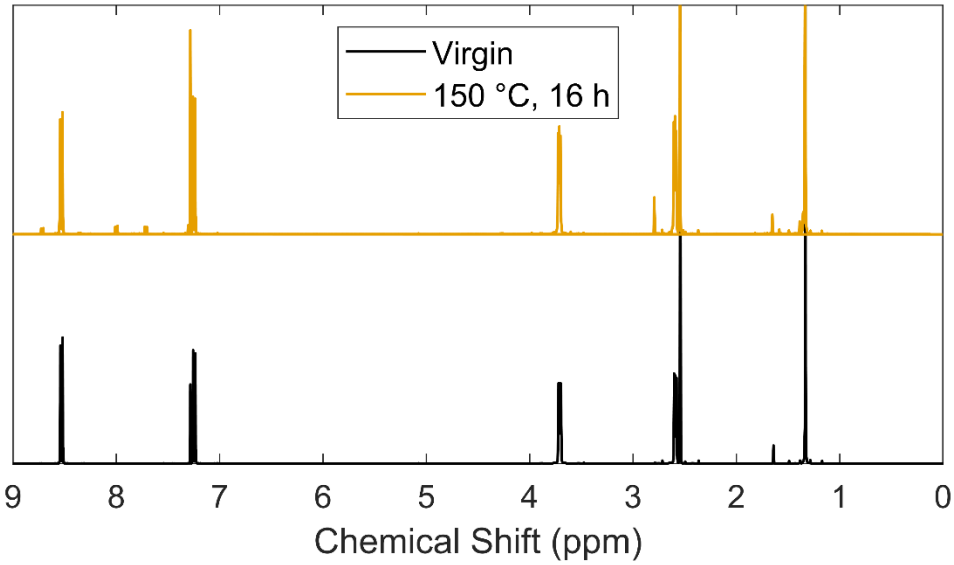

Figure S4.8. NMR of I907 before (above) and after (below) thermal treatment (150 °C, 20 h) in $CDCl_3$. Initiator remains largely intact as would be anticipated.

Differential Scanning Calorimetry

Differential Scanning Calorimetry DSC was performed on approximately 5 mg for I-907 and 2 mg for MPP in hermetically sealed aluminum pans using a TA Instruments Discovery DSC 2500. Samples were heated from -10 °C to 250 °C, cooled to -10 °C, then heated to 250 °C. Heating and cooling steps were performed at 5 °C/min.

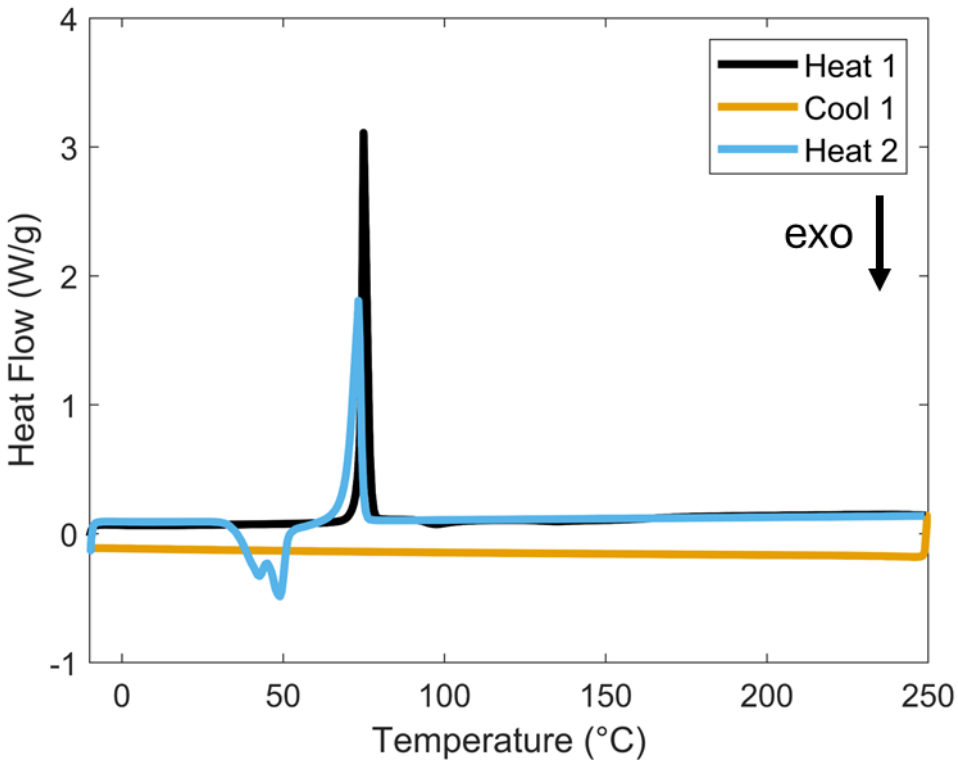

Figure S4.9. DSC of I907 demonstrates thermal stability when heated to 250 °C. Melting point is 75 °C on first heat. Crystallization followed by a reduction in melting temperature is observed on second heat, which is consistent with smaller, less stable, crystallization. Small exotherms can be noted in heat 1, such as that at 100 °C, which may relate to the minor degradation noted by color change and denaturing shown in the NMR (Fig S6).

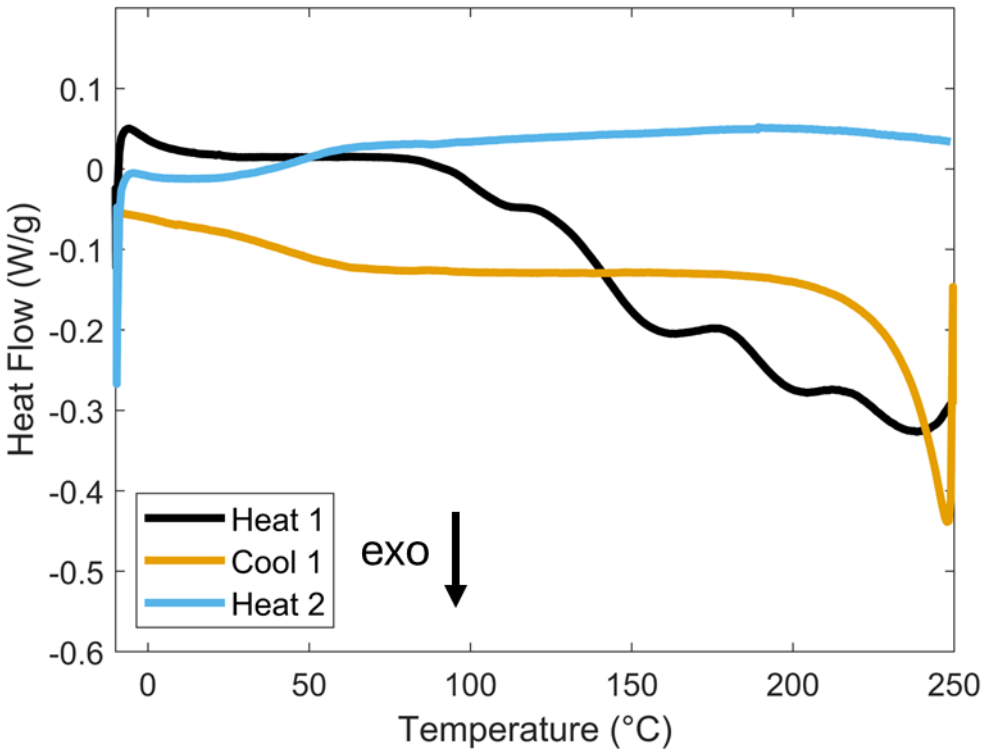

Figure S4.10. DSC of title formulation demonstrating epoxy cure. Polymerization does not occur until approximately 80 °C demonstrating sequence-controlled orthogonality of the epoxy cure. Cures at temperatures exceeding the 150 °C threshold used in this work may be of utility for faster polymerization than the 150 °C used; however, higher risk of side reactions, particularly due to urethane dissociation should be noted.

FT-IR Kinetics of Epoxy Cure

FT-IR was monitored in real time on a Nicolet 8700. The sample was prepared between glass slides with 250 μm vinyl spacers and heated in the instrument at 150 °C while monitored. The epoxy peak at 4525 cm^{-1} was monitored.

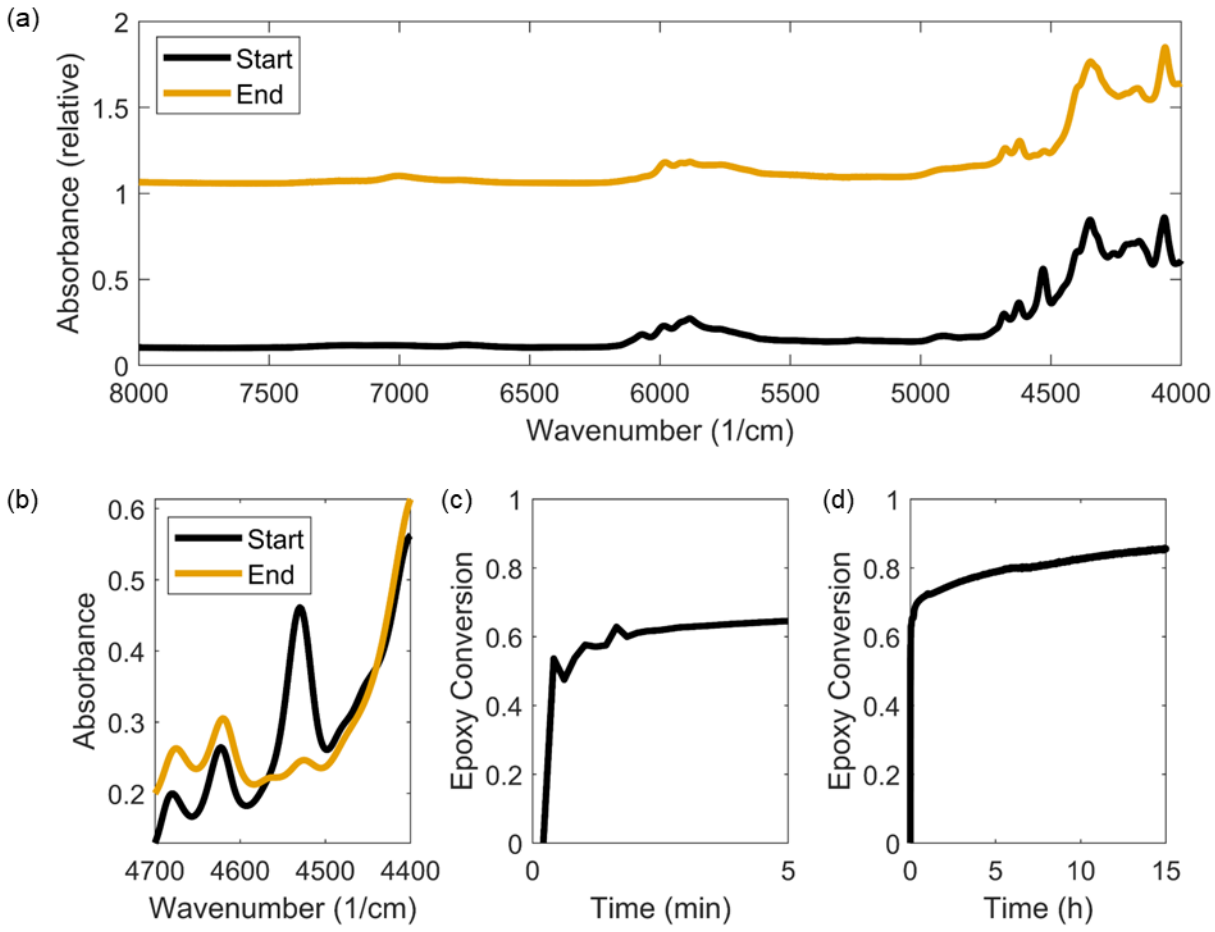

Figure S4.11. FT-IR to track epoxy functionality decreases during thermal step of title MPP films. (a) Near-IR spectra at start and end of 15 h thermal cure. (b) The peak of interest at 4530 cm^{-1} is convoluted. Upon isolating the peak (Figure S4.11), the conversion of the epoxy can be assessed on (c) short and (d) long timelines. A large portion of the

epoxy cures rapidly at 150 °C; however, notably higher conversions are achieved with longer cure duration.

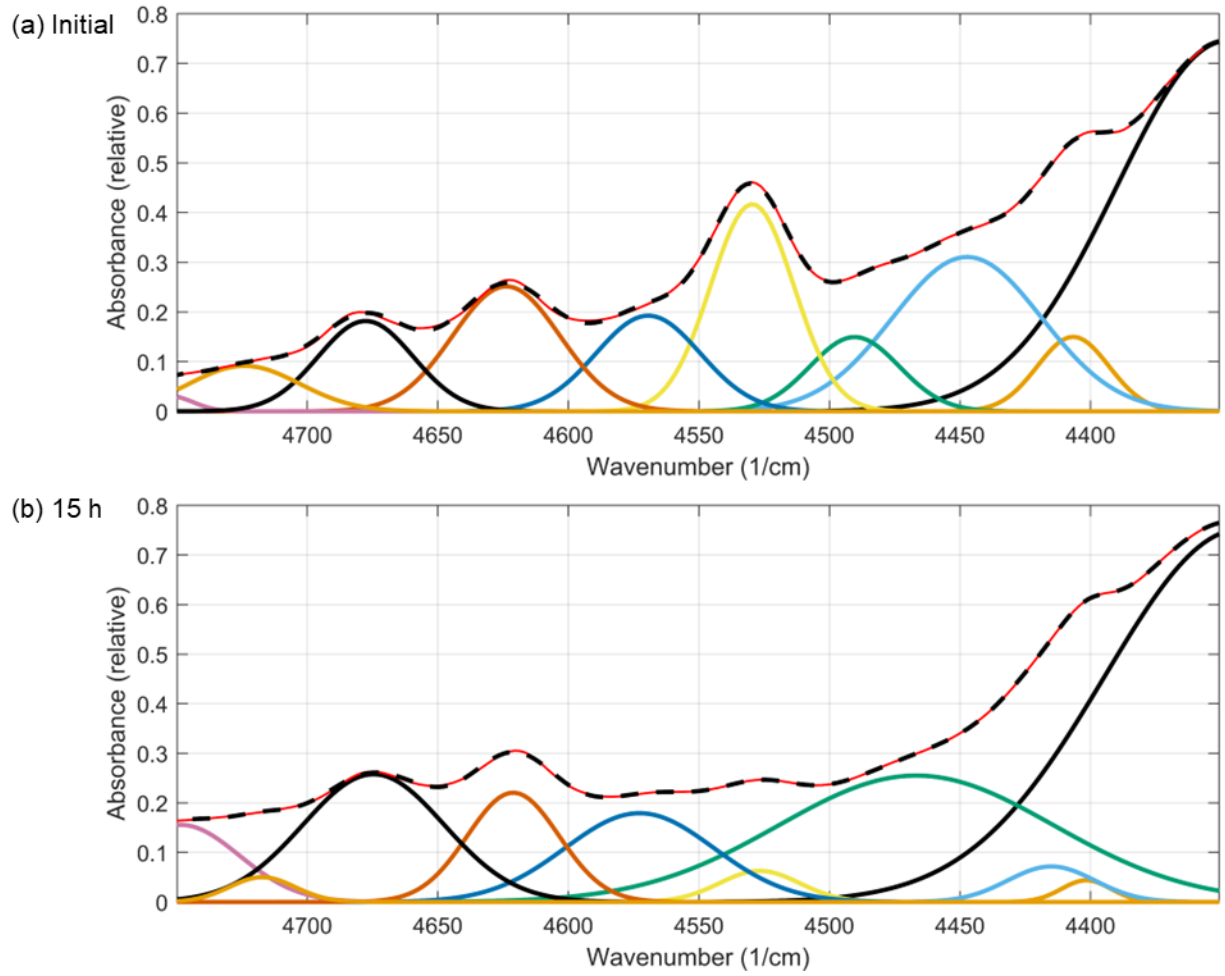

Figure S4.12. Example deconvolutions at (a) t = 0 and (b) t = 15 h to assess epoxy conversion. Raw data is in red, while the fit is the dashed black line. All other curves are Gaussians. The peak of interest is the yellow peak at 4530 cm^{-1}.

Mechanical Cure Kinetics

Mechanical properties were monitored at a frequency of 1 Hz via a rapid temperature rise to 150 °C then held for 16h. Since storage modulus monitored over T_g, the evolution of the rubbery modulus reflects the crosslink density evolution from the epoxy cure.

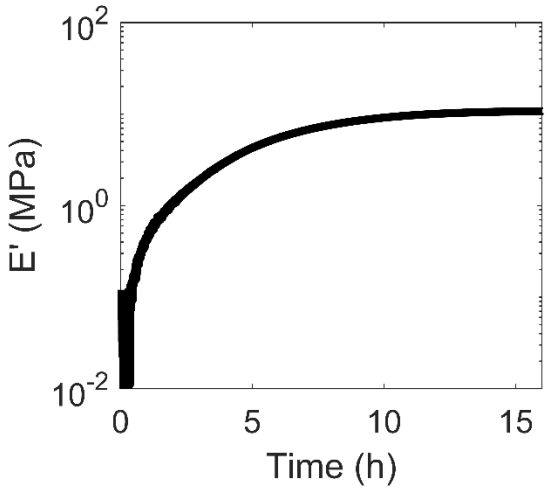

Figure S4.13. Evolution of rubbery modulus at 150 °C over the course of the epoxy cure.

Dual-Cured Pattern Analysis

Pertaining to the methods and limitations of Figure 4b&c: As samples were not loaded precisely the same on the optical profilometer, efforts must be made to shift the axes and rotation prior to comparing subtracting surface profiles from each other. A best-fit was determined by assessing the minimum root-mean-square roughness of the resulting subtraction over rotation values as fine as 0.02 degrees and single pixel x- and y-offset. Within this limited processing, most of the data falls within two resolution units (60 nm units) demonstrating that the epoxy-cured patterned films have not evolved following light exposure.

The cured fixing effect can be further visualized by Figure S4.12. Feature depth was assessed across each row of pixels by assessing the average difference between the feature minimal and the local maxima between features. The local maxima therefore correspond with the center of the patterned features and are most appropriate for comparison. This variable demonstrates an 88% decrease in feature depth following the 15 h floodcure sample (405 nm, 20 mW/cm^2). In contrast, less than a 1% change occurs in the epoxy cured sample when exposed to 16 h floodcure.

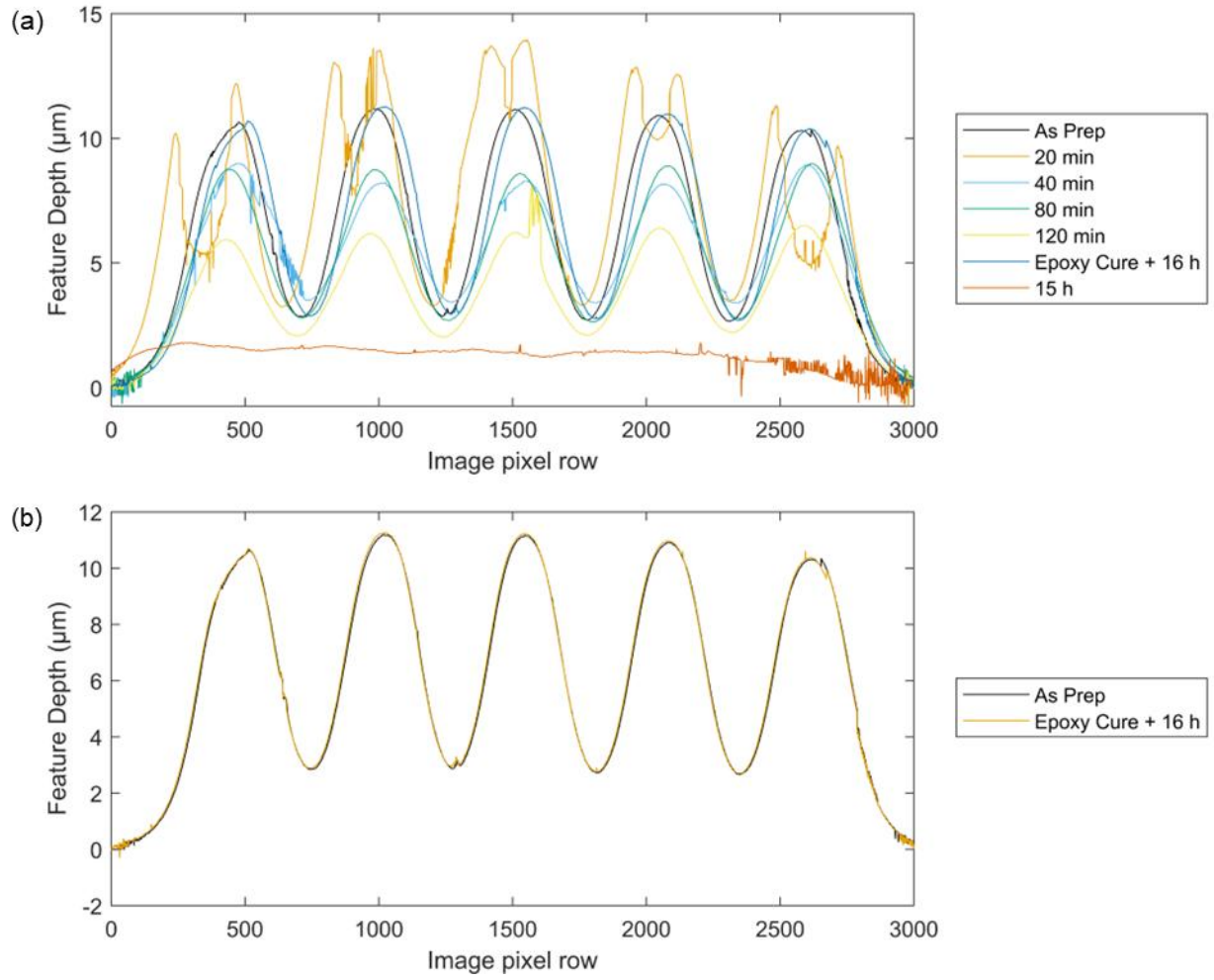

Figure S4.14. Feature depth as a function of pixel row from optical profilometry images. (a) Demonstrates the pattern loss over time under 405 nm, 20 mW/cm^2 flood cure. Notably, after 15 h amplitude is low there is very little difference in amplitude as a function of row, demonstrating features have been lost. (b) x-axis correction for variation in images to overlap the patterns to demonstrate clear retention of features when flood cure occurs in stage 2 material.

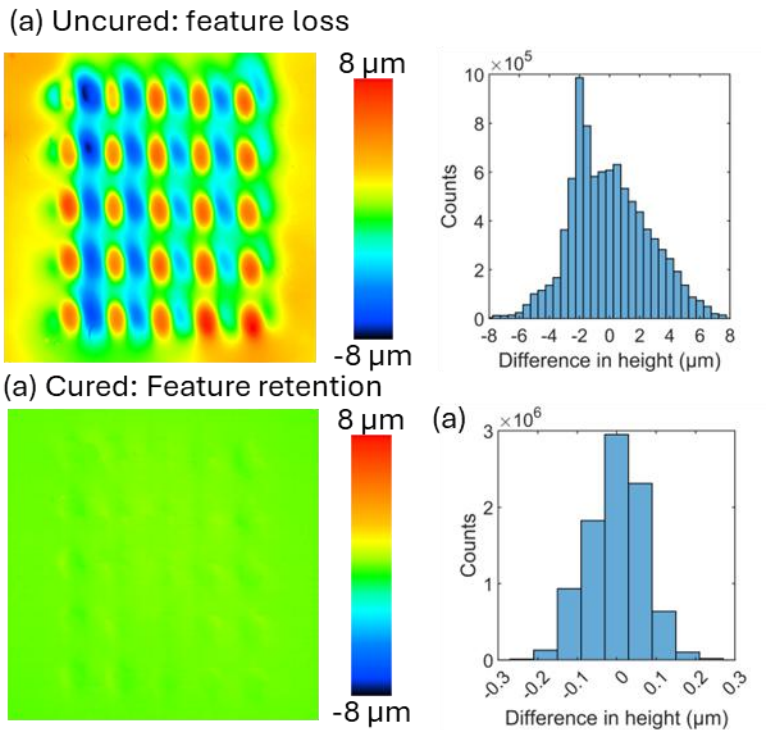

Figure S4.15. Image and histogram representation of image subtraction presented in Figure 4.4. (a) Deviation from mean between patterned sample and uncured 20 mW/cm^2, 405 nm LED exposure for 15 h. (b) Deviation from mean between patterned sample and thermally cured (150 °C, 16 h) then 20 mW/cm^2, 405 nm LED exposure for 16 h.

Dual-Cured Stress Relaxation

Stress relaxation of thermally cured films was assessed on an Exceed Model E42 to allow for larger applied forces and increased stability relative to what can be accomplished via the RSA G2. Cured samples (40 mm x 10 mm x 250 μm) were strained by 1% then exposed to at 3 min intervals (405 nm, 20 mW/cm^2). A nearly instantaneous decrease in force was observed upon irradiation, but this effect is promptly reversed upon turning the light off. This effect can be attributed to thermal expansion due to light absorption and free volume changes associated with allyl sulfide addition fragmentation process. Following settling occurs in early timepoints, bulk relaxation is not noted, as is critical to fixing the MPP films.

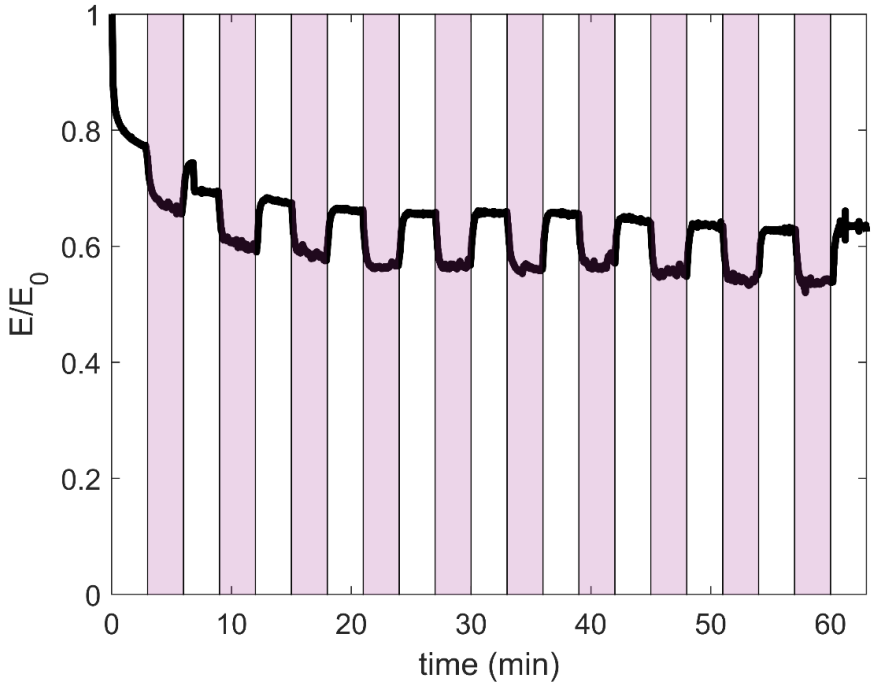

Figure S4.16. Stress relaxation of cured epoxy films. Films were strained by 1% and exposed to a 405 nm LED at 3 min intervals (purple) at an intensity of 20 mW/cm^2. Upon

irradiation, stress is temporarily relieved, but permanent stress relaxation due to irradiation is not clearly observed.

Reducing Epoxy Content

To demonstrate the phenomena does not necessitate the large portion (65 wt%) of epoxy, an analog was prepared using only 30 wt% BADGE with the same design considerations noted in SI Section 2.

Chemical	Mass (g)	Equivalents	Functionality (-OH or -NCO)	wt% of Total
PolyTHF 1k	1.2	1.0	2	18
BADGE	2.0	4.9	0.03	30
Desmodur N3900	1.0	1.7	2.8	15
HDI	0.73	3.7	2	11
ASdiol	1.2	5.0	2	19
I907	0.33	1.0	--	5.0
BF_3 ethylamine	0.13	1.0	--	2.0

Table S4.2. Formulation details of reduced epoxy variant.

Thermomechanical analysis and stress relaxation results are presented in Figure 4.15. Due to the reduced epoxy content, an increase in the polyurethane crosslink density is anticipated. This effect on the material is confirmed in that the rubbery modulus of the stage 1 material is over 3 times higher, relating to a crosslink density of 300 mM (Figure S3.16). In contrast, the crosslink density provided via epoxy is dramatically reduced as is the effect of the stiff core; overall dropping the T_g to 49 °C. Additionally, due to the increase

in crosslink density to the rubbery stage, the dynamics are notably slowed. These modified properties result in reduced depth of patterning under the same conditions as the standard sample; however, curing the epoxy clearly still allows for retention of the topographical pattern (Figure S4.17).

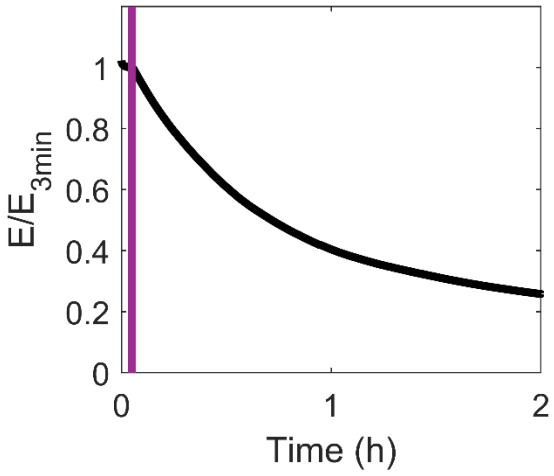

Figure S4.17. Stress relaxation of sample containing 30 wt% BADGE under 20% strain when exposed to 405 nm light (LED, 20 mW/cm^2), turned on at 3 min. Rate of relaxation is reduced from that presented in Figure 4.1.

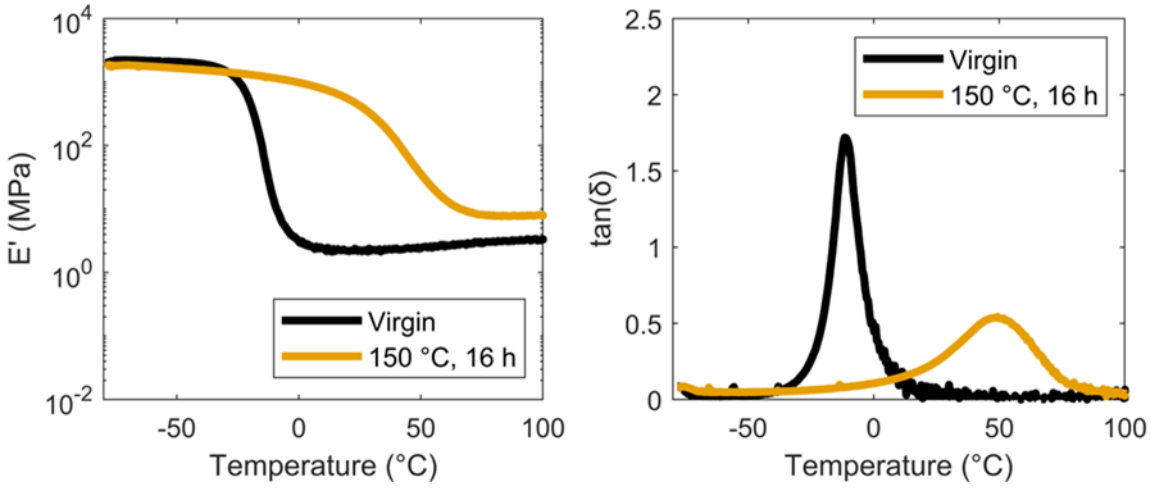

Figure S4.18. Temperature sweeps to compare initial and thermally cured materials for samples containing 30 wt% BADGE. Tg increased from -11 to 49 °C.

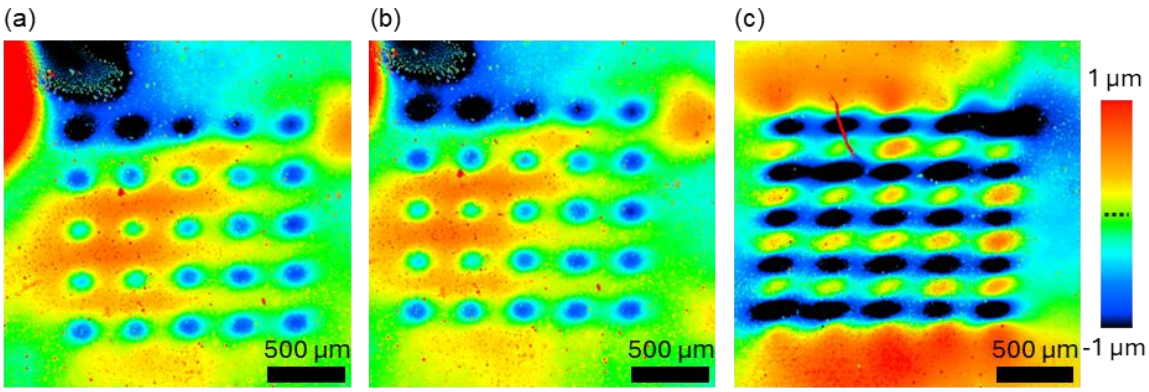

Figure S4.19. Pattern loss and retention after cure is samples containing 30 wt% BADGE. (a) Pattern as prepared comprised of 252 µm circles exposed to 20 mW/cm^2 405 nm light for 40 min. (b) Samples exposed to 16 h of light (20 mW/cm^2, 405 nm) after epoxy cure. (c) Samples exposed to 16 h of light (20 mW/cm^2, 405 nm) before epoxy cure. Curing epoxy allows for retention of topographical pattern.

Resolution Testing Replicates

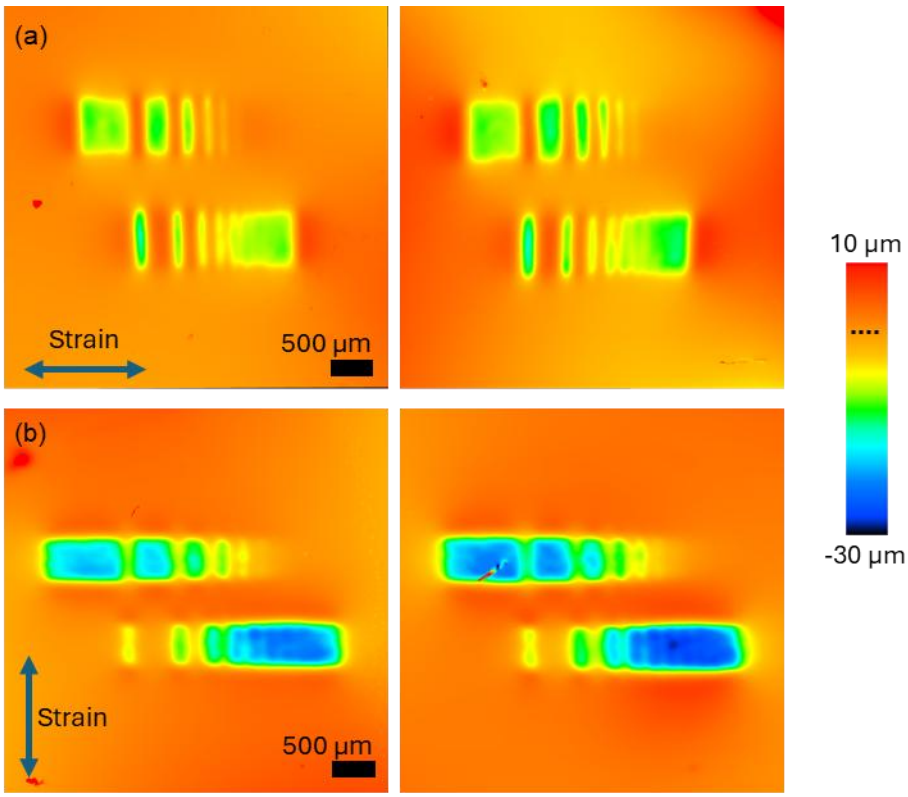

Figure S4.20. Additional replicates of patterns in Figure 4.5 to demonstrate reproducibility. (a) Strain applied in the long direction of the lines. (b) Strain applied in short direction. All patterns were applied to 250 µm thin films under 20% strain and exposed for 40 min at 20 mW/cm^2 with a 405 nm laser.

4.8.3 Additional References

(1) Fenoli, C. R.; Bowman, C. N. Synthesis of Novel Trithiocarbonate and Allyl Sulfide Containing Monomers. *Polym. Chem.* **2013**, *5* (1), 62–68. https://doi.org/10.1039/C3PY00709J.

(2) Flory, P. J. Molecular Size Distribution in Three Dimensional Polymers. I. Gelation1. *J. Am. Chem. Soc.* **1941**, *63* (11), 3083–3090. https://doi.org/10.1021/ja01856a061.

(3) Stockmayer, W. H. Theory of Molecular Size Distribution and Gel Formation in Branched Polymers II. General Cross Linking. *J. Chem. Phys.* **1944**, *12* (4), 125–131. https://doi.org/10.1063/1.1723922.

(4) Hiemenz, P. C.; Lodge, T. P. *Polymer Chemistry*, 2nd ed.; CRC Press: Boca Raton, 2007. https://doi.org/10.1201/9781420018271.

(5) Wiechert, E. *Ueber elastische Nachwirkung*; Druck von Hartung, 1889.

(6) Allonas, X.; Lalevée, J.; Fouassier, J.-P. Investigation of Cleavage Processes in Photoinitiators: From Experiments to Molecular Modeling. *J. Photochem. Photobiol. Chem.* **2003**, *159* (2), 127–133. https://doi.org/10.1016/S1010-6030(03)00177-1.

(7) Dietlin, C.; Podgorska-Golubska, M.; Andrzejewska, E. The Efficiency of Photoinitiators in Ionic Liquids. *J. Photochem. Photobiol. Chem.* **2014**, *281*, 8–17. https://doi.org/10.1016/j.jphotochem.2014.03.005.

(8) Dietliker, K. *A Compilation of Photoinitiators Commercially Available for UV Today*; SITA, 2002.

Chapter 5: Validation of Mechanophotopatterning Model

Alexander J. Osterbaan, Chenhao Zhang, Zachary R. Mora, H. Jerry Qi, Xiaohao Sun, Christopher N. Bowman

All modeling components performed by Xiaohao Sun.

5.1 Abstract

Mechanophotopatterning provides a procedurally facile methodology for the preparation of surface features. The coupling of mechanical strain with photoinduced, spatially patterned, dynamic stress relaxation results in an analog response that necessitates further investigation. Herein, a computational model is leveraged to match the experimental patterns. Deployment of this model with machine learning is anticipated to enhance the ability to pattern features precisely by this methodology.

5.2 Introduction

Covalent adaptable networks (CANs) are capable of rearranging network topology due to dynamic reactions and therefore, exhibit macroscopic stress relaxation when activated. Due to the spatiotemporal control provided by light activation, photosensitive CANs, such as those that incorporate radically-mediated allyl sulfides, may have their viscoelastic response patterned. Patterning of a strained film results in thinning of the material in the area undergoing stress relaxation, resulting in surface topography.[1,2] This mechanophotopatterning process is complex as it involves simultaneous mechanical deformations and chemical reactions that lead to complex chemorheology. Therefore, finite element (FE) simulations hold promise to gain fundamental understandings on the

key factors governing the evolution of surface profiles.[3] FE models allow for a solution to forward problems; in this case, predicting a surface profile from an exposure pattern. For a complex target surface profile, a machine learning and optimization algorithm approach may be more appropriate to reverse engineering the process.[4,5]

5.3 Methods and Results

The addition-fragmentation-chain transfer (AFT) capable film used herein, as well as the methods for mechanophotopatterning, stress relaxation, and topography assessment via optical profilometry, have all been previously reported.[2] As such, films were thermally cured to fix their surface topography, thereby being consistent with previous work.

The constitutive models of CAN materials have been studied in many previous works,[6–10] and subsequently summarized by Yui and co-workers.[3] To employ this method, experimental stress relaxation tests, performed under a constant light intensity, are used to characterize the viscoelasticity. The numerical fitting of experimental results is then performed to identify the material parameters. Through numerical tests, a two-term relaxation model is adopted as it describes the practical behavior better than the one-term model. In this case, the stress is expressed as

Equation 5.1

$$s = s_1^{-\frac{t}{\tau_1}} + (1 - s_1)^{-\frac{t}{\tau_2}}$$

where s, s_1 all are normalized stresses, t is time, and τ_1, τ_2, are characteristic relaxation times. Figure 5.1 presents a comparison between the experimental results (solid lines) and the numerical fits (dotted lines), demonstrating the model's capability to capture the

material's relaxation behavior sufficiently. It is notable that different precure exposure durations result in distinct stress relaxation behavior, which is attributed to photochemical reactions. For the sake of simplicity, curves of different conditions were fit using different sets of parameters, instead of developing a unified model taking the effects of precure into account. This effectively captures the essential physics of mechanophotopatterning process in the simulations. The model parameters obtained from the fitting process, are provided in Table 5.1.

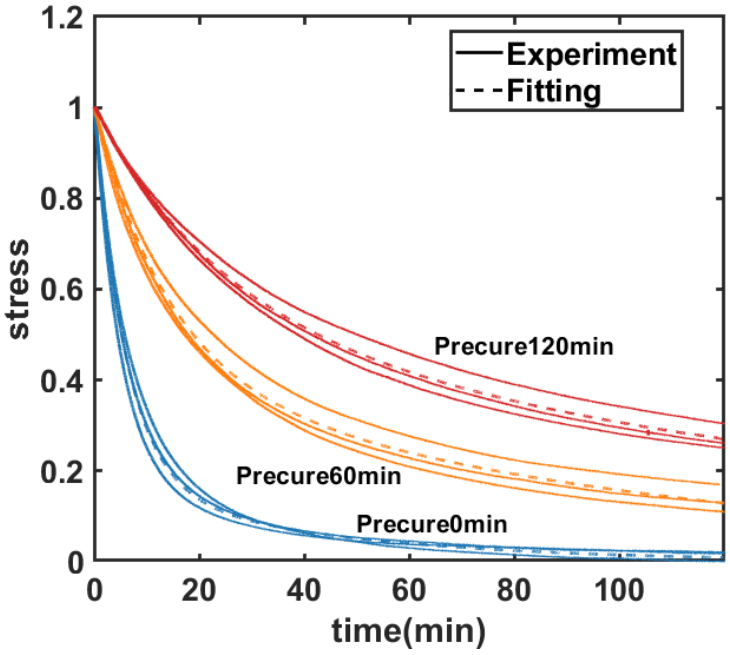

Figure 5.1. Experimental result curve and fitting curve of a 250 μm polyurethane thin film containing AFT-capable allyl sulfide moieties with 5 wt% I907, consistent with previously work.[2] Samples are exposed with 20 mW/cm^2 of 405 nm light (Thorlabs M405L2-C5) both during precure and when time = 0.

Table 5.1. Parameter values of the two-branch relaxation model of a 250 μm polyurethane thin film containing AFT-capable allyl sulfide moieties with 5 wt% I907, consistent with previously work.[2] Values are relative to an exposure with 20 mW/cm^2 of 405 nm light (Thorlabs M405L2-C5).

	Precure 0 min	**Precure 60 min**	**Precure 120 min**
s_1	**0.826**	**0.581**	**0.470**
τ_1 (min)	**6.048**	**14.046**	**24.969**
τ_2 (min)	**41.139**	**101.736**	**174.473**

As performed by collaborators, the FE simulations were performed using the commercial software ABAQUS (version 2023, Dassault Systèmes Simulia Corp., Johnston, RI, USA). In the simulations, the light-activated viscoelasticity of the CAN[7,11] is approximated using an incompressible visco-hyperelastic model combining the neo-Hookean hyperelastic model and the Porny-series model.[6] A light-dependent shifting factor is specified through a user subroutine UTRS (which tunes the relaxation times to numerically infinite values to mimic a purely hyperelastic behavior), which results in no stress relaxation when the light is off. In contrast, the fitted relaxation behavior (Table 5.1), is used when the light is on. It should be noted that when a specific illumination pattern is applied to a stretched film, the material initially within the illuminated region may creep out of the region due to stress relaxation over time. This effect is easily captured through UTRS where the coordinates of each material integration point are accessed, in each time increment, to determine whether it lies within the illuminated region, and tune the relaxation times accordingly. Therefore, materials outside the illuminated region maintain hyperelastic behavior while those within the region follow the viscoelastic model.

Furthermore, through UTRS, one also varies the illuminated region in each time increment, thereby enabling the simulation of spatiotemporal evolution of the illumination pattern.

Next, FE simulations are performed comparably to the representative light patterns considered in the experiments. Figure 5.2a shows primary steps for the simulation of each pattern: (1) stretching (20% strain) the film and holding two ends, (2) light illumination on the given pattern, (3) global illumination, and (4) strain release. Figure 5.2b shows the illumination patterns, including rectangles (1598μm×1598μm, 1598μm×802μm, 1598μm×398μm, 1598μm×202μm), cross shape (composed of 5×531μm squares), and composite shape (consisting of an 802μm-diameter circle combined with an 802μm-side square). The corresponding experimental results are shown in Figure 5.2c.

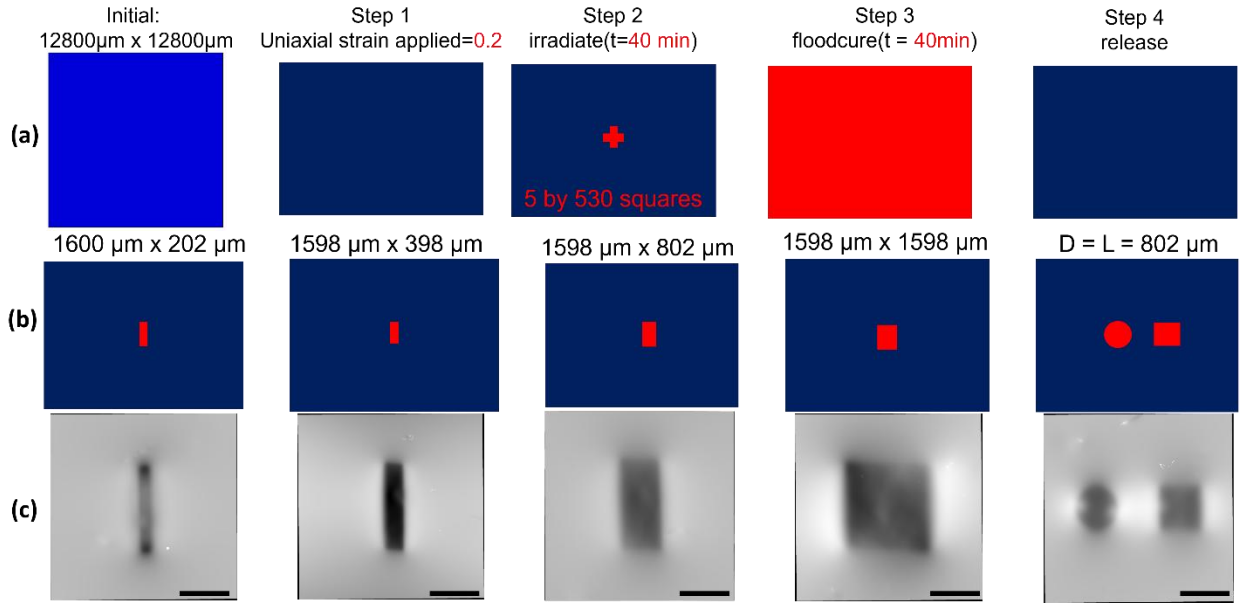

Figure 5.2. (a) Four steps of the simulations on simple patterns (b) Five other illumination patterns. (c) Experimental topography as assessed by optical profilometry using 250 μm polyurethane thin film containing AFT-capable allyl sulfide moieties with 5 wt% I907, consistent with previously work,[2] prepared under 20% strain. Red denotes 20 mW/cm^2

exposure for 40 min. Scale bar denotes 1 mm. Height scale of 55 μm from low (black) to high (white).

Experimental surface height profiles were converted to the thickness ratio data, i.e., the stretch ratio in the thickness direction as denoted by λ_3, for the comparison with simulations. Specifically, material deformation was assumed to occur symmetrically on both sides perpendicular to the film, rather than on one side away from the film. Under this assumption, the thickness ratio λ_3 is evaluated. In Figure 5.3, contours of λ_3 on the film, as well as a plot of the λ_3 values along the x and y paths, are shown for three representative patterns. Quantitative agreement with the profile is achieved between the simulations and experiments, validating the FE model. The simulation results also reveal that during the local illumination of the stretched film, the stress relaxation in the local region caused a strain redistribution of the entire film. In other words, as the illuminated region is constant, the material initially inside the region, particularly near the boundaries, creeps out of the region; whilst the material outside the region, could also enter the region due to the Poisson's effect. The complex flow pattern leads to material redistribution, resulting in a discrepancy between the achieved pattern and the light pattern.

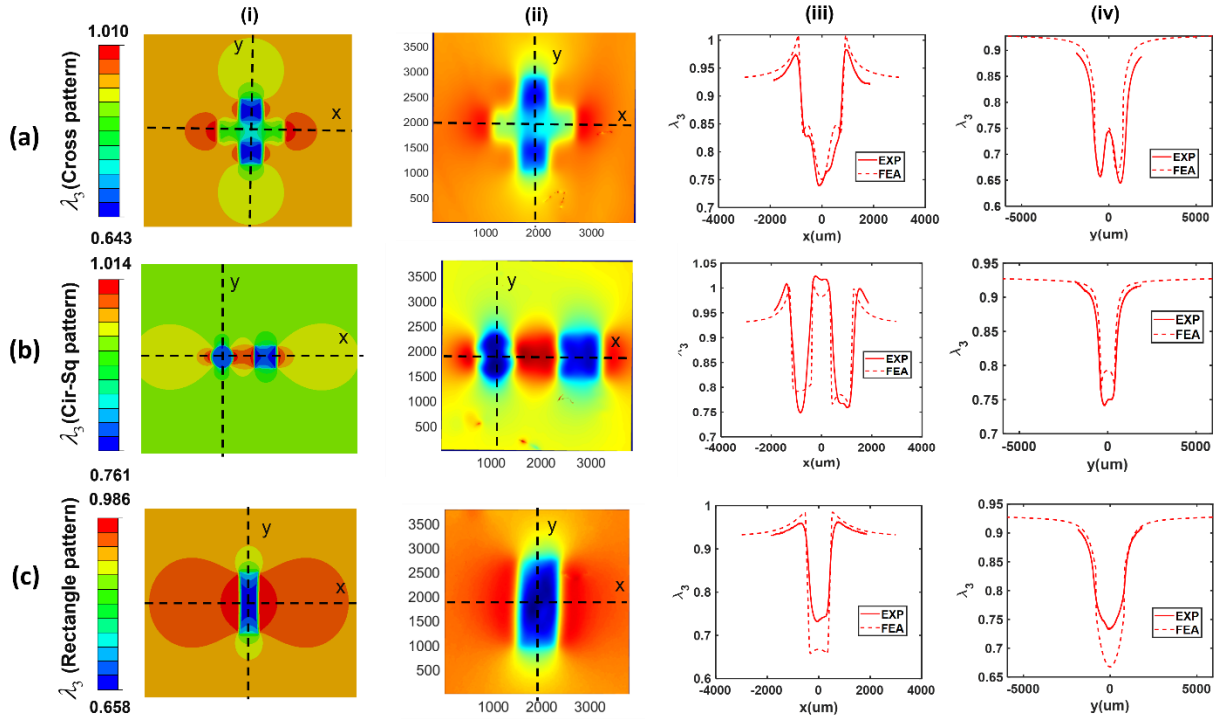

Figure 5.3. Analysis of three illumination patterns prepared under 20% strain: (a) Cross, (b) Composite shape (802 μm-diameter circle with 802 μm-side square) and (c) Rectangle (1598 μm × 802 μm). Each row shows: (i) FEM contour plot of λ_3, (ii) experimental result using 250 μm polyurethane thin film containing AFT-capable allyl sulfide moieties with 5 wt% I907, consistent with previously work,[2] exposed at 20 mW/cm^2 with 405 nm light (Thorlabs M405L2-C5), (iii) x-direction λ_3 profile comparison, and (iv) y-direction λ_3 profile comparison.

The inverse design problem of producing an exposure pattern from a final topography is challenging and as yet unachieved. The employment of this validated FE simulation to produce a large dataset for machine learning holds promise toward conquering this challenge.

5.4 References

(1) Kloxin, C. J.; Scott, T. F.; Park, H. Y.; Bowman, C. N. Mechanophotopatterning on a Photoresponsive Elastomer. *Adv. Mater.* **2011**, *23* (17), 1977–1981. https://doi.org/10.1002/adma.201100323.

(2) Osterbaan, A. J.; Trujillo-Lemon, M.; Seymour, G. T.; Mora, Z. R.; McLeod, R. R.; Bowman, C. N. Dual-Cure Dynamic Networks for Mechanophotopatterning of Surface Topography. *Macromolecules* **2025**, *58* (4), 1975–1981. https://doi.org/10.1021/acs.macromol.4c03018.

(3) Yue, L.; Kuang, X.; Sun, X.; Qi, H. J. Chapter 15 - Recyclable Thermoset Polymers: Beyond Self-Healing. In *Recent Advances in Smart Self-Healing Polymers and Composites (Second Edition)*; Li, G., Feng, X., Eds.; Woodhead Publishing Series in Composites Science and Engineering; Woodhead Publishing, 2022; pp 483–511. https://doi.org/10.1016/B978-0-12-823472-3.00012-6.

(4) Sun, X.; Yue, L.; Yu, L.; Shao, H.; Peng, X.; Zhou, K.; Demoly, F.; Zhao, R.; Qi, H. J. Machine Learning-Evolutionary Algorithm Enabled Design for 4D-Printed Active Composite Structures. *Adv. Funct. Mater.* **2022**, *32* (10), 2109805. https://doi.org/10.1002/adfm.202109805.

(5) Sun, X.; Yue, L.; Yu, L.; Forte, C. T.; Armstrong, C. D.; Zhou, K.; Demoly, F.; Zhao, R. R.; Qi, H. J. Machine Learning-Enabled Forward Prediction and Inverse Design of 4D-Printed Active Plates. *Nat. Commun.* **2024**, *15* (1), 5509. https://doi.org/10.1038/s41467-024-49775-z.

(6) Yu, L.; Sun, X.; Jin, Y.; Zhang, W.; Long, R. Mechanics of Vitrimer Particle Compression and Fusion under Heat Press. *Int. J. Mech. Sci.* **2021**, *201*, 106466. https://doi.org/10.1016/j.ijmecsci.2021.106466.

(7) Long, R.; Qi, H. J.; Dunn, M. L. Thermodynamics and Mechanics of Photochemcially Reacting Polymers. *J. Mech. Phys. Solids* **2013**, *61* (11), 2212–2239. https://doi.org/10.1016/j.jmps.2013.06.008.

(8) Sun, X.; Wu, H.; Long, R. Thermomechanics of a Temperature Sensitive Covalent Adaptable Polymer with Bond Exchange Reactions. *Soft Matter* **2016**, *12* (43), 8847–8860. https://doi.org/10.1039/C6SM01857B.

(9) Long, K. N.; Scott, T. F.; Jerry Qi, H.; Bowman, C. N.; Dunn, M. L. Photomechanics of Light-Activated Polymers. *J. Mech. Phys. Solids* **2009**, *57* (7), 1103–1121. https://doi.org/10.1016/j.jmps.2009.03.003.

(10) Vernerey, F. J.; Long, R.; Brighenti, R. A Statistically-Based Continuum Theory for Polymers with Transient Networks. *J. Mech. Phys. Solids* **2017**, *107*, 1–20. https://doi.org/10.1016/j.jmps.2017.05.016.

(11) Cox, L. M.; Sun, X.; Wang, C.; Sowan, N.; Killgore, J. P.; Long, R.; Wu, H.-A.; Bowman, C. N.; Ding, Y. Light-Stimulated Permanent Shape Reconfiguration in Cross-Linked Polymer Microparticles. *ACS Appl. Mater. Interfaces* **2017**, *9* (16), 14422–14428. https://doi.org/10.1021/acsami.7b02759.

Chapter 6: A Versatile Photoresist Scaffolding for Variable Material Property, Precision Tomographic Volumetric Additive Manufacturing

Alexander J. Osterbaan, Gabriel T. Seymour, Robert R. McLeod, Christopher N. Bowman
Volumetric Additive Manufacturing performed by Gabriel T. Seymour.

6.1 Abstract

A tunable degradable polyurethane scaffold enables accessibility of a wide range of low viscosity monomers, and thus their thermomechanical properties, without risking settling due to gravity in volumetric additive manufacturing. Addition of a stable radical inhibitor combined with real-time mechanical and chemical kinetics enables consistent simultaneous 3D printing at high resolution as demonstrated by the preparation of 250 μm diameter rods with overprinted discs. Degradation of thioester moieties by aminolysis resulted in minimal mechanical property deterioration and less than 2% mass loss for glassy parts including formulations including 67 wt% tri(ethylene glycol) dimethacrylate or tricyclodecanedimethanol dimethacrylate. Rubbery 67% hexyl methacrylate parts have an expected reduction crosslink density but an elongation to break of 70% is achieved in tensile testing. Final moduli of parts vary by 3 orders of magnitude, from low MPa to high hundreds of MPa, based on varying monomer composition, crosslink density and glass transition temperature.

6.2 Introduction

Advancements in 3D printing technologies have propelled the field from use as a prototyping tool to enabling additive manufacturing. This distinction stems from the increasing use of methods such as fused deposition modeling (FDM), stereolithography (SLA) and digital light processing (DLP) to produce parts with both the desired geometry and properties.[1–3] The repetition of 1D or 2D processing steps produces these parts; however, this sequence results in inherent defects due to the dimensional mismatch between the preparation dimensions and the final 3D part.[4] In contrast, tomographic volumetric additive manufacturing (VAM) and xolography seek to overcome this limitation by leveraging three-dimensional control over photopolymerization.[5,6] Therefore, these 3D methodologies do not necessitate printed supports, nor do they have interfacial defects. Xolography accomplishes this feat through a dual-wavelength process in the three physical dimensions, necessitating both wavelengths to trigger the reaction.[6–8]

In contrast, VAM take a tomographic approach by shifting in the relative positions of the exposure source to the sample, typically by spinning the resin vial, coupled with a change in exposure pattern.[5,9,10] The result is the accumulation of polymerization events in the areas that have received sufficient exposure, allowing for simultaneous 3D printing. Although the in-part distinction is often considered as a threshold light dose within a voxel, the kinetics and diffusion of overcoming the inhibition threshold (whether oxygen or an added species), and reaction kinetics thereafter, are fundamentally more complex.[11]

VAM necessitates a shift away from resin philosophies used for SLA and DLP. Notably, where SLA and DLP benefit from low viscosities, the preparation of a 3D part in a volume is susceptible to settling due to gravity— resulting in a preference for higher

viscosities or even gels.[12–14] As such, the library of available monomers for VAM, and thus its capacity for custom property profiles, is inherently limited. One approach to overcome this limitation was presented by Toombs et al.[12] in the form of a thermoreversible scaffold based on hydrogen bonding provided by ethyl cellulose. Although an excellent proof-of-concept, the optical clarity of printed parts, and the limited range of monomers that could be used that limits the final material properties, leaves room for improvement as these factors are critical for high fidelity printing and achievement of the desired properties for the application, respectively.

Motivated by expanding the available property space and increasing part quality in VAM, this work demonstrates a readily modifiable scaffolding platform. A polyurethane-base network provides a tunable chemical environment through careful polyol selection. The inclusion and tuning of degradable moieties, as well as work-up conditions and matrix attachment points that copolymerize with the monomer, facilitate degradation without damaging the final part. In brief, this approach uses a degradable organogel that is functionalized with copolymerizable moieties, swollen by the desired monomer formulation, as a negative photoresist (Scheme 6.1). Furthermore, this work notes additional characterization, and composition considerations to improve consistency of the printing process.

Scheme 6.1. Volumetric additive manufacturing (VAM) with a degradable scaffold. The covalently crosslinked scaffold is prepared prior to printing and contains writing monomer (blue), inhibitor (red), and initiator (not pictured). The scaffold has attachment points for the writing monomer to create permanent connections when photopolymerized. A part is the prevented from settling while written via tomographic VAM. In this case, a cone is prepared by the projection of triangular images as the vial spins. Part formation begins when the inhibitor is depleted. The area outside the part decreases in inhibitor content, but as it is not depleted, it does not polymerize. The scaffold is then removed by degrading the susceptible moieties (yellow), revealing the patterned polymerized object.

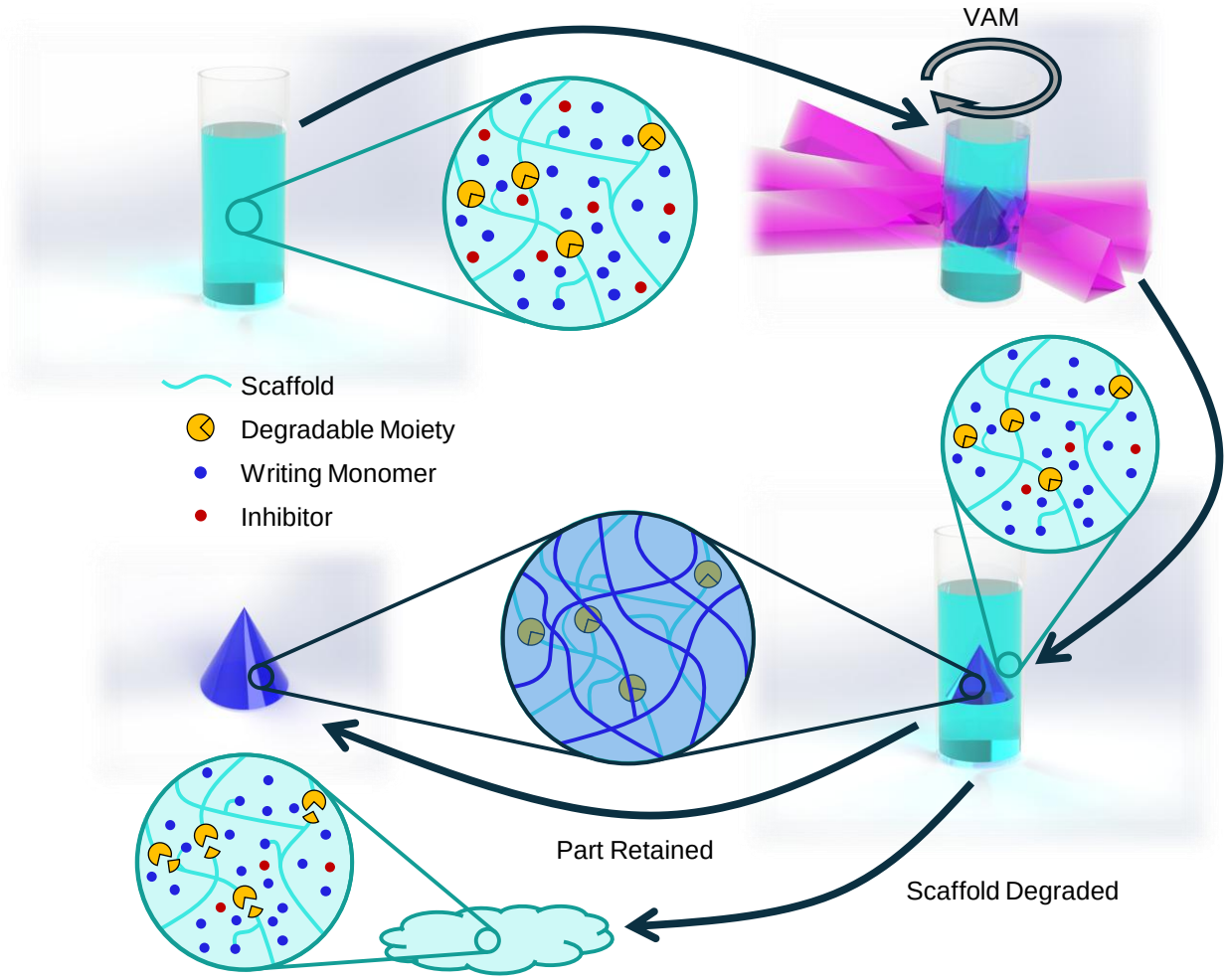

6.3 Experimental

6.3.1. Materials

Desmodur N 3900 was donated by Covestro AG. SR350 (trimethylolpropane trimethacrylate, TMPTMA) and SR348 (ethoxylated bisphenol A dimethacryalte, E-BPADMA) were donated by Arkema. 1,6-Hexanediol dimethacrylate (X-877-7446, HDDMA) was donated by Esstech Inc. All other materials were purchased from common suppliers (Tokyo Chemical Industries, MilliporeSigma, Fisher Scientific, and AA Blocks), and used as received without further purification. Other than the precursor thioester (TE1) synthesis, the reactants and monomers used include poly(ethylene glycol) (M_n ≈ 600 g/mol), poly(tetramethylene ether) glycol (M_n ≈ 650 g/mol), pentaerythritol ethoxylate (15/4 EO/OH), 2-methyl-4′-(methylthio)-2-morpholinopropiophenone (I907), (2,2,6,6-tetramethylpiperidin-1-yl)oxyl (TEMPO), 2-hydroxyethyl methacrylate (HEMA), tri(ethylene glycol) dimethacrylate (TEGDMA), tricyclodecanedimethanol dimethacrylate (TCDDMA), hexyl methacrylate (HMA), ethylene glycol dimethacrylate (EGDMA), di(ethylene glycol) methyl ether methacrylate (DEGMEM), t-butyl methacrylate (tBMA), ethylene glycol ethyl ether methacrylate (EGEEMA), ethylene glycol phenyl ether methacrylate (EGPEMA), poly(ethylene glycol) dimethacrylate (M_n ≈ 500 g/mol, PEGDMA), amino-2-propanol (AP), cyclohexylamine (CHA), 28% aqueous ammonia, and dibutyltin dilaurate (DBTDL).

6.3.2 Thioester Precursor (TE1), Synthesis

The synthesis of TE1 was adapted from a previously reported procedure[15] and details are found in the Supporting Information.

6.3.3 Degradable Polyol Synthesis

Poly(ethylene glycol) thioester (PEG-TE):

To a 500 mL round-bottomed flask equipped with a magnetic stir bar, Dean Stark distillation receiver, and condenser, 20.0 g of TE1 (97 mmol, 1 equiv.) was combined with 116.4 g of poly(ethylene glycol) ($M_n \approx 600$ g/mol, 194 mmol, 2 equiv.) in 150 mL of toluene. 10 drops of sulfuric acid were added and the reaction was allowed to reflux for 2 days. After this period, the volatiles were removed under reduced pressure, and the residue was then diluted with 600 mL brine and washed with diethyl ether (4 x 300 mL) prior to extraction into chloroform (3 x 600 mL). The extract was dried over sodium sulfate, filtered, and reduced in vacuo yielding 114 g of a clear liquid (86% yield).

^{1}H NMR (400 MHz, DMSO-d_6): δ = 4.12 (m, 4H), 3.36 (t, 1.5H) 3.53-3.35 (m, ≈60H), 3.14 (t, 1H), 2.89 (t, 1H), 2.79 (m, 0.5H), 2.68-2.61 (m, 4H), 1.84-1.55 (m, ≈60H).

Poly(ethylene glycol) thioester (pTHF-TE):

Poly(ethylene glycol) thioester was prepared consistently with PEG-TE, with the exemption that after reflux, the crude was passed through a plug comprised of basic alumina followed by celite. The volatiles were then removed under reduced pressure to produce a clear liquid with a 70% yield.

^{1}H NMR (400 MHz, $CDCl_3$): δ = 4.24 (m, 4H), 3.75-3.56 (m, ≈120H), 3.11 (t, 2H), 2.88 (t, 2H), 2.69-2.60 (m, 4H).

Scheme 6.2. (a) Preparation of the precursor degradable polyol by Fischer esterification for future implementation in the urethane scaffold. The resulting polyol-TE has a statistical distribution of sizes and number of degradable thioester moieties. The unfunctionalized portion of the polyol is thus not degradable. The choice of polyol enables the range of compatible monomers. (b) Degradation of thioester moiety by aminolysis to form an amide and thiol.

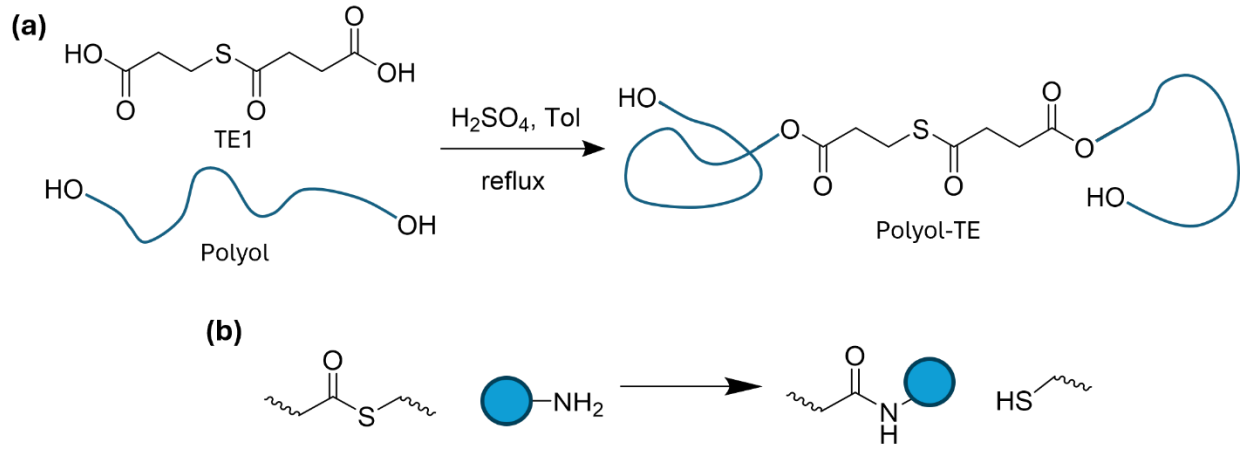

6.3.4 Preparation of Degradable Photoresist

As a general procedure based on the preparation on a 100 g scale of 2:1 TEGDMA:PEG-TE scaffold, 8.59 g of Desmoudur N3900 (17.0 mmol, 1 equiv), was combined with 0.857 g pethaerithritol ethyxolyate (1.10 mmol, 0.063 equiv), 1.94 g HEMA (14.9 mmol, 0.87 equiv), 20.2 g PEG-TE (14.2 mmol, 0.84 equiv), and 78 mg TEMPO (0.50 mmol). The mixture was stirred prior to the addition of monomer, 67 g TEGDMA (230 mmol, 14 equiv), and 1.40 g I907 (5.0 mmol), as the initiator, then stirred and degassed once homogenous. Subsequently, 0.50 g of DBTDL (0.79 mmol), was added and the mixture was vortexed and degassed prior to being cast. Casting geometries included 1-dram vials (Fischer Brand, 15 mm OD) for VAM printing, as well as various

thickness films (10 to 800 μm). Thin films were prepared between Rain-X treated glass slides using vinyl spacers (Precision Brand), unless otherwise specified.

When using monofunctional methacrylates as the monomer, 2 wt% of the total monomer contribution is substituted with dimethacrylate to promote crosslinking. TEGDMA was used for PEG-TE scaffolds while TCDMMA was used in the case of pTHF-TE scaffolds.

6.3.5 Dynamic Mechanical Analysis

Dynamic temperature sweeps were carried out on a TA instruments RSA G2. Thin films (500 μm x 10 mm x 20 mm) were cured for 30 min via 400-500 nm filtered mercury arc lamp (Acticure 4000), at 20 mW/cm^2 and thermally post-cured at 150 °C for 30 min. Samples were heated from -80 to 200 °C at a ramp rate of 3 °C and with a frequency of 1 Hz and oscillatory strain of 0.03%. The T_g was determined as the peak of the tan delta curve.

6.3.6 Scaffold Degradation

The degradation solution was prepared by mixing 20% v/v amine (amino-2-propanol, cyclohexylamine, ammonia), in the desired solvent. Approximately 20 times the mass of degradation solution relative to scaffold was used. Polypropylene mesh was used to support the printed parts from the bottom of the container in cases where not all degradable components are solubilized. After degradation, the printed parts were readily separated by filtration or manual removal.

Scaffold degradation studies were performed on samples comprised of approximately 0.2 g material in the shape of quarter-cylinders originating from the 1-dram vials used for VAM

(6 mm radius, 5 mm height). Samples were blotted on Kimwipes prior to each measurement and stored at 25 °C between measurements.

Mass change studies on photopolymerized parts were performed consistently with the scaffold degradation studies, but with samples of 10 mm height. Samples were polymerized (400-500 nm, 20 mW/cm^2, 30 min), under a nitrogen atmosphere to prevent oxygen inhibition from affecting the outer surface. Samples were immersed in the degradation solution for 40 h and mass change was compared between dry samples.

6.3.7 Tensile Testing

An MTS Exceed E42 universal testing machine equipped with a 500 N load cell was used to assess the engineering stress–strain curve (stress relative to initial cross-section). Young's modulus, ultimate stress, elongation at break, and toughness were determined from the stress-strain curve. Dogbone samples consistent with ASTM dogbone die D638-V, except for a 15 mm gage length (3.15 mm width and an 800 μm thickness), were used.[16] Samples were clamped and strained at a crosshead rate of 0.1 mm/min. Photocured samples (400-500 nm, 20 mW/cm^2, 30 min) were treated in degradation solution (typically 20% v/v in solvent), for durations greater than that needed to degrade the uncured equivalent. Control experiments were comprised of samples that were not treated with the degradation solution.

6.3.8 Combined FT-IR Rheology

To assess mechanical property evolution and chemical conversion simultaneously, near FT-IR (Thermo Scientific, Nicolet 8700), and a rotational rheometer (TA Instruments,

ARES G2), were coupled in parallel consistent with previous work.[17,18] A detailed schematic and description of the apparatus are available in the Scheme S6.2. Samples were monitored for 3 min prior to 20 mW/cm^2 exposure by 405 nm laser (250 mW, Civil Laser), to resemble VAM printing. Near IR was monitored at a resolution of 4 cm^{-1}. Conversion was assessed by the depletion of the methacrylate peak at 6150 cm^{-1}. Shear rheology was monitored on 500 μm thick, 8 mm diameter films under 3 N compression and a 0.1% oscillation at 1 Hz. The inhibition time was defined as the duration between when the light was turned on and when the methacrylate conversion reached 3%.

6.2.9 Resolution Testing in 2D

Samples for 2D resolution testing were prepared with a thickness of 10 μm between one methacrylate functionalized slide and one fluorinated slide (procedure in SI) rather than using Rain-X. The sample was then exposed to 100 mW/cm^2 of patterned 405 nm light for a pre-specified duration. The pattern was achieved via a digital micromirror device (Vialux V-9001) with each resulting 2.47 μm square pixel, either set off or always on for the duration of the exposure, in conjunction with a laser (Civil Laser, 405 nm, 3.5 W, multimode fiber-coupled). The pattern was comprised of lines (critical dimension test) and gaps (resolution test) progressively doubling width from 1 to 512 pixels.

6.3.10 VAM Printing

The VAM printer used to demonstrate volumetric printing in these materials is included in Scheme S6.1. In this setup, a 3.5 W, 405 nm laser (Civil Laser) illuminates a digital micromirror device (Vialux V-9001) which is imaged to the print volume with a doubly

telecentric imaging system with a magnification of –1, yielding a maximum projection intensity of 125 mW/cm^2. Additionally, another imaging system and camera (Teledyne FLIR Blackfly S BFS-U3-63S4M) are used to detect and correct for misalignment in the system as described previously.[19] The imaging system and camera used for misalignment detection and correction are focused so the camera is conjugate to the digital micromirror device. A shadowgram illumination and imaging system is used for print monitoring and consists of a 4.5 mW, 520 nm laser (Thorlabs PL251), an imaging system, and a camera (Teledyne FLIR Blackfly S BFS-U3-120S4M). A rotation stage (Newport URS150BCC) equipped with a vial mount is situated such that the vial rotates freely in an index matching fluid (Cargille labs, product no. 16212) to mitigate refraction at the vial exterior.

Prior to any printing, the digital micromirror device (DMD) – misalignment detection camera pixel-to-pixel relationship was determined by projecting a 120 column x 75 row grid of individual pixels distributed regularly across the DMD and determining the corresponding camera location of each detected centroid. Then, the sample vial submerged in the index matching fluid and mounted to the rotation stage. Misalignment detection was completed by setting the laser power to low, turning on all pixels on the DMD, and taking an image of the vial at 60 different angles evenly spaced across a full rotation of the rotation stage. The exposure intensity during misalignment detection was less than 100 μW/cm^2 and the total exposure time was less than 4.5 seconds.

All ‘rod and disk’ prints were completed by sequentially printing the rod, then printing the disk. The projection images were generated to project maximum intensity in-part, and minimize intensity out-of-part, ensuring uniform exposure intensity across the interior of the rod and disk throughout the duration of the print. Each print was completed with 360

projections, or one projection per degree of rotation, with the exposure intensity maximized at 125 mW/cm^2 and the projection images transformed to correct for misalignment of the vial, projector, and rotation stage. Print timing of a specific rod-disk combination (e.g. 250 μm diameter, 2 mm long rod and 250 μm thick, 2 mm diameter disk) was determined by monitoring the printed object in the shadowgram and stopping the print when the diameter of the printed object matched the desired diameter. For a rod-disk combination consisting of 250 μm diameter, 2 mm long rod and 250 μm thick, 2 mm diameter disk, the print time was 438 seconds and 324 seconds, respectively.

6.4 Results and Discussion

6.4.1 Monomer Compatibility and Material Properties

Herein, an organogel comprised of a degradable polyurethane scaffold and methacrylate monomer(s) is leveraged as a negative photoresist as presented in Figure 6.1. The hydrophilicity and other aspects of the polyurethane chemical environment are readily tuned by the choice of polyol, enabling the use of a wide variety of monomers from water-soluble poly(ethylene glycol) dimethacrylates to the aliphatic hexyl methacrylate; with a list of monomers that these matrices have been used to compatibilize provided in Scheme 6.3.

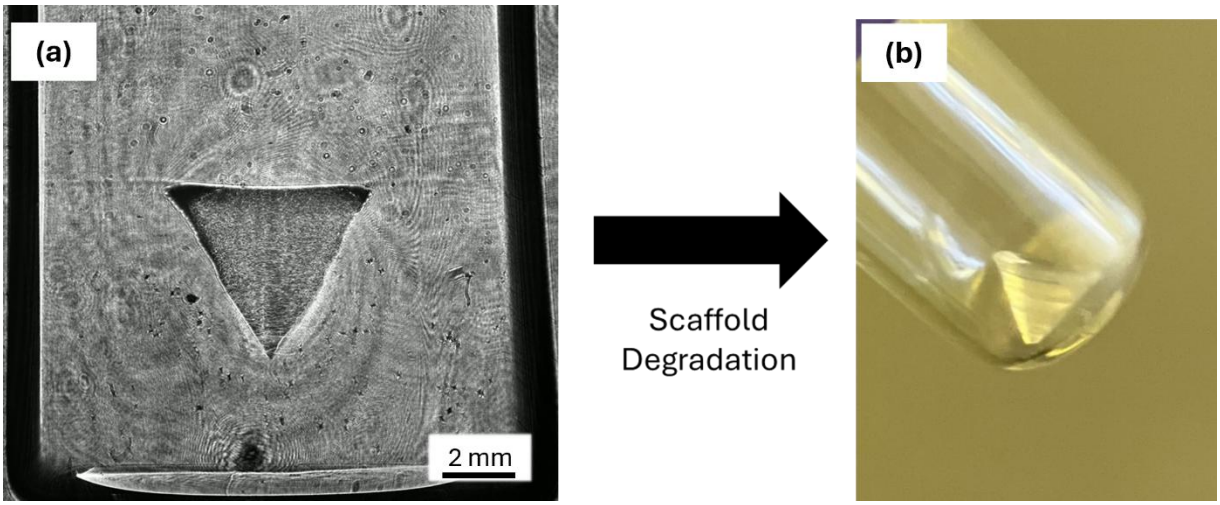

Figure 6.1. (a) Shadowgram of a VAM printed cone into 2:1 TEGDMA : PEG-TE scaffold. Part printed by patterned exposure as the vial spins. The degradable polyurethane scaffold supports part during VAM printing. (b) Released part following scaffold degradation by 20% v/v amino-2-propanol in water for 16 h.

Scheme 6.3. List of monomers and the matrices that have been used to compatibilize them. Monomers that were not compatible with PEG-TE scaffold were then tested with pTHF-TE scaffold. Asterisk denotes viscosity increase rather than urethane-driven gelation. Scaffold composition tunning and monomer purification are potential avenues to widen compatibility and promote gelation.

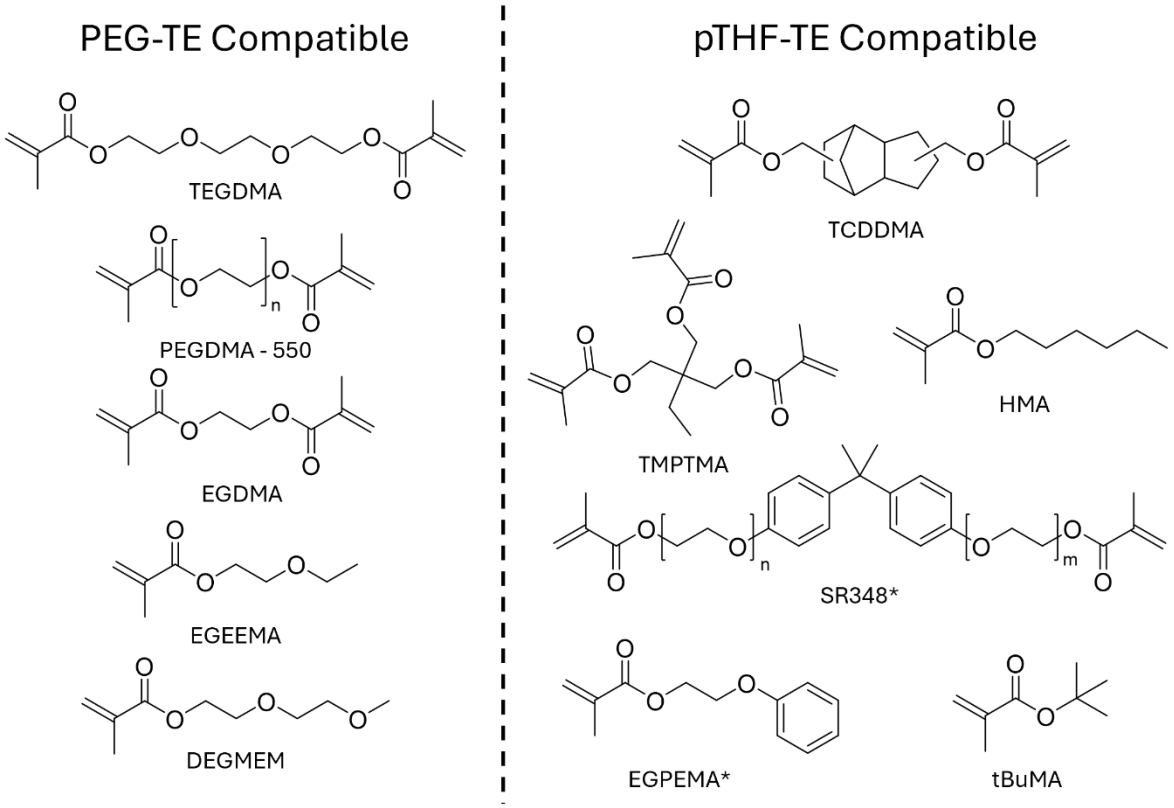

The utility of a wide variety of monomers enables tuning of thermomechanical properties. This tuning is not only dependent on the monomer(s) selected, but also on the relative ratio of monomer to scaffold. Therefore, final parts with moduli ranging from a few MPa to hundreds of MPa are readily achievable by this methodology. Thermomechanical properties for some of these combinations are presented in Figure 6.2 and others are presented in Figure S6.2.

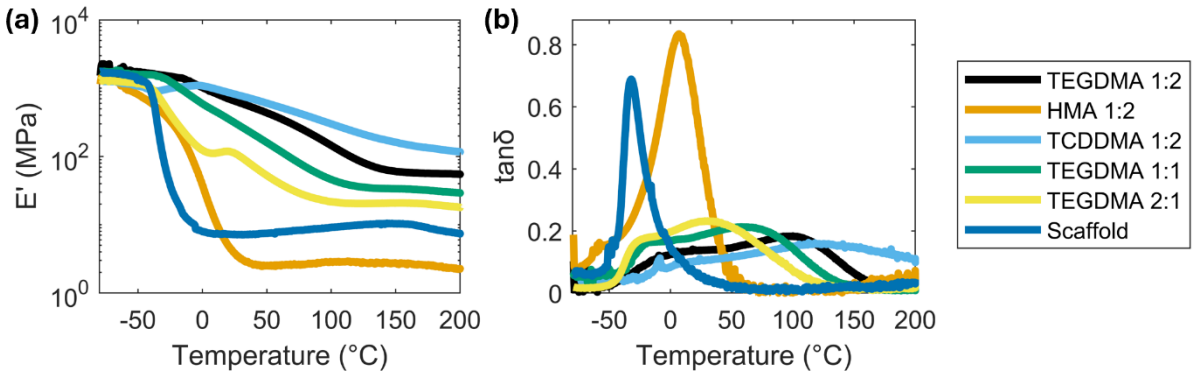

Figure 6.2. Dynamic mechanical analysis of various monomers and relative compositions of scaffold:monomer. Neat pTHF-TE scaffold is provided as a reference. Thin films cured with a 400-500 nm filtered Hg arc lamp (20 mW/cm^2) for 30 min. Glassy samples were post-cured at 150 °C for 30 min. (a) A wide distribution of ambient moduli and crosslink density are achievable. (b) Tunable T_g. HMA monomer contains 2% TCDDMA to promote crosslinking.

6.4.2 Scaffold Degradation

Scaffold degradability arises from the inclusion of a thioester group in the backbone. As a proof-of-concept, this thioester is degraded by aminolysis in solution. Both scaffold compositions (PEG-TE and pTHF-TE), readily degrade when swollen by 20% v/v amino-2-proponal in ethyl acetate as demonstrated in Figure 6.3a. In contrast, degradation systems such as aqueous ammonia that primarily degrade at the interface due to limited swelling progress more slowly (Figure 6.3b).

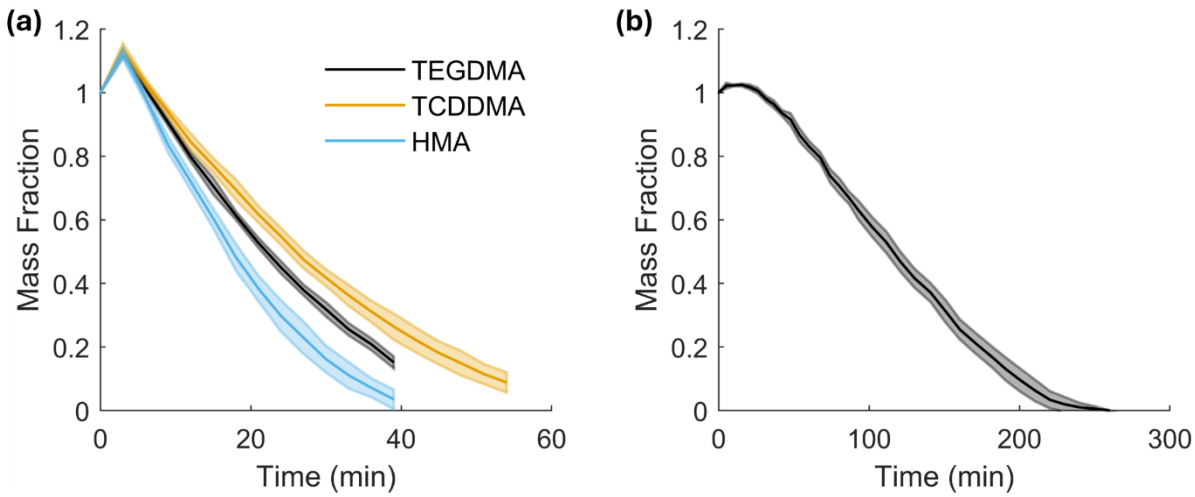

Figure 6.3. Degradation of organogels (1:2 scaffold:monomer) in amines. Mass fraction is defined relative to the initial dry mass. Shading denotes standard deviation range for n = 3 samples. (a) Degradation in 20% v/v amino-2-propanol in ethyl acetate. Samples are comprised of 2:1 TEGDMA : PEG-TE scaffold, 2:1 TCDDMA : pTHF-TE scaffold, and 2:1 HMA : pTHF-TE scaffold. (b) TEGDMA in 28% v/v aqueous ammonia. Water penetrates the PEG-TE scaffolding poorly and therefore the degree of swelling decreases and degradation time increases.

The combination of a degradable polyol and multifunctional monomer would result in a large sol fraction upon thioester degradation, even in the exposed regions where polymerization occurs. Extraction of an unfunctionalized scaffold from an exposed region would inevitably lead to shrinkage and reduction in the mechanical properties during the scaffold degradation step. In contrast, if the scaffold is functionalized in a manner that promotes copolymerization between the scaffold and the matrix monomer, degradation of the thioesters would not lead to significant mass loss or reduction in the mechanical performance. To achieve this aim, hydroxy-functionalized methacrylates such as HEMA

are included in the scaffold formulation to promote attachment while still permitting the gelation and degelation processes to occur as desired. HEMA facilitates direct connection of written monomer to the scaffold. As such, these components of the scaffold are no longer extractable. HEMA, having a single hydroxy functional group, results in dead-ends in the initial scaffold formation; and thus, if included in large quantities, must be countered by a multifunctional hydroxy such as PE to keep the scaffold crosslink density at the same level. Therefore, the combination of PE and HEMA enables control of the crosslink density and connections between the monomer and scaffold as presented in Figure 6.4. In a simple model, the extractable fraction from a printed part and modulus were mapped as a function of the theoretical Flory-Stockmayer gel point[20–22] and the portion of thioester degradation needed to degel by varying HEMA and PE content. The border of the colored area of these plots demonstrates the limits for achievable critical gel point conversion and the thioester degradation threshold. The coloring within these bounds reflects the properties at that point, such as the formulation herein marked with a black circle. Details can be found in the Supporting Information. Notably, this simple model neglects defects, including loops. Therefore, it was anticipated that the simulation underestimated critical gel point, extractable mass loss (sol fraction), and scaffold modulus, while overestimating degradation threshold.

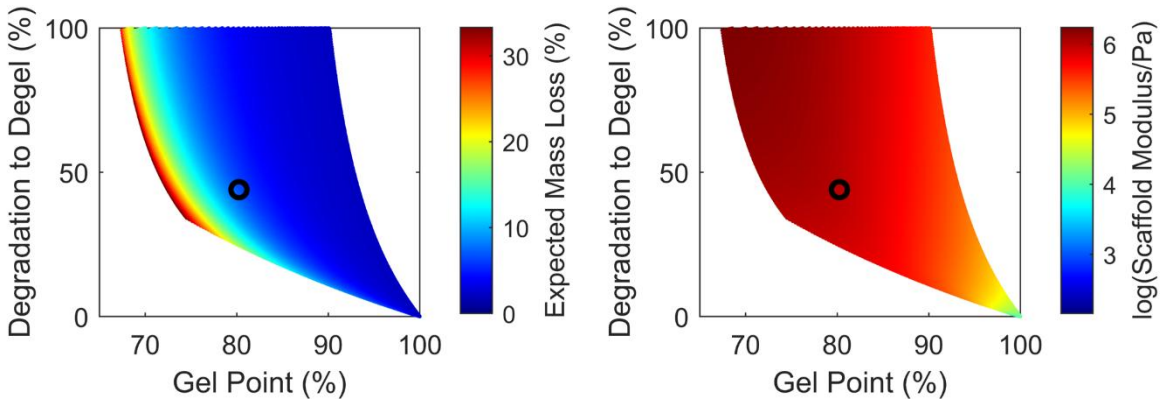

Figure 6.4. Approximate formulation space of scaffold theoretical gel point and percentage of thioester that need to be degraded to degel. Variation in HEMA, PE, PEG-TE, and TNCO, but with maintained stoichiometric alcohol to isocyanate, determine the accessible space (colored area). The formulation used herein represented by black circles. White area denotes areas that are inaccessible due to formulation constraints or non-degradability. The color schemes demonstrate the properties overlaid in the formulation space including (a) extractable mass (sol fraction), of a printed part and (b) storage modulus of the virgin scaffold for a 1:2 scaffold:monomer formulation using PEG-TE. Variation in HEMA, PE, PEG-TE, and TNCO are allowed, but with maintained stoichiometric alcohol to isocyanate. Formulation used herein represented by black circles. White area denotes areas that are inaccessible due to formulation constraints or non-degradability. A consistent selection for low extractable fraction, prompt degradation, and sufficiently high modulus is desirable. Model does not account for polymerization no-idealities including loops, impurities, and side reactions.

6.4.3 Effect of Degradation of Part Properties

The use of development solution to degrade the scaffold results in further design considerations. The selection of amine and solvent for the development solution must be made both on account of the matrix monomer and scaffold composition combined. Generally, it is desirable to minimize compatibility with the part, but maximize the uptake and degradation of thioesters in the unprinted scaffold. However, since the scaffold material persists as a component of the printed part, this selection is non-trivial. Additionally, the use of an amine-based development solution inherently prevents the

system from incorporating acrylates as the matrix due to Michael addition. To eliminate any propensity for Michael addition, methacrylate monomers and scaffold attachment are used.

Degradation testing was conducted on fully cured samples (20 mW/cm^2, 400-500 nm filtered Hg arc lamp, 30 min), but the final selection must be based on the desired green properties of the printed part. Thin films of TEGDMA and TCDDMA were assessed for mass loss and tensile mechanical properties (Table 6.1 and 6.2). Except for the TEGDMA and pTHF-TE formulation degraded with amino-2-propanol in water, the degradation solution resulted in a decrease in ultimate tensile stress and elongation to break. Interestingly, the mass of the TCDDMA and PEG-TE formulation increased upon exposure to the degradation solution. This behavior is attributed to the addition of amine during the cleavage of thioester groups without subsequent extraction as well as solvent retention.

It is generally desirable that the degradation process be fast, but not at the consequence of permeating the part. Therefore, a solvent-amine combination that readily infiltrates the scaffold, but not the printed part, is desired. In the case of TEGDMA, AP in water demonstrates the most promise (Table 6.1) as properties are hardly modified as water readily penetrates the PEG-TE scaffold. In contrast, TCDDMA used a pTHF-TE, which is not permeable to water. Consequently, surface degradation progresses very slowly. A more aliphatic amine, such as CHA, or a less polar solvent, such as methanol, enabled degradation on reasonable timescales (Table 6.2). TCDDMA parts suffer mechanical damage from either option, and further tuning is desirable. Alternatively, since

the scaffold degradation step occurred first, it may have had a negative consequence on the thermal postcure. A thermal initiator would overcome this limitation.

TEGDMA + PEG-TE	Ultimate Stress (MPa)	Strain to Break (%)	Toughness (MPa)	Young's Modulus (MPa)	Mass Change (%)
Control	26 ± 1	16 ± 5	3 ± 1	340 ± 30	N/A
Water + AP	24 ± 1	14 ± 6	2 ± 1	360 ± 40	+4 ± 3
EtOAc + AP	20 ± 2	12 ± 5	2 ± 1	320 ± 30	+3 ± 1
Ammonia	21 ± 3	11 ± 4	1.5 ± 0.7	340 ± 70	+1.5 ± 0.5

Table 6.1. Tensile properties and mass change of 2:1 TEGDMA : PEG-TE scaffold under various degradation conditions. Samples cured (20 mW/cm2, 400-500 nm, 30 min) prior to exposure to a degradation solution comprised of 20% v/v amino-2-propanol (AP) in solvent or 28% aqueous ammonia.

TCDDMA + pTHF-TE	Ultimate Stress (MPa)	Strain to Break (%)	Toughness (MPa)	Young's Modulus (MPa)	Mass Change (%)
Control	32 ± 4	13 ± 2	2.5 ± 0.7	380 ± 40	N/A
MeOH + AP	25 ± 5	8 ± 3	1.2 ± 0.7	453 ± 20	0 ± 1
EtOH + AP	25 ± 5	8 ± 2	1.1 ± 0.5	480 ± 40	-1 ± 2
H_2O + CHA	26 ± 5	9 ± 2	1.4 ± 0.6	420 ± 50	-1 ± 1

Table 6.2. Tensile properties and mass change of 2:1 TCDDMA : pTHF-TE scaffold under various degradation conditions. Samples cured (20 mW/cm^2, 400-500 nm, 30 min), prior

to exposure to degradation solution comprised of 20% v/v amine (amino-2-propanol (AP) or cyclohexylamine (CHA)) in solvent. Tensile samples were thermally post-cured at 150 °C for 30 min.

In contrast to glassy printed parts, which inherently resist degradation due to reduced free volume, rubbery parts are at greater risk of damage during extraction. As such, the monomer and degradation solution compatibility is more critical. Table 6.3 presents the tensile properties and mass change for 2:1 HMA:pTHF scaffold photopolymerized samples. The modulus of HMA networks is reduced due to the cleavage of thioesters throughout the network. Ethanol and AP demonstrate promise for degrading this system with minimal damage, though 10% mass increase due to solvent uptake is higher than preferable. Notably, the system remains transparent and increases its strain to break from 65% to 77% after exposure to the degradation solution. Therefore, the scaffold not only shows promise for the preparation of elastomeric parts, but harnessing the degradation can result in crosslink density decreases post-printing without substantial mass loss.

HMA + pTHF-TE	Ultimate Stress (MPa)	Strain to Break (%)	Toughness (MPa)	Young's Modulus (MPa)	Mass Change (%)
Control	1.3 ± 0.2	65 ± 7	0.5 ± 0.1	2.07 ± 0.05	N/A
MeOH + AP	0.6 ± 0.1	60 ± 20	0.2 ± 0.1	1 ± 1	+6 ± 1
EtOH + AP	0.75 ± 0.05	77.2 ± 0.8	0.28 ± 0.04	1.1 ± 0.3	+10 ± 3

Table 6.3. Tensile properties and mass change of 2:1 HMA : pTHF-TE scaffold under various degradation conditions. Samples cured (20 mW/cm^2, 400-500 nm, 30 min), prior to exposure to degradation solution comprised of 20% v/v amino-2-propanol (AP) in solvent.

6.4.4 Real-Time Chemical Kinetics and Rheology

In order to best inform the printing process, simultaneous rheology and real-time FT-IR were performed. This hybrid methodology enables the methacrylate reaction to be tracked both chemically and by the mechanical property evolution. Therefore, these curves provide not only an understanding of the dose required to overcome an inhibition threshold, but also the relationship between print time and the combination of green part modulus and conversion. In the scope of this work, this relationship is critical for understanding the subsequent degradation step. In Figure 6.5a, a monofunctional methacrylate (HMA), only resulted in a 1 order of magnitude change in modulus upon polymerization but has the capacity to reach full conversion. Maximizing conversion in this case is important as any unreacted monomer has the potential of being extracted by

solvent. In contrast, difunctional monomers presented in Figure 6.5b-c did not reach full conversion due to vitrification. However, this reduction in free volume limited extraction of the sol fraction with proper degradation solution selection. Furthermore, the conversions demonstrated are expected to have low sol fractions for the dimethacrylate chain growth system. However, the conversions achieved leave room for post-processing and therefore, higher moduli than those achieved by photopolymerization alone.

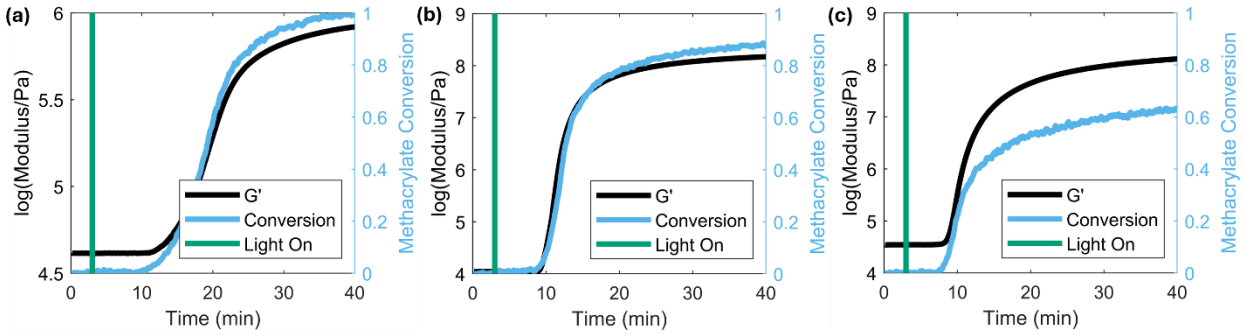

Figure 6.5. Combined FT-IR and rheology evolution for subset of available monomers. All samples are 1:2 scaffold:monomer with 50 mM I907 and 5 mM TEMPO. Exposure of 20 mW/cm^2 with 405 nm laser to most closely simulate VAM exposure. (a) 98% HMA, 2% TCDDMA in pTHF-TE scaffold. (b) TEGDMA in PEG-TE scaffold. (c) TCDDMA in pTHF-TE scaffold.

Additionally, this method promptly demonstrates the theoretical benefits of adding inhibitor to the system. Within VAM, significant light exposure occurs to voxels outside the desired print geometry. Traditionally, it is anticipated that oxygen inhibition alone is suitable to prevent out-of-part polymerization; however, enhanced control is achieved via the addition of an inhibitor.[12,14,23] To affirm this benefit, a metric of this control is presented as a ratio of the inhibition time (i.e., the time that the light is one before polymerization

starts) to print time (the time from when polymerization starts until a desired modulus that corresponds to the necessary green strength is achieved) with the higher ratio being desirable. FT-IR and rheology were measured simultaneously for varied quantities of added TEMPO as presented in Figure 6.6. TEMPO was selected as it does not react during the scaffold formation, nor does it need oxygen to inhibit the reaction.[24] The inhibition ratios as a function of the targeted green modulus are presented. A consistent and sufficiently high inhibition ratio is desirable for improving the printing resolution, such as that demonstrated in the 5 mM TEMPO case. Additionally, the high inhibition ratio corresponding to a high green modulus is favorable to protect the parts in this system from damage during scaffold degradation.

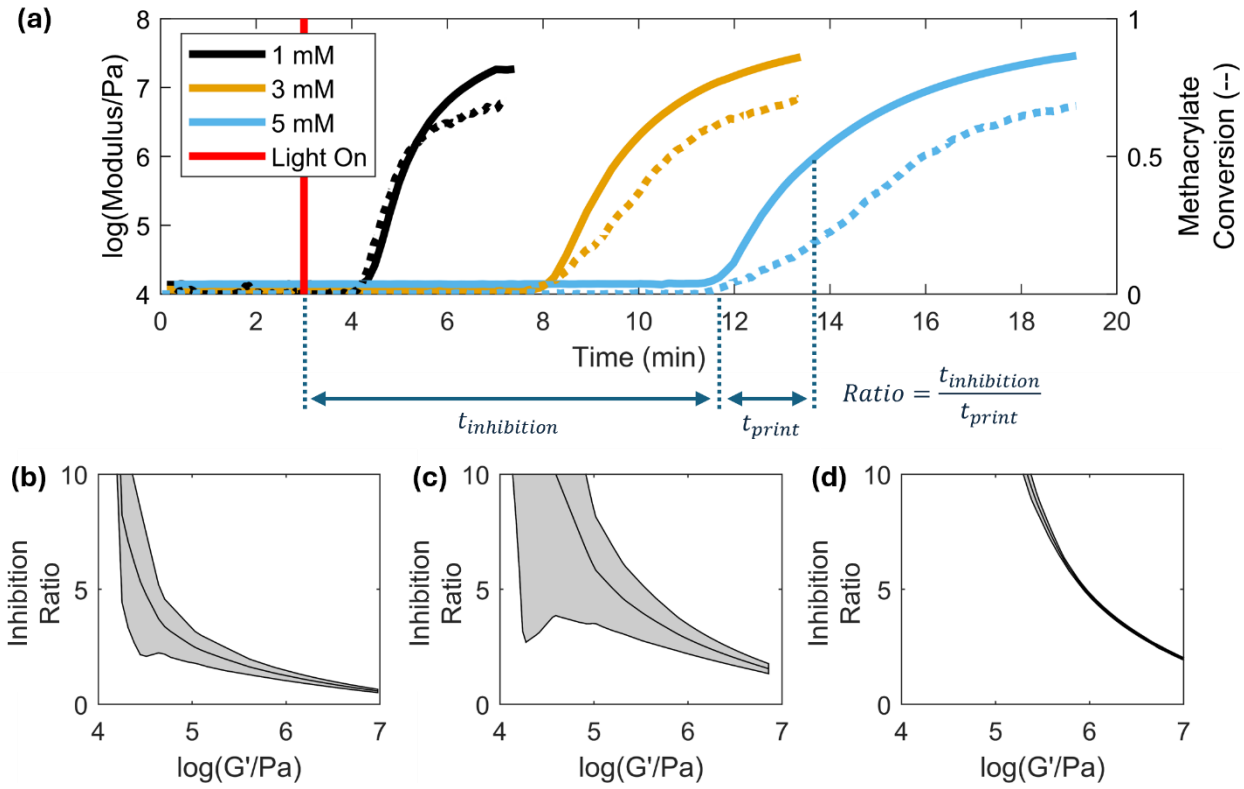

Figure 6.6. (a) Combined FT-IR and rheology evolution for varied TEMPO content in 1:2 TEGDMA with 50 mM I907. Exposure of 20 mW/cm^2 with 405 nm laser to most closely

simulate VAM exposure. Solid lines denote sheer storage modulus (G'), while dashed lines represent conversion as assessed simultaneously by FT-IR. Example inhibition ratio for 5 mM TEMPO sample to a green part modulus of 1 MPa is labeled. (b-d) Inhibition ratios (inhibition time/print time) as a function of green part modulus for (b) 1 mM, (c) 3 mM, and (d) 5 mM TEMPO. Shading denotes standard deviation over triplicates from the same batch.

6.4.5 Resolution Testing and VAM Printing

Additional considerations include the achievable resolution and critical dimensions for these resins. Figure 6.7a-b presents 2D testing in a 10 μm thick film that has been exposed to degradation conditions. Inhibition provided by oxygen, and the added TEMPO, as they diffuse from out-of-part regions to in-part regions impact the achievable feature size during the patterning process.[5,25–27] However, this 2D measurement does not translate directly to VAM so testing in that context is crucial. A simple resolution test in the form of rods is presented in Figure 6.7c. However, a print geometry that tests resolution in cylindrical coordinates, noting the known radial resolution dependence in VAM,[28] is necessary to properly characterize spatial limitations.

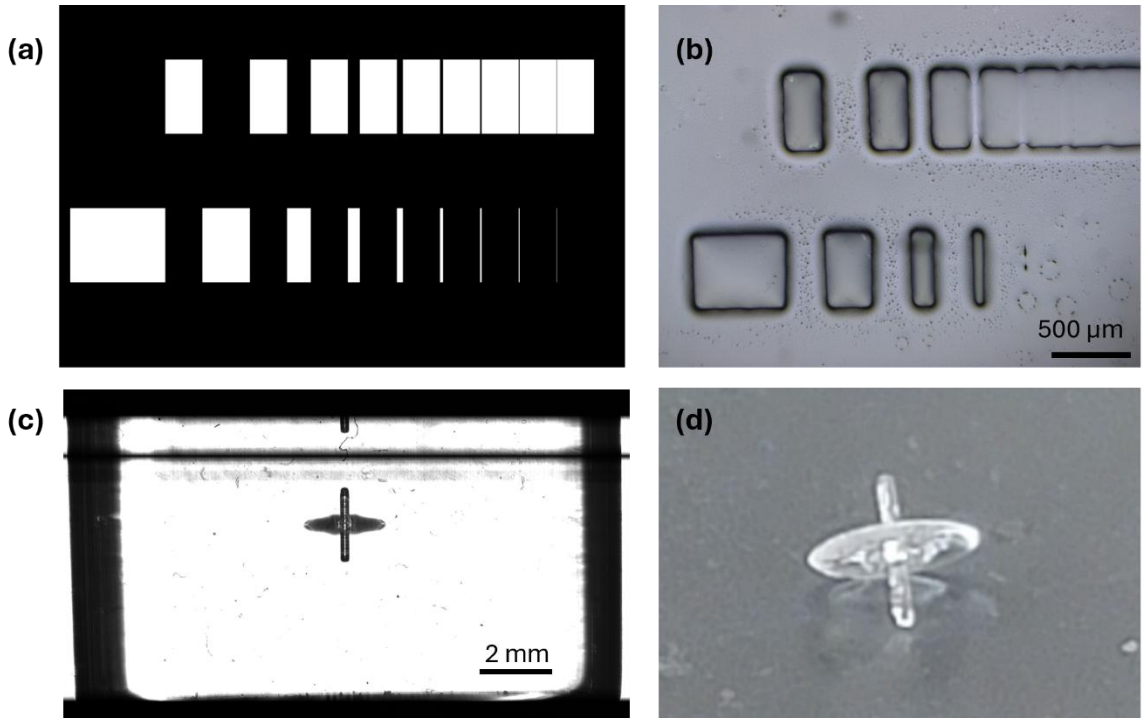

Figure 6.7. Resolution testing of degradable scaffold system (a) 2D exposure to assess resolution and critical dimension in a 2D context. Smallest features are single pixel (2.47 µm), and double in size for each step. (b) 1:2 TCDDMA, 50 mM I907, 5 mM TEMPO, exposed 100 mW/cm^2 with 405 nm laser (5 min). Degraded in 20% v/v AP in EtOAc for 2 h. Resolution and critical dimension limit of 80 µm in 10 µm film. (c) 250 µm VAM printed rod. A disk (2 mm diameter, 250 µm thickness) is overprinted on the rod. (d) Part revealed upon degradation of the scaffold in 20% v/v AP in EtOAc (5 h).

Finally, the scaffolding support enables delays in printing. The disk around the rod in Figure 6.7c was printed in a second phase after the rod was printed. Therefore, this methodology allows for the temporal separation of complex geometries, noting sensitive areas of high resolution. Furthermore, a print delay allows redistribution of initiator and

inhibitor via diffusion. This approach effectively resets the printing capacity of the resin, critically at interfaces, with a somewhat lowered inhibition ratio.

6.5 Conclusions

A widely tunable negative photoresist for VAM is presented. The method is compatible with a wide array of otherwise inaccessible low viscosity monomers, enabling storage moduli at ambient ranging over three orders of magnitude. Parts were printed and suffered less than 2% mass loss in exposed regions during exposure to the solution that completely degrades unexposed regions. These films also maintained similar mechanical properties upon proper amine-based degradation solution selection. The benefits of added inhibitor to increase the non-linear response of the system were characterized by real-time chemical and mechanical analysis. This real-time analysis of inhibited resins informs not only the print contrast but also provides reliable print duration allowing for high reproducibility. Rods of 250 μm diameter were VAM printed consistently. Finally, disks were overprinted, thereby demonstrating the capacity to pause and continue prints.

6.6 References

(1) Saleh Alghamdi, S.; John, S.; Roy Choudhury, N.; Dutta, N. K. Additive Manufacturing of Polymer Materials: Progress, Promise and Challenges. *Polymers* **2021**, *13* (5), 753. https://doi.org/10.3390/polym13050753.

(2) Tan, L. J.; Zhu, W.; Zhou, K. Recent Progress on Polymer Materials for Additive Manufacturing. *Adv. Funct. Mater.* **2020**, *30* (43), 2003062. https://doi.org/10.1002/adfm.202003062.

(3) Ligon, S. C.; Liska, R.; Stampfl, J.; Gurr, M.; Mülhaupt, R. Polymers for 3D Printing and Customized Additive Manufacturing. *Chem. Rev.* **2017**, *117* (15), 10212–10290. https://doi.org/10.1021/acs.chemrev.7b00074.

(4) Whyte, D. J.; Doeven, E. H.; Sutti, A.; Kouzani, A. Z.; Adams, S. D. Volumetric Additive Manufacturing: A New Frontier in Layer-Less 3D Printing. *Addit. Manuf.* **2024**, *84*, 104094. https://doi.org/10.1016/j.addma.2024.104094.

(5) Shusteff, M.; Browar, A. E. M.; Kelly, B. E.; Henriksson, J.; Weisgraber, T. H.; Panas, R. M.; Fang, N. X.; Spadaccini, C. M. One-Step Volumetric Additive Manufacturing of Complex Polymer Structures. *Sci. Adv.* **2017**, *3* (12), eaao5496. https://doi.org/10.1126/sciadv.aao5496.

(6) Regehly, M.; Garmshausen, Y.; Reuter, M.; König, N. F.; Israel, E.; Kelly, D. P.; Chou, C.-Y.; Koch, K.; Asfari, B.; Hecht, S. Xolography for Linear Volumetric 3D Printing. *Nature* **2020**, *588* (7839), 620–624. https://doi.org/10.1038/s41586-020-3029-7.

(7) Corrigan, N.; Li, X.; Zhang, J.; Boyer, C. Xolography for the Production of Polymeric Multimaterials. *Adv. Mater. Technol.* **2024**, *9* (15), 2400162. https://doi.org/10.1002/admt.202400162.

(8) Stüwe, L.; Geiger, M.; Röllgen, F.; Heinze, T.; Reuter, M.; Wessling, M.; Hecht, S.; Linkhorst, J. Continuous Volumetric 3D Printing: Xolography in Flow. *Adv. Mater.* **2024**, *36* (4), 2306716. https://doi.org/10.1002/adma.202306716.

(9) Kelly, B. E.; Bhattacharya, I.; Heidari, H.; Shusteff, M.; Spadaccini, C. M.; Taylor, H. K. Volumetric Additive Manufacturing via Tomographic Reconstruction. *Science* **2019**, *363* (6431), 1075–1079. https://doi.org/10.1126/science.aau7114.

(10) Loterie, D.; Delrot, P.; Moser, C. High-Resolution Tomographic Volumetric Additive Manufacturing. *Nat. Commun.* **2020**, *11* (1), 852. https://doi.org/10.1038/s41467-020-14630-4.

(11) Weisgraber, T. H.; de Beer, M. P.; Huang, S.; Karnes, J. J.; Cook, C. C.; Shusteff, M. Virtual Volumetric Additive Manufacturing (VirtualVAM). *Adv. Mater. Technol.* **2023**, *8* (23), 2301054. https://doi.org/10.1002/admt.202301054.

(12) Toombs, J. T.; Shan, I. K.; Taylor, H. K. Ethyl Cellulose-Based Thermoreversible Organogel Photoresist for Sedimentation-Free Volumetric Additive Manufacturing. *Macromol. Rapid Commun.* **2023**, *44* (7), 2200872. https://doi.org/10.1002/marc.202200872.

(13) Salajeghe, R.; Meile, D. H.; Kruse, C. S.; Marla, D.; Spangenberg, J. Numerical Modeling of Part Sedimentation during Volumetric Additive Manufacturing. *Addit. Manuf.* **2023**, *66*, 103459. https://doi.org/10.1016/j.addma.2023.103459.
(14) Madrid-Wolff, J.; Toombs, J.; Rizzo, R.; Bernal, P. N.; Porcincula, D.; Walton, R.; Wang, B.; Kotz-Helmer, F.; Yang, Y.; Kaplan, D.; Zhang, Y. S.; Zenobi-Wong, M.; McLeod, R. R.; Rapp, B.; Schwartz, J.; Shusteff, M.; Talyor, H.; Levato, R.; Moser, C. A Review of Materials Used in Tomographic Volumetric Additive Manufacturing. *MRS Commun.* **2023**, *13* (5), 764–785. https://doi.org/10.1557/s43579-023-00447-x.
(15) Worrell, B. T.; McBride, M. K.; Lyon, G. B.; Cox, L. M.; Wang, C.; Mavila, S.; Lim, C.-H.; Coley, H. M.; Musgrave, C. B.; Ding, Y.; Bowman, C. N. Bistable and Photoswitchable States of Matter. *Nat. Commun.* **2018**, *9* (1), 2804. https://doi.org/10.1038/s41467-018-05300-7.
(16) Standard, A. D638-02a. *Stand. Test Method Tensile Prop. Plast. West Conshohocken PA USA ASTM Int.* **2002**.
(17) Shah, P. K.; Stansbury, J. W.; Bowman, C. N. Application of an Addition–Fragmentation-Chain Transfer Monomer in Di(Meth)Acrylate Network Formation to Reduce Polymerization Shrinkage Stress. *Polym. Chem.* **2017**, *8* (30), 4339–4351. https://doi.org/10.1039/C7PY00702G.
(18) Medel, S.; Bosch, P.; Grabchev, I.; Shah, P. K.; Liu, J.; Aguirre-Soto, A.; Stansbury, J. W. Simultaneous Measurement of Fluorescence, Conversion and Physical/Mechanical Properties for Monitoring Bulk and Localized Photopolymerization Reactions in Heterogeneous Systems. *RSC Adv.* **2016**, *6* (47), 41275–41286. https://doi.org/10.1039/C6RA06341A.
(19) Seymour, G.; McLeod, R. R. Detection and Correction of Misalignment for High Fidelity Volumetric Additive Manufacturing. *Opt. Express* **2025**, *33* (4), 6894–6908. https://doi.org/10.1364/OE.540200.
(20) Flory, P. J. Molecular Size Distribution in Three Dimensional Polymers. I. Gelation1. *J. Am. Chem. Soc.* **1941**, *63* (11), 3083–3090. https://doi.org/10.1021/ja01856a061.
(21) Stockmayer, W. H. Theory of Molecular Size Distribution and Gel Formation in Branched Polymers II. General Cross Linking. *J. Chem. Phys.* **1944**, *12* (4), 125–131. https://doi.org/10.1063/1.1723922.
(22) Stockmayer, W. H. Molecular Distribution in Condensation Polymers. *J. Polym. Sci.* **1952**, *9* (1), 69–71. https://doi.org/10.1002/pol.1952.120090106.
(23) Cook, C. C.; Fong, E. J.; Schwartz, J. J.; Porcincula, D. H.; Kaczmarek, A. C.; Oakdale, J. S.; Moran, B. D.; Champley, K. M.; Rackson, C. M.; Muralidharan, A.; McLeod, R. R.; Shusteff, M. Highly Tunable Thiol-Ene Photoresins for Volumetric Additive Manufacturing. *Adv. Mater.* **2020**, *32* (47), 2003376. https://doi.org/10.1002/adma.202003376.

(24) Maafa, I. M. Inhibition of Free Radical Polymerization: A Review. *Polymers* **2023**, *15* (3), 488. https://doi.org/10.3390/polym15030488.
(25) Zhang, Y.; de Haan, H.; Houlahan, K.; Sampson, K. L.; Webber, D.; Orth, A.; Lacelle, T.; Gaburici, L.; Lam, R.; Deore, B.; Paquet, C. Impact of Oxygen Inhibition on Acrylate Photopolymerization in Tomographic Volumetric Printing. Social Science Research Network: Rochester, NY February 26, 2025. https://doi.org/10.2139/ssrn.5157227.
(26) O'Brien, A. K.; Bowman, C. N. Impact of Oxygen on Photopolymerization Kinetics and Polymer Structure. *Macromolecules* **2006**, *39* (7), 2501–2506. https://doi.org/10.1021/ma051863l.
(27) Jariwala, A. S.; Ding, F.; Boddapati, A.; Breedveld, V.; Grover, M. A.; Henderson, C. L.; Rosen, D. W. Modeling Effects of Oxygen Inhibition in Mask-based Stereolithography. *Rapid Prototyp. J.* **2011**, *17* (3), 168–175. https://doi.org/10.1108/13552541111124734.
(28) Orth, A.; Webber, D.; Zhang, Y.; Sampson, K. L.; de Haan, H. W.; Lacelle, T.; Lam, R.; Solis, D.; Dayanandan, S.; Waddell, T.; Lewis, T.; Taylor, H. K.; Boisvert, J.; Paquet, C. Deconvolution Volumetric Additive Manufacturing. *Nat. Commun.* **2023**, *14* (1), 4412. https://doi.org/10.1038/s41467-023-39886-4.

6.7 Supporting Information

6.7.1 Procedure for Materials Synthesis

Precursor thioester (TE1) synthesis

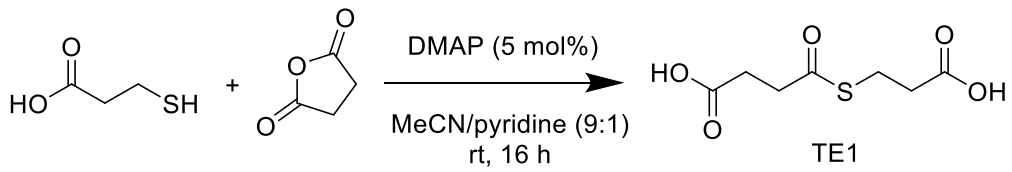

Procedure is adapted from previously published methodology.[1] To a 1.00 L round-bottomed flask equipped with a magnetic stir bar, 50.0 g (500 mmol, 1.00 equiv) of succinic anhydride was dissolved in 450 mL of anhydrous acetonitrile followed by 50.0 mL of anhydrous pyridine. Once homogenous, 43.5 mL (53.0 g, 500 mmol, 1.00 equiv) of 3-mercatopropionic acid and 3.05 g (24.98 mmol, 0.05 equiv, 5.00 mol%) DMAP were added. The reaction vessel was sealed under air and stirred overnight at ambient. The solution was then reduced in vacuo, dissolved in ethyl acetate (1 L), and acidified with 1 M aqueous HCl to a pH of 1. The aqueous layer was back-extracted (2 x 250 mL EtOAc). The combined organics were dried over Na_2SO_4, filtered, and reduced in vacuo. The resulting white solid was washed with chloroform and yielded 94.7 g (92% yield) of TE1. ^{1}H NMR (400 MHz, MeOD-d_3): δ = 3.12 (t, 2H), 2.92 (t, 2H), 2.66-2.58 (m, 4H).

6.7.2 Supplementary Figures and Analysis

Additional Light Source Information

Intensity of Acticure 4000 mercury arc lamp (400-500 nm filter) used for general sample curing and the 405 nm laser (250 mW, Civil Laser) used for simultaneous FT-IR and rheometry were assessed by Thorlabs PM100D radiometer equipped with a Thorlabs S120VC photodiode sensor. Light intensity for 2D resolution testing and VAM printing (Civil Laser, 405 nm, 3.5 W, multimode fiber-coupled) were assessed by Thorlabs PM16-121. In all cases, the 405 nm calibration point was used.

VAM Writer Schematic

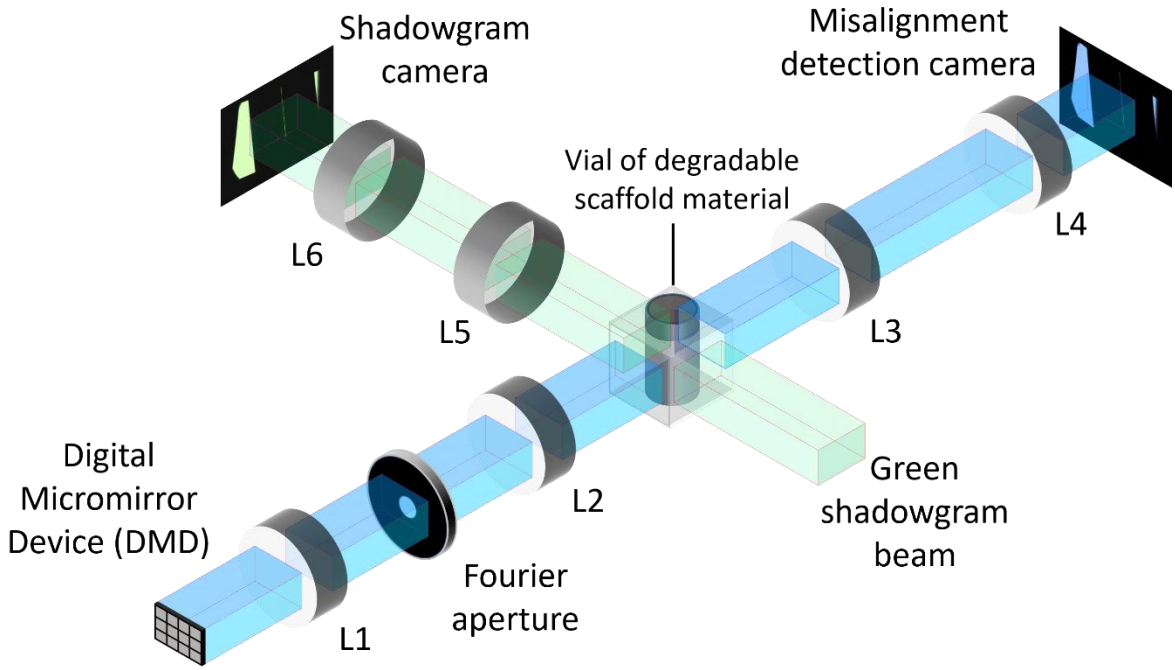

Scheme S1. Schematic of a VAM system. Images are projected from a DMD and imaged through a doubly-telecentric imaging system (lenses L1 and L2) to a vial submerged in an index matched bath. The vial is mechanically coupled to a rotation mechanism (not shown). A doubly-telecentric imaging system (lenses L3 and L4) and camera are added such that the camera is conjugate to the DMD and vial. The camera is used to detect and correct for misalignment in the system. A diverging green beam illuminates the vial and an imaging system (lenses L5 and L6) images the vial to a camera to capture a shadowgram for in situ monitoring of prints.

Simultaneous FT-IR and Rheometry Details

From the Nicolet 8700 FT-IR, the fiber-coupled (Thorlabs M59L02) IR beam is collimated with a lens (Thorlabs AC127-025-C), then is directed to the sample plane with a broadband mirror (TA Instruments UV Curing Accessory for ARES-G2), and finally is coupled to another fiber, leading back to the FTIR, using a fixed focus collimation lens (Thorlabs F220SMA-C).

A 250 mW, 405 nm laser (Civil Laser) coupled to a 600 μm diameter, 0.22 NA fiber (Thorlabs M160L02) is imaged to the sample using a doubly-telectric imaging system consisting of (L1) a 4.6 mm fiber-coupled lens (Thorlabs CFC5-A) and (L2) a 75 mm lens (Thorlabs LA4725-A-ML), creating a 9.8 mm diameter circular illumination area at the sample plane. The 405 nm light is combined with the IR beam using a dichroic (Thorlabs DMLP650) and is blocked by a colored glass longpass filter with a 780 nm cutoff (Thorlabs FGL780) to keep the 405 nm light from saturating the FTIR detector.

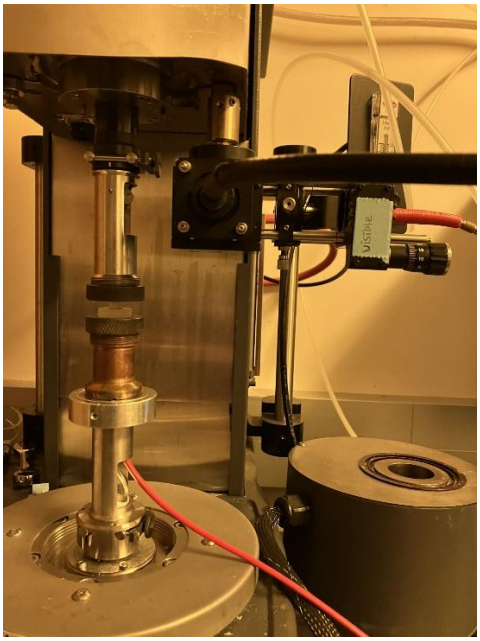

Figure S6.1: Picture of the hybrid FT-IR and rheology apparatus.

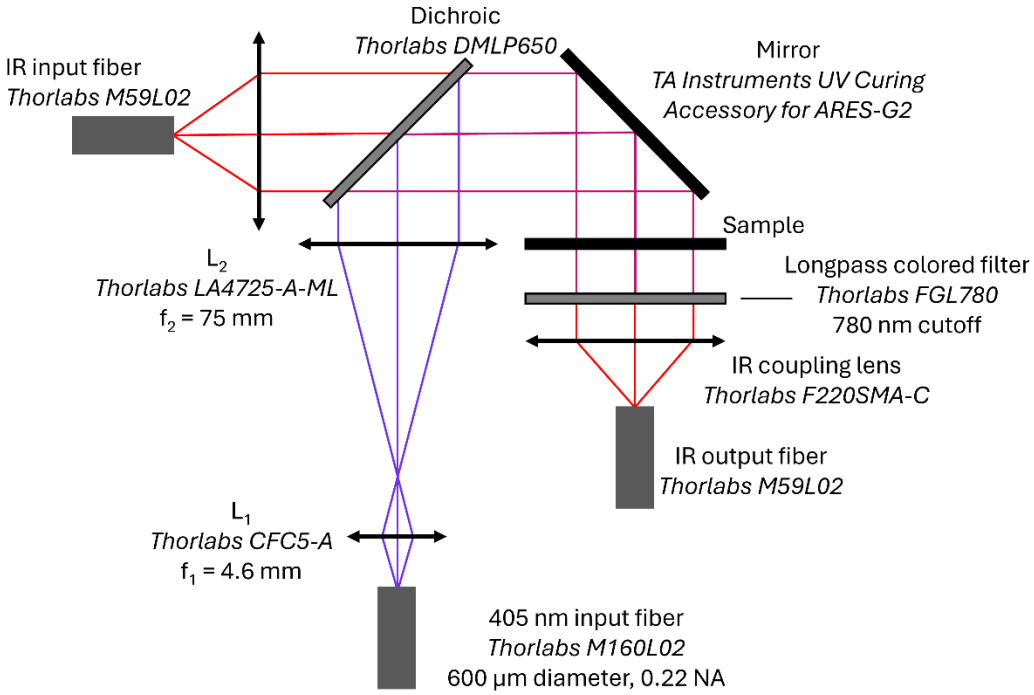

Scheme S6.2. Schematic representation of hybrid FT-IR and rheology optics.

Dynamic Mechanic Analysis of Remaining Monomers

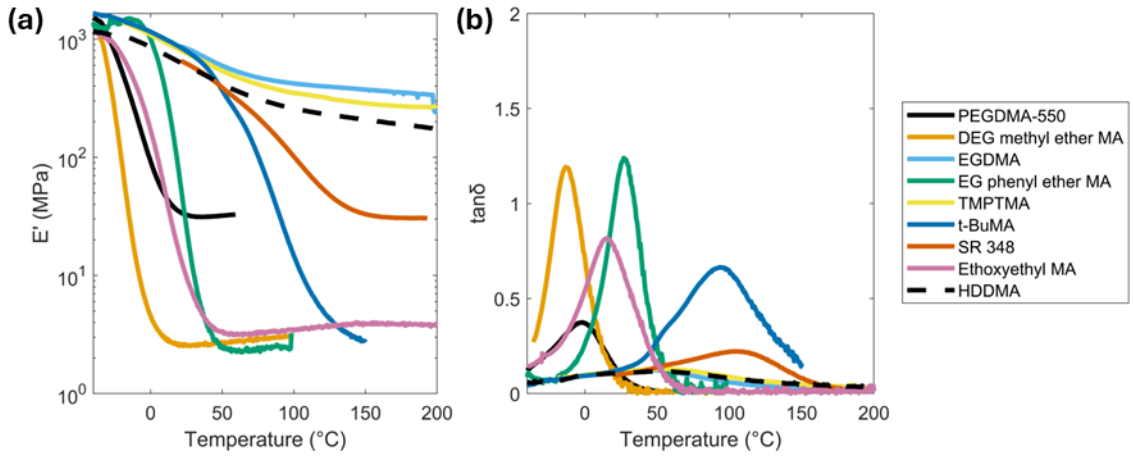

Figure S6.2. Temperature sweeps of (a) storage modulus and (b) tanδ for additional validated monomers. All formulations are 2:1 monomer:scaffold using the respective scaffold from Scheme 6.3.

Simulation Methods

To assess the available tuning within the scaffold itself, a simple model was developed. Methods notably neglect the effects of loops, as well as incomplete and side reactions. The model is comprised of four steps:

I) Theoretical critical gel point (p_c) is assessed by the Flory-Stockmayer method[2–4] in the stoichiometric case:

$$p_c = \frac{1}{\sqrt{1 - f_{w,NCO}}\sqrt{1 - f_{w,OH}}}$$

where f_w is the weighted functionality

$$f_w = \frac{\sum f_i^2 N_i}{\sum f_i N_i}$$

where f_i is the functionality of a molecule, and N_i is the number of molecules. In this work, $f_{w,NCO}$ was roughly estimated as 2.8, consistent with the supplier's described isocyanate content in Desmodur N3900. Gel point was assessed for the available space of polyol-TE, HEMA, and pentaerythritol ethoxylate (PE). Once HEMA content was too high to gel a specified ratio of polyol-TE and PE, higher HEMA content cases were not necessary to calculate.

II) The proportion of thioesters that need to be broken to de-gel was assessed by reverse engineering the method above. Cleavage of a polyol-TE-polyol results in the equivalent of two f = 1 fragments with respect to the polyurethane network formation. As such, $f_{w,-OH}$ for the polyurethane network can be reframed with respect to thioester degradation. Therefore, if the polyurethane network is no longer capable of forming at full conversion, the network has de-gelled. The synthetic method for polyol-TE results in a statistical

distribution was accounted for as 25% of chains contain no thioesters and half of the species contain multiple thioesters resulting in unproductive cleavage.

If the formulation would both gel and degrade, the following steps were assessed as well:

III) The extractable mass was assessed as the portion of materials that was either connected to HEMA, and thus connected to the printed part if converted. A simple model simulated the connectivity of the network assuming all thioesters were cleaved. Starting with a TNCO species with 2.8 available ends, a random -OH was selected based on the ratio of polyol-TE, HEMA, and PE. The mass of the respective group and change in number of available ends was modified according to the species type. HEMA and degradable polyol-TE portions subtract 1 from the available ends. In contrast, non-degradable polyol and PE add 1 and 3 ends respectively, which each become 1.8 ends due to the addition of TNCO to any available hydroxy end-group.

If HEMA was connected to the fragment, or the number of available ends exceeded 100, the test fragment was considered connected. Connected and unconnected fragment molecular weights were normalized by the number of TNCO in the fragment. The extractable fraction was assessed as the ratio of unconnected TNCO to connected TNCO multiplied by the scaffold mass. Free species, such as initiators and catalysts, were added to this mass. The effect of polyol-TE oligomers with 3 or greater polyols was neglected.

IV) Modulus estimation of the scaffold was based on a crosslink density simulation. Similar to the extractable mass simulation, fragments were assessed starting from a singular TNCO. Based on -OH selection, the crosslink density with respect to the number of TNCO in the fragment were modified. HEMA reduces the crosslink count by 1, while all polyol-TE maintain increase the crosslink count by 0.8 as the connect to a TNCO.

Similarly, PE connects to 3 TNCO, thus contributing 2 itself and 2.4 for the TNCO. Elastic activity was assumed for species that reached 500 end-groups. The crosslink count was then normalized to the number of TNCO in the fragment. The number of crosslinks in the scaffold was then determined as the product of this crosslinking contribution and the total mols of TNCO per gram of material. Modulus was estimated from crosslink density according to the following:

$$\rho_{crosslinks} = \frac{E'}{3RT}$$

where E' is the storage modulus at temperature T in the rubbery regime.[5]

Additional Simulation Results

Additional tunning options for the scaffold composition and ratio with respect to monomer can be informed by the model. Examples are presented in Figures S3-S6.

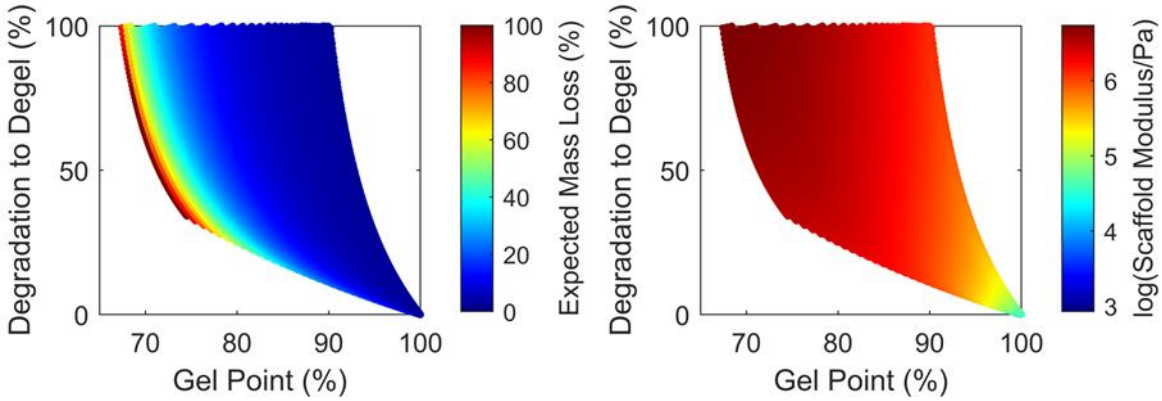

Figure S6.3. Available tuning space, including extractable mass and scaffold modulus, for a formulation using no writing monomer. Although possible to print into such a formulation, damage upon degradation necessitates robust investigation.

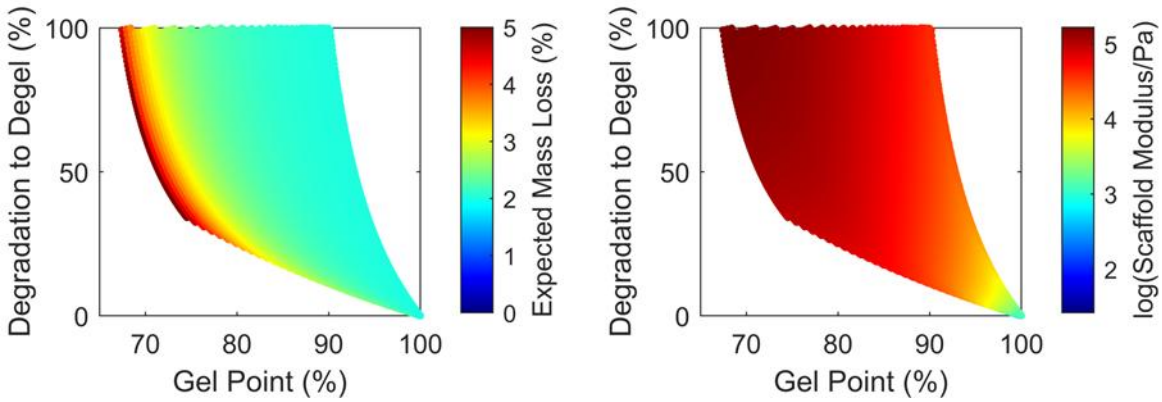

Figure S6.4. Available tuning space, including extractable mass and scaffold modulus, for 95% monomer content. The extractable mass is significantly reduced. Defects, notably loops, will result in deviation from the model.

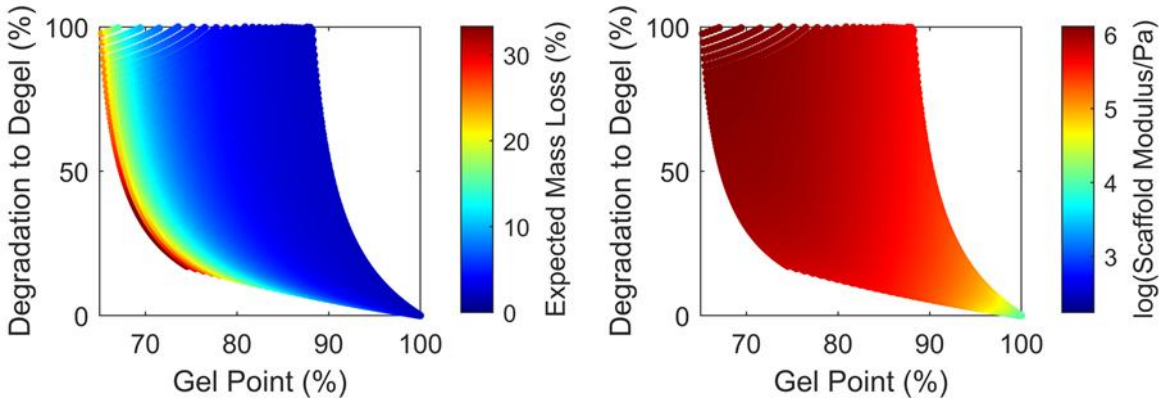

Figure S6.5. Available tuning space, including extractable mass and scaffold modulus, for polyol-TE prepared in a 1.5:1 polyol:TE ratio. Due to the decrease in non-degradable polyol-TE species, the available space with respect to gel point and degradation to de-gel increased.

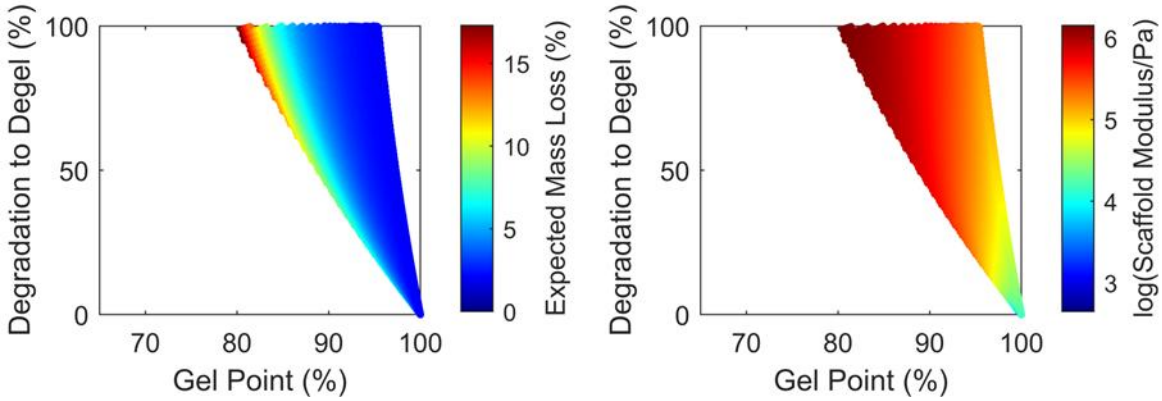

Figure S6.6. Available tuning space, including extractable mass and scaffold modulus, for polyol-TE prepared in a 5:1 polyol:TE ratio. The proportion of non-degradable polyol species increases, dramatically limiting the available space. An intentional combination of polyol-TE-polyol and non-degradable fragments is preferable for tunning space relative to the statistical distribution. Additionally, the non-degradable polyol results in an expansion of the low-modulus region as it functions as a chain extender.

Degradation Damage Stress-Strain Curves

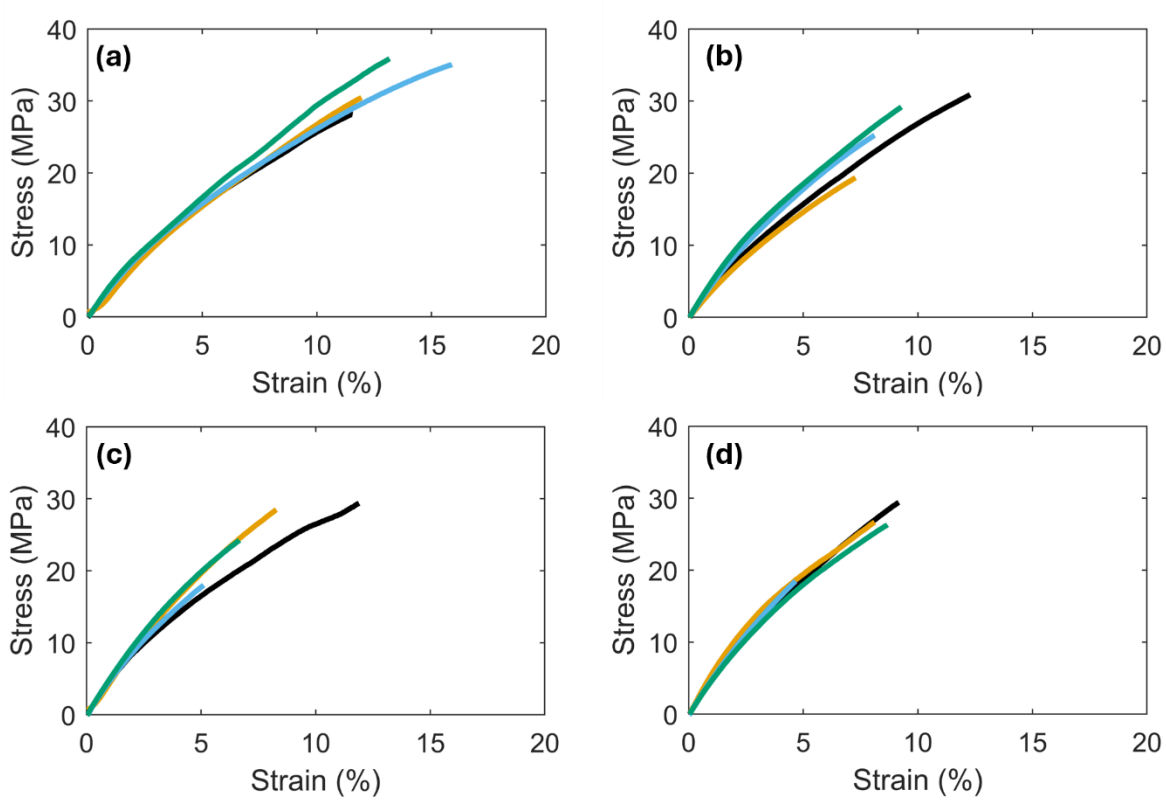

Figure S6.7. Stress-strain curves for 2:1 TCDDMA:pTHF-TE scaffold in (a) control, (b) 20 % v/v cyclohexylamine in water for 16 h, (c) 20% v/v amino-2-propanol in methanol for 16 h, (d) 20% v/v amino-2-propanol in ethanol for 4 h. All films were post-cured following degradation treatment for 30 min at °C.

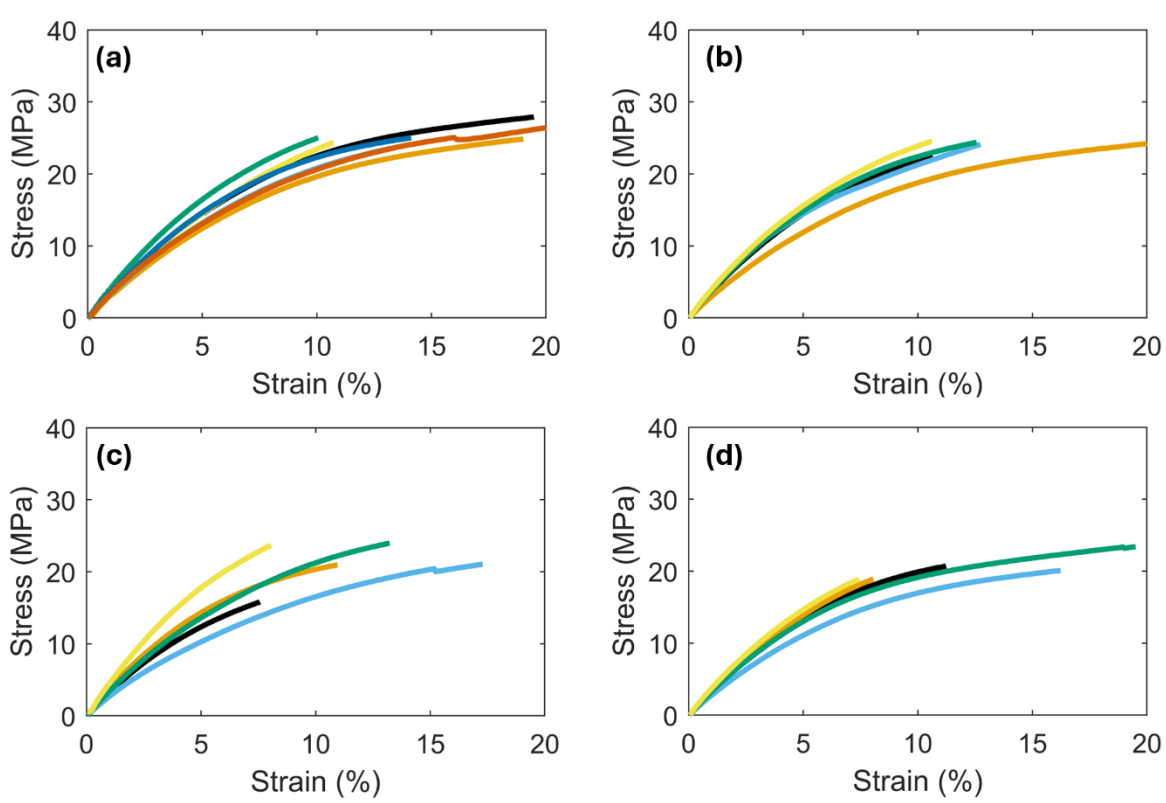

Figure S6.8. Stress-strain curves for 2:1 TEGDMA:PEG-TE scaffold in (a) control, (b) 20 % v/v amino-2-propanol in water for 1 h, (c) 28% aqueous ammonia for 4 h, (d) v/v amino-2-propanol in ethylacetate for 1 h.

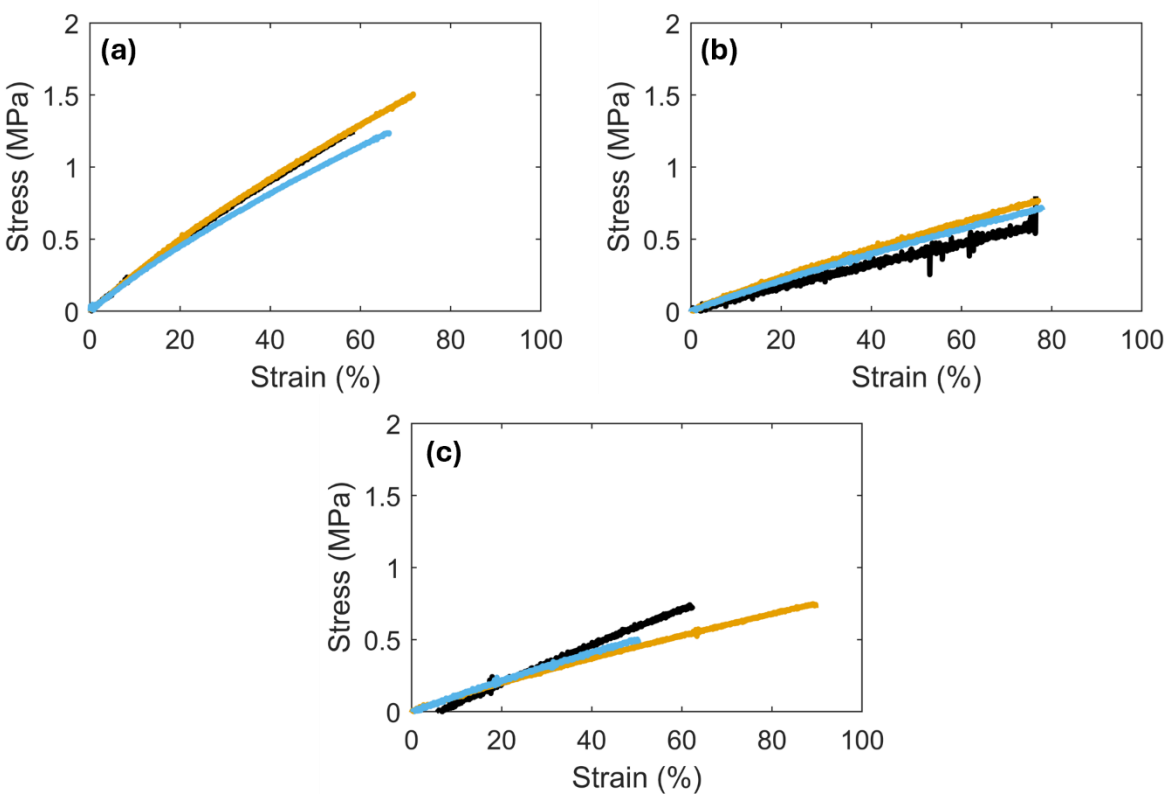

Figure S6.9. Stress-strain curves for 2:1 HMA:pTHF-TE scaffold in (a) control, (b) 20 % v/v amino-2-propanol in ethanol for 3 h, (c) 20 % v/v amino-2-propanol in methanol for 16 h.

6.7.3 Additional References

(1) Worrell, B. T.; McBride, M. K.; Lyon, G. B.; Cox, L. M.; Wang, C.; Mavila, S.; Lim, C.-H.; Coley, H. M.; Musgrave, C. B.; Ding, Y.; Bowman, C. N. Bistable and Photoswitchable States of Matter. *Nat. Commun.* **2018**, *9* (1), 2804. https://doi.org/10.1038/s41467-018-05300-7.

(2) Flory, P. J. Molecular Size Distribution in Three Dimensional Polymers. I. Gelation1. *J. Am. Chem. Soc.* **1941**, *63* (11), 3083–3090. https://doi.org/10.1021/ja01856a061.

(3) Stockmayer, W. H. Theory of Molecular Size Distribution and Gel Formation in Branched Polymers II. General Cross Linking. *J. Chem. Phys.* **1944**, *12* (4), 125–131. https://doi.org/10.1063/1.1723922.

(4) Stockmayer, W. H. Molecular Distribution in Condensation Polymers. *J. Polym. Sci.* **1952**, *9* (1), 69–71. https://doi.org/10.1002/pol.1952.120090106.

(5) Hiemenz, P. C.; Lodge, T. P. *Polymer Chemistry*, 2nd ed.; CRC Press: Boca Raton, 2007. https://doi.org/10.1201/9781420018271.

Chapter 7: Conclusions and Future Recommendations

This thesis focused on the development of sequentially orthogonal multistage networks to overcome the mismatch in desirable processing and end-use properties of photopolymers. In the first portion of this thesis, a 3-stage urethane/acrylate/epoxide system was designed to prepare glassy holographic photopolymers. Whereas in the second part of this thesis, a dual-cure dynamic covalent network was leveraged to permanently fix the topography produced by mechanophotopatterning. Lastly, the third part of this thesis developed a photoresist which was designed for volumetric additive manufacturing, that enabled the use of an array of monomers previously inaccessible to VAM-based processes, prevented settling due to gravity, and enabled consistent print times with high resolution. As to the remainder of this thesis, it summarizes the projects' results and proposes considerations for future work.

7.1 Multistage Holographic Photopolymers

The mechanical properties of holographic photopolymers are inherently limited in the writing stage, due to the necessity for rapid monomer transport. Aim 1 sought to overcome this limitation by implementing a post-processing step in the form of epoxide homopolymerization to dramatically modify thermomechanical properties while maintaining optical performance. The 3-stage urethane/acrylate/epoxide system was controlled sequentially by an ambient cure; 405 nm patterned and flood cure; and 365 nm acid activation followed by high temperature cure; all as described in Chapter 3 of this thesis.

Furthermore, the mechanical properties were modified by the process resulting in an increase from the initial T_g of -22 °C to 101 °C and GPa modulus following epoxide cure. The diffraction grating structure was preserved throughout this process, with a final index contrast of 0.0057, and a diffraction efficiency of 89% in a 50 μm film. Therefore, this process allowed hologram writing with the ease provided by the photopolymer, and enabled a self-supporting structure as the final product.

Proposed future work building on Aim 1 consists of:

1) Increasing Bulk Refractive Index and Refractive Index Contrast. The multistage approach is not limited to the composition presented. Although the material no longer necessitates supporting and protective layers, the thickness remains a critical variable for application. Enhancing index contrast allows for high performance in thinner materials. Furthermore, the bulk refractive index is of interest in the field due to its effect on the maximum field-of-view for curved surfaces. In light of these factors, the chemical selection for matrix, writing monomer, and hardener, as well as their relative abundance, are paramount for industrial application.

2) Evaluation of Self-Supported Films. Long-term performance of open glassy holographic polymers should be evaluated. Relevant variables include scratch resistance and interfacial fouling. Post-modification of, or further polymerization onto the surface(s), may be warranted to ensure consistent high performance without necessitating a separate protective layer of material.

3) Thermal Evaluation. An initial temperature study of these glassy holograms compared to traditional counterparts, demonstrated that both performed well up to 70 °C. However, a robust study as to the consequences of thermal expansion and variation in refractive

index on holographic performance, would inform high temperature applications. Of note, the standard polyurethane-based matrix is susceptible to dynamic covalent rearrangement at temperatures outside the previous range of study. Therefore, severe consequences, both for immediate and long-term performance, may appear upon thermal exposure.

7.2 Dual-Cure Mechanophotopatterning

Mechanophotopatterning serves as a facile method to prepare surface features by simply straining and photopatterning a film. However, previous methodologies leveraging allyl sulfides were inherently limited to post-pattern topography development, due to further radically-mediated rearrangement. Alternatively, dual-cure methodologies were limited as patterning of the material permanently necessarily modified that same area. As such, Aim 2 sought to enable a methodology to pattern films by the superior dynamic covalent methodology, while preventing further evolution once the desired topography was achieved.

In Chapter 4, 65 wt% latent rigid core epoxide in the form of bisphenol A diglycidol ether was combined with a polyurethane which included the radically-mediated dynamic sulfide moieties. These films were processed by mechanophotopatterning, and fixed via an epoxide thermal cure. The final feature height was within 1% of the original, after extended light exposure. This effect stems from the combination of the non-dynamic percolated network in conjunction with the dramatic reduction in free volume as the T_g of the material increase from -12 °C to 96 °C due to the epoxide homopolymerization.

Furthermore, in Chapter 5, a computational model is validated for designing and forming complex patterns by mechanophotopatterning. The forward problem of calculating film topography from an exposure pattern is accomplished by finite element (FE) simulation. The complexity associated with stress relaxation and mass transport out of and into the exposed region, as well as the release of residual strain, is captured.

Proposed future work building on Aim 2 consists of:

1) Advanced Strain and Patterning. The fixed topography methodology allows for an investigation of features with high resolution via optical profilometry. The work presented in Chapter 4 is limited to uniaxial strains; however, the consequences of alternative strain fields, such as biaxial and radial, are not fully realized. Researchers may find promise in sequential patterning under different strain fields which could enable patterns that are not readily accessible in a single strain.

2) Application of Machine Learning to Reverse-Engineer Patterns. Optimizing the illumination pattern, or sequence of patterns, to achieve a desired complex topography is inherently more complicated than the forward problem simulated by FE. The use of the validated FE simulation to produce a large dataset for analysis, by an integrated machine learning (ML) and optimization algorithm, is a promising direction to reverse-engineer this process. Understanding this patterning methodology may serve as the final step necessary to practically implement mechanophotopatterning for the preparation of surface reliefs. Notably, an ML approach holds promise to design for topographies with steep features while accounting for residual forces.

7.3 Photoresist for Volumetric Additive Manufacturing (VAM)

VAM holds promise as a method to print simultaneously the entirety of a 3D part; however, improvement is needed before it is leveraged as a manufacturing technique. Since parts are printed within the volume all at once, they are susceptible to gravitational forces, and therefore only high viscosity resins or gels are viable. Further, consistency in print duration and assessment of resolution leave room for improvement. Aim 3 seeks to progress in that trajectory via the introduction of a versatile scaffolding system.

In Chapter 6, the tuning of choice of polyol within a polyurethane scaffold enabled the use of a library of low-viscosity monomers, and therefore, their thermomechanical properties. The unprinted scaffold was degraded by the aminolysis of thioester moieties with minimal damage to the printed parts. Instrumentally, the inclusion of inhibitor in the form of TEMPO was demonstrated to provide consistent print times and contrast between the desired in-part and out-of-part. Consistent 250 μm rods were patterned and isolated.

Proposed future work building on Aim 3 consists of:

1) Alternative Degradation Chemistry. The use of aminolysis to degrade thioesters has inherent limitations including the aminolysis of esters, inaccessibility of acrylate monomers, and mass extraction of the printed parts. Alternative degradable, or dynamic, chemistry may better serve the available monomer library and the final part quality. Notable options include leveraging thioester dynamics rather than degradation, as well as low-temperature dynamic chemistries, such as thiol-anhydride and boronic esters.

2) VAM Resolution Print. A resolution and critical dimension test for VAM has yet to be standardized. Although simple parts, such as rods and spheres, generally show print capacity, a part, or sequence of parts, that clearly demonstrates the consistently

achievable resolution with respect to the VAM geometry, is key to characterizing both materials and optics quality. As such, future design must account for VAM specific considerations— including the radial variation in resolution anticipated in the technique.

3) Imbedded Object and Sequential Printing. The use of a scaffold allows for the support of foreign objects within the print media. This would enable a part to be printed connected to, or around, the other object. Additionally, as prints are themselves supported, printing occurs in multiple steps to account for resolution considerations. In particular, sequential printing may provide time for inhibitor redistribution or reduce the lensing to areas of risk as parts develop.

4) Multimaterial Printing. The standard approach for variation of material properties in VAM is via greyscale printing. Alternatively, patterning of the resin itself, as enabled by a scaffold, may produce variable properties throughout a print. The necessary patterning would also increase in complexity due to variations in kinetics. Researchers interested in studying multimaterial prints also need to consider monomer diffusion resulting in variation from the initial deposition pattern.

BIBLIOGRAPHY

Accardo, J. V.; Kalow, J. A. Reversibly Tuning Hydrogel Stiffness through Photocontrolled Dynamic Covalent Crosslinks. *Chem. Sci.* **2018**, *9* (27), 5987–5993. https://doi.org/10.1039/C8SC02093K.

Accardo, J. V.; McClure, E. R.; Mosquera, M. A.; Kalow, J. A. Using Visible Light to Tune Boronic Acid–Ester Equilibria. *J. Am. Chem. Soc.* **2020**, *142* (47), 19969–19979. https://doi.org/10.1021/jacs.0c08551.

Adzima, B. J.; Kloxin, C. J.; DeForest, C. A.; Anseth, K. S.; Bowman, C. N. 3D Photofixation Lithography in Diels–Alder Networks. *Macromol. Rapid Commun.* **2012**, *33* (24), 2092–2096. https://doi.org/10.1002/marc.201200599.

Adzima, B. J.; Tao, Y.; Kloxin, C. J.; DeForest, C. A.; Anseth, K. S.; Bowman, C. N. Spatial and Temporal Control of the Alkyne–Azide Cycloaddition by Photoinitiated Cu(II) Reduction. *Nat. Chem.* **2011**, *3* (3), 256–259. https://doi.org/10.1038/nchem.980.

Ahn, D.; Stevens, L. M.; Zhou, K.; Page, Z. A. Rapid High-Resolution Visible Light 3D Printing. *ACS Cent. Sci.* **2020**, *6* (9), 1555–1563. https://doi.org/10.1021/acscentsci.0c00929.

Albini, A. Norrish' Type I and II Reactions and Their Role in the Building of Photochemical Science. *Photochem. Photobiol. Sci.* **2021**, *20* (1), 161–181. https://doi.org/10.1007/s43630-020-00003-9.

Alim, M. D.; Glugla, D. J.; Mavila, S.; Wang, C.; Nystrom, P. D.; Sullivan, A. C.; McLeod, R. R.; Bowman, C. N. High Dynamic Range (Δn) Two-Stage Photopolymers via Enhanced Solubility of a High Refractive Index Acrylate Writing Monomer. *ACS Appl. Mater. Interfaces* **2018**, *10* (1), 1217–1224. https://doi.org/10.1021/acsami.7b15063.

Allonas, X.; Lalevée, J.; Fouassier, J.-P. Investigation of Cleavage Processes in Photoinitiators: From Experiments to Molecular Modeling. *J. Photochem. Photobiol. Chem.* **2003**, *159* (2), 127–133. https://doi.org/10.1016/S1010-6030(03)00177-1.

Andreu, A.; Su, P.-C.; Kim, J.-H.; Ng, C. S.; Kim, S.; Kim, I.; Lee, J.; Noh, J.; Subramanian, A. S.; Yoon, Y.-J. 4D Printing Materials for Vat Photopolymerization. *Addit. Manuf.* **2021**, *44*, 102024. https://doi.org/10.1016/j.addma.2021.102024.

Aubert, S.; Bezagu, M.; Spivey, A. C.; Arseniyadis, S. Spatial and Temporal Control of Chemical Processes. *Nat. Rev. Chem.* **2019**, *3* (12), 706–722. https://doi.org/10.1038/s41570-019-0139-6.

Bagheri, A.; Jin, J. Photopolymerization in 3D Printing. *ACS Appl. Polym. Mater.* **2019**, *1* (4), 593–611. https://doi.org/10.1021/acsapm.8b00165.

Berg, G. J.; Gong, T.; Fenoli, C. R.; Bowman, C. N. A Dual-Cure, Solid-State Photoresist Combining a Thermoreversible Diels–Alder Network and a Chain Growth Acrylate Network. *Macromolecules* **2014**, *47* (10), 3473–3482. https://doi.org/10.1021/ma500244r.

Bhattacharya, I.; Toombs, J.; Taylor, H. High Fidelity Volumetric Additive Manufacturing. *Addit. Manuf.* **2021**, *47*, 102299. https://doi.org/10.1016/j.addma.2021.102299.

Bin Rusayyis, M. A.; Torkelson, J. M. Reprocessable and Recyclable Chain-Growth Polymer Networks Based on Dynamic Hindered Urea Bonds. *ACS Macro Lett.* **2022**, *11* (4), 568–574. https://doi.org/10.1021/acsmacrolett.2c00045.

Bond, S. G.; Ebdon, J. R. Photolysis of Vinyl Ketone Copolymers: 3. Norrish Type 1 versus Modified Norrish Type 2 Chain Scission in Some Methyl Methacrylate-Aryl Vinyl Ketone Copolymers. *Polymer* **1994**, *35* (19), 4079–4082. https://doi.org/10.1016/0032-3861(94)90578-9.

Bongiardina, N. J.; Soars, S. M.; Podgorski, M.; Bowman, C. N. Radical-Disulfide Exchange in Thiol–Ene–Disulfidation Polymerizations. *Polym. Chem.* **2022**, *13* (27), 3991–4003. https://doi.org/10.1039/D2PY00172A.

Boulden, J. E.; Cramer, N. B.; Schreck, K. M.; Couch, C. L.; Bracho-Troconis, C.; Stansbury, J. W.; Bowman, C. N. Thiol–Ene–Methacrylate Composites as Dental Restorative Materials. *Dent. Mater.* **2011**, *27* (3), 267–272. https://doi.org/10.1016/j.dental.2010.11.001.

Bracher, P. J.; Snyder, P. W.; Bohall, B. R.; Whitesides, G. M. The Relative Rates of Thiol–Thioester Exchange and Hydrolysis for Alkyl and Aryl Thioalkanoates in Water. *Orig. Life Evol. Biospheres* **2011**, *41* (5), 399–412. https://doi.org/10.1007/s11084-011-9243-4.

Brown, T. E.; Carberry, B. J.; Worrell, B. T.; Dudaryeva, O. Y.; McBride, M. K.; Bowman, C. N.; Anseth, K. S. Photopolymerized Dynamic Hydrogels with Tunable Viscoelastic Properties through Thioester Exchange. *Biomaterials* **2018**, *178*, 496–503. https://doi.org/10.1016/j.biomaterials.2018.03.060.

Capelot, M.; Unterlass, M. M.; Tournilhac, F.; Leibler, L. Catalytic Control of the Vitrimer Glass Transition. *ACS Macro Lett.* **2012**, *1* (7), 789–792. https://doi.org/10.1021/mz300239f.

Castagna, R.; Di Donato, A.; Francescangeli, O.; Lucchetta, D. E. Polymer-Based High Diffraction Efficiency and High Resolution Volume Holographic Transmission Gratings. *Chemosensors* **2022**, *10* (9), 356. https://doi.org/10.3390/chemosensors10090356.

Chappelow, C. C.; Pinzino, C. S.; Power, M. D.; Holder, A. J.; Morrill, J. A.; Jeang, L.; Eick, J. D. Photoreactivity of Vinyl Ether/Oxirane-Based Resin Systems. *J. Appl. Polym. Sci.* **2002**, *86* (2), 314–326. https://doi.org/10.1002/app.10961.

Chen, D.; Li, J.; Yuan, Y.; Gao, C.; Cui, Y.; Li, S.; Wang, H.; Peng, C.; Liu, X.; Wu, Z.; Ye, J. A New Strategy to Improve the Toughness of Epoxy Thermosets by Introducing the Thermoplastic Epoxy. *Polymer* **2022**, *240*, 124518. https://doi.org/10.1016/j.polymer.2022.124518.

Chen, D.; Ni, C.; Xie, L.; Li, Y.; Deng, S.; Zhao, Q.; Xie, T. Homeostatic Growth of Dynamic Covalent Polymer Network toward Ultrafast Direct Soft Lithography. *Sci. Adv.* **2021**, *7* (43), eabi7360. https://doi.org/10.1126/sciadv.abi7360.

Chen, F.; Gao, F.; Zhong, J.; Shen, L.; Lin, Y. Fusion of Biobased Vinylogous Urethane Vitrimers with Distinct Mechanical Properties. *Mater. Chem. Front.* **2020**, *4* (9), 2723–2730. https://doi.org/10.1039/D0QM00302F.

Chen, K.; Campbell, J. A.; Lewis, D. A. Influence of Postprinting Conditions on Morphologies in a Three-Dimensional Printable Dual-Cure Interpenetrating Dimethacrylate/Epoxy Polymer Network. *ACS Appl. Polym. Mater.* **2022**, *4* (12), 9076–9084. https://doi.org/10.1021/acsapm.2c01435.

Chen, L.; Zhang, L.; Griffin, P. J.; Rowan, S. J. Impact of Dynamic Bond Concentration on the Viscoelastic and Mechanical Properties of Dynamic Poly(Alkylurea-Co-Urethane) Networks. *Macromol. Chem. Phys.* **2020**, *221* (1), 1900440. https://doi.org/10.1002/macp.201900440.

Chen, T.; Fang, L.; Li, X.; Gao, D.; Lu, C.; Xu, Z. Self-Healing Polymer Coatings of Polyurea-Urethane/Epoxy Blends with Reversible and Dynamic Bonds. *Prog. Org. Coat.* **2020**, *147*, 105876. https://doi.org/10.1016/j.porgcoat.2020.105876.

Chen, X.; Dam, M. A.; Ono, K.; Mal, A.; Shen, H.; Nutt, S. R.; Sheran, K.; Wudl, F. A Thermally Re-Mendable Cross-Linked Polymeric Material. *Science* **2002**, *295* (5560), 1698–1702. https://doi.org/10.1126/science.1065879.

Chen, X.; Tagami, N.; Konno, H.; Nakamura, T.; Takeyama, S.; Pan, X.; Yamaguchi, M. Computational See-through Screen Camera Based on a Holographic Waveguide Device. *Opt. Express* **2022**, *30* (14), 25006–25019. https://doi.org/10.1364/OE.462111.

Colburn, W. S.; Haines, K. A. Volume Hologram Formation in Photopolymer Materials. *Appl. Opt.* **1971**, *10* (7), 1636–1641. https://doi.org/10.1364/AO.10.001636.

Colvin, V. L.; Larson, R. G.; Harris, A. L.; Schilling, M. L. Quantitative Model of Volume Hologram Formation in Photopolymers. *J. Appl. Phys.* **1997**, *81* (9), 5913–5923. https://doi.org/10.1063/1.364378.

Cook, C. C.; Fong, E. J.; Schwartz, J. J.; Porcincula, D. H.; Kaczmarek, A. C.; Oakdale, J. S.; Moran, B. D.; Champley, K. M.; Rackson, C. M.; Muralidharan, A.; McLeod, R. R.; Shusteff, M. Highly Tunable Thiol-Ene Photoresins for Volumetric Additive Manufacturing. *Adv. Mater.* **2020**, *32* (47), 2003376. https://doi.org/10.1002/adma.202003376.

Cook, W. D.; Chausson, S.; Chen, F.; Le Pluart, L.; Bowman, C. N.; Scott, T. F. Photopolymerization Kinetics, Photorheology and Photoplasticity of Thiol–Ene–

Allylic Sulfide Networks. *Polym. Int.* **2008**, *57* (3), 469–478. https://doi.org/10.1002/pi.2357.

Corrigan, N.; Li, X.; Zhang, J.; Boyer, C. Xolography for the Production of Polymeric Multimaterials. *Adv. Mater. Technol.* **2024**, *9* (15), 2400162. https://doi.org/10.1002/admt.202400162.

Corrigan, N.; Yeow, J.; Judzewitsch, P.; Xu, J.; Boyer, C. Seeing the Light: Advancing Materials Chemistry through Photopolymerization. *Angew. Chem. Int. Ed.* **2019**, *58* (16), 5170–5189. https://doi.org/10.1002/anie.201805473.

Cox, L. M.; Li, Z.; Sowan, N.; Nair, D.; Xiao, J.; Bowman, C. N.; Ding, Y. Reconfigurable Surface Patterns on Covalent Adaptive Network Polymers Using Nanoimprint Lithography. *Polymer* **2014**, *55* (23), 5933–5937. https://doi.org/10.1016/j.polymer.2014.09.024.

Cox, L. M.; Sun, X.; Wang, C.; Sowan, N.; Killgore, J. P.; Long, R.; Wu, H.-A.; Bowman, C. N.; Ding, Y. Light-Stimulated Permanent Shape Reconfiguration in Cross-Linked Polymer Microparticles. *ACS Appl. Mater. Interfaces* **2017**, *9* (16), 14422–14428. https://doi.org/10.1021/acsami.7b02759.

Cramer, N. B.; Couch, C. L.; Schreck, K. M.; Boulden, J. E.; Wydra, R.; Stansbury, J. W.; Bowman, C. N. Properties of Methacrylate–Thiol–Ene Formulations as Dental Restorative Materials. *Dent. Mater.* **2010**, *26* (8), 799–806. https://doi.org/10.1016/j.dental.2010.04.005.

Cramer, N. B.; Couch, C. L.; Schreck, K. M.; Carioscia, J. A.; Boulden, J. E.; Stansbury, J. W.; Bowman, C. N. Investigation of Thiol-Ene and Thiol-Ene–Methacrylate Based Resins as Dental Restorative Materials. *Dent. Mater.* **2010**, *26* (1), 21–28. https://doi.org/10.1016/j.dental.2009.08.004.

Davies, S.; Hu, Y.; Jiang, N.; Blyth, J.; Kaminska, M.; Liu, Y.; Yetisen, A. K. Holographic Sensors in Biotechnology. *Adv. Funct. Mater.* **2021**, *31* (47), 2105645. https://doi.org/10.1002/adfm.202105645.

de Beer, M. P.; van der Laan, H. L.; Cole, M. A.; Whelan, R. J.; Burns, M. A.; Scott, T. F. Rapid, Continuous Additive Manufacturing by Volumetric Polymerization Inhibition Patterning. *Sci. Adv.* **2019**, *5* (1), eaau8723. https://doi.org/10.1126/sciadv.aau8723.

Decker, C. Kinetic Study and New Applications of UV Radiation Curing. *Macromol. Rapid Commun.* **2002**, *23* (18), 1067–1093. https://doi.org/10.1002/marc.200290014.

Decker, C.; Masson, F.; Schwalm, R. Dual-Curing of Waterborne Urethane-Acrylate Coatings by UV and Thermal Processing. *Macromol. Mater. Eng.* **2003**, *288* (1), 17–28. https://doi.org/10.1002/mame.200290029.

del Barrio, J.; Sánchez-Somolinos, C. Light to Shape the Future: From Photolithography to 4D Printing. *Adv. Opt. Mater.* **2019**, *7* (16), 1900598. https://doi.org/10.1002/adom.201900598.

DeSimone, J. M.; Ermoshkin, A.; Ermoshkin, N.; Samulski, E. T. Continuous Liquid Interphase Printing. US9205601B2, December 8, 2015. https://patents.google.com/patent/US9205601B2/en (accessed 2025-02-02).

Dietliker, K. *A Compilation of Photoinitiators Commercially Available for UV Today*; SITA, 2002.

Dietlin, C.; Podgorska-Golubska, M.; Andrzejewska, E. The Efficiency of Photoinitiators in Ionic Liquids. *J. Photochem. Photobiol. Chem.* **2014**, *281*, 8–17. https://doi.org/10.1016/j.jphotochem.2014.03.005.

Dizon, J. R. C.; Gache, C. C. L.; Cascolan, H. M. S.; Cancino, L. T.; Advincula, R. C. Post-Processing of 3D-Printed Polymers. *Technologies* **2021**, *9* (3), 61. https://doi.org/10.3390/technologies9030061.

Engelen, S.; Dolinski, N. D.; Chen, C.; Ghimire, E.; Lindberg, C. A.; Crolais, A. E.; Nitta, N.; Winne, J. M.; Rowan, S. J.; Du Prez, F. E. Vinylogous Urea - Urethane Vitrimers: Accelerating and Inhibiting Network Dynamics through Hydrogen Bonding. *Angew. Chem. n/a* (n/a), e202318412. https://doi.org/10.1002/ange.202318412.

Fairbanks, B. D.; Singh, S. P.; Bowman, C. N.; Anseth, K. S. Photodegradable, Photoadaptable Hydrogels via Radical-Mediated Disulfide Fragmentation Reaction. *Macromolecules* **2011**, *44* (8), 2444–2450. https://doi.org/10.1021/ma200202w.

Fan, C.-J.; Wen, Z.-B.; Xu, Z.-Y.; Xiao, Y.; Wu, D.; Yang, K.-K.; Wang, Y.-Z. Adaptable Strategy to Fabricate Self-Healable and Reprocessable Poly(Thiourethane-Urethane) Elastomers via Reversible Thiol–Isocyanate Click Chemistry. *Macromolecules* **2020**, *53* (11), 4284–4293. https://doi.org/10.1021/acs.macromol.0c00239.

Fan, F.; Liu, C.; Wang, S.; Lv, J.; Li, W.; Fu, Y.; Xu, H. Swelling-Induced 3D Photopatterning on a Diselenide-Containing Elastomer. *J. Mater. Chem. C* **2019**, *7* (35), 10777–10782. https://doi.org/10.1039/C9TC03536B.

Fang, X.; Ren, H.; Gu, M. Orbital Angular Momentum Holography for High-Security Encryption. *Nat. Photonics* **2020**, *14* (2), 102–108. https://doi.org/10.1038/s41566-019-0560-x.

Faria-e-Silva, A. L.; Casselli, D. S. M.; Lima, G. S.; Ogliari, F. A.; Piva, E.; Martins, L. R. M. Kinetics of Conversion of Two Dual-Cured Adhesive Systems. *J. Endod.* **2008**, *34* (9), 1115–1118. https://doi.org/10.1016/j.joen.2008.06.016.

Fava, A.; Iliceto, A.; Camera, E. Kinetics of the Thiol-Disulfide Exchange. *J. Am. Chem. Soc.* **1957**, *79* (4), 833–838. https://doi.org/10.1021/ja01561a014.

Fenoli, C. R.; Bowman, C. N. Synthesis of Novel Trithiocarbonate and Allyl Sulfide Containing Monomers. *Polym. Chem.* **2013**, *5* (1), 62–68. https://doi.org/10.1039/C3PY00709J.

Ferrara, M. A.; Borbone, F.; Coppola, G. Holographic Optical Lenses Recorded on a Glassy Matrix-Based Photopolymer for Solar Concentrators. *Photonics* **2021**, *8* (12), 585. https://doi.org/10.3390/photonics8120585.

Flory, P. J. Molecular Size Distribution in Three Dimensional Polymers. I. Gelation1. *J. Am. Chem. Soc.* **1941**, *63* (11), 3083–3090. https://doi.org/10.1021/ja01856a061.

Flory, P. J. Molecular Size Distribution in Three Dimensional Polymers. I. Gelation1. *J. Am. Chem. Soc.* **1941**, *63* (11), 3083–3090. https://doi.org/10.1021/ja01856a061.

Foxton, R. M.; Nakajima, M.; Tagami, J.; Miura, H. Bonding of Photo and Dual-Cure Adhesives to Root Canal Dentin. *Oper. Dent.-Univ. Wash.-* **2003**, *28* (5), 543–551.

Galli, P.; Evans, R. A.; Bertarelli, C.; Bianco, A. Cyclic Allylic Sulfide Based Photopolymer for Holographic Recording Showing High Refractive Index Modulation. *J. Polym. Sci.* **2021**, *59* (13), 1399–1413. https://doi.org/10.1002/pol.20210192.

Ge, J.; Trujillo, M.; Stansbury, J. Synthesis and Photopolymerization of Low Shrinkage Methacrylate Monomers Containing Bulky Substituent Groups. *Dent. Mater.* **2005**, *21* (12), 1163–1169. https://doi.org/10.1016/j.dental.2005.02.002.

Ghaemy, M. The Polymerization Mechanism and Kinetics of DGEBA with BF3-EDA. *Eur. Polym. J.* **1998**, *34* (8), 1151–1156. https://doi.org/10.1016/S0014-3057(97)00247-4.

Griffini, G.; Invernizzi, M.; Levi, M.; Natale, G.; Postiglione, G.; Turri, S. 3D-Printable CFR Polymer Composites with Dual-Cure Sequential IPNs. *Polymer* **2016**, *91*, 174–179. https://doi.org/10.1016/j.polymer.2016.03.048.

Grigore, M. E. Methods of Recycling, Properties and Applications of Recycled Thermoplastic Polymers. *Recycling* **2017**, *2* (4), 24. https://doi.org/10.3390/recycling2040024.

Guo, B.; Wang, M.; Zhang, D.; Sun, M.; Bi, Y.; Zhao, Y. High Refractive Index Monomers for Improving the Holographic Recording Performance of Two-Stage Photopolymers. *ACS Appl. Mater. Interfaces* **2023**, *15* (20), 24827–24835. https://doi.org/10.1021/acsami.3c01446.

Guo, B.; Wang, M.; Zhang, D.; Sun, M.; Gao, H.; Bi, Y.; Zhao, Y. High-Performance Holographic Photopolymers Based on Low Refractive Index Host Matrices Containing Fluoroelastomers. *ACS Appl. Polym. Mater.* **2024**, *6* (5), 2964–2971. https://doi.org/10.1021/acsapm.3c03180.

Guzmán, D.; Ramis, X.; Fernández-Francos, X.; De la Flor, S.; Serra, A. New Bio-Based Materials Obtained by Thiol-Ene/Thiol-Epoxy Dual Curing Click Procedures from Eugenol Derivates. *Eur. Polym. J.* **2017**, *93*, 530–544. https://doi.org/10.1016/j.eurpolymj.2017.06.026.

Guzmán, D.; Ramis, X.; Fernández-Francos, X.; Serra, A. Preparation of Click Thiol-Ene/Thiol-Epoxy Thermosets by Controlled Photo/Thermal Dual Curing Sequence. *RSC Adv.* **2015**, *5* (123), 101623–101633. https://doi.org/10.1039/C5RA22055F.

Han, H.; Wang, J.; Wu, Y.; Zhang, J. Optical Realization of 360° Cylindrical Holography. *Opt. Express* **2022**, *30* (11), 19597–19610. https://doi.org/10.1364/OE.458406.

Harant, A. W.; Khire, V. S.; Thibodaux, M. S.; Bowman, C. N. Thiol−Ene Photopolymer Grafts on Functionalized Glass and Silicon Surfaces. *Macromolecules* **2006**, *39* (4), 1461–1466. https://doi.org/10.1021/ma0522007.

Hein, P. R.; Miller, H. C.; Brewster, W. D. Photopolymer for Use as a Solder Mask. US4666821A, May 19, 1987. https://patents.google.com/patent/US4666821A/en (accessed 2025-02-02).

Hiemenz, P. C.; Lodge, T. P. *Polymer Chemistry*, 2nd ed.; CRC Press: Boca Raton, 2007. https://doi.org/10.1201/9781420018271.

Hogg, P. J. Toughening of Thermosetting Composites with Thermoplastic Fibres. *Mater. Sci. Eng. A* **2005**, *412* (1), 97–103. https://doi.org/10.1016/j.msea.2005.08.028.

Hou, H.; Yin, J.; Jiang, X. Reversible Diels–Alder Reaction To Control Wrinkle Patterns: From Dynamic Chemistry to Dynamic Patterns. *Adv. Mater.* **2016**, *28* (41), 9126–9132. https://doi.org/10.1002/adma.201602105.

Hoyle, C. E.; Bowman, C. N. Thiol–Ene Click Chemistry. *Angew. Chem. Int. Ed.* **2010**, *49* (9), 1540–1573. https://doi.org/10.1002/anie.200903924.

Hoyle, C. E.; Lee, T. Y.; Roper, T. Thiol–Enes: Chemistry of the Past with Promise for the Future. *J. Polym. Sci. Part Polym. Chem.* **2004**, *42* (21), 5301–5338. https://doi.org/10.1002/pola.20366.

Hu, Y.; Kowalski, B. A.; Mavila, S.; Podgórski, M.; Sinha, J.; Sullivan, A. C.; McLeod, R. R.; Bowman, C. N. Holographic Photopolymer Material with High Dynamic Range (Δn) via Thiol–Ene Click Chemistry. *ACS Appl. Mater. Interfaces* **2020**, *12* (39), 44103–44109. https://doi.org/10.1021/acsami.0c08872.

Hu, Y.; Podgórski, M.; Mavila, S.; Sinha, J.; Fairbanks, B. D.; McLeod, R. R.; Bowman, C. N. Dynamic Polymer Binder with Light-Regulated Molecular Weight via Addition–Fragmentation Chain Transfer for Holographic Recording. *Macromolecules* **2023**, *56* (6), 2536–2541. https://doi.org/10.1021/acs.macromol.2c02334.

Hu, Y.; Trujillo-Lemon, M.; Sias, A. N.; Dobson, A. L.; Podgórski, M.; Singh, J.; Mavila, S.; McLeod, R. R.; Bowman, C. N. Reducing Haze of Holographic Gratings Recorded in a Two-Stage Photopolymer. *Macromolecules* **2025**. https://doi.org/10.1021/acs.macromol.4c02398.

Ito, T.; Okazaki, S. Pushing the Limits of Lithography. *Nature* **2000**, *406* (6799), 1027–1031. https://doi.org/10.1038/35023233.

Jariwala, A. S.; Ding, F.; Boddapati, A.; Breedveld, V.; Grover, M. A.; Henderson, C. L.; Rosen, D. W. Modeling Effects of Oxygen Inhibition in Mask-based Stereolithography. *Rapid Prototyp. J.* **2011**, *17* (3), 168–175. https://doi.org/10.1108/13552541111124734.

Karpov, G. M.; Obukhovsky, V. V.; Smirnova, T. N.; Lemeshko, V. V. Spatial Transfer of Matter as a Method of Holographic Recording in Photoformers. *Opt. Commun.* **2000**, *174* (5), 391–404. https://doi.org/10.1016/S0030-4018(99)00712-9.

Kelly, B. E.; Bhattacharya, I.; Heidari, H.; Shusteff, M.; Spadaccini, C. M.; Taylor, H. K. Volumetric Additive Manufacturing via Tomographic Reconstruction. *Science* **2019**, *363* (6431), 1075–1079. https://doi.org/10.1126/science.aau7114.

King, N.; Tay, F.; Pashley, D.; Hashimoto, M.; Ito, S.; Brackett, W.; Garcia-Godoy, F.; Sunico, M. Conversion of One-Step to Two-Step Self-Etch Adhesives for Improved Efficacy and Extended Application. *Am. J. Dent.* **2005**, *18*, 126–134.

Kloxin, C. J.; Scott, T. F.; Bowman, C. N. Stress Relaxation via Addition−Fragmentation Chain Transfer in a Thiol-Ene Photopolymerization. *Macromolecules* **2009**, *42* (7), 2551–2556. https://doi.org/10.1021/ma802771b.

Kloxin, C. J.; Scott, T. F.; Park, H. Y.; Bowman, C. N. Mechanophotopatterning on a Photoresponsive Elastomer. *Adv. Mater.* **2011**, *23* (17), 1977–1981. https://doi.org/10.1002/adma.201100323.

Kogelnik, H. Coupled Wave Theory for Thick Hologram Gratings. *Bell Syst. Tech. J.* **1969**, *48* (9), 2909–2947. https://doi.org/10.1002/j.1538-7305.1969.tb01198.x.

Kowalski, B. A.; McLeod, R. R. Design Concepts for Diffusive Holographic Photopolymers. *J. Polym. Sci. Part B Polym. Phys.* **2016**, *54* (11), 1021–1035. https://doi.org/10.1002/polb.24011.

Kuenstler, A. S.; Bowman, C. N. Catalytic Control of Crystallization in Dynamic Networks. *ACS Macro Lett.* **2023**, 133–139. https://doi.org/10.1021/acsmacrolett.2c00703.

Lawrence, J. R.; O'Neill, F. T.; Sheridan, J. T. Photopolymer Holographic Recording Material. *Optik* **2001**, *112* (10), 449–463. https://doi.org/10.1078/0030-4026-00091.

Lei, Z. Q.; Xiang, H. P.; Yuan, Y. J.; Rong, M. Z.; Zhang, M. Q. Room-Temperature Self-Healable and Remoldable Cross-Linked Polymer Based on the Dynamic Exchange of Disulfide Bonds. *Chem. Mater.* **2014**, *26* (6), 2038–2046. https://doi.org/10.1021/cm4040616.

Li, B.; Wang, J.; Chen, C.; Li, Y.; Yang, R.; Chen, N. Spherical Self-Diffraction for Speckle Suppression of a Spherical Phase-Only Hologram. *Opt. Express* **2020**, *28* (21), 31373–31385. https://doi.org/10.1364/OE.401679.

Li, J.; Li, T.; Ma, X.; Su, Z.; Yin, J.; Jiang, X. Light-Induced Programmable 2D Ordered Patterns Based on a Hyperbranched Poly(Ether Amine) (hPEA)-Functionalized

Graphene Film. *ACS Appl. Mater. Interfaces* **2021**, *13* (1), 1704–1713. https://doi.org/10.1021/acsami.0c15099.

Lian, Q.; Yang, F.; Xin, H.; Li, D. Oxygen-Controlled Bottom-up Mask-Projection Stereolithography for Ceramic 3D Printing. *Ceram. Int.* **2017**, *43* (17), 14956–14961. https://doi.org/10.1016/j.ceramint.2017.08.014.

Liang, S.; Yan, P.-Y.; Zhang, G. High Performance EUV Mask. US20040126670A1, July 1, 2004. https://patents.google.com/patent/US20040126670A1/en (accessed 2025-02-02).

Ligon, S. C.; Liska, R.; Stampfl, J.; Gurr, M.; Mülhaupt, R. Polymers for 3D Printing and Customized Additive Manufacturing. *Chem. Rev.* **2017**, *117* (15), 10212–10290. https://doi.org/10.1021/acs.chemrev.7b00074.

Lim, K. T. P.; Liu, H.; Liu, Y.; Yang, J. K. W. Holographic Colour Prints for Enhanced Optical Security by Combined Phase and Amplitude Control. *Nat. Commun.* **2019**, *10* (1), 25. https://doi.org/10.1038/s41467-018-07808-4.

Lin, J.-T.; Cheng, D.-C.; Chen, K.-T.; Liu, H.-W. Dual-Wavelength (UV and Blue) Controlled Photopolymerization Confinement for 3D-Printing: Modeling and Analysis of Measurements. *Polymers* **2019**, *11* (11), 1819. https://doi.org/10.3390/polym11111819.

Long, K. N.; Scott, T. F.; Jerry Qi, H.; Bowman, C. N.; Dunn, M. L. Photomechanics of Light-Activated Polymers. *J. Mech. Phys. Solids* **2009**, *57* (7), 1103–1121. https://doi.org/10.1016/j.jmps.2009.03.003.

Long, R.; Qi, H. J.; Dunn, M. L. Thermodynamics and Mechanics of Photochemcially Reacting Polymers. *J. Mech. Phys. Solids* **2013**, *61* (11), 2212–2239. https://doi.org/10.1016/j.jmps.2013.06.008.

Loterie, D.; Delrot, P.; Moser, C. High-Resolution Tomographic Volumetric Additive Manufacturing. *Nat. Commun.* **2020**, *11* (1), 852. https://doi.org/10.1038/s41467-020-14630-4.

Lu, H.; Carioscia, J. A.; Stansbury, J. W.; Bowman, C. N. Investigations of Step-Growth Thiol-Ene Polymerizations for Novel Dental Restoratives. *Dent. Mater.* **2005**, *21* (12), 1129–1136. https://doi.org/10.1016/j.dental.2005.04.001.

Lyon, G. B.; Cox, L. M.; Goodrich, J. T.; Baranek, A. D.; Ding, Y.; Bowman, C. N. Remoldable Thiol–Ene Vitrimers for Photopatterning and Nanoimprint Lithography. *Macromolecules* **2016**, *49* (23), 8905–8913. https://doi.org/10.1021/acs.macromol.6b01281.

Ma, S. J.; Mannino, S. J.; Wagner, N. J.; Kloxin, C. J. Photodirected Formation and Control of Wrinkles on a Thiol–Ene Elastomer. *ACS Macro Lett.* **2013**, *2* (6), 474–477. https://doi.org/10.1021/mz400166e.

Maafa, I. M. Inhibition of Free Radical Polymerization: A Review. *Polymers* **2023**, *15* (3), 488. https://doi.org/10.3390/polym15030488.

Madrid-Wolff, J.; Toombs, J.; Rizzo, R.; Bernal, P. N.; Porcincula, D.; Walton, R.; Wang, B.; Kotz-Helmer, F.; Yang, Y.; Kaplan, D.; Zhang, Y. S.; Zenobi-Wong, M.; McLeod, R. R.; Rapp, B.; Schwartz, J.; Shusteff, M.; Talyor, H.; Levato, R.; Moser, C. A Review of Materials Used in Tomographic Volumetric Additive Manufacturing. *MRS Commun.* **2023**, *13* (5), 764–785. https://doi.org/10.1557/s43579-023-00447-x.

Medel, S.; Bosch, P.; Grabchev, I.; Shah, P. K.; Liu, J.; Aguirre-Soto, A.; Stansbury, J. W. Simultaneous Measurement of Fluorescence, Conversion and Physical/Mechanical Properties for Monitoring Bulk and Localized Photopolymerization Reactions in Heterogeneous Systems. *RSC Adv.* **2016**, *6* (47), 41275–41286. https://doi.org/10.1039/C6RA06341A.

Mei, B.; Evans, C. M.; Schweizer, K. S. Self-Consistent Theory for Structural Relaxation, Dynamic Bond Exchange Times, and the Glass Transition in Polymeric Vitrimers. *Macromolecules* **2024**. https://doi.org/10.1021/acs.macromol.4c00038.

Mikulchyk, T.; Oubaha, M.; Kaworek, A.; Duffy, B.; Lunzer, M.; Ovsianikov, A.; E-Gul, S.-; Naydenova, I.; Cody, D. Synthesis of Fast Curing, Water-Resistant and Photopolymerizable Glass for Recording of Holographic Structures by One- and Two-Photon Lithography. *Adv. Opt. Mater.* **2022**, *10* (6), 2102089. https://doi.org/10.1002/adom.202102089.

Miller, D. B.; Alim, M. D.; McLeod, R. R. Reflection Suppression via Elastomeric Films. *Opt. Lett.* **2019**, *44* (24), 6021. https://doi.org/10.1364/OL.44.006021.

Mitra, J.; Tripathi, G.; Sharma, A.; Basu, B. Scaffolds for Bone Tissue Engineering: Role of Surface Patterning on Osteoblast Response. *RSC Adv.* **2013**, *3* (28), 11073–11094. https://doi.org/10.1039/C3RA23315D.

Mochulsky, M.; Tobolsky, A. V. Chemorheology of Polysulfide Rubbers. *Ind. Eng. Chem.* **1948**, *40* (11), 2155–2163. https://doi.org/10.1021/ie50467a030.

Moharam, M. G.; Young, L. Criterion for Bragg and Raman-Nath Diffraction Regimes. *Appl. Opt.* **1978**, *17* (11), 1757. https://doi.org/10.1364/AO.17.001757.

Montarnal, D.; Capelot, M.; Tournilhac, F.; Leibler, L. Silica-Like Malleable Materials from Permanent Organic Networks. *Science* **2011**, *334* (6058), 965–968. https://doi.org/10.1126/science.1212648.

Nair, D. P.; Cramer, N. B.; Gaipa, J. C.; McBride, M. K.; Matherly, E. M.; McLeod, R. R.; Shandas, R.; Bowman, C. N. Two-Stage Reactive Polymer Network Forming Systems. *Adv. Funct. Mater.* **2012**, *22* (7), 1502–1510. https://doi.org/10.1002/adfm.201102742.

Narayanan, J.; Jungman, M. J.; Patton, D. L. Hybrid Dual-Cure Polymer Networks via Sequential Thiol–Ene Photopolymerization and Thermal Ring-Opening Polymerization of Benzoxazines. *React. Funct. Polym.* **2012**, *72* (11), 799–806. https://doi.org/10.1016/j.reactfunctpolym.2012.07.012.

Nguyen, P. Q. M.; Yeo, L.-P.; Lok, B.-K.; Lam, Y.-C. Patterned Surface with Controllable Wettability for Inkjet Printing of Flexible Printed Electronics. *ACS Appl. Mater. Interfaces* **2014**, *6* (6), 4011–4016. https://doi.org/10.1021/am4054546.

O'Brien, A. K.; Bowman, C. N. Impact of Oxygen on Photopolymerization Kinetics and Polymer Structure. *Macromolecules* **2006**, *39* (7), 2501–2506. https://doi.org/10.1021/ma051863l.

Odian, G. Radical Chain Polymerization. In *Principles of Polymerization*; John Wiley & Sons, Ltd, 2004; pp 199–349. https://doi.org/10.1002/047147875X.ch2.

Oh, M. S.; Lee, J. H.; Hong, C.; Lee, H.-N.; Kim, C. K. Development of Photolithography Process for Printed Circuit Board Using Liquid Crystal Mask in Place of Photomask. *Jpn. J. Appl. Phys.* **2012**, *51* (9S2), 09MF16. https://doi.org/10.1143/JJAP.51.09MF16.

Orth, A.; Webber, D.; Zhang, Y.; Sampson, K. L.; de Haan, H. W.; Lacelle, T.; Lam, R.; Solis, D.; Dayanandan, S.; Waddell, T.; Lewis, T.; Taylor, H. K.; Boisvert, J.; Paquet, C. Deconvolution Volumetric Additive Manufacturing. *Nat. Commun.* **2023**, *14* (1), 4412. https://doi.org/10.1038/s41467-023-39886-4.

Osterbaan, A. J.; Trujillo-Lemon, M.; Seymour, G. T.; Mora, Z. R.; McLeod, R. R.; Bowman, C. N. Dual-Cure Dynamic Networks for Mechanophotopatterning of Surface Topography. *Macromolecules* **2025**, *58* (4), 1975–1981. https://doi.org/10.1021/acs.macromol.4c03018.

Paral, S. K.; Lin, D.-Z.; Cheng, Y.-L.; Lin, S.-C.; Jeng, J.-Y. A Review of Critical Issues in High-Speed Vat Photopolymerization. *Polymers* **2023**, *15* (12), 2716. https://doi.org/10.3390/polym15122716.

Park, C.-H.; Lee, S.-W.; Park, J.-W.; Kim, H.-J. Preparation and Characterization of Dual Curable Adhesives Containing Epoxy and Acrylate Functionalities. *React. Funct. Polym.* **2013**, *73* (4), 641–646. https://doi.org/10.1016/j.reactfunctpolym.2013.01.012.

Park, H. Y.; Kloxin, C. J.; Abuelyaman, A. S.; Oxman, J. D.; Bowman, C. N. Stress Relaxation via Addition–Fragmentation Chain Transfer in High Tg, High Conversion Methacrylate-Based Systems. *Macromolecules* **2012**, *45* (14), 5640–5646. https://doi.org/10.1021/ma300228z.

Park, H. Y.; Kloxin, C. J.; Scott, T. F.; Bowman, C. N. Covalent Adaptable Networks as Dental Restorative Resins: Stress Relaxation by Addition–Fragmentation Chain Transfer in Allyl Sulfide-Containing Resins. *Dent. Mater.* **2010**, *26* (10), 1010–1016. https://doi.org/10.1016/j.dental.2010.06.007.

Patel, T.; Oh, J. K. Dynamic Covalent Adaptive Polymer Network Materials Based on Hindered Urea Bonds. *J. Macromol. Sci. Part A* **2023**, *0* (0), 1–14. https://doi.org/10.1080/10601325.2023.2206860.

Pei, Z.; Yang, Y.; Chen, Q.; Wei, Y.; Ji, Y. Regional Shape Control of Strategically Assembled Multishape Memory Vitrimers. *Adv. Mater.* **2016**, *28* (1), 156–160. https://doi.org/10.1002/adma.201503789.

Peng, H.; Nair, D. P.; Kowalski, B. A.; Xi, W.; Gong, T.; Wang, C.; Cole, M.; Cramer, N. B.; Xie, X.; McLeod, R. R.; Bowman, C. N. High Performance Graded Rainbow Holograms via Two-Stage Sequential Orthogonal Thiol–Click Chemistry. *Macromolecules* **2014**, *47* (7), 2306–2315. https://doi.org/10.1021/ma500167x.

Pi, H.; Li, W.; Shi, Z.; Chen, H.; Jiang, X. Effect of Monomers on the Holographic Properties of Poly(Vinyl Alcohol)-Based Photopolymers. *ACS Appl. Polym. Mater.* **2020**, *2* (11), 5208–5218. https://doi.org/10.1021/acsapm.0c00960.

Pinner, S. H. Functionality of Non-Equivalent Mixtures. *J. Polym. Sci.* **1956**, *21* (97), 153–157. https://doi.org/10.1002/pol.1956.120219718.

Podgórski, M.; Fairbanks, B. D.; Kirkpatrick, B. E.; McBride, M.; Martinez, A.; Dobson, A.; Bongiardina, N. J.; Bowman, C. N. Toward Stimuli-Responsive Dynamic Thermosets through Continuous Development and Improvements in Covalent Adaptable Networks (CANs). *Adv. Mater.* **2020**, *32* (20), 1906876. https://doi.org/10.1002/adma.201906876.

Podgórski, M.; Nair, D. P.; Chatani, S.; Berg, G.; Bowman, C. N. Programmable Mechanically Assisted Geometric Deformations of Glassy Two-Stage Reactive Polymeric Materials. *ACS Appl. Mater. Interfaces* **2014**, *6* (9), 6111–6119. https://doi.org/10.1021/am405371r.

Pricci, A.; de Tullio, M. D.; Percoco, G. Analytical and Numerical Models of Thermoplastics: A Review Aimed to Pellet Extrusion-Based Additive Manufacturing. *Polymers* **2021**, *13* (18), 3160. https://doi.org/10.3390/polym13183160.

Priest, C. Surface Patterning of Bonded Microfluidic Channels. *Biomicrofluidics* **2010**, *4* (3), 032206. https://doi.org/10.1063/1.3493643.

Rånby, B. Photodegradation and Photo-Oxidation of Synthetic Polymers. *J. Anal. Appl. Pyrolysis* **1989**, *15*, 237–247. https://doi.org/10.1016/0165-2370(89)85037-5.

Regehly, M.; Garmshausen, Y.; Reuter, M.; König, N. F.; Israel, E.; Kelly, D. P.; Chou, C.-Y.; Koch, K.; Asfari, B.; Hecht, S. Xolography for Linear Volumetric 3D Printing. *Nature* **2020**, *588* (7839), 620–624. https://doi.org/10.1038/s41586-020-3029-7.

Ren, G.; Wang, L.; Chen, Q.; Xu, Z.; Xu, J.; Sun, D. pH Switchable Emulsions Based on Dynamic Covalent Surfactants. *Langmuir* **2017**, *33* (12), 3040–3046. https://doi.org/10.1021/acs.langmuir.6b04546.

Romeo, A.; Lacour, S. P. Concurrent Photopatterning of Elastic Modulus and Structures in Photosensitive Silicone Elastomers. *Extreme Mech. Lett.* **2015**, *3*, 1–7. https://doi.org/10.1016/j.eml.2015.04.002.

Rossegger, E.; Höller, R.; Reisinger, D.; Strasser, J.; Fleisch, M.; Griesser, T.; Schlögl, S. Digital Light Processing 3D Printing with Thiol–Acrylate Vitrimers. *Polym. Chem.* **2021**, *12* (5), 639–644. https://doi.org/10.1039/D0PY01520B.

Ruiz de Luzuriaga, A.; Solera, G.; Azcarate-Ascasua, I.; Boucher, V.; Grande, H.-J.; Rekondo, A. Chemical Control of the Aromatic Disulfide Exchange Kinetics for Tailor-Made Epoxy Vitrimers. *Polymer* **2022**, *239*, 124457. https://doi.org/10.1016/j.polymer.2021.124457.

Sabel, T.; Lensen, M. C.; Sabel, T.; Lensen, M. C. Volume Holography: Novel Materials, Methods and Applications. In *Holographic Materials and Optical Systems*; IntechOpen, 2017. https://doi.org/10.5772/67001.

Salajeghe, R.; Meile, D. H.; Kruse, C. S.; Marla, D.; Spangenberg, J. Numerical Modeling of Part Sedimentation during Volumetric Additive Manufacturing. *Addit. Manuf.* **2023**, *66*, 103459. https://doi.org/10.1016/j.addma.2023.103459.

Saleh Alghamdi, S.; John, S.; Roy Choudhury, N.; Dutta, N. K. Additive Manufacturing of Polymer Materials: Progress, Promise and Challenges. *Polymers* **2021**, *13* (5), 753. https://doi.org/10.3390/polym13050753.

Saleh, B. E. A.; Teich, M. C. *Fundamentals of Photonics*; John Wiley & Sons, 2019.

Sang, X.; Fan, F. C.; Choi, S.; Jiang, C.; Yu, C.; Yan, B.; Dou, W. Three-Dimensional Display Based on the Holographic Functional Screen. *Opt. Eng.* **2011**, *50* (9), 091303. https://doi.org/10.1117/1.3596176.

Schäfer, C.; Meyer, S. P.; Osswald, T. A. A Novel Extrusion Process for the Production of Polymer Micropellets. *Polym. Eng. Sci.* **2018**, *58* (12), 2264–2275. https://doi.org/10.1002/pen.24847.

Schowengerdt, B. Materials and Process Considerations for AR Glasses. In *Advances in Patterning Materials and Processes XLI*; SPIE, 2024; Vol. 12957, p 129570E. https://doi.org/10.1117/12.3012902.

Schwartz, J. J.; Boydston, A. J. Multimaterial Actinic Spatial Control 3D and 4D Printing. *Nat. Commun.* **2019**, *10* (1), 791. https://doi.org/10.1038/s41467-019-08639-7.

Seymour, G.; McLeod, R. R. Detection and Correction of Misalignment for High Fidelity Volumetric Additive Manufacturing. *Opt. Express* **2025**, *33* (4), 6894–6908. https://doi.org/10.1364/OE.540200.

Shah, P. K.; Stansbury, J. W.; Bowman, C. N. Application of an Addition–Fragmentation-Chain Transfer Monomer in Di(Meth)Acrylate Network Formation to Reduce Polymerization Shrinkage Stress. *Polym. Chem.* **2017**, *8* (30), 4339–4351. https://doi.org/10.1039/C7PY00702G.

Sheridan, J. T.; Lawrence, J. R. Nonlocal-Response Diffusion Model of Holographic Recording in Photopolymer. *JOSA A* **2000**, *17* (6), 1108–1114. https://doi.org/10.1364/JOSAA.17.001108.

Shim, J. S.; Lee, S. Y.; Song, S.-Y.; Jha, N.; Ryu, J. J. Polymerization Efficiency of Dental Dual-Cured Resin Cement Light-Cured at Various Times after the

Initiation of Chemical Activation. *Int. J. Polym. Mater. Polym. Biomater.* **2020**, *69* (10), 622–628. https://doi.org/10.1080/00914037.2019.1596912.

Shin, S.; Kwon, Y.; Hwang, C.; Jeon, W.; Yu, Y.; Paik, H.-J.; Lee, W.; Kwon, M. S.; Ahn, D. Visible-Light-Driven Rapid 3D Printing of Photoresponsive Resins for Optically Clear Multifunctional 3D Objects. *Adv. Mater.* **2024**, *36* (19), 2311917. https://doi.org/10.1002/adma.202311917.

Shore, B. W.; Perry, M. D.; Britten, J. A.; Boyd, R. D.; Feit, M. D.; Nguyen, H. T.; Chow, R.; Loomis, G. E.; Li, L. Design of High-Efficiency Dielectric Reflection Gratings. *JOSA A* **1997**, *14* (5), 1124–1136. https://doi.org/10.1364/JOSAA.14.001124.

Shusteff, M.; Browar, A. E. M.; Kelly, B. E.; Henriksson, J.; Weisgraber, T. H.; Panas, R. M.; Fang, N. X.; Spadaccini, C. M. One-Step Volumetric Additive Manufacturing of Complex Polymer Structures. *Sci. Adv.* **2017**, *3* (12), eaao5496. https://doi.org/10.1126/sciadv.aao5496.

Soman, B.; Evans, C. M. Effect of Precise Linker Length, Bond Density, and Broad Temperature Window on the Rheological Properties of Ethylene Vitrimers. *Soft Matter* **2020**. https://doi.org/10.1039/D0SM01544J.

Somers, P.; Münchinger, A.; Maruo, S.; Moser, C.; Xu, X.; Wegener, M. The Physics of 3D Printing with Light. *Nat. Rev. Phys.* **2024**, *6* (2), 99–113. https://doi.org/10.1038/s42254-023-00671-3.

Sowan, N.; Lu, Y.; Kolb, K. J.; Cox, L. M.; Long, R.; Bowman, C. N. Enhancing the Toughness of Composites via Dynamic Thiol–Thioester Exchange (TTE) at the Resin–Filler Interface. *Polym. Chem.* **2020**, *11* (29), 4760–4767. https://doi.org/10.1039/D0PY00563K.

Sowan, N.; Song, H. B.; Cox, L. M.; Patton, J. R.; Fairbanks, B. D.; Ding, Y.; Bowman, C. N. Light-Activated Stress Relaxation, Toughness Improvement, and Photoinduced Reversal of Physical Aging in Glassy Polymer Networks. *Adv. Mater.* **2021**, *33* (5), 2007221. https://doi.org/10.1002/adma.202007221.

Standard, A. D638-02a. *Stand. Test Method Tensile Prop. Plast. West Conshohocken PA USA ASTM Int.* **2002**.

Stockmayer, W. H. Molecular Distribution in Condensation Polymers. *J. Polym. Sci.* **1952**, *9* (1), 69–71. https://doi.org/10.1002/pol.1952.120090106.

Stockmayer, W. H. Theory of Molecular Size Distribution and Gel Formation in Branched Polymers II. General Cross Linking. *J. Chem. Phys.* **1944**, *12* (4), 125–131. https://doi.org/10.1063/1.1723922.

Studer, K.; Decker, C.; Beck, E.; Schwalm, R. Thermal and Photochemical Curing of Isocyanate and Acrylate Functionalized Oligomers. *Eur. Polym. J.* **2005**, *41* (1), 157–167. https://doi.org/10.1016/j.eurpolymj.2004.09.004.

Stüwe, L.; Geiger, M.; Röllgen, F.; Heinze, T.; Reuter, M.; Wessling, M.; Hecht, S.; Linkhorst, J. Continuous Volumetric 3D Printing: Xolography in Flow. *Adv. Mater.* **2024**, *36* (4), 2306716. https://doi.org/10.1002/adma.202306716.

Sun, X.; Wu, H.; Long, R. Thermomechanics of a Temperature Sensitive Covalent Adaptable Polymer with Bond Exchange Reactions. *Soft Matter* **2016**, *12* (43), 8847–8860. https://doi.org/10.1039/C6SM01857B.

Sun, X.; Yue, L.; Yu, L.; Forte, C. T.; Armstrong, C. D.; Zhou, K.; Demoly, F.; Zhao, R. R.; Qi, H. J. Machine Learning-Enabled Forward Prediction and Inverse Design of 4D-Printed Active Plates. *Nat. Commun.* **2024**, *15* (1), 5509. https://doi.org/10.1038/s41467-024-49775-z.

Sun, X.; Yue, L.; Yu, L.; Shao, H.; Peng, X.; Zhou, K.; Demoly, F.; Zhao, R.; Qi, H. J. Machine Learning-Evolutionary Algorithm Enabled Design for 4D-Printed Active Composite Structures. *Adv. Funct. Mater.* **2022**, *32* (10), 2109805. https://doi.org/10.1002/adfm.202109805.

P. Sutherland, B.; Kabra, M.; J. Kloxin, C. Expanding the Thiol–X Toolbox: Photoinitiation and Materials Application of the Acid-Catalyzed Thiol–Ene (ACT) Reaction. *Polym. Chem.* **2021**, *12* (10), 1562–1570. https://doi.org/10.1039/D0PY01593H.

T. Worrell, B.; Mavila, S.; Wang, C.; M. Kontour, T.; Lim, C.-H.; K. McBride, M.; B. Musgrave, C.; Shoemaker, R.; N. Bowman, C. A User's Guide to the Thiol-Thioester Exchange in Organic Media: Scope, Limitations, and Applications in Material Science. *Polym. Chem.* **2018**, *9* (36), 4523–4534. https://doi.org/10.1039/C8PY01031E.

Tan, L. J.; Zhu, W.; Zhou, K. Recent Progress on Polymer Materials for Additive Manufacturing. *Adv. Funct. Mater.* **2020**, *30* (43), 2003062. https://doi.org/10.1002/adfm.202003062.

Tauk, L.; Schröder, A. P.; Decher, G.; Giuseppone, N. Hierarchical Functional Gradients of pH-Responsive Self-Assembled Monolayers Using Dynamic Covalent Chemistry on Surfaces. *Nat. Chem.* **2009**, *1* (8), 649–656. https://doi.org/10.1038/nchem.400.

Toombs, J. T.; Shan, I. K.; Taylor, H. K. Ethyl Cellulose-Based Thermoreversible Organogel Photoresist for Sedimentation-Free Volumetric Additive Manufacturing. *Macromol. Rapid Commun.* **2023**, *44* (7), 2200872. https://doi.org/10.1002/marc.202200872.

Trentler, T. J.; Boyd, J. E.; Colvin, V. L. Epoxy Resin−Photopolymer Composites for Volume Holography. *Chem. Mater.* **2000**, *12* (5), 1431–1438. https://doi.org/10.1021/cm9908062.

Tumbleston, J. R.; Shirvanyants, D.; Ermoshkin, N.; Janusziewicz, R.; Johnson, A. R.; Kelly, D.; Chen, K.; Pinschmidt, R.; Rolland, J. P.; Ermoshkin, A.; Samulski, E. T.; DeSimone, J. M. Continuous Liquid Interface Production of 3D Objects. *Science* **2015**, *347* (6228), 1349–1352. https://doi.org/10.1126/science.aaa2397.

Uchida, N. Calculation of Diffraction Efficiency in Hologram Gratings Attenuated along the Direction Perpendicular to the Grating Vector. *J. Opt. Soc. Am.* **1973**, *63* (3), 280. https://doi.org/10.1364/JOSA.63.000280.

Unruh, C. C.; Leubner, G. W.; Smith, J. A. C. Light-Sensitive Polymers for Making Printing Plates. US2861058A, November 18, 1958. https://patents.google.com/patent/US2861058A/en (accessed 2025-02-02).

van der Laan, H. L.; Burns, M. A.; Scott, T. F. Volumetric Photopolymerization Confinement through Dual-Wavelength Photoinitiation and Photoinhibition. *ACS Macro Lett.* **2019**, *8* (8), 899–904. https://doi.org/10.1021/acsmacrolett.9b00412.

Vernerey, F. J.; Long, R.; Brighenti, R. A Statistically-Based Continuum Theory for Polymers with Transient Networks. *J. Mech. Phys. Solids* **2017**, *107*, 1–20. https://doi.org/10.1016/j.jmps.2017.05.016.

Wang, C.; Mavila, S.; Worrell, B. T.; Xi, W.; Goldman, T. M.; Bowman, C. N. Productive Exchange of Thiols and Thioesters to Form Dynamic Polythioester-Based Polymers. *ACS Macro Lett.* **2018**, *7* (11), 1312–1316. https://doi.org/10.1021/acsmacrolett.8b00611.

Wang, Q.; Yuan, G. H.; Kiang, K. S.; Sun, K.; Gholipour, B.; Rogers, E. T. F.; Huang, K.; Ang, S. S.; Zheludev, N. I.; Teng, J. H. Reconfigurable Phase-Change Photomask for Grayscale Photolithography. *Appl. Phys. Lett.* **2017**, *110* (20), 201110. https://doi.org/10.1063/1.4983198.

Wang, S.; Li, B.; Zheng, J.; Surat'man, N. E. B.; Wu, J.; Wang, N.; Xu, X.; Zhu, J.; Loh, X. J.; Li, Z. Nanotechnology in Covalent Adaptable Networks: From Nanocomposites to Surface Patterning. *ACS Mater. Lett.* **2023**, *5* (2), 608–628. https://doi.org/10.1021/acsmaterialslett.2c01083.

Weisgraber, T. H.; de Beer, M. P.; Huang, S.; Karnes, J. J.; Cook, C. C.; Shusteff, M. Virtual Volumetric Additive Manufacturing (VirtualVAM). *Adv. Mater. Technol.* **2023**, *8* (23), 2301054. https://doi.org/10.1002/admt.202301054.

Whyte, D. J.; Doeven, E. H.; Sutti, A.; Kouzani, A. Z.; Adams, S. D. Volumetric Additive Manufacturing: A New Frontier in Layer-Less 3D Printing. *Addit. Manuf.* **2024**, *84*, 104094. https://doi.org/10.1016/j.addma.2024.104094.

Wiechert, E. *Ueber elastische Nachwirkung*; Druck von Hartung, 1889.

Worrell, B. T.; McBride, M. K.; Lyon, G. B.; Cox, L. M.; Wang, C.; Mavila, S.; Lim, C.-H.; Coley, H. M.; Musgrave, C. B.; Ding, Y.; Bowman, C. N. Bistable and Photoswitchable States of Matter. *Nat. Commun.* **2018**, *9* (1), 2804. https://doi.org/10.1038/s41467-018-05300-7.

Xi, W.; Peng, H.; Aguirre-Soto, A.; Kloxin, C. J.; Stansbury, J. W.; Bowman, C. N. Spatial and Temporal Control of Thiol-Michael Addition via Photocaged Superbase in Photopatterning and Two-Stage Polymer Networks Formation. *Macromolecules* **2014**, *47* (18), 6159–6165. https://doi.org/10.1021/ma501366f.

Xiong, J.; Yin, K.; Li, K.; Wu, S.-T. Holographic Optical Elements for Augmented Reality: Principles, Present Status, and Future Perspectives. *Adv. Photonics Res.* **2021**, *2* (1), 2000049. https://doi.org/10.1002/adpr.202000049.

Yang, D.; Shi, Y.; Yu, X. Photomask and Photoresist. In *Handbook of Integrated Circuit Industry*; Wang, Y., Chi, M.-H., Lou, J. J.-C., Chen, C.-Z., Eds.; Springer Nature: Singapore, 2024; pp 1717–1742. https://doi.org/10.1007/978-981-99-2836-1_78.

Yang, S.; Zhang, Y.-W.; Zeng, K. Analysis of Nanoindentation Creep for Polymeric Materials. *J. Appl. Phys.* **2004**, *95* (7), 3655–3666. https://doi.org/10.1063/1.1651341.

Yavitt, F. M.; Brown, T. E.; Hushka, E. A.; Brown, M. E.; Gjorevski, N.; Dempsey, P. J.; Lutolf, M. P.; Anseth, K. S. The Effect of Thiol Structure on Allyl Sulfide Photodegradable Hydrogels and Their Application as a Degradable Scaffold for Organoid Passaging. *Adv. Mater.* **2020**, *32* (30), 1905366. https://doi.org/10.1002/adma.201905366.

Yetisen, A. K. The Prospects for Holographic Sensors. In *Holographic Sensors*; Yetisen, A. K., Ed.; Springer International Publishing: Cham, 2015; pp 149–162. https://doi.org/10.1007/978-3-319-13584-7_7.

Yu, L.; Sun, X.; Jin, Y.; Zhang, W.; Long, R. Mechanics of Vitrimer Particle Compression and Fusion under Heat Press. *Int. J. Mech. Sci.* **2021**, *201*, 106466. https://doi.org/10.1016/j.ijmecsci.2021.106466.

Yue, L.; Kuang, X.; Sun, X.; Qi, H. J. Chapter 15 - Recyclable Thermoset Polymers: Beyond Self-Healing. In *Recent Advances in Smart Self-Healing Polymers and Composites (Second Edition)*; Li, G., Feng, X., Eds.; Woodhead Publishing Series in Composites Science and Engineering; Woodhead Publishing, 2022; pp 483–511. https://doi.org/10.1016/B978-0-12-823472-3.00012-6.

Zeng, X.; Liu, G.; Tao, W.; Ma, Y.; Zhang, X.; He, F.; Pan, J.; Mei, L.; Pan, G. A Drug-Self-Gated Mesoporous Antitumor Nanoplatform Based on pH-Sensitive Dynamic Covalent Bond. *Adv. Funct. Mater.* **2017**, *27* (11), 1605985. https://doi.org/10.1002/adfm.201605985.

Zhang, S.; Yan, L.; Altman, M.; Lässle, M.; Nugent, H.; Frankel, F.; Lauffenburger, D. A.; Whitesides, G. M.; Rich, A. Biological Surface Engineering: A Simple System for Cell Pattern Formation. *Biomaterials* **1999**, *20* (13), 1213–1220. https://doi.org/10.1016/S0142-9612(99)00014-9.

Zhang, X.; Xi, W.; Huang, S.; Long, K.; Bowman, C. N. Wavelength-Selective Sequential Polymer Network Formation Controlled with a Two-Color Responsive Initiation System. *Macromolecules* **2017**, *50* (15), 5652–5660. https://doi.org/10.1021/acs.macromol.7b01117.

Zhang, Y.; de Haan, H.; Houlahan, K.; Sampson, K. L.; Webber, D.; Orth, A.; Lacelle, T.; Gaburici, L.; Lam, R.; Deore, B.; Paquet, C. Impact of Oxygen Inhibition on

Acrylate Photopolymerization in Tomographic Volumetric Printing. Social Science Research Network: Rochester, NY February 26, 2025. https://doi.org/10.2139/ssrn.5157227.

Zhao, G.; Mouroulis, P. Diffusion Model of Hologram Formation in Dry Photopolymer Materials. *J. Mod. Opt.* **1994**, *41* (10), 1929–1939. https://doi.org/10.1080/09500349414551831.

Appendix: Shedding Light on the Reproducibility Crisis Surrounding Photo-Induced Processes

Meagan N. Arguien and Alexander J. Osterbaan with the following co-authors:

Adam L. Dobson, Zachary R. Mora, Andrew N. Sias, Dyuti Chakraborty, Mohammed N. Khan, William Rears, Benjamin D. Fairbanks, Sean P. Keyser, Lois Asiedua-Ahenkorah, Christopher J. Kloxin, Timothy F. Scott, Robert R. McLeod, and Christopher N. Bowman

A1 Abstract

A critical issue that currently exists in scientific publications is reproducibility of content. This problem is particularly present in literature containing photo-induced processes. 150 articles published in a variety of journals (impact factor > 4.0) from the disciplines “polymer chemistry,” “organic chemistry,” and “physics,” as assigned by Web of Science, were assessed for photo reproducibility. The conditions assessed for reproducibility included the photo conditions (light source emission spectra, light source intensity, duration of light exposure), sample geometry (surface/ boundary layers and sample thickness), and sample composition (active chromophore description, amount of active chromophore, and other absorbing species). From this analysis, it was determined that only 52% in polymer science, 40% in chemistry, and 56% in physics literature, were determined to be reproducible with regards to the spectrum of the light source, highlighting the reproducibility issue. An explanation is provided herein for why each of the assessment points are critical for successful reproduction of a photo-induced process as well as modeling that illustrates the variance photo-process derived properties that ensues from ambiguous conditions.

A2 Introduction

As outlined in Monya Baker's Nature article, "1,500 scientists lift the lid on reproducibility," a critical issue exists in the reproducibility of scientific literature.[1] This issue is particularly problematic and prominent in publications pertaining to light induced processes. While a thermal process requires primarily just a temperature to be reproducible, a photodriven process requires emission spectra, light intensity, exposure duration, sample thickness and geometry, sample boundary conditions, initiator description and concentration, and the absorbance of other species, at a minimum, to facilitate reproducibility.

According to Web of Science, between 2000 and 2020 there was an increase of more than 700% in papers published pertaining to photo-induced processes.[2] This interest in light-driven processes stems from the simplicity and accessibility of the use of light for a variety of applications, including polymerization, photothermal heating, isomerization, and many other photoinitiated reactions. Unfortunately, a significant deficit in reproducibility has arisen in this field due to inconsistent and incomplete experimental reporting.

Although many articles are robust in their synthetic elements, the experimental descriptions of the photochemistry are lacking on a few fronts. In many cases, the incident photon flux is not described explicitly. Instead, bulb information – including wattage rating, and a distance from the sample are provided. This description is insufficient to understand the incident intensity on a given sample. If a photo-activated process is to be reproduced, it is necessary to have an incident flux, often in the units of mW/cm^2 with respect to a defined wavelength. This is particularly notable in the case of polychromatic sources, as

the emission spectra should be sufficiently described. Additionally, a comprehensive UV-Vis spectra or complete description of all absorbing species in the sample are critical elements that are often overlooked in many novel synthetic publications. Another issue that commonly arises pertains to the geometric considerations of the sample. Sample thickness has a major impact on homogeneity of the photoactivated process throughout the sample due to light attenuation, both by the active elements and other absorbing species. Sample thickness relative to angle of exposure should always be provided explicitly and optical thickness should be considered when relevant. Furthermore, boundary conditions are often neglected but are critical in cases such as oxygen inhibited systems.

This study presents the analysis of 150 articles from a variety of high impact journals to provide a sufficient statistical data set that assesses the nature of this problem. These articles are sourced through a Web of Science search for articles published in 2020, 2021, and 2022 that contain the words “photo” or “light” in the title or as a keyword. From this large data set, 50 random papers from each of the polymer, chemistry, and physics categories, as set by Web of Science, are assessed for photo process reproducibility. The qualifications for photo reproducibility included emission spectra, light intensity (area normalized), exposure duration, thickness (or alternative geometry), boundary conditions, initiator/chromophore absorbance, initiator/chromophore concentration, and other absorbing species information.

A3 Methods

A3.1.1 Paper Selection

To assess the current state of reproducibility, 150 papers that met certain eligibility criteria were selected at random for review. The disciplines “polymer chemistry,”[3–52] “organic chemistry,”[53–102] and “physics,”[103–152] as assigned by Web of Science, were equally represented in the review. Eligibility criteria included a publication date between 2020 and 2022, publication in a journal with a 2022 impact factor of 4.0 or greater, and the word “light” or “photo” as a title or keyword. Of critical importance, the work was required to include a photoinduced process (i.e. photo-initiation, photo-excitation, photo-reduction). Therefore, passive measurements, such as UV-Vis, or modelling work that did not have experimental validation, were not eligible for inclusion in the data collection presented herein. Works were also excluded if access was not readily available, or if redactions were made.

Works were assessed for reproducibility criteria and assessed as “Determinable” if the critical information was listed explicitly or could be calculated or sourced if the work was being reproduced. If the information could not be solidly confirmed, that category for the paper in question was considered “Not Determinable.” If a work performed multiple relevant experiments, and if any relevant procedure was not replicable based on the information provided, the work was considered “Not Determinable.”

A3.1.2 Spectral Distribution

Spectral distribution was assessed to be reproducible if either of the following were provided in the paper or supplemental text: (1) A part number for a bulb or a part number

for a lamp that only utilizes one type of bulb; and (2) The spectrum of light used for exposure. Although lasers are often nominally a single wavelength, they have narrow spectral distributions. Furthermore, there are additional spectral considerations for a laser that are frequently provided through a part number (such as in the case of single- or multi-modal spectral distribution). Therefore, the reproducibility criteria above can be applied equally to laser light sources as to broader spectrum light sources.

A3.1.3 Spectral Intensity

Regarding light intensity, it must be presented in the form of power per area to be reproducible. This is often presented in units of mW/cm^2, though other units, such as “sun”, satisfy this requirement as well. In contrast, the electrical power rating of the bulb does not satisfy the threshold for reproducibility.

A3.1.4 Exposure Duration

To be satisfactorily reproducible, it must be noted when the light was turned on and off. Furthermore, this information should also include both the total duration, and relevant on-off cycling, of the light in question. Duration and cycling were not assumed from figures that were not explicitly labeled— such as in frequent cases of presenting photoelectrical *IV-T* cycling.

A3.1.5 Sample Thickness

The sample depth relative to the incident angle of the light denotation, was required for the work to be considered reproducible. In the case of a simple thin-film geometry, this

is merely thickness. However, to satisfy this requirement in the case of cuvette or other geometries, both the thickness and relative direction of the light needed to be noted for the condition to be “Determinable.”

A3.1.6 Boundary Conditions

Boundary conditions were considered “Determinable” if all relevant surfaces were defined. These boundary conditions are defined as the surfaces between the incident light and the material undergoing a photo process as well as the containment surfaces of the material. In many applications, these surfaces are glass, quartz, or air to minimize the consequence on the incident light. However, the composition of the relevant surfaces must also be accounted for as they relate to heat and mass transport.

A3.1.7 Chromophore Absorbance

With any photo-driven process, the chromophore species should be clearly identified for the work to be reproduced. Although an absorbance spectrum is preferable, this category was assessed as providing sufficient information for reproducibility if sufficient sample preparation was presented, such that another user could perform their own UV-Vis on the absorbing species. This criterion was met if synthesis of a novel chromophore was specified.

A3.1.8 Chromophore Concentration

In order to satisfy reproducibility standards, the composition of the entire material must be well defined within a text. Specifically, the chromophore concentration was assessed either from a standard unit (wt%, M, ppm) or the samples are prepared neat.

A3.2 Light Spectra

Light spectra for various light sources were obtained with an Ocean Optics Flame Spectrometer (FLAME-S-VIS-NIR, 350-1000 nm) using OceanView software (v2.0.8). Spectra were normalized relative to maxima for comparison.

A3.3 Incident Intensity Assessment

Power readings of an EFOS A4000 Acticure UV light source equipped with a 400-500 nm filter were measured using two power meter sensor heads: a Thorlabs PM16-120 silicon detector and a Thorlabs S425C thermal detector. The PM16-120 measurement was taken using the Thorlabs optical power meter software (v1.0.2), the S425C measurement was made using a Thorlabs PM100D power meter console.

The light source output coupler was mounted to one end of a 5-inch lens tube, the other end of the lens tube was affixed directly to each detector head via the included mechanical threading. The opaque lens tube blocked external light and ensured consistent illumination between the two detectors. Each detector was zeroed in this condition, then set to the detection wavelengths of interest (405 nm and 436 nm). The irradiance over the detector area was recorded.

A3.4 Photo-condition modeling

A first-principles, free volume-based kinetic model was used to demonstrate the importance of reported photopolymerization conditions on material properties. Details of the model are reported in Dobson and Bowman.[153] In brief, the model features a free-radical photopolymerization scheme consisting of chain-length dependent termination, light attenuation, material diffusion, heat transfer to the environment and from reaction exotherm, oxygen inhibition, and free volume-controlled kinetic parameters. The importance of accurate reporting of the determinable reproducibility criteria is simulated by a model system. Except where otherwise noted, the model system consisted of a 0.5 mm thick bulk divinyl homopolymerization (hexanediol diacrylate, HDDA), with 0.01 M I819 photoinitiator cured with 10 mW/cm^2 coherent 405 nm light. The material surface nearest the light source was assumed to have Dirichlet boundary conditions for both oxygen concentration and temperature, and the surface farthest from the light source was assumed to have no flux conditions for all energy and material balances. Monomer conversion as a function of both depth into the material and time of exposure was simulated, and differences emerging due to parameters required for reproducibility were noted.

A3.5 Photo-rheology

The impact of reflective boundary conditions was demonstrated with a rotational rheometer (TA Instruments, ARES G2). To minimize attenuation and ensure slow reaction, samples were comprised of 1 wt% 2-methyl-4-(methylthio)-2-morpholinopropiophenone (I907, purchased Sigma-Aldrich) photoinitiator in poly(ethylene glycol) 400 diacrylate

(PEGDA, SR344, donated by Arkema). Samples were monitored for 2 min prior to 1 mW/cm^2 exposure by 405 nm laser (250 mW, Civil Laser) as detected by Thorlabs S120VC, to minimize the effect of wavelength distribution. Shear rheology was monitored on 250 μm thick, 8 mm diameter samples under 0 N compression and a 1% oscillation at 1 Hz. Polymerization was compared between samples on a steel lower surface and a lower surface comprised of a quartz head followed by a 780 nm cut-off filter (Thorlabs FGL780) to minimize reflection. The inhibition time was defined as the duration between when the light was turned on and a storage modulus of 10 Pa.

A3.6 UV-Vis Spectroscopy

The absorbance spectrum of 1 wt% Irgacure 907 in acetonitrile was assessed over the 350 to 500 nm range with a Thermo Scientific Evolution 300. A quartz cuvette (1 cm path length), containing acetonitrile was used as the reference relative to the sample in a matching cuvette.

A3.7 Distance from bulb intensity variability measurement

The intensity of eight bulbs (Ecosmart, A19F8DE26835Z) was measured at a distance of 10 cm from the tip of the bulb connected to a standard light bulb socket. Measurements were taken both with the bulb in a vertical orientation to the detector as well as a horizontal orientation (Scheme 1) using a Thorlabs S120VC silicon detector, connected to a Thorlabs PM100D, measuring relative to the 530 nm calibration.

Scheme A1. Illustration of light bulb orientation and measurement of distance relative to the radiometer detector. The distance from the tip of the bulb to the detector, 10 cm, is indicated by *x.*

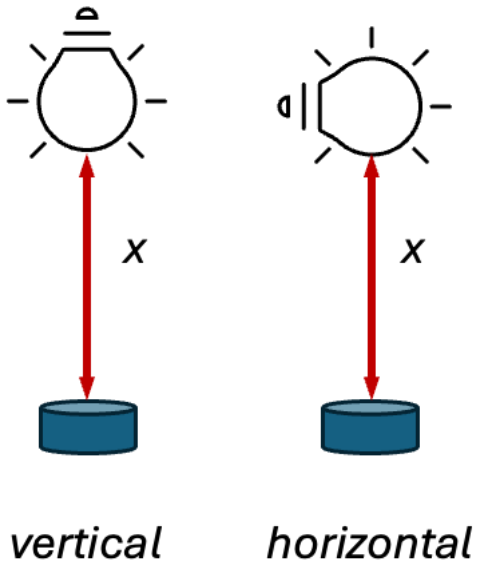

A4. Results and Discussion

Overall, the reproducibility of a given photo process, in any manuscript, requires the presence of three critical components: photo conditions, geometry considerations, and composition considerations. The results of the analyzed papers on these fronts are summarized in Figures A9, A10, and A11.

A4.1 Photo conditions

Amongst the criteria studied, the characterization of the light used to perform photoinduced processed stood out as the least reproducible. Clearly, this is a critical issue as the entire purpose of the experiments evaluated in this study was to use light to cause a material change (chemical or physical). Therefore, clear articulation of the light

spectrum, intensity, and exposure duration, are critical not only to interpreting a result, but also to reproducing the results.

A4.1.1 Emission spectrum of light source

Of the papers surveyed, only 52% in polymer science, 40% in chemistry, and 56% in physics literature, were assessed as reproducible with regards to the spectrum of the light source. The spectrum of the light source is critical as it not only informs which chromophores will be activated at a given wavelength, but also the corresponding attenuation. For this reason, not all light sources with nominally the same characteristic wavelength are created equal. Two different 405 nm LED may have different broadness; and both are certainly different from a multi-peaked 400-500 nm filtered mercury arc bulb (Figures A1-3). Furthermore, denoting the color of a light source as “blue” or “red” is far less than sufficient, since it neither distinguishes the peak wavelength nor the distribution. Additional nuances in the consequences of spectra will be discussed throughout. The core consideration is that the bulk of literature is not reproducible in the current fashion. This signals both a lack of fundamental understanding of photophysics and a crisis toward reproducing these works.

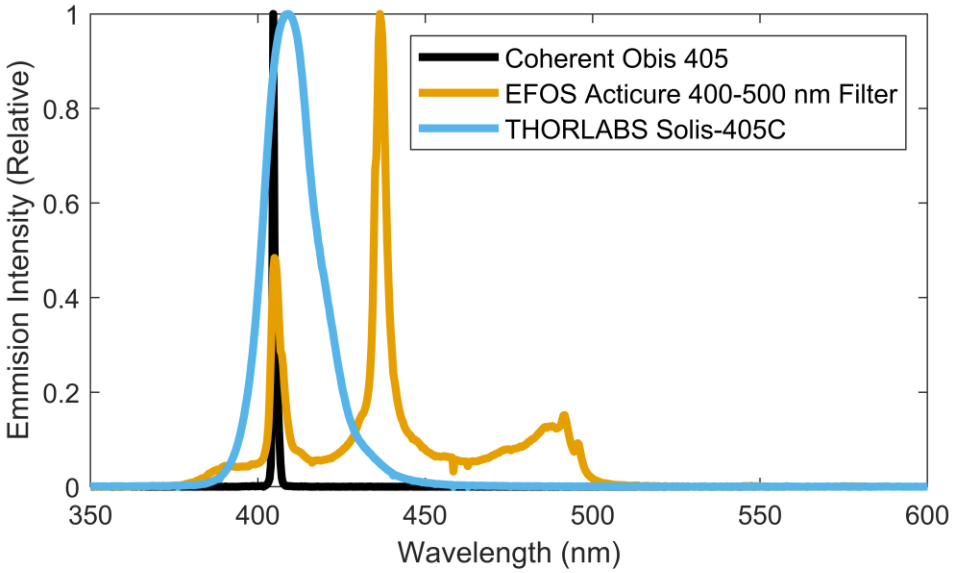

Figure A1. Types of light sources that are nominally used as 405 nm sources with the laser providing the narrowest spectra centered at 405 nm, the LED providing a broader distribution actually centered at 409 nm, and the Acticure mercury arc-lamp which has a complex spectrum with narrow peaks of higher intensity at 405 nm and 445 nm. Further, the filter is not a hard cut-off at 400 nm as a user may expect by its label alone. Differences in incident spectra result in downstream impacts on absorbance and attenuation and therefore spectra must be fully defined for reproducibility.

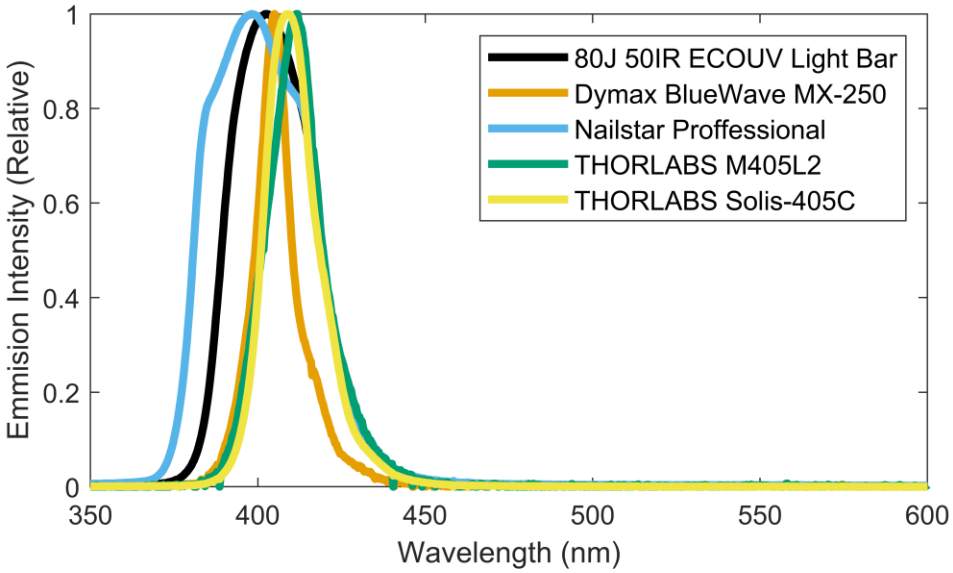

Figure A2. Nominal 405 nm LEDs showing the variance in both center wavelength and width. Therefore, solely listing the wavelength of an LED does not provide sufficient information to reproduce the work.

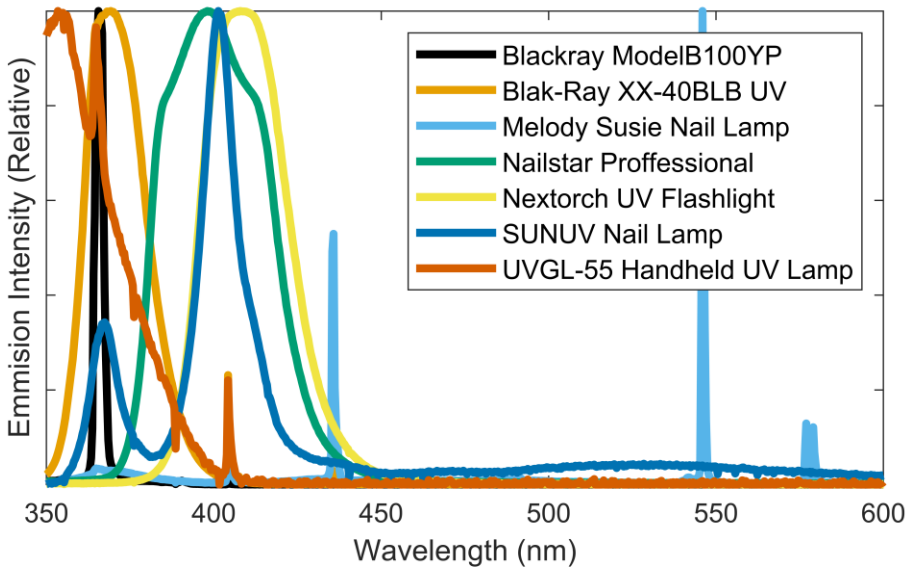

Figure A3. Various sources nominally labeled “UV” include sources a wide array of center wavelengths. Therefore “UV light” does not provide sufficient information for reproduction

of work. Further, it should be noted that some sources labeled “UV” fall within the visible range as much of the their emission spectra exceed 400 nm.

Additional nuances persist within reporting the spectra of lamps. For example, although a part number often suffices, exemptions do exist. In the case of some light boxes, a variety of bulbs are compatible; thus reporting only the box part number, is not sufficient for fulfilling the reproducibility requirement as assessed in this study. Characterization and reporting of photo-mediated reaction conditions can be particularly important when applying equipment intended for purposes outside of the lab. There are a variety of potential justifications for use of mass produced light sources. Nail polish-curing LED lamps, for example, are relatively inexpensive, conveniently available from a variety of vendors, and provide adequate power output for many applications where wavelengths around 365-405 nm are appropriate. However, these lamps’ emission vary from model to model within and among suppliers. Thorough analysis of the output spectra is warranted to allow for adequate reproducibility.

One example of the difficulties associated with employing consumer products in the laboratory setting is the use of blacklight blue light sources. Blacklight blue lamps are perhaps most widely known for their recreational use in dance clubs, where the invisible UVA light excites fluorophores in clothing or on surfaces painted with fluorescent paint. There are two common phosphors used in black light blue lamps. The $BaSi_2O_5$:Pb phosphor emits a broad spectrum with a maximum centered around 350 nm while the SrB_4O_7:Eu phosphor provides a more narrow emission peak centered around 370 nm. Little difference is noticeable in the performance of these bulbs (both labeled simply

“BLB”) in the nightclub. If, however, the process of interest relies on the light to excite a chromophore that absorbs at 340 nm, but with very little absorbance at 370 nm (e.g. photoinitiated polymerization with 1-hydroxycyclohexyl-phenyl ketone or 2-hydroxy-4′-(2-hydroxyethoxy)-2-methylpropiophenone) a dramatic difference in performance between the two lamps may be expected. Despite their different respective emissions, the phosphor used in the manufacturing of a bulb may not be readily discernible from the supplier-provided product description alone.

A4.1.2 Light source intensity

Furthermore, incident intensity of light is crucial to understanding the kinetic rates involved within a photo-induced process. Of our survey, only 42% of polymer science, 36% of chemistry, and 40% of physics literature was reproducible in this capacity. This deficiency corresponded most commonly to a lack of understanding the power output of a light source versus the power input or bulb energy rating, often given in watts (W). Even if the total energy delivered to a sample is known, non-linear processes are susceptible to the combination of intensity and time, such as the polymerization of HDDA shown in Figure A4.

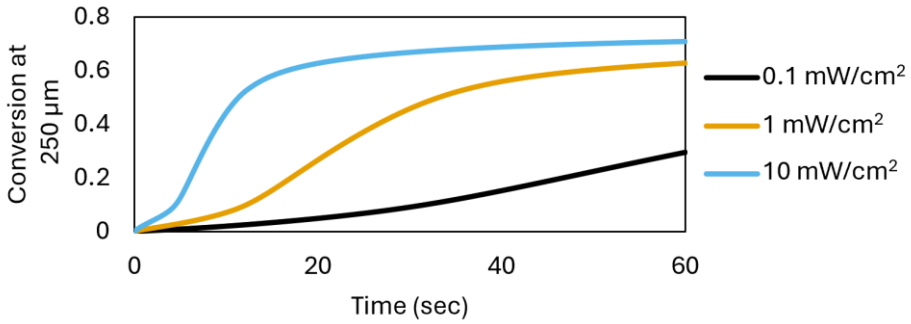

Figure A4. First principles model demonstrating the effect of intensity on the polymerization of HDDA. Photo-induced process conditions: 10 mW/cm^2, 405 nm (coherent) light, 0.01 M I819 (initiator), conducting boundary layer, no oxygen boundary.

The bulb power rating does not correspond to the light intensity at the exposure site, not only because the energy is inaccurate, but also because the total power is not normalized by area. 1 mW of power spread over a square kilometer is trivial; however, 1 mW over a square millimeter is equivalent to the standard unit of 1 sun of exposure. Of additional note, many authors declared a distance between the bulb and the sample, which is yet again insufficient for the reasons outlined above. To demonstrate this, eight bulbs were held a distance of 10 cm from a commercially sourced bulb and the intensity of the light source measured. When the bulb was placed in a vertical orientation to the detector, there was 3.6% variability in the measured intensity while when the bulb was placed in a horizontal orientation to the detector, there was 5.4% variability in the measured intensity.

The measurement technique for assessing incident intensity also informs reproducibility. There are a variety of common misconceptions pertaining to radiometers

that should be noted when measuring intensity. First, there are two primary types of optical power meters: photodiode and thermal. Photodiode sensors count the quantity of absorbed photons normalized to a calibration for absorbance and quantum yield at a specified wavelength. Under these constraints, these sensors fail to account for variations relative to the selected and calibrated wavelength that come from a broad spectrum. In contrast, thermal sensors only need to account for quantum yield as they directly measure the power absorbed. However, spectral distribution should still be noted when interpreting these measurements. It was experimentally assessed that an EFOS Acticure mercury-arc lamp with an intensity of 20.9 mW/cm^2 relative to the 405 nm calibration, while using a thermal power meter (Thorlabs S425C), is consistent with a measured intensity of 28.4 mW/cm^2 relative to the 405 nm calibration using a photodiode detector (Thorlabs PM16-120). This overestimation of incident intensity in power units by photodiode is expected as the instrumentation interprets incoming distribution of photons as, on average, higher energy 405 nm species. For robustness, it is therefore valuable to not only report intensity, but also the detector used to determine the reported intensity.

A4.1.3 Duration of light exposure

In addition to the distribution of light and the intensity, the duration of exposure dictates the extent to which a system can be activated. Within the study, authors did generally well in this category with 78% of polymer science, 74% of chemistry, and 84% of physics articulating both when the light was turned on (if relevant), and how long the exposure lasted.

Often, the intensity and time of a reaction is combined into the concept of dose—noting the total incident energy that was received. This method of expressing dose in an experiment, although reproducible, should be generally discouraged. The concept of dose fails to capture the nuances of non-linear processes, such as the rate of bimolecular terminating photopolymerizations, which are classically modeled as half-order with respect to initiation rate. Additional examples include systems that degrade with time, which in and of themselves provide further justification for the need to clearly articulate the temporal scope of a photo-induced process.

A4.2 Geometry

An additional criterion that was studied was the geometry of the material being irradiated. This is necessary to understand the absorbance of the photons throughout the specimen. Within this consideration are the boundary or surface layer composition and the material thickness.

A4.2.1 Surface and boundary layers

The composition of the surface boundary layer(s) is critical in understanding both the ability of light to pass though the layer as well as its interaction with the photo-driven process.

In some cases, the boundary layer is a sheet of glass, quartz, or plastic with an important distinction between the wavelengths that can penetrate these materials. Additionally, if other materials act as a physical barrier, then their ability to scatter, absorb, or filter the light matters greatly in the intensity and what wavelengths will reach the

material. This point comes up most frequently with samples characterized with photo-rheology where both a quartz plate and a steel plate will sandwich the material, allowing transmission of the light source from one side and reflection of the light from the other (Figure A5).

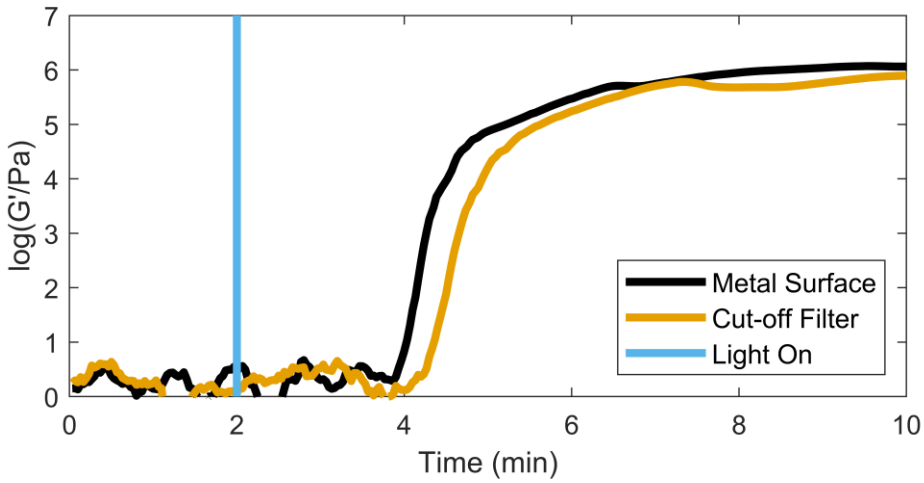

Figure A5. Impact of surface reflection on photopolymerization as assessed by rheometry. PEGDA 400 containing 1 wt% I907 (250 µm thickness), is exposed to 1 mW/cm^2, 405 nm light (250 mW, Civil Laser) starting at 2 minutes. The reflective steel lower surface (black) resulted in overcoming the oxygen inhibition, resulting in polymerization, 15% faster than the non-reflective combination of a lower quartz plate and cut-off filter (yellow).

In the case where there is no physical barrier between the material being irradiated and the light source, the gas over the material can significantly interact with the photo-driven process. In the case of an air layer, the presence of oxygen has been known to be an efficient quencher of excited triplet state molecules, effectively inhibiting some photo-polymerizations (Figure A6).

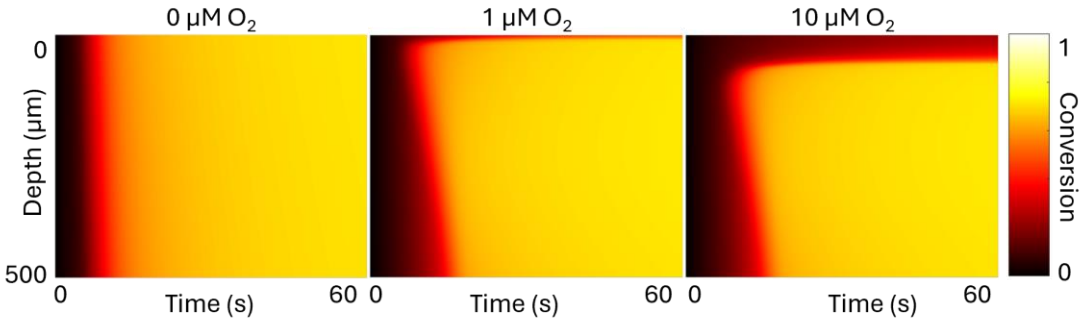

Figure A6. First principles model of the polymerization of HDDA with variable oxygen concentration. Oxygen concentration is both throughout the material at t=0 and has capacity to diffuse from the upper boundary. Increased availability of oxygen from the upper boundary results in larger inhibition layer. Photo-induced process conditions: 10 mW/cm^2, 405 nm (coherent) light, 0.01 M I819 (initiator), isothermal.

Furthermore, thermal transport is of consequence, depending on the nature of the photo-induced reaction. This consideration applies not only to actively heated surfaces, but also to general conductive and convective heat transfer (Figure A7). Of further complication, absorbance of light can also result in photothermal process, intentional or unintentional, that necessitate consideration of this variable.

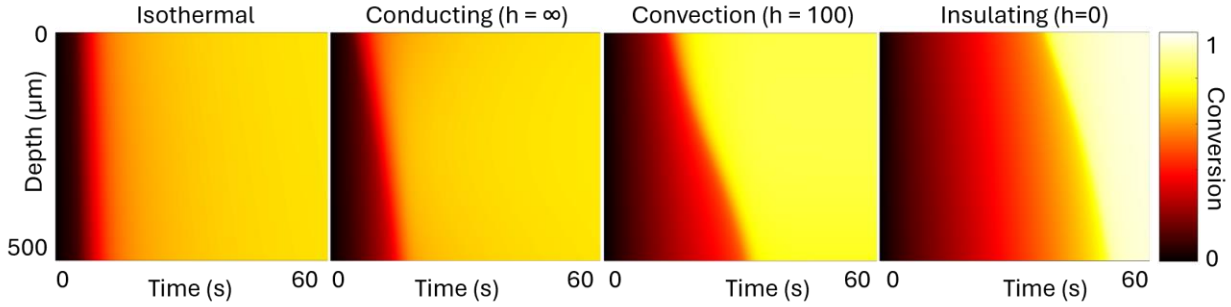

Figure A7. First principles model of the polymerization of HDDA with varied thermal transport at the upper interface. Though reaction is delayed, the increase in temperature,

due to failure to dissipate heat of polymerization, in the convection and insulated condition results in higher achievable conversion. Photo-induced process conditions: 10 mW/cm^2, 405 nm (coherent) light, 0.01 M I819 (initiator), no oxygen transport boundary.

A4.2.2 Sample thickness

An additional critical geometry consideration in photo processes is the thickness of the material being irradiated. This correlates directly with the light attenuation within the material being irradiated. Light attenuation invariably causes inhomogeneities within the irradiated sample that lead to conversion gradients throughout the depth.

Within the geometry considerations, there is also the need to express any natural limitations of the system. This is most clearly articulated with biology related publications where expressing the exposure thickness through various tissues or cells can provide an inherent challenge, but the thickness of irradiation is still a critical consideration, especially considering limited success many wavelengths have with penetrating different biological tissues.

This leads to an inherent challenge with spin coating and fibers where measuring the thickness of the samples has a significant degree of variability throughout the material, creating ambiguous architecture that in some cases may be generalized by a single measurement that does not fully apply to the area of photo-exposure as a whole.

A4.3 Composition

As a generality, authors well articulate the compositions of their samples. This is not unexpected as robust preparation methods are standard. However, additional considerations exist pertaining to the consequences of the composition.

A4.3.1 Active chromophore description

For a photo-process to proceed, photons must be absorbed. Therefore, a chromophore or set of chromophores are necessary in order to absorb these photons. For reproducibility, the composition is all that is necessary and therefore the majority of literature is reproducible (96% overall). However, an absorbance spectrum is necessary to truly understand the absorbance.

Even with an absorbance spectrum obtained, further information is necessary to understand attenuation and kinetics of a system. Attenuation in transmission is based on the absorption of photons throughout the depth in accordance with

$$\frac{dI}{dz} = -I\varepsilon c \qquad \text{(Equation A1)}$$

where I is the intensity of light of wavelength λ at depth z, ε is the Napierian molar absorptivity of the chromophore with respect to wavelength λ, and c is chromophore concentration. In the case of a single chromophore at constant concentration with respect to depth, the relation becomes Beer-Lambert,

$$A = -\log_{10} T = \frac{\varepsilon b c}{\ln(10)} \qquad \text{(Equation A2)}$$

where A is absorbance; T is transmittance; b is the path length, or in this case, sample thickness. Frequently, multiple absorbing species are present, whether intended for the process, generated in-situ, or simply another component. Multiple chromophores result

in a linear combination with respect to their differential absorption. This consideration is of particular importance when additional absorbers result in deviation from an experimental assumption that the sample is optically thin.

$$\frac{dI_\lambda}{dz} = -I_\lambda(\varepsilon_1 c_1 + \varepsilon_2 c_2 + \varepsilon_3 c_3 + \cdots \varepsilon_n c_n) \quad \text{(Equation A3)}$$

Often, bulk material is nominally optically thin if less than 20% of the light is absorbed, though this threshold is arbitrary. Critically, absorbance throughout the depth of a sample results in heterogeneity in exposure that therefore can impact the property homogeneity.

Furthermore, the absorbance of a chromophore, in combination with the initiation spectrum and intensity, impacts the rate of the photo-induced process according to a model such as

$$\frac{dc}{dt} = -f\phi I\varepsilon c \quad \text{(Equation A4)}$$

where ϕ is quantum yield, the fraction of absorbed photons that result in the desired process, and t is time. In this case, c reflects the concentration of a consumed chromophore with efficiency f; however, the key consideration is that photons must be absorbed for the photoinduced process to progress. Therefore, the total kinetic rate as a function of depth is dependent on a wide variety of considerations that have been addressed to this point, readily demonstrated in Figure A8.

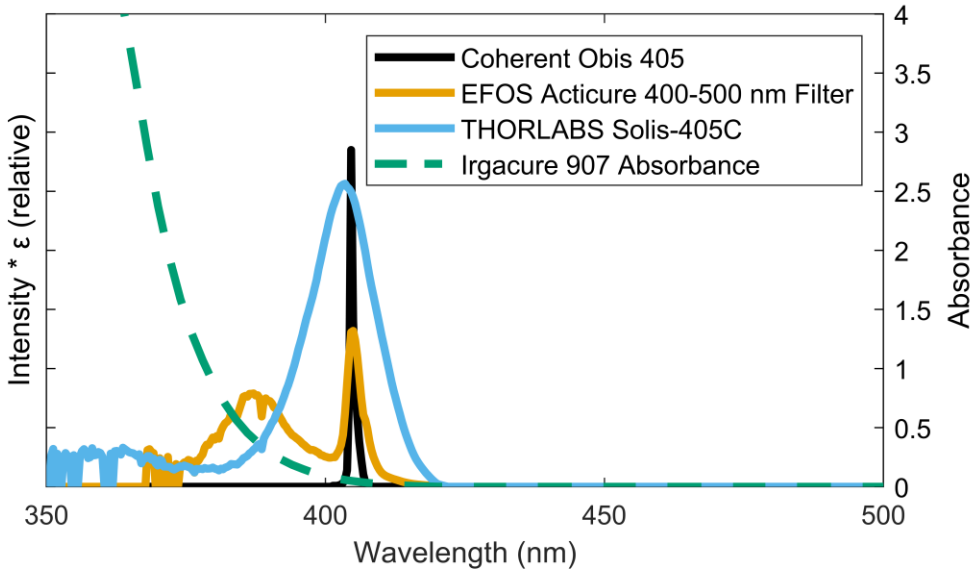

Figure A8. Absorbance spectrum of I907 at 1 wt% in acetonitrile with a 1 cm path length (green). This chromophore has a large change in absorbance in the region of interest, thus photoinitiation is particularly sensitive to differences of light source. The abundance of absorbed photons is estimated by the product of spectral intensity (normalized by maximum peak) from Figure A1 with the I907 molar absorptivity coefficient corresponding to those wavelengths. The height of the curve denotes the absorbed abundance of a particular wavelength of photon informing kinetic rate, attenuation, and homogeneity. Photobleaching, the process in which chromophore absorbance relative to the irradiation wavelength are depleted, and its counterpart, photodarking, complicate these considerations further.

A4.3.2 Amount of active chromophore

Expanding on the necessity to know what chromophore is absorbing, the concentration of this species is further critical as previously demonstrated in Eqn A1. Yet

again, reporting of formulation composition is routine and therefore 93.3% of the total papers satisfied reproducibility in this category.

The amount of absorbing material has implications beyond absorbance. Particularly, if the chromophore is consumed by the process, such as initiation, the quantity of chromophore must be sufficient to reach the desired extent of reaction.

A4.3.3 Other absorbing species

Although the combination of intended chromophores was discussed in section A4.3.1, authors are responsible for understanding the absorption of all species in play. Although not a key contributor to reproducibility, absorbing and scattering species impact homogeneity and are important for performing good photo-science. By our evaluation, nearly 20% of the total papers studied contained clear issues pertaining to unintended consequences of species absorbing or scattering light in the materials. Consequences most often pertained to inhomogeneity as a function of depth, due to attenuation; however, other considerations included photothermal effects and side reactions.

A4.4 Additional Considerations

There are numerous additional advanced considerations that pertain to performing high-quality photo-science, including collimation, intensity uniformity, polarization, bulb aging, bulb temperature dependence, and the angle dependence of filters. However, the outline herein focuses on what is necessary for reproducibility.

A5. Checklist for Other Papers

We advise the implementation of the following gold standard checklist for authors, reviewers, and editors in the context of photoinduced reactions literature.

1) Inform spectral distribution of the light as either (a) a provided emission spectrum or (b) a part number that is sufficient to describe the spectrum. Note filters if applicable.
2) Normalize incident power by area, thereby report as intensity. Variation on mW/cm^2 is most appropriate generally, though solar simulators may benefit from the standard unit of ‘sun’.
3) Note exposure duration and, if relevant, should include full cycling history.
4) Define sample thickness relative to the incident angle. If samples are not flat, instead define completely.
5) Denote boundary conditions, particularly those relevant to material, optical, and thermal transport.
6) Provide a robust description of chromophore(s). Although not necessary for reproducibility, provide absorbance spectra for novel or unique chromophores.
7) Specify chromophore concentration.
8) Note additional absorbing or scattering species not used to induce the photoreaction.

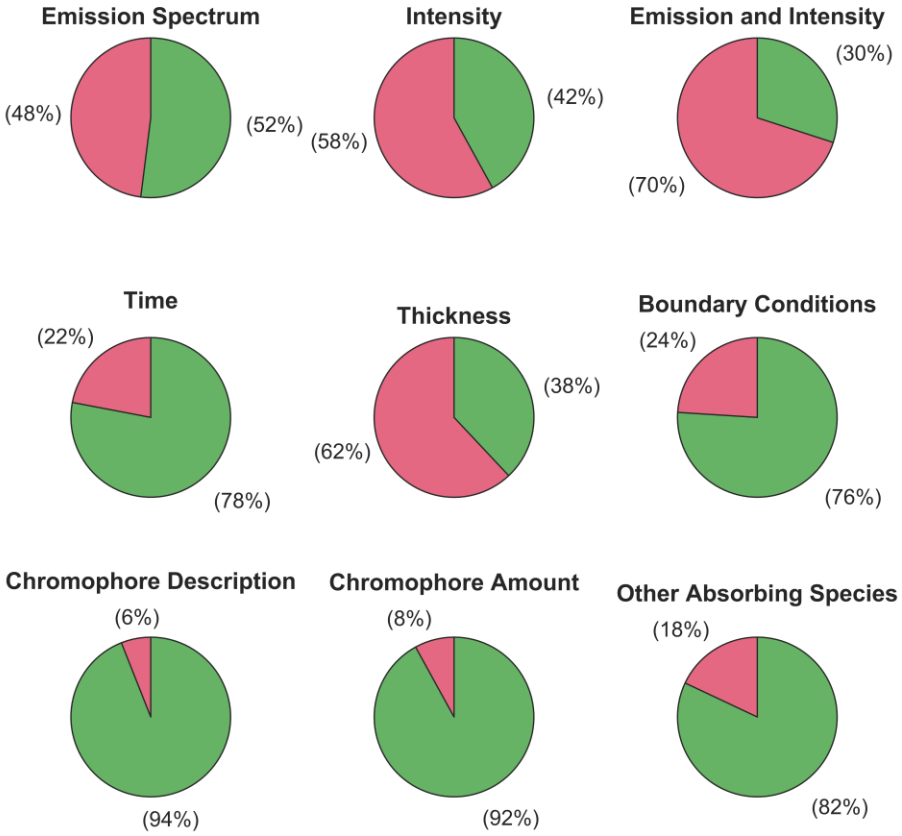

Figure A9. Summarized results for 50 polymer chemistry papers.[3–52] "Determinable" categorization in green while "Non-Determinable" in red. "Emission and Intensity" is the union of the two categories.

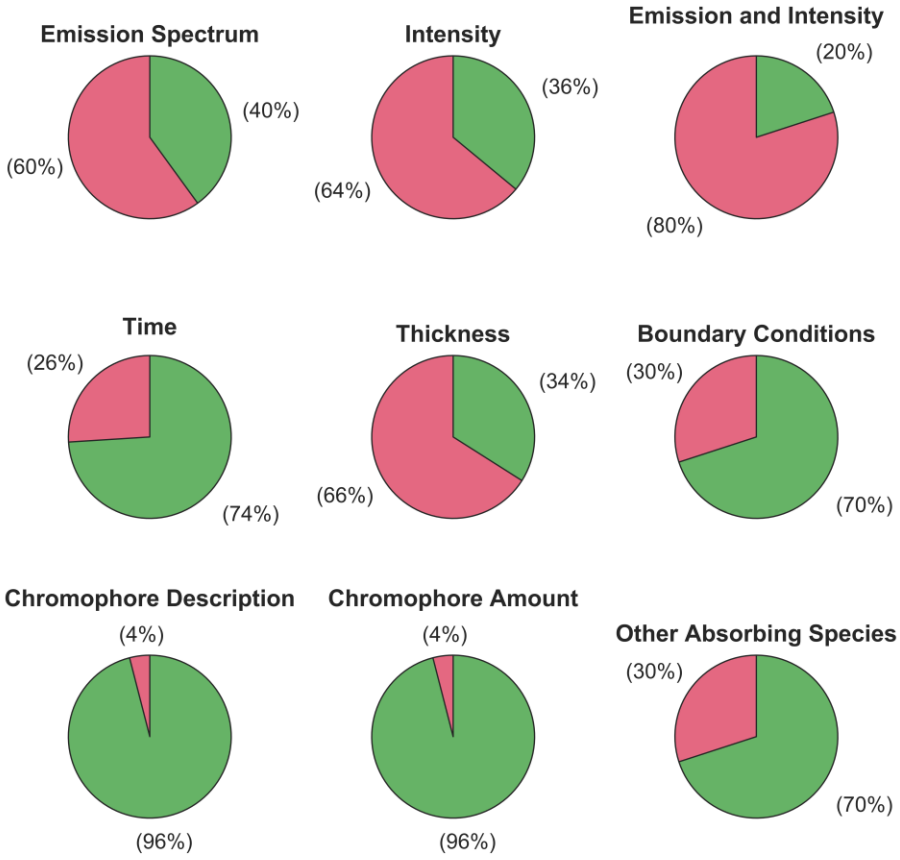

Figure A10. Summarized results for 50 organic chemistry papers.[53–102] “Determinable” categorization in green while “Non-Determinable” in red. “Emission and Intensity” is the union of the two categories.

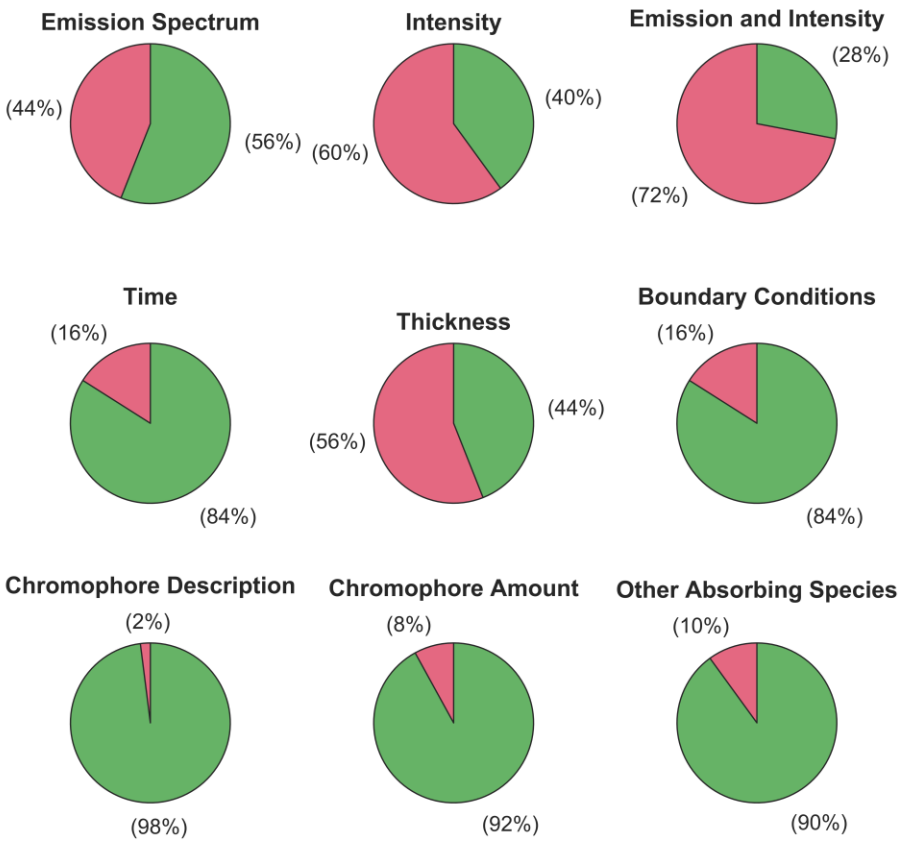

Figure A11. Summarized results for 50 physics papers. [103–152] "Determinable" categorization in green while "Non-Determinable" in red. "Emission and Intensity" is the union of the two categories.

A6. References

(1) Baker, M. 1,500 Scientists Lift the Lid on Reproducibility. *Nature* **2016**, *533* (7604), 452–454. https://doi.org/10.1038/533452a.

(2) Clarivate™ (Web of Science™). © Clarivate 2024. All Rights Reserved.

(3) Wu, J.; Zhang, X.; Yan, C.; Li, J.; Zhou, L.; Yin, X.; He, Y.; Zhao, Y.; Liu, M. A Bioinspired Strategy to Construct Dual-Superlyophobic PPMB Membrane for Switchable Oil/Water Separation. *J. Membr. Sci.* **2023**, *665*, 121128. https://doi.org/10.1016/j.memsci.2022.121128.

(4) Kocaarslan, A.; Yılmaz, G.; Topcu, G.; Demirel, L.; Yagcı, Y. A Novel Photoinduced Ligation Approach for Cross-Linking Polymerization, Polymer Chain-End Functionalization, and Surface Modification Using Benzoyl Azides. *Macromol. Rapid Commun.* **2021**, *42* (14), 2100166. https://doi.org/10.1002/marc.202100166.

(5) Huang, G.; Qian, G.; Yan, Y.; Xu, D.; Xu, C.; Fu, L.; Lin, B. A Super Long-Acting and Anti-Photolysis Pesticide Release Platform through Self-Assembled Natural Polymer-Based Polyelectrolyte. *React. Funct. Polym.* **2020**, *146*, 104429. https://doi.org/10.1016/j.reactfunctpolym.2019.104429.

(6) Ma, C.; Han, T.; Efstathiou, S.; Marathianos, A.; Houck, H. A.; Haddleton, D. M. Aggregation-Induced Emission Poly(Meth)Acrylates for Photopatterning via Wavelength-Dependent Visible-Light-Regulated Controlled Radical Polymerization in Batch and Flow Conditions. *Macromolecules* **2022**, *55* (22), 9908–9917. https://doi.org/10.1021/acs.macromol.2c01413.

(7) Huerta-Madroñal, M.; Caro-León, J.; Espinosa-Cano, E.; Aguilar, M. R.; Vázquez-Lasa, B. Chitosan – Rosmarinic Acid Conjugates with Antioxidant, Anti-Inflammatory and Photoprotective Properties. *Carbohydr. Polym.* **2021**, *273*, 118619. https://doi.org/10.1016/j.carbpol.2021.118619.

(8) Guo, R.; Bai, L.; Dong, G.; Chai, D.; Lang, K.; Mou, Z.; Zhao, M. Construction of ZnO/Keggin Polyoxometalate Nano-Heterojunction Catalyst for Efficient Removal of Rhodamine B in Aqueous Solution. *J. Inorg. Organomet. Polym. Mater.* **2022**, *32* (5), 1599–1615. https://doi.org/10.1007/s10904-022-02251-x.

(9) Rastogi, P.; Venner, C. H.; Visser, C. W. Deposition Offset of Printed Foam Strands in Direct Bubble Writing. *Polymers* **2022**, *14* (14), 2895. https://doi.org/10.3390/polym14142895.

(10) Heshmati Aghda, N.; Torres Hurtado, S.; Abdulsahib, S. M.; Lara, E. J.; Tunnell, J. W.; Betancourt, T. Dual Photothermal/Chemotherapy of Melanoma Cells with Albumin Nanoparticles Carrying Indocyanine Green and Doxorubicin Leads to Immunogenic Cell Death. *Macromol. Biosci.* **2022**, *22* (2), 2100353. https://doi.org/10.1002/mabi.202100353.

(11) Xiao, L.; Li, Q.; Liu, Y.; Fu, X.; Zhao, Y.; Cai, J.; Yin, X.; Hou, L. Durable and Recyclable Conjugated Microporous Polymer Mediated Controlled Radical

Polymerization under White LED Light Irradiation. *Polym. Chem.* **2021**, *12* (46), 6714–6723. https://doi.org/10.1039/D1PY01241J.
(12) Bošnjaković, D.; Fleisch, M.; Zhang, X.; Drevenšek-Olenik, I. Electrically Tuneable Optical Diffraction Gratings Based on a Polymer Scaffold Filled with a Nematic Liquid Crystal. *Polymers* **2021**, *13* (14), 2292. https://doi.org/10.3390/polym13142292.
(13) Wang, M.; Xu, Z.; Guo, Y.; Hou, Y.; Li, P.; Niu, Q. J. Engineering a Superwettable Polyolefin Membrane for Highly Efficient Oil/Water Separation with Excellent Self-Cleaning and Photo-Catalysis Degradation Property. *J. Membr. Sci.* **2020**, *611*, 118409. https://doi.org/10.1016/j.memsci.2020.118409.
(14) Liao, X.; Dai, P.; Wang, Y.; Zhang, X.; Liao, Y.; You, X.; Razaqpur, A. G. Engineering Anti-Scaling Superhydrophobic Membranes for Photothermal Membrane Distillation. *J. Membr. Sci.* **2022**, *650*, 120423. https://doi.org/10.1016/j.memsci.2022.120423.
(15) Wang, J.-M.; Wang, H.; Chen, E.-C.; Chen, Y.-J.; Wu, T.-M. Enhanced Photodegradation Stability in Poly(Butylene Adipate-Co-Terephthalate) Composites Using Organically Modified Layered Zinc Phenylphosphonate. *Polymers* **2020**, *12* (9), 1968. https://doi.org/10.3390/polym12091968.
(16) Zhang, K.; Xiao, M.; Zhang, L.; Chen, Y.; Tan, J. Exploiting Wavelength Orthogonality in Photoinitiated RAFT Dispersion Polymerization and Photografting for Monodisperse Surface-Functional Polymeric Microspheres. *ACS Macro Lett.* **2022**, *11* (6), 716–722. https://doi.org/10.1021/acsmacrolett.2c00228.
(17) Lei, X.; Xie, A.; Yuan, X.; Hou, X.; Lu, J.; Liu, P.; Xiang, Z.; Chen, G.; Xing, T. Fabrication of Superhydrophobic and Light-Absorbing Polyester Fabric Based on Caffeic Acid. *Polymers* **2022**, *14* (24), 5536. https://doi.org/10.3390/polym14245536.
(18) Shen, Y.; Gallet-Pandellé, A.; Kurita, H.; Narita, F. Fabrication, Tensile Properties, and Photodecomposition of Basalt Fiber-Reinforced Cellulose Acetate Matrix Composites. *Polymers* **2021**, *13* (22), 3944. https://doi.org/10.3390/polym13223944.
(19) Xue, X.; Zhang, J.; Li, M.; Ao, C.; Wang, Q.; Zhao, J.; Zhang, W.; Lu, C. Facile Fabrication of Three-Dimensional Nanofibrous Foams of Cellulose@g-C3N4@Cu2O with Superior Visible-Light Photocatalytic Performance. *Carbohydr. Polym.* **2023**, *303*, 120455. https://doi.org/10.1016/j.carbpol.2022.120455.
(20) Han, Z.; Yu, H.; Pei, Q. Fluorene Derivatives for Efficient Prompt Scintillation in Plastic Scintillators. *ACS Appl. Polym. Mater.* **2022**, *4* (6), 4424–4431. https://doi.org/10.1021/acsapm.2c00391.
(21) Wang, Y.; Wang, X.; Montclare, J. K. Free-Standing Photocrosslinked Protein Polymer Hydrogels for Sustained Drug Release. *Biomacromolecules* **2021**, *22* (4), 1509–1522. https://doi.org/10.1021/acs.biomac.0c01721.
(22) Zhong, Y.; Liu, K.; Chen, W.; Lu, W. High-Definition Mass Spectrometry Tracking: Enhanced Photocatalytic Chain Scission and Mineralization of Polyamide 6 Microplastics under Solar Irradiation. *Polymer* **2022**, *262*, 125495. https://doi.org/10.1016/j.polymer.2022.125495.

(23) Souza, D. C.; Amorim, S. M.; Cadamuro, R. D.; Fongaro, G.; Peralta, R. A.; Peralta, R. M.; Puma, G. L.; Moreira, R. F. Hydrophobic Cellulose-Based and Non-Woven Fabrics Coated with Mesoporous TiO2 and Their Virucidal Properties under Indoor Light. *Carbohydr. Polym. Technol. Appl.* **2022**, *3*, 100182. https://doi.org/10.1016/j.carpta.2021.100182.
(24) Ma, L.; Li, D.; Wang, L.; Ma, X. In Situ Hydrothermal Synthesis of α-MnO2 Nanowire/Activated Carbon Hollow Fibers from Cotton Stalk Composite: Dual-Effect Cyclic Visible Light Photocatalysis Performance. *Cellulose* **2020**, *27* (15), 8937–8948. https://doi.org/10.1007/s10570-020-03405-1.
(25) Sabel-Grau, T. Influence of Pre-Exposure on the Material Response of Epoxy-Based Volume Holographic Recording Material. *Polymers* **2022**, *14* (11), 2193. https://doi.org/10.3390/polym14112193.
(26) Kaya, K.; Alkan, E. A.; Yasa, M.; Süerkan, A.; Udum, Y. A.; Toppare, L.; Yagci, Y. Light Induced Step-Growth Polymerization of Donor-Acceptor-Donor (DAD) Type Monomers Based on Thiophene – [1,2,5] Chalcogenazolo[3,4-f]-Benzo [1,2,3] Triazole – Thiophene. *Eur. Polym. J.* **2021**, *161*, 110831. https://doi.org/10.1016/j.eurpolymj.2021.110831.
(27) Wang, J.; Karami, P.; Ataman, N. C.; Pioletti, D. P.; Steele, T. W. J.; Klok, H.-A. Light-Activated, Bioadhesive, Poly(2-Hydroxyethyl Methacrylate) Brush Coatings. *Biomacromolecules* **2020**, *21* (1), 240–249. https://doi.org/10.1021/acs.biomac.9b01196.
(28) Ding, M.; Yuan, W.; Xu, S.; Yu, C.; Zheng, Y.; Zhou, J.; Shan, G.; Bao, Y.; Pan, P. Light-Induced Crystalline Size Heterogeneity of Polymers Enables Programmable Writing, Morphing, and Mechanical Performance Designing. *ACS Macro Lett.* **2022**, *11* (6), 739–746. https://doi.org/10.1021/acsmacrolett.2c00237.
(29) Abad, M.; Mendoza, G.; Usón, L.; Arruebo, M.; Piñol, M.; Sebastián, V.; Oriol, L. Microfluidic Synthesis of Block Copolymer Micelles: Application as Drug Nanocarriers and as Photothermal Transductors When Loading Pd Nanosheets. *Macromol. Biosci.* **2022**, *22* (5), 2100528. https://doi.org/10.1002/mabi.202100528.
(30) Watanabe, T.; Yasuhara, Y.; Ono, T. Multilayer Poly(Ionic Liquid) Microcapsules Prepared by Sequential Phase Separation and Subsequent Photopolymerization in Ternary Emulsion Droplets. *ACS Appl. Polym. Mater.* **2022**, *4* (1), 348–356. https://doi.org/10.1021/acsapm.1c01315.
(31) Chen, L.; Dong, Q.; Shi, Q.; Du, Y.; Zeng, Q.; Zhao, Y.; Wang, J. J. Novel 2,3-Dialdehyde Cellulose-Based Films with Photodynamic Inactivation Potency by Incorporating the β-Cyclodextrin/Curcumin Inclusion Complex. *Biomacromolecules* **2021**, *22* (7), 2790–2801. https://doi.org/10.1021/acs.biomac.1c00165.
(32) Roig-Sanchez, S.; Kam, D.; Malandain, N.; Sachyani-Keneth, E.; Shoseyov, O.; Magdassi, S.; Laromaine, A.; Roig, A. One-Step Double Network Hydrogels of

Photocurable Monomers and Bacterial Cellulose Fibers. *Carbohydr. Polym.* **2022**, *294*, 119778. https://doi.org/10.1016/j.carbpol.2022.119778.
(33) Lee, S.; Oh, J.; Han, M. S. Photoactivatable Artificial Peroxidase System Using a Dimanganese Complex and Its Application to Light-Controlled Synthesis of Hydrogel. *ACS Appl. Polym. Mater.* **2023**, *5* (1), 67–75. https://doi.org/10.1021/acsapm.2c01102.
(34) Kovalchuk, A. I.; Kobzar, Y. L.; Tkachenko, I. M.; Kurioz, Y. I.; Tereshchenko, O. G.; Shekera, O. V.; Nazarenko, V. G.; Shevchenko, V. V. Photoactive Fluorinated Poly(Azomethine)s with Azo Groups in the Main Chain for Optical Storage Applications and Controlling Liquid Crystal Orientation. *ACS Appl. Polym. Mater.* **2020**, *2* (2), 455–463. https://doi.org/10.1021/acsapm.9b00906.
(35) Choy, S.; Bui, H. T.; Van Lam, D.; Lee, S.-M.; Kim, W.; Hwang, D. S. Photocatalytic Exoskeleton: Chitin Nanofiber for Retrievable and Sustainable TiO2 Carriers for the Decomposition of Various Pollutants. *Carbohydr. Polym.* **2021**, *271*, 118413. https://doi.org/10.1016/j.carbpol.2021.118413.
(36) Wu, L.; Di Cio, S.; Azevedo, H. S.; Gautrot, J. E. Photoconfigurable, Cell-Remodelable Disulfide Cross-Linked Hyaluronic Acid Hydrogels. *Biomacromolecules* **2020**, *21* (12), 4663–4672. https://doi.org/10.1021/acs.biomac.0c00603.
(37) Pankin, D. V.; Mamonova, D. V.; Mongilyov, I.; Manshina, A. A.; Islamova, R. M. Photocured Organofunctional Silicon-Based Polymer and Its Y2O3 Nanocomposite as the Luminescence Tracer of Thermal History. *ACS Appl. Polym. Mater.* **2022**, *4* (11), 8357–8364. https://doi.org/10.1021/acsapm.2c01307.
(38) Zhang, M.; Wan, T.; Fan, P.; Shi, K.; Chen, X.; Yang, H.; Liu, X.; Xu, W.; Zhou, Y. Photopolymerizable Chitosan Hydrogels with Improved Strength and 3D Printability. *Int. J. Biol. Macromol.* **2021**, *193*, 109–116. https://doi.org/10.1016/j.ijbiomac.2021.10.137.
(39) Dong, H.; Liu, G.; Zhang, H. Preparation of Photodeformable Azobenzene Polymer Fibers by Post-Crosslinking Strategy: Understanding the Structure-Property Relationship. *Eur. Polym. J.* **2020**, *135*, 109863. https://doi.org/10.1016/j.eurpolymj.2020.109863.
(40) Ren, Y.; Zhao, Z.; Jiang, W.; Zhang, G.; Tan, Y.; Guan, Y.; Zhou, L.; Cui, L.; Choi, S. W.; Li, M.-X. Preparation of Y2O3/TiO2-Loaded Polyester Fabric and Its Photocatalytic Properties under Visible Light Irradiation. *Polymers* **2022**, *14* (14), 2760. https://doi.org/10.3390/polym14142760.
(41) Liu, Z.; He, L.; Gui, Q.; Yuan, Y.; Zhang, H. Preparation, Property Manipulation and Application of α-Cyanostilbene-Containing Photoresponsive Liquid Crystal Elastomers with Different Alkoxy Tail Length. *Eur. Polym. J.* **2021**, *147*, 110332. https://doi.org/10.1016/j.eurpolymj.2021.110332.

(42) Keyvan Rad, J.; Ghomi, A. R.; Karimipour, K.; Mahdavian, A. R. Progressive Readout Platform Based on Photoswitchable Polyacrylic Nanofibers Containing Spiropyran in Photopatterning with Instant Responsivity to Acid–Base Vapors. *Macromolecules* **2020**, *53* (5), 1613–1622. https://doi.org/10.1021/acs.macromol.9b02603.
(43) Emam, H. E.; Ahmed, H. B.; Gomaa, E.; Helal, M. H.; Abdelhameed, R. M. Recyclable Photocatalyst Composites Based on Ag3VO4 and Ag2WO4 @MOF@cotton for Effective Discoloration of Dye in Visible Light. *Cellulose* **2020**, *27* (12), 7139–7155. https://doi.org/10.1007/s10570-020-03282-8.
(44) Truong, V. X.; Barner-Kowollik, C. Red-Light Driven Photocatalytic Oxime Ligation for Bioorthogonal Hydrogel Design. *ACS Macro Lett.* **2021**, *10* (1), 78–83. https://doi.org/10.1021/acsmacrolett.0c00767.
(45) Wang, D.; Garra, P.; Fouassier, J. P.; Lalevée, J. Silane/Iodonium Salt as Redox/Thermal/Photoinitiating Systems in Radical and Cationic Polymerizations for Laser Write and Composites. *Polym. Chem.* **2020**, *11* (4), 857–866. https://doi.org/10.1039/C9PY01819K.
(46) Wang, C.; Fan, W.; Li, Z.; Xiong, J.; Zhang, W.; Wang, Z. Sonochemistry-Assisted Photocontrolled Atom Transfer Radical Polymerization Enabled by Manganese Carbonyl. *Polym. Chem.* **2022**, *13* (34), 4908–4914. https://doi.org/10.1039/D2PY00682K.
(47) Ávila-López, M. A.; Bonilla-Cruz, J.; Méndez-Nonell, J.; Lara-Ceniceros, T. E. Strong and Lightweight Stereolithographically 3D-Printed Polymer Nanocomposites with Low Friction and High Toughness. *Polymers* **2022**, *14* (17), 3628. https://doi.org/10.3390/polym14173628.
(48) Burk, M. H.; Langbehn, D.; Hernández Rodríguez, G.; Reichstein, W.; Drewes, J.; Schröder, S.; Rehders, S.; Strunskus, T.; Herges, R.; Faupel, F. Synthesis and Investigation of a Photoswitchable Copolymer Deposited via Initiated Chemical Vapor Deposition for Application in Organic Smart Surfaces. *ACS Appl. Polym. Mater.* **2021**, *3* (3), 1445–1456. https://doi.org/10.1021/acsapm.0c01312.
(49) Galarraga, J. H.; Dhand, A. P.; Enzmann, B. P. I.; Burdick, J. A. Synthesis, Characterization, and Digital Light Processing of a Hydrolytically Degradable Hyaluronic Acid Hydrogel. *Biomacromolecules* **2023**, *24* (1), 413–425. https://doi.org/10.1021/acs.biomac.2c01218.
(50) Foli, G.; Degli Esposti, M.; Morselli, D.; Fabbri, P. Two-Step Solvent-Free Synthesis of Poly(Hydroxybutyrate)-Based Photocurable Resin with Potential Application in Stereolithography. *Macromol. Rapid Commun.* **2020**, *41* (11), 1900660. https://doi.org/10.1002/marc.201900660.
(51) Kiliclar, H. C.; Gencosman, E.; Yagci, Y. Visible Light Induced Conventional Step-Growth and Chain-Growth Condensation Polymerizations by Electrophilic Aromatic

Substitution. *Macromol. Rapid Commun.* **2022**, *43* (1), 2100584. https://doi.org/10.1002/marc.202100584.

(52) Lu, Z.; Yang, H.; Fu, X.; Zhao, Y.; Xiao, L.; Zhang, Z.; Hou, L. Visible Light-Regulated Heterogeneous Catalytic PET-RAFT by High Crystallinity Covalent Organic Framework. *Macromol. Rapid Commun.* **2021**, *42* (20), 2100384. https://doi.org/10.1002/marc.202100384.

(53) Liu, S.; Zhou, X.; Qin, J.; Wei, C.; Hu, Y. 3-D Nitrogen-Doped Carbon Cage Encapsulated Ultrasmall MoC Nanoparticles for Promoting Simultaneous ZnIn2S4 Photocatalytic Hydrogen Generation and Organic Wastewater Degradation. *J. Colloid Interface Sci.* **2023**, *635*, 59–71. https://doi.org/10.1016/j.jcis.2022.12.073.

(54) Baran, W.; Cholewiński, M.; Sobczak, A.; Adamek, E. A New Mechanism of the Selective Photodegradation of Antibiotics in the Catalytic System Containing TiO2 and the Inorganic Cations. *Int. J. Mol. Sci.* **2021**, *22* (16), 8696. https://doi.org/10.3390/ijms22168696.

(55) Hu, Y.; Fan, Y.-C.; Jiang, X.-H.; Zhou, L.-M.; Cheng, Z.-J. A Ratiometric Fluorescent Sensing of Proanthocyanidins by MnO2 Nanosheets Simultaneously Tuning the Photoluminescence of Au/AgNCs and Thiamine. *Talanta* **2021**, *234*, 122607. https://doi.org/10.1016/j.talanta.2021.122607.

(56) Stivanin, M. L.; Gallo, R. D. C.; Spadeto, J. P. M.; Cormanich, R. A.; Jurberg, I. D. A Visible Light-Mediated Three-Component Strategy Based on the Ring-Opening of Cyclic Ethers with Aryldiazoacetates and Nucleophiles. *Org. Chem. Front.* **2022**, *9* (5), 1321–1326. https://doi.org/10.1039/D1QO01780B.

(57) Xu, F.; Zou, Q.; Xiong, G.; Zhang, H.; Wang, F.; Wang, Y. Activated Single-Phase Ti4O7 Nanosheets with Efficient Use of Precious Metal for Inspired Oxygen Reduction Reaction. *Chem. – Eur. J.* **2022**, *28* (68), e202202580. https://doi.org/10.1002/chem.202202580.

(58) Wang, J.; Li, X. Asymmetric β-Arylation of Cyclopropanols Enabled by Photoredox and Nickel Dual Catalysis. *Chem. Sci.* **2022**, *13* (10), 3020–3026. https://doi.org/10.1039/D1SC07237D.

(59) Xiong, M.; Shan, X.; Liu, C.; Yang, L.; Meng, M.; Di, Y.; Gan, Z. Broadband Photodetectors Based on Enhanced Photothermal Effect of Polymer Encapsulated Graphene Film. *Appl. Surf. Sci. Adv.* **2021**, *3*, 100050. https://doi.org/10.1016/j.apsadv.2020.100050.

(60) Liu, M.-S.; Shu, W. Catalytic, Metal-Free Amide Synthesis from Aldehydes and Imines Enabled by a Dual-Catalyzed Umpolung Strategy under Redox-Neutral Conditions. *ACS Catal.* **2020**, *10* (21), 12960–12966. https://doi.org/10.1021/acscatal.0c04070.

(61) Lin, M.; Zou, S.; Li, T.; Karges, J.; Chen, Y.; Zhao, Y.; Ji, L.; Chao, H. Chiral Rhodium(III)–Azobenzene Complexes as Photoswitchable DNA Molecular Locks. *Chem. Commun.* **2022**, *58* (27), 4324–4327. https://doi.org/10.1039/D2CC00932C.

(62) Chava, R. K.; Son, N.; Kang, M. Controllable Oxygen Doping and Sulfur Vacancies in One Dimensional CdS Nanorods for Boosted Hydrogen Evolution Reaction. *J. Alloys Compd.* **2021**, *873*, 159797. https://doi.org/10.1016/j.jallcom.2021.159797.
(63) Hao, M.; Chen, Z.; Liu, X.; Liu, X.; Zhang, J.; Yang, H.; Waterhouse, G. I. N.; Wang, X.; Ma, S. Converging Cooperative Functions into the Nanospace of Covalent Organic Frameworks for Efficient Uranium Extraction from Seawater. *CCS Chem.* **2022**, *4* (7), 2294–2307. https://doi.org/10.31635/ccschem.022.202201897.
(64) Sadale, S. B.; Neumann-Spallart, M. Drop-Cast Tungsten Trioxide Semiconducting Films in Photoelectrocatalysis. *J. Electroanal. Chem.* **2020**, *877*, 114502. https://doi.org/10.1016/j.jelechem.2020.114502.
(65) Guo, T.; Jiang, L.; Wang, K.; Li, Y.; Huang, H.; Wu, X.; Zhang, G. Efficient Persulfate Activation by Hematite Nanocrystals for Degradation of Organic Pollutants under Visible Light Irradiation: Facet-Dependent Catalytic Performance and Degradation Mechanism. *Appl. Catal. B Environ.* **2021**, *286*, 119883. https://doi.org/10.1016/j.apcatb.2021.119883.
(66) Ahmad, A.; Yerlikaya, G.; Zia-ur-Rehman; Paksoy, H.; Kardaş, G. Enhanced Photoelectrochemical Water Splitting Using Gadolinium Doped Titanium Dioxide Nanorod Array Photoanodes. *Int. J. Hydrog. Energy* **2020**, *45* (4), 2709–2719. https://doi.org/10.1016/j.ijhydene.2019.11.117.
(67) Ali, S.; Ali, H.; Siddique, M.; Gulab, H.; Haleem, M. A.; Ali, J. Exploring the Biosynthesized Gold Nanoparticles for Their Antibacterial Potential and Photocatalytic Degradation of the Toxic Water Wastes under Solar Light Illumination. *J. Mol. Struct.* **2020**, *1215*, 128259. https://doi.org/10.1016/j.molstruc.2020.128259.
(68) Wang, J.; Kuo, M.; Zeng, P.; Xu, L.; Chen, S.; Peng, T. Few-Layer BiVO4 Nanosheets Decorated with SrTiO3: Rh Nanoparticles for Highly Efficient Visible-Light-Driven Overall Water Splitting. *Appl. Catal. B Environ.* **2020**, *279*, 119377. https://doi.org/10.1016/j.apcatb.2020.119377.
(69) Mo, Z.; Wang, K.; Yang, H.; Ou, Z.; Tong, Y.; Yu, T.; Wang, Y.; Tsiakaras, P.; Song, S. Heterojunction Architecture of pTTh Nanoflowers with CuOx Nanoparticles Hybridized for Efficient Photoelectrocatalytic Degradation of Organic Pollutants. *Appl. Catal. B Environ.* **2020**, *277*, 119249. https://doi.org/10.1016/j.apcatb.2020.119249.
(70) Fang, M.-H.; Chen, K.-C.; Majewska, N.; Leśniewski, T.; Mahlik, S.; Leniec, G.; Kaczmarek, S. M.; Yang, C.-W.; Lu, K.-M.; Sheu, H.-S.; Liu, R.-S. Hidden Structural Evolution and Bond Valence Control in Near-Infrared Phosphors for Light-Emitting Diodes. *ACS Energy Lett.* **2021**, *6* (1), 109–114. https://doi.org/10.1021/acsenergylett.0c02373.
(71) Chen, Y.-C.; Chen, D.-B.; Zeng, G.; Li, X.-X.; Li, Y.-C.; Zhao, X.-F.; Chen, N.; Wang, T.-Y.; Yang, Y.-G.; Zhang, D. W.; Lu, H.-L. High Performance Solar-Blind Photodetectors Based on Plasma-Enhanced Atomic Layer Deposition of Thin

Ga2O3 Films Annealed under Different Atmosphere. *J. Alloys Compd.* **2023**, *936*, 168127. https://doi.org/10.1016/j.jallcom.2022.168127.
(72) Qi, Y.; Zhang, X.; Huang, X.; Zhang, Y.; Shi, M.; Zhao, Y. High-Efficient Lignin-Based Polymerizable Macromolecular Photoinitiator with UV-Blocking Property for Visible Light Polymerization. *Int. J. Biol. Macromol.* **2022**, *204*, 234–244. https://doi.org/10.1016/j.ijbiomac.2022.01.199.
(73) Choi, G. H.; Kim, D. J.; Moon, J.; Kim, J. H.; Park, J. T. High-Order Diffraction Grating as Light Harvesters for Solar Energy Conversion. *J. Electroanal. Chem.* **2020**, *873*, 114490. https://doi.org/10.1016/j.jelechem.2020.114490.
(74) Wang, J.-W.; Ma, F.; Jin, T.; He, P.; Luo, Z.-M.; Kupfer, S.; Karnahl, M.; Zhao, F.; Xu, Z.; Jin, T.; Lian, T.; Huang, Y.-L.; Jiang, L.; Fu, L.-Z.; Ouyang, G.; Yi, X.-Y. Homoleptic Al(III) Photosensitizers for Durable CO2 Photoreduction. *J. Am. Chem. Soc.* **2023**, *145* (1), 676–688. https://doi.org/10.1021/jacs.2c11740.
(75) Kumar, R.; Khan, M. A.; Anupama, A. V.; Krupanidhi, S. B.; Sahoo, B. Infrared Photodetectors Based on Multiwalled Carbon Nanotubes: Insights into the Effect of Nitrogen Doping. *Appl. Surf. Sci.* **2021**, *538*, 148187. https://doi.org/10.1016/j.apsusc.2020.148187.
(76) Stepikhova, M. V.; Dyakov, S. A.; Peretokin, A. V.; Shaleev, M. V.; Rodyakina, E. E.; Novikov, A. V. Interaction of Ge(Si) Self-Assembled Nanoislands with Different Modes of Two-Dimensional Photonic Crystal. *Nanomaterials* **2022**, *12* (15), 2687. https://doi.org/10.3390/nano12152687.
(77) Li, Y.; Zhu, H.; Duan, J.; Wu, Y.; Wu, D. Laser-Induced Photoexcited Audible Sound Effect Based on Reticular 2-Bromo-2-Methylpropionic Acid Modified Fe3O4 Nanoparticle Aggregates. *Nanoscale* **2022**, *14* (45), 16787–16796. https://doi.org/10.1039/D2NR04895G.
(78) Allen, M. J.; Lien, H.-M.; Prine, N.; Burns, C.; Rylski, A. K.; Gu, X.; Cox, L. M.; Mangolini, F.; Freeman, B. D.; Page, Z. A. Multimorphic Materials: Spatially Tailoring Mechanical Properties via Selective Initiation of Interpenetrating Polymer Networks. *Adv. Mater.* **2023**, *35* (9), 2210208. https://doi.org/10.1002/adma.202210208.
(79) Alam, S.; Sahu, T. K.; Qureshi, M. One-Dimensional Co(OH)F as a Noble Metal-Free Redox Mediator and Hole Extractor for Boosted Photoelectrochemical Water Oxidation in Worm-like Bismuth Vanadate. *ACS Sustain. Chem. Eng.* **2021**, *9* (14), 5155–5165. https://doi.org/10.1021/acssuschemeng.1c00288.
(80) Yurdakal, S.; Çetinkaya, S.; Özcan, L.; Gök, Ö.; Palmisano, L. Partial Photoelectrocatalytic Oxidation of 3-Pyridinemethanol by Pt, Au and Pd Loaded TiO2 Nanotubes on Ti Plate. *Catal. Today* **2021**, *380*, 248–258. https://doi.org/10.1016/j.cattod.2020.11.003.
(81) Kapuge, T. K.; Thalgaspitiya, W. R. K.; Rathnayake, D.; He, J.; Kerns, P.; Suib, S. L. Photo-Generated Reactive Oxygen Species Assisted Tandem Amine Homocoupling and Amine-Alcohol Cross-Coupling Reaction on Mesoporous Spinel Cobalt Oxide.

Appl. Catal. B Environ. **2020**, *268*, 118386. https://doi.org/10.1016/j.apcatb.2019.118386.

(82) Inoue, S.; Yan, Y.-N.; Yamanishi, K.; Kataoka, Y.; Kawamoto, T. Photocatalytic and Electrocatalytic Hydrogen Production Using Nickel Complexes Supported by Hemilabile and Non-Innocent Ligands. *Chem. Commun.* **2020**, *56* (19), 2829–2832. https://doi.org/10.1039/C9CC09568C.

(83) Xu, J.; Green, N. J.; Russell, D. A.; Liu, Z.; Sutherland, J. D. Prebiotic Photochemical Coproduction of Purine Ribo- and Deoxyribonucleosides. *J. Am. Chem. Soc.* **2021**, *143* (36), 14482–14486. https://doi.org/10.1021/jacs.1c07403.

(84) Liu, H.; Liang, J.; shao, L.; Du, J.; Gao, Q.; Fu, S.; Li, L.; Hu, M.; Zhao, F.; Zhou, J. Promoting Charge Separation in Dual Defect Mediated Z-Scheme MoS2/g-C3N4 Photocatalysts for Enhanced Photocatalytic Degradation Activity: Synergistic Effect Insight. *Colloids Surf. Physicochem. Eng. Asp.* **2020**, *594*, 124668. https://doi.org/10.1016/j.colsurfa.2020.124668.

(85) Hemmerling, J.; Quinn, J.; Linic, S. Quantifying Losses and Assessing the Photovoltage Limits in Metal–Insulator–Semiconductor Water Splitting Systems. *Adv. Energy Mater.* **2020**, *10* (12), 1903354. https://doi.org/10.1002/aenm.201903354.

(86) Wang, H.; Wang, M.; Chi, H.; Zhang, S.; Wang, Y.; Wu, D.; Wei, Q. Sandwich-Type Photoelectrochemical Immunosensor for Procalcitonin Detection Based on Mn2+ Doped CdS Sensitized Bi2WO6 and Signal Amplification of NaYF4:Yb, Tm Upconversion Nanomaterial. *Anal. Chim. Acta* **2021**, *1188*, 339190. https://doi.org/10.1016/j.aca.2021.339190.

(87) Cao, R.; Wang, G.; Ren, X.; Duan, P.-C.; Wang, L.; Li, Y.; Chen, X.; Zhu, R.; Jia, Y.; Bai, F. Self-Assembled Porphyrin Nanoleaves with Unique Crossed Transportation of Photogenerated Carriers to Enhance Photocatalytic Hydrogen Production. *Nano Lett.* **2022**, *22* (1), 157–163. https://doi.org/10.1021/acs.nanolett.1c03550.

(88) Zhang, G.; Zhang, J.; Wang, Y.; Wu, Y.; Li, Q.; Liang, Y.; Qi, W.; Rao, H.; Su, R.; He, Z. Self-Assembly of Multifunctional Hydrogels with Polyoxometalates Helical Arrays Using Nematic Peptide Liquid Crystal Template. *J. Colloid Interface Sci.* **2020**, *578*, 218–228. https://doi.org/10.1016/j.jcis.2020.05.116.

(89) Sui, C.; Tan, R.; Liu, Z.; Li, X.; Xu, W. Smart Chemical Oxidative Polymerization Strategy To Construct Au@PPy Core–Shell Nanoparticles for Cancer Diagnosis and Imaging-Guided Photothermal Therapy. *Bioconjug. Chem.* **2023**, *34* (1), 257–268. https://doi.org/10.1021/acs.bioconjchem.2c00549.

(90) Liu, Z.; Xie, X.; Huang, Z.; Lin, F.; Liu, S.; Chen, Z.; Qin, S.; Fan, X.; Chen, P. R. Spatially Resolved Cell Tagging and Surfaceome Labeling via Targeted Photocatalytic Decaging. *Chem* **2022**, *8* (8), 2179–2191. https://doi.org/10.1016/j.chempr.2022.04.016.

(91) Ghiat, I.; Saadi, A.; Bachari, K.; Coville, N. J.; Boudjemaa, A. Spherical NiCu Phyllosilicate Photocatalysts for Hydrogen Generation. *Int. J. Hydrog. Energy* **2021**, *46* (75), 37656–37669. https://doi.org/10.1016/j.ijhydene.2020.10.203.
(92) Li, B.; Cui, Y.; Feng, Y.; Wu, C.; Yan, Y.; Meng, M. Study of Enhanced Photocatalytic Performance Mechanisms towards a New Binary-Bi Heterojunction with Spontaneously Formed Interfacial Defects. *Appl. Surf. Sci.* **2020**, *532*, 147412. https://doi.org/10.1016/j.apsusc.2020.147412.
(93) Zhang, S.; Yuan, Y.; Gu, J.; Huang, X.; Li, P.; Yin, K.; Xiao, Z.; Wang, D. Surface Defect-Induced Electronic Structures of Lead-Free Cs2AgBiBr6 Double-Perovskite for Efficiently Solar-Driven Photocatalytic Performance. *Appl. Surf. Sci.* **2023**, *609*, 155446. https://doi.org/10.1016/j.apsusc.2022.155446.
(94) Ali, G.; Jazib Abbas Zaidi, S.; Abdul Basit, M.; Park, T. J. Synergetic Performance of Systematically Designed G-C3N4/rGO/SnO2 Nanocomposite for Photodegradation of Rhodamine-B Dye. *Appl. Surf. Sci.* **2021**, *570*, 151140. https://doi.org/10.1016/j.apsusc.2021.151140.
(95) Li, Z.; Ji, W.-W.; Hao, L.-Y.; Yin, L.-J.; Xu, X.; Agathopoulos, S.; Lee, M.-H. Synthesis of G-La2Si2O7:Eu2+ Phosphors by Addition of AlF3: Experimental and Theoretical Analysis. *J. Alloys Compd.* **2020**, *844*, 156127. https://doi.org/10.1016/j.jallcom.2020.156127.
(96) Ovcharenko, A.; Weissenboeck, F. P.; Rentmeister, A. Tag-Free Internal RNA Labeling and Photocaging Based on mRNA Methyltransferases. *Angew. Chem. Int. Ed.* **2021**, *60* (8), 4098–4103. https://doi.org/10.1002/anie.202013936.
(97) Erol, E.; Vahedigharehchopogh, N.; Ekim, U.; Uza, N.; Çelikbilek Ersundu, M.; Ersundu, A. E. Ultra-Stable Eu3+/Dy3+ Co-Doped CsPbBr3 Quantum Dot Glass Nanocomposites with Tunable Luminescence Properties for Phosphor-Free WLED Applications. *J. Alloys Compd.* **2022**, *909*, 164650. https://doi.org/10.1016/j.jallcom.2022.164650.
(98) Fu, Y.; Helbert, H.; Simeth, N. A.; Crespi, S.; Spoelstra, G. B.; van Dijl, J. M.; van Oosten, M.; Nazario, L. R.; van der Born, D.; Luurtsema, G.; Szymanski, W.; Elsinga, P. H.; Feringa, B. L. Ultrafast Photoclick Reaction for Selective 18F-Positron Emission Tomography Tracer Synthesis in Flow. *J. Am. Chem. Soc.* **2021**, *143* (27), 10041–10047. https://doi.org/10.1021/jacs.1c02229.
(99) Miao, Y.-Q.; Kang, J.-X.; Ma, Y.-N.; Chen, X. Visible Light-Mediated Synthesis of Amides from Carboxylic Acids and Amine-Boranes. *Green Chem.* **2021**, *23* (10), 3595–3599. https://doi.org/10.1039/D1GC01157J.
(100) Katagiri, T.; Kita, Y.; Amao, Y. Visible-Light Driven Enantioselective *L*-Lactate Synthesis with a Combination System of Biocatalyst and Dye-Sensitized NAD+ Reduction. *Catal. Today* **2023**, *410*, 289–294. https://doi.org/10.1016/j.cattod.2022.04.018.

(101) Wei, H.; Zhang, B.; Lei, M.; Lu, Z.; Liu, J.; Guo, B.; Yu, Y. Visible-Light-Mediated Nano-Biomineralization of Customizable Tough Hydrogels for Biomimetic Tissue Engineering. *ACS Nano* **2022**, *16* (3), 4734–4745. https://doi.org/10.1021/acsnano.1c11589.

(102) Guo, P.; Hu, X. ZIF-Derived CoFe2O4/Fe2O3 Combined with g-C3N4 as High-Efficient Photocatalysts for Enhanced Degradation of Levofloxacin in the Presence of Peroxymonosulfate. *J. Alloys Compd.* **2022**, *914*, 165338. https://doi.org/10.1016/j.jallcom.2022.165338.

(103) Alsaif, M. M. Y. A.; Haque, F.; Alkathiri, T.; Krishnamurthi, V.; Walia, S.; Hu, Y.; Jannat, A.; Mohiuddin, M.; Xu, K.; Khan, M. W.; Ma, Q.; Wang, Y.; Pillai, N.; Murdoch, B. J.; Dickey, M. D.; Zhang, B. Y.; Ou, J. Z. 3D Visible-Light-Driven Plasmonic Oxide Frameworks Deviated from Liquid Metal Nanodroplets. *Adv. Funct. Mater.* **2021**, *31* (52), 2106397. https://doi.org/10.1002/adfm.202106397.

(104) Zhang, C.; Wang, K.; Guo, X.; Tang, Y. A Cationic Conjugated Polymer with High 808 Nm NIR-Triggered Photothermal Conversion for Antibacterial Treatment. *J. Mater. Chem. C* **2022**, *10* (7), 2600–2607. https://doi.org/10.1039/D1TC03128G.

(105) Lee, H.; Partanen, M.; Lee, M.; Jeong, S.; Lee, H. J.; Kim, K.; Ryu, W.; Dholakia, K.; Oh, K. A Laser-Driven Optical Atomizer: Photothermal Generation and Transport of Zeptoliter-Droplets along a Carbon Nanotube Deposited Hollow Optical Fiber. *Nanoscale* **2022**, *14* (13), 5138–5146. https://doi.org/10.1039/D1NR06211E.

(106) Zhao, S.; Yang, X.; Xu, Y.; Weng, Z.; Liao, L.; Wang, X. A Sprayable Superhydrophobic Dental Protectant with Photo-Responsive Anti-Bacterial, Acid-Resistant, and Anti-Fouling Functions. *Nano Res.* **2022**, *15* (6), 5245–5255. https://doi.org/10.1007/s12274-022-4136-6.

(107) Chang, L.; Wang, D.; Huang, Z.; Wang, C.; Torop, J.; Li, B.; Wang, Y.; Hu, Y.; Aabloo, A. A Versatile Ionomer-Based Soft Actuator with Multi-Stimulus Responses, Self-Sustainable Locomotion, and Photoelectric Conversion. *Adv. Funct. Mater.* **2023**, *33* (6), 2212341. https://doi.org/10.1002/adfm.202212341.

(108) Meng, X.; Zhang, B.; Yi, Y.; Cheng, H.; Wang, B.; Liu, Y.; Gong, T.; Yang, W.; Yao, Y.; Wang, H.; Bu, W. Accurate and Real-Time Temperature Monitoring during MR Imaging Guided PTT. *Nano Lett.* **2020**, *20* (4), 2522–2529. https://doi.org/10.1021/acs.nanolett.9b05267.

(109) Matveev, A. T.; Konopatsky, A. S.; Leybo, D. V.; Volkov, I. N.; Kovalskii, A. M.; Varlamova, L. A.; Sorokin, P. B.; Fang, X.; Kulinich, S. A.; Shtansky, D. V. Amorphous MoSxOy/h-BNxOy Nanohybrids: Synthesis and Dye Photodegradation. *Nanomaterials* **2021**, *11* (12), 3232. https://doi.org/10.3390/nano11123232.

(110) Haider, A. A.; Cun, Y.; Bai, X.; Xu, Z.; Zi, Y.; Qiu, J.; Song, Z.; Huang, A.; Yang, Z. Anti-Counterfeiting Applications by Photochromism Induced Modulation of Reversible Upconversion Luminescence in TiO2:Yb3+,Er3+ Ceramic. *J. Mater. Chem. C* **2022**, *10* (16), 6243–6251. https://doi.org/10.1039/D2TC00859A.

(111) Zhang, Y.-S.; Jiang, S.-A.; Lin, J.-D.; Lee, C.-R. Bio-Inspired Design of Active Photo-Mechano-Chemically Dual-Responsive Photonic Film Based on Cholesteric Liquid Crystal Elastomers. *J. Mater. Chem. C* **2020**, *8* (16), 5517–5524. https://doi.org/10.1039/C9TC05758G.

(112) Lohmann, S.-H.; Cai, T.; Morrow, D. J.; Chen, O.; Ma, X. Brightening of Dark States in CsPbBr3 Quantum Dots Caused by Light-Induced Magnetism. *Small* **2021**, *17* (37), 2101527. https://doi.org/10.1002/smll.202101527.

(113) Guo, J.; Hao, Y.; Kuklin, A. V.; Bao, W.; Wageh, S.; Al-Hartomy, O. A.; Al-sehemi, A. G.; Ågren, H.; Gao, L.; Zhang, H. Broadband Nonlinear Response and Ultrafast Photonics Applications in Few-Layer MBene. *ACS Photonics* **2023**, *10* (7), 2353–2362. https://doi.org/10.1021/acsphotonics.2c01548.

(114) Du, P.; Niu, P.; Yang, Y.; Chen, R.; Yin, L.-C.; Fan, F.; Liu, G. Constructing Anatase–Brookite TiO2 Phase Junction by Thermal Topotactic Transition to Promote Charge Separation for Superior Photocatalytic H2 Generation. *J. Phys. Chem. Lett.* **2022**, *13* (19), 4244–4250. https://doi.org/10.1021/acs.jpclett.2c00964.

(115) Kim, E.; Do, K. H.; Wang, J.; Hong, Y.; Putta Rangappa, A.; Amaranatha Reddy, D.; Praveen Kumar, D.; Kim, T. K. Construction of 1D TiO2 Nanotubes Integrated Ultrathin 2D ZnIn2S4 Nanosheets Heterostructure for Highly Efficient and Selective Photocatalytic CO2 Reduction. *Appl. Surf. Sci.* **2022**, *587*, 152895. https://doi.org/10.1016/j.apsusc.2022.152895.

(116) Agarwal, A. K.; Pant, K. K.; Mishra, S. K. Development of Microlens Arrays With Large Focal Number and High Fill Factor for Wavefront Sensing Applications. *IEEE Sens. J.* **2021**, *21* (18), 20990–20997. https://doi.org/10.1109/JSEN.2021.3097129.

(117) Yang, Z.; Li, H.; Cui, X.; Zhu, J.; Li, Y.; Zhang, P.; Li, J. Direct Z-Scheme Nanoporous BiVO4/CdS Quantum Dots Heterojunction Composites as Photoanodes for Photocathodic Protection of 316 Stainless Steel under Visible Light. *Appl. Surf. Sci.* **2022**, *603*, 154394. https://doi.org/10.1016/j.apsusc.2022.154394.

(118) Yang, Q.; Shen, J.; Jiang, H.; Leng, C.; Zhang, Z.; Nie, C.; Huang, D.; Li, X.; Feng, S.; Zhou, D.; Luo, W.; Yao, W.; Wang, L.; Sun, L.; Wei, X. Dual-Color Photodetection Based on Speed-Differentiated Photoresponse with High Photogain. *ACS Photonics* **2021**, *8* (4), 1027–1033. https://doi.org/10.1021/acsphotonics.1c00136.

(119) Liu, G.; Wang, B.; Zhu, X.; Ding, P.; Zhao, J.; Li, H.; Chen, Z.; Zhu, W.; Xia, J. Edge-Site-Rich Ordered Macroporous BiOCl Triggers C□O Activation for Efficient CO2 Photoreduction. *Small* **2022**, *18* (6), 2105228. https://doi.org/10.1002/smll.202105228.

(120) Liu, S.; Li, M.-Y.; Xiong, K.; Gao, J.; Lan, X.; Zhang, D.; Gao, L.; Zhang, J.; Tang, J. Efficient Quantum Dot Infrared Solar Cells with Enhanced Low-Energy Photon Conversion via Optical Engineering. *Nano Res.* **2023**, *16* (2), 2392–2398. https://doi.org/10.1007/s12274-022-4906-1.

(121) Lin, Z.; Zhu, W.; Zeng, Y.; Shu, Y.; Hu, H.; Chen, W.; Li, J. Enhanced Photodetection Range from Visible to Shortwave Infrared Light by ReSe2/MoTe2 van Der Waals Heterostructure. *Nanomaterials* **2022**, *12* (15), 2664. https://doi.org/10.3390/nano12152664.

(122) Chen, Y.; Shu, T.; Lai, T.; Wu, H. Excitation-Density and Excess-Energy Dependence of Ultrafast Dynamics of Photoexcited Carriers in Intrinsic Bulk CdTe. *Results Phys.* **2021**, *31*, 105047. https://doi.org/10.1016/j.rinp.2021.105047.

(123) Yang, T.; Li, Y.; Han, S.; Liu, Y.; Xu, Z.; Li, M.; Wang, J.; Ma, Y.; Luo, J.; Sun, Z. Exploiting Two-Dimensional Hybrid Perovskites Incorporating Secondary Amines for High-Performance Array Photodetection. *J. Mater. Chem. C* **2020**, *8* (37), 12848–12853. https://doi.org/10.1039/D0TC03382K.

(124) Zhang, M.; Zhao, M.; Chen, R.; Liu, J.; Liu, Q.; Yu, J.; Li, R.; Liu, P.; Wang, J. Fabrication of the Pod-like KCC-1/TiO2 Superhydrophobic Surface on AZ31 Mg Alloy with Stability and Photocatalytic Property. *Appl. Surf. Sci.* **2020**, *499*, 143933. https://doi.org/10.1016/j.apsusc.2019.143933.

(125) Gao, F.; Chen, H.; Feng, W.; Hu, Y.; Shang, H.; Xu, B.; Zhang, J.; Xu, C.-Y.; Hu, P. High-Performance van Der Waals Metal-Insulator-Semiconductor Photodetector Optimized with Valence Band Matching. *Adv. Funct. Mater.* **2021**, *31* (35), 2104359. https://doi.org/10.1002/adfm.202104359.

(126) Chen, S.; Gai, X.; Liang, J.; Ye, K.; Liu, Y.; Wang, Y. Highly Efficient Phosphorescent Organic Light-Emitting Diodes Based on Novel Bipolar Iridium Complexes with Easily-Tuned Emission Colors by Adjusting Fluorine Substitution on Phenylpyridine Ligands. *J. Mater. Chem. C* **2021**, *9* (26), 8329–8336. https://doi.org/10.1039/D1TC01498F.

(127) Ussia, M.; Urso, M.; Kment, S.; Fialova, T.; Klima, K.; Dolezelikova, K.; Pumera, M. Light-Propelled Nanorobots for Facial Titanium Implants Biofilms Removal. *Small* **2022**, *18* (22), 2200708. https://doi.org/10.1002/smll.202200708.

(128) Chiu, P.-H.; Cheng, W.-H.; Lee, M.-T.; Yasuda, K.; Song, J.-M. Low-Thermal-Budget Photonic Sintering of Hybrid Pastes Containing Submicron/Nano CuO/Cu2O Particles. *Nanomaterials* **2021**, *11* (7), 1864. https://doi.org/10.3390/nano11071864.

(129) Yin, S.; Chen, J.; Wu, Y.; Chen, Z.; Yuan, T.; Liu, Q.; Wang, Y.; Hou, H. Mechanisms of Impurity-Enhanced Spatial Carrier Separation and Photocatalytic Activity of F–N Codoped *m*-ZrO2 Nanocrystals. *J. Phys. Chem. Solids* **2020**, *140*, 109363. https://doi.org/10.1016/j.jpcs.2020.109363.

(130) Laferrière, P.; Yeung, E.; Giner, L.; Haffouz, S.; Lapointe, J.; Aers, G. C.; Poole, P. J.; Williams, R. L.; Dalacu, D. Multiplexed Single-Photon Source Based on Multiple Quantum Dots Embedded within a Single Nanowire. *Nano Lett.* **2020**, *20* (5), 3688–3693. https://doi.org/10.1021/acs.nanolett.0c00607.

(131) Guo, Y.; Yan, R.; Wang, X.; Liang, G.; Yang, A.; Li, J. Near-Infrared Light-Controlled Activation of Adhesive Peptides Regulates Cell Adhesion and

Multidifferentiation in Mesenchymal Stem Cells on an Up-Conversion Substrate. *Nano Lett.* **2022**, *22* (6), 2293–2302. https://doi.org/10.1021/acs.nanolett.1c04534.

(132) Pang, H.; Tian, C.; He, G.; Zhang, D.; Yang, J.; Zhang, Q.; Liu, R. NIR-Absorbing Prussian Blue Nanoparticles for Transarterial Infusion Photothermal Therapy of VX2 Tumors Implanted in Rabbits. *Nanoscale* **2021**, *13* (18), 8490–8497. https://doi.org/10.1039/D1NR01394G.

(133) Muralidhar, J. R.; Kodama, K.; Hirose, T.; Ito, Y.; Kawamoto, M. Noncovalent Functionalization of Single-Walled Carbon Nanotubes with a Photocleavable Polythiophene Derivative. *Nanomaterials* **2022**, *12* (1), 52. https://doi.org/10.3390/nano12010052.

(134) Serra, J.; Sequeira, S.; Domingos, I.; Paracana, A.; Maçôas, E.; Melo, L. V.; Pires, B. J.; Cardoso, S.; Leitao, D. C.; Alves, H. Organic Single Crystal Patterning Method for Micrometric Photosensors. *Adv. Funct. Mater.* **2021**, *31* (47), 2105638. https://doi.org/10.1002/adfm.202105638.

(135) Pei, L.; Ma, Z.; Zhong, J.; Li, W.; Wen, X.; Guo, J.; Liu, P.; Zhang, Z.; Mao, Q.; Zhang, J.; Yan, S.; Zou, Z. Oxygen Vacancy-Rich Sr2MgSi2O7:Eu2+,Dy3+ Long Afterglow Phosphor as a Round-the-Clock Catalyst for Selective Reduction of CO2 to CO. *Adv. Funct. Mater.* **2022**, *32* (49), 2208565. https://doi.org/10.1002/adfm.202208565.

(136) Zhang, T.; Jiang, Z.; Chen, L.; Pan, C.; Sun, S.; Liu, C.; Li, Z.; Ren, W.; Wu, A.; Huang, P. PCN-Fe(III)-PTX Nanoparticles for MRI Guided High Efficiency Chemo-Photodynamic Therapy in Pancreatic Cancer through Alleviating Tumor Hypoxia. *Nano Res.* **2020**, *13* (1), 273–281. https://doi.org/10.1007/s12274-019-2610-6.

(137) Paul, S.; Samanta, A. Phase-Stable and Highly Luminescent CsPbI3 Perovskite Nanocrystals with Suppressed Photoluminescence Blinking. *J. Phys. Chem. Lett.* **2022**, *13* (25), 5742–5750. https://doi.org/10.1021/acs.jpclett.2c01463.

(138) Kim, J.; Park, H. K.; Cho, Y.; Kim, S.; Yang, K.-J.; Kim, D.-H.; Kang, J.-K.; Jo, W. Photo-Excited Carrier Transport and Secondary Phases of Na-Engineered Kesterite Flexible Thin Films. *Sol. Energy Mater. Sol. Cells* **2023**, *250*, 112091. https://doi.org/10.1016/j.solmat.2022.112091.

(139) Bolzonello, L.; Bernal-Texca, F.; Gerling, L. G.; Ockova, J.; Collini, E.; Martorell, J.; van Hulst, N. F. Photocurrent-Detected 2D Electronic Spectroscopy Reveals Ultrafast Hole Transfer in Operating PM6/Y6 Organic Solar Cells. *J. Phys. Chem. Lett.* **2021**, *12* (16), 3983–3988. https://doi.org/10.1021/acs.jpclett.1c00822.

(140) Silva, P. D.; Bano, S.; Pogue, B. W.; Wang, K. K.; Maytin, E. V.; Hasan, T. Photodynamic Priming with Triple-Receptor Targeted Nanoconjugates That Trigger T Cell-Mediated Immune Responses in a 3D in Vitro Heterocellular Model of Pancreatic Cancer. *Nanophotonics* **2021**, *10* (12), 3199–3214. https://doi.org/10.1515/nanoph-2021-0304.

(141) Cai, L.-Z.; Guo, P.-Y.; Wang, M.-S.; Guo, G.-C. Photoinduced Magnetic Phase Transition and Remarkable Enhancement of Magnetization for a Photochromic Single-Molecule Magnet. *J. Mater. Chem. C* **2021**, *9* (7), 2231–2235. https://doi.org/10.1039/D0TC05490A.

(142) Singh, A.; Joseph, J. P.; Gupta, D.; Miglani, C.; Mavlankar, N. A.; Pal, A. Photothermally Switchable Peptide Nanostructures towards Modulating Catalytic Hydrolase Activity. *Nanoscale* **2021**, *13* (31), 13401–13409. https://doi.org/10.1039/D1NR03655F.

(143) Ma, J.; Liu, X.; Wang, R.; Zhang, F.; Tu, G. Plasmon-Induced near-Field and Resonance Energy Transfer Enhancement of Photodegradation Activity by Au Wrapped CuS Dual-Chain. *Nano Res.* **2022**, *15* (6), 5671–5677. https://doi.org/10.1007/s12274-022-4129-5.

(144) Dymerska, A.; Zielińska, B.; Sielicki, K.; Chen, X.; Mijowska, E. Porous Silica Matrix as an Efficient Strategy to Boosted Photocatalytic Performance of Titania/Carbon Composite. *Diam. Relat. Mater.* **2022**, *125*, 109027. https://doi.org/10.1016/j.diamond.2022.109027.

(145) Chen, B.; Yang, N.; Wang, P.; Xiang, Y.; Chen, H. Post-Side Chain Engineering of Difluorinated Benzothiadiazole-Based Conjugated Microporous Polymer for Enhanced Photocatalytic H2 Evolution. *Appl. Surf. Sci.* **2020**, *499*, 143865. https://doi.org/10.1016/j.apsusc.2019.143865.

(146) Yang, M.; Wang, K.; Li, Y.; Yang, K.; Jin, Z. Pristine Hexagonal CdS Assembled with NiV LDH Nanosheet Formed P-n Heterojunction for Efficient Photocatalytic Hydrogen Evolution. *Appl. Surf. Sci.* **2021**, *548*, 149212. https://doi.org/10.1016/j.apsusc.2021.149212.

(147) Hemmerling, J.; Quinn, J.; Linic, S. Quantifying Losses and Assessing the Photovoltage Limits in Metal–Insulator–Semiconductor Water Splitting Systems. *Adv. Energy Mater.* **2020**, *10* (12), 1903354. https://doi.org/10.1002/aenm.201903354.

(148) Liu, Y.; Gong, Z.; Lv, H.; Ren, H.; Xing, X. Rational Design of Au Decorated Mn0.5Cd0.5S/WO3 Step-Scheme Heterostructure with Multichannel Charge Transfer and Efficient H2 Generation. *Appl. Surf. Sci.* **2020**, *526*, 146734. https://doi.org/10.1016/j.apsusc.2020.146734.

(149) Zhang, J.; Nuño Ruano, P.; Le-Roux, X.; Montesinos-Ballester, M.; Marris-Morini, D.; Cassan, E.; Vivien, L.; Lanzillotti-Kimura, N. D.; Ramos, C. A. Subwavelength Control of Photons and Phonons in Release-Free Silicon Optomechanical Resonators. *ACS Photonics* **2022**, *9* (12), 3855–3862. https://doi.org/10.1021/acsphotonics.2c00791.

(150) Palluel, M.; Tran, N. M.; Daro, N.; Buffière, S.; Mornet, S.; Freysz, E.; Chastanet, G. The Interplay between Surface Plasmon Resonance and Switching Properties in Gold@Spin Crossover Nanocomposites. *Adv. Funct. Mater.* **2020**, *30* (17), 2000447. https://doi.org/10.1002/adfm.202000447.

(151) Zhao, F.; Song, Y.; Liu, X.; Zhang, X.; Ma, C.; Wang, G.; Fu, Y.; Ma, H. Unraveling Electron-Deficient Setaria-Viridis-like Co3O4@MnO2 Heterostructure with Superior Photoelectrocatalytic Efficiency for Water Remediation. *Appl. Surf. Sci.* **2022**, *573*, 151473. https://doi.org/10.1016/j.apsusc.2021.151473.
(152) He, Y.; Shu, C.-C.; Guo, Y.; Long, M.; Xu, H. Visualizing Ultrasmall Silica–CTAB Hybrid Nanoparticles for Generating High Photoluminescence. *J. Mater. Chem. C* **2020**, *8* (19), 6413–6421. https://doi.org/10.1039/D0TC00797H.